

EPITAXIAL STRAIN ENGINEERING OF SUPERCONDUCTIVITY IN RUTHENATE THIN FILMS

A Dissertation

Presented to the Faculty of the Graduate School

of Cornell University

in Partial Fulfillment of the Requirements for the Degree of

Doctor of Philosophy

by

Jacob Paul Ruf

December 2019

© 2019 Jacob Paul Ruf

This work is licensed under a Creative Commons
Attribution-NonCommercial-ShareAlike 4.0 International License.

SOME RIGHTS RESERVED

EPITAXIAL STRAIN ENGINEERING OF SUPERCONDUCTIVITY IN RUTHENATE
THIN FILMS

Jacob Paul Ruf, Ph.D.

Cornell University 2019

Superconductivity is among the most fascinating emergent states of quantum matter. Despite garnering intense research interest over the past 100 years, a detailed understanding of how features of the electronic structure determine superconducting properties has remained elusive. For example, the ability to deterministically enhance the superconducting transition temperature (T_c) by design, rather than by serendipity, has been a long sought-after goal in condensed matter physics and materials science, but achieving this objective may require new tools, techniques and approaches.

This dissertation describes an approach towards achieving this goal referred to as *strain engineering exploiting epitaxy*. Superconducting thin films of two different ruthenium oxide materials, Sr_2RuO_4 and RuO_2 , are synthesized by molecular-beam epitaxy on deliberately lattice-mismatched substrates, and a comprehensive suite of characterization techniques—including x-ray diffraction, low-energy electron diffraction, electrical transport, angle-resolved photoemission spectroscopy (ARPES), and density functional theory (DFT) calculations—are applied to understand the relevant structure-property relationships in these materials. Namely, we seek to identify how substrate-imposed strains freeze in specific distortions of the parent bulk crystal structure in thin films, how these distortions couple to the electronic structure, and ultimately, how these distortions affect the superconducting T_c .

In the extremely disorder-sensitive unconventional superconductor Sr_2RuO_4 , we demonstrate that synthesizing epitaxial thin films on substrates that apply anisotropic in-plane strains is a facile way to increase the energy scale of superconductivity, to values

well in excess of the bulk T_c . This observation is in good agreement with recent work on single crystals subject to uniaxial pressure. We then employ results for films synthesized on different substrates that apply different modes and magnitudes of biaxial strain to gain insight into the exact mechanism that drives this T_c enhancement. Our results suggest that enhancing the density of states near the Fermi level, E_F —achieved by tuning the proximity of E_F to a Van Hove singularity in the electronic structure—is not the only factor that boosts T_c in strained Sr_2RuO_4 .

In RuO_2 , we report the first instance of transmuted a normal metal into a superconductor through the application of epitaxial strain. Bulk RuO_2 is not known to be superconducting down to the lowest measured temperatures. In agreement with this observation, we show that lightly strained RuO_2 thin films synthesized on isostructural (101)-oriented TiO_2 substrates are also non-superconducting; in contrast, we show that superconductivity having T_c s up to ≈ 2 K can be realized by synthesizing more heavily strained RuO_2 thin films on (110)-oriented TiO_2 substrates. Using ARPES measurements supported by DFT simulations, we reveal the primary electronic mechanism underlying this strain-stabilized superconductivity in $\text{RuO}_2/\text{TiO}_2(110)$: the anisotropic strains imposed by the substrate redistribute the charge carriers amongst the manifold of $4d$ states near E_F , partially depopulating flat bands with $d_{||}$ orbital character, and thereby increase the density of states near E_F .

Taken together, our results indicate that epitaxial strain engineering can likely be broadly applied to modulate superconductivity in a wide variety of multi-orbital systems, extending well beyond just the ruthenates investigated in this dissertation. In addition to being a practically feasible route to enhancing T_c and discovering new superconductors, this method also enables detailed investigations of the electronic structure. Therefore, we propose that the approach outlined here of close feedback between thin-film synthesis, structural and electrical characterization, and materials-specific calculations, could be a powerful platform moving forward in the quest to rationally control superconductivity.

BIOGRAPHICAL SKETCH

Jacob Ruf was born in St. Louis, Missouri almost thirty years ago, and has had an obsessive interest in playing and watching sports ever since then. Among the only things that rivals Jacob's passion for sports is his love of math and science. From a young age, he has always enjoyed math, and upon realizing in Mr. Murray's high school physics courses that math could actually be applied to solve "real-world" problems, he was almost instantly hooked on physics as well.

This newfound appreciation for physics continued to grow during Jacob's tenure as an undergraduate at the University of Illinois at Urbana-Champaign, where he attended from 2008 until graduating in 2011 with a Bachelor of Science degree in Engineering Physics. During this time, he had the great fortune to work in Prof. Peter Abbamonte's research group and to learn condensed matter physics at the very institution and laboratories where this field was born 60 years earlier.

Convinced that there was not much cooler—literally or figuratively—than superconductivity, Jacob moved to Ithaca, NY in the Fall of 2012 to start graduate school in Physics at Cornell University. He began working in Prof. Kyle Shen's research group the following summer, and since then has been hard at work learning and honing many tools of the solid-state physics trade that run the gamut from materials synthesis to materials characterization to materials computation. Perhaps best of all: he still enjoys going into the lab/office each day! Jacob's research applying these tools to discover and better understand new superconductors earned him a National Science Foundation IGERT Fellowship in 2013, a Master of Science degree in Physics from Cornell in 2015, and has culminated in his doctoral thesis, presented here.

To Mom, Dad, Michelle, and Dennis.

ACKNOWLEDGEMENTS

During the course of my Ph.D, I've been the beneficiary of much help, guidance, and support from an immense number of folks, in and outside of the lab. I am incredibly grateful for these interactions, and also remiss that I've probably forgotten to acknowledge some of these people here. But, without further ado...

Thanks to my cohorts in the Shen group for your friendship, collaboration, and (occasionally) commiseration. I could not have asked for a better mentor than Phil King to teach me how to run experiments when I first joined the group. I also really appreciated learning equal parts science and ultrahigh vacuum minutiae from the more senior grad students and postdocs in the group — John Harter, Eric Monkman, Danny Shai, Yuefeng Nie, Masaki Uchida, Yang Liu, Jason Kawasaki, and Shuolong Yang. It has been my pleasure to work with my peers in the group — Shouvik Chatterjee, Bulat Burganov, Ed Lochocki, Haofei Wei, Brendan Faeth, Jocienne Nelson, and Chris Parzyck — on everything from routine maintenance tasks, to building and implementing a new manipulator for the ARPES system, to running experiments in Duffield and at synchrotrons around the world. To the more recent additions to the group — Ludi Miao, Luca Moreschini, Saien Xie, and Shuyuan Zhang — it's been great getting to know you, and I trust that the lab is in capable hands moving forward.

Thanks as well to the many members of the Schlom group, past and present, that I have crossed paths with during my time at Cornell. It's been nice to share lab space with such capable and pleasant people — especially as the Shen group has continued to stuff far too many vacuum chambers into far too little space in Duffield 308! Some names that come to mind are: Tassilo Heeg, Alex Melville, Rainer Held, Carolina Adamo, Alice Galdi, Julia Mundy, Charles Brooks, John Heron, Jessica Burton, Natalie Dawley, Zhe Wang, Eva Smith, Rachel Steinhardt, Jake Sun, and Matt Barone. In particular, I am especially grateful for the opportunity to collaborate with Hari Nair, Hanjong Paik, and Nate Schreiber: without the heroic efforts of you guys in growing the best ruthenate

thin films the world has ever seen, basically none of the experiments presented in this thesis would have been possible. I'm glad we remain great friends outside of the lab, and I'm using the present tense above because I hope we continue to work together moving forward.

Experimental physics only progresses if the equipment needed to collect data is functional and operated by people who know what they're doing. On this front, I would like to thank all of the folks at the Cornell High Energy Synchrotron Source — especially the staff scientists Jacob Ruff (two fs!) and Ken Finkelstein — for helping us run a variety of (sometimes crazy) experiments there over the years. I think CHESS is a gem, personally and scientifically, for how down-to-earth, homemade, and customizable it is; I hope it retains this spirit of being *the synchrotron where you can try anything* when it returns to operation later this year. Special thanks to Jacob Ruff for tolerating being constantly mistaken for me in email exchanges, *etc.*, despite him being the much more accomplished condensed matter physicist of the two of us. Over at Clark Hall and elsewhere on campus: thanks to Eric Smith for providing a steady supply of liquid helium over the years for photoemission and transport experiments; thanks also to Jon Shu, Steve Kriske, Maura Weathers, John Grazul, and others for your hard work keeping the CCMR sample preparation and characterization facilities up and running.

Besides our extremely fruitful collaboration with Darrell Schlom's group, I've also been fortunate to work with many other excellent collaborators, near and far, during my time in graduate school. Thanks to Von Braun Nascimento for helping me learn how to run LEED- $I(V)$ simulations when I was first starting down this path early in graduate school and realizing that — despite regularly performing photoemission experiments — no one in our group was (or is) a *bona fide* surface scientist. On the electron microscopy side of things, thanks to Berit Goodge, David Baek, Celesta Chang, Lena Kourkoutis, and David Muller for imaging the many flavors of ruthenate thin films we have grown over the years. We are very lucky to have *two* world-class electron microscopy groups right

down the hallway from our labs. Thanks to Matt Ferguson, Katja Nowack, Yawen Fang, and Brad Ramshaw for your groups' work on magnetic and electrical characterization of Sr_2RuO_4 thin films; for a problem as enigmatic as the superconductivity in Sr_2RuO_4 , it's great to have the perspective of multiple different probes. Likewise, thanks to Youcheng Wang and Peter Armitage for your excellent work measuring the optical conductivity of CaRuO_3 , SrRuO_3 , and Sr_2RuO_4 thin films, and for many enlightening discussions over the years. Thanks to Dan Weinstock, Oleg Gorobtsov, and Andrej Singer for your synchrotron x-ray scattering measurements of RuO_2 and Ca_2RuO_4 . Thanks to Beth Nowadnick, Hyowon Park, Qiang Han, Andy Millis, Betül Pamuk, and Craig Fennie for running a myriad of sophisticated calculations on a vast array of different materials, ranging from LaNiO_3 to Ca_2RuO_4 to RuO_2 , to help us interpret what would otherwise be confusing experimental results. Special thanks to Beth (during her time at Cornell) and Craig for getting me started running my own DFT calculations (and answering numerous questions along the way) — as the saying goes: teach a man to fish, and you feed him for a lifetime.

On the more “nuts and bolts” side of experimental physics research, thanks to Rodney, Stan, Bob, Jeff, Chris, and Rob in the LASSP professional machine shop for bringing to life many crazy designs from our group for (sometimes exotic) chunks of metal. Special thanks to Nate Ellis — proprietor of much wisdom about machining and life in general — for teaching me how to machine and ensuring that I didn't lose any digits doing so. Thanks to Linda Hatch and Rob Sprankle in the purchasing department for putting through many POs on our behalf, and thanks to Leonard Freelove and Jason Spicer for always faithfully delivering these packages (big and small) to our labs and offices in Clark. Upstairs in Clark, it was a pleasure to have the LASSP staff of Douglas Milton, Caroline Brockner, Jonathan Fuller, and Judy Wilson always willing to assist with our administrative needs and questions.

Without the unwavering support of my advisor, Kyle Shen, none of my interactions with all of the great people mentioned above would have been possible. Thanks, Kyle,

for your guidance over the years — and more generally, for being an inspiring role model for how a very successful researcher who cares deeply about his students operates. I've always been impressed by the amount of time you invest in developing all aspects of your students (as scientists and presenters of science), and your hands-on approach to helping us solve problems (both scientific and technical). Likewise, many thanks to Darrell Schlom for enabling all of the materials synthesis that forms the foundation of any exciting new physics our group might be lucky enough to discover. Darrell's encyclopedic knowledge of oxides and thin films is astounding, his enthusiasm for these topics is contagious, and it's generally just been a pleasure to work under bosses who are always willing to support your experiments, even when things don't appear to be working.

While all of the research I have done during my Ph.D seems quite enjoyable in retrospect, there is surely some element of nostalgia in play here. In reality, I certainly would not have lasted this long without the friendship of many folks outside of work. Thanks to my grad school friends — Ed, Jill, Chris, Jay, Mandy, Orlando, Dan, Sarah, and others — for the many conversations (group chats qualify!), meals, and of course, copious amounts of alcohol that we have shared together over the years. You all are the best crew of drinking partners a guy could ask for...maybe someday we'll master that golfing hobby of ours. Similarly, thanks to the many folks I've played kickball, soccer, and ultimate frisbee with over the years. My time spent out on those fields — and afterwards, at the Westy and elsewhere — will always remain among my fondest memories of Ithaca. And to the frisbee boys: it sure is nice to be leaving Cornell with *two t-shirts* as back-to-back intramural league champs!

Finally, thanks most of all to my immediate family — Mom, Dad, sister Michelle, and brother-in-law Dennis — and to my extended family for your constant love and encouragement. To a collection of engineers and lawyers and *real doctors*, my decision to pursue a Ph.D in something as divorced from everyday life as physics probably seemed “interesting” at best, and quixotic at worst — especially when I explained that not only do we not

know the *answers* ahead of time to the questions we're researching, sometimes we don't even know *how to answer* these questions! Nonetheless, you all were consistently steadfast in your support of my endeavors — and lo and behold, despite many failed experiments requiring much persistence, we've (slowly) made a lot of progress in deciphering some of the mysteries presented to us by Nature. This dissertation is dedicated to you. I've enjoyed having many of you come to Ithaca over the years, and I hope you'll continue to visit regularly as I continue in academia, even though Dresden is a bit further away.

Jacob Ruf
Ithaca, New York
November 2019

TABLE OF CONTENTS

Biographical Sketch	iii
Dedication	iv
Acknowledgements	v
Table of Contents	xiii
List of Tables	xiii
List of Figures	xv
1 Introduction	1
1.1 From band metals to Fermi liquids to superconductors	3
1.1.1 Band theory	3
1.1.2 Landau Fermi liquid theory	5
1.1.3 Superconductivity	7
1.2 Outline of the text	16
2 Molecular-beam epitaxy	18
2.1 A brief history of MBE	18
2.2 Overview of oxide MBE	19
2.2.1 Effusion cells and electron-beam sources	21
2.2.2 Oxygen sources	24
2.2.3 Substrate heater, pucks, and manipulator	25
2.2.4 Reflection high-energy electron diffraction	27
2.3 Growth of ruthenate thin films by MBE	30
2.3.1 Adsorption-controlled growth windows	31
2.3.2 Strain engineering exploiting epitaxy	35
3 Thin-film characterization techniques	37
3.1 X-ray diffraction	37
3.1.1 General formalism	38
3.1.2 Application to epitaxial thin films	39
3.1.3 X-ray reflectivity	43
3.1.4 Reciprocal space maps	45
3.1.5 Experimental apparatus	46
3.2 Electrical transport	49
3.2.1 Basic phenomenology	49
3.2.2 Experimental apparatus	53
3.3 Angle-resolved photoemission spectroscopy	54
3.3.1 General formalism	55
3.3.2 Energy and momentum conservation \implies bandstructure	55
3.3.3 From bandstructure to single-particle spectral functions	58
3.3.4 Other factors that affect ARPES intensities	63
3.3.5 Experimental apparatus	67
3.4 Low-energy electron diffraction	74
3.4.1 General formalism	75

4	Epitaxial strain tuning of superconductivity in Sr_2RuO_4	81
4.1	Introduction to Sr_2RuO_4	83
4.1.1	Crystal structure	83
4.1.2	Charge, orbital, and spin degrees of freedom	85
4.1.3	Fermi liquid regime	86
4.1.4	Superconductivity in bulk Sr_2RuO_4	89
4.2	Strain tuning of superconductivity and the normal-state electronic structure in Sr_2RuO_4	95
4.2.1	Strain effects on superconductivity	96
4.2.2	Strain effects on the normal-state electronic structure	99
4.3	Synthesis and characterization of epitaxially strained Sr_2RuO_4 thin films	101
4.3.1	Film growth by molecular-beam epitaxy	103
4.3.2	DFT calculations	105
4.3.3	Electrical transport measurements	111
4.3.4	XRD and STEM measurements	117
4.4	Discussion and Conclusions	130
5	Strain-stabilized superconductivity in RuO_2	133
5.1	Introduction to the rutile family of materials	134
5.1.1	Structural degrees of freedom	134
5.1.2	Charge and orbital degrees of freedom	136
5.1.3	Structural, electronic, and magnetic properties specific to RuO_2	138
5.2	Synthesis and characterization of RuO_2 thin films	144
5.2.1	Film growth by molecular-beam epitaxy	144
5.2.2	Electrical transport measurements	145
5.2.3	X-ray diffraction and scanning transmission electron microscopy measurements	151
5.2.4	Dependence of superconductivity on film thickness for $\text{RuO}_2(110)$	157
5.3	Discussion and Conclusions	160
6	Strain-induced changes to the electronic structure of RuO_2	169
6.1	Electronic structure calculations	170
6.1.1	Technical details	170
6.1.2	Structural relaxations	171
6.1.3	Basic electronic structure of RuO_2	174
6.1.4	Effects of strain on the electronic structure	175
6.1.5	Effects of $+U$ on the electronic structure	176
6.2	ARPES and LEED results for strained $\text{RuO}_2(110)$ samples	178
6.2.1	LEED images and angle-integrated valence band spectrum	179
6.2.2	Fermi surface and near- E_F quasiparticle dispersions	180
6.3	Evolution of electronic structure with strain	187
6.3.1	Results on $\text{RuO}_2(110)$ films of different thicknesses	188
6.3.2	Results on $\text{RuO}_2(110)$ and $\text{RuO}_2(101)$ films	195
6.4	Discussion and Conclusions	199

7	Conclusions and Future Work	204
7.1	Conclusions	204
7.2	Future Work - Sr_2RuO_4	207
7.3	Future Work - RuO_2	209
	Bibliography	212

LIST OF TABLES

1.1	Types of Cooper pairing	12
4.1	Crystal structures used in DFT simulations of Sr_2RuO_4	108
5.1	Electrical and structural properties of RuO_2 thin films	161
6.1	Crystal structures used in DFT simulations of RuO_2	174
6.2	Summary of ARPES and LEED measurements for RuO_2 thin films	201

LIST OF FIGURES

2.1	Oxide MBE schematic	22
2.2	TOMBE diagrams for Sr_2RuO_4 and SrRuO_3	32
2.3	High-RRR ruthenate thin films grown by MBE	33
3.1	N -slit interference function	42
3.2	X-ray reflectivity simulations	45
3.3	XRD schematic	48
3.4	ARPES schematic	57
3.5	Spectral functions of a non-interacting electron gas and a Fermi liquid . . .	61
3.6	Schematic of Cornell ARPES system	68
3.7	LEED schematic	76
3.8	LEED- $I(V)$ simulations	80
4.1	Crystal structures of the Ruddlesden-Popper series of strontium ruthenates	84
4.2	Local orbital level structure of Sr_2RuO_4	87
4.3	Fermi surfaces of bulk Sr_2RuO_4	88
4.4	Disorder dependence of superconductivity in bulk Sr_2RuO_4	92
4.5	Evolution of superconductivity versus uniaxial pressure	97
4.6	Evolution of normal-state electronic structure versus uniaxial pressure . . .	100
4.7	Substrates available for growth of perovskite-based oxide thin films	105
4.8	Fermi surfaces of epitaxially strained Sr_2RuO_4 thin films - DFT	109
4.9	Density of states of epitaxially strained Sr_2RuO_4 thin films - DFT	110
4.10	Resistivity of $\text{Sr}_2\text{RuO}_4/\text{NdGaO}_3(110)$ and bulk Sr_2RuO_4	112
4.11	Resistivity of $\text{Sr}_2\text{RuO}_4/\text{NdGaO}_3(110)$ and $\text{Sr}_2\text{RuO}_4/\text{LSAT}(001)$	113
4.12	Disorder dependence of superconductivity in Sr_2RuO_4 thin films	114
4.13	Dependence of superconductivity on film thickness in different genera- tions of Sr_2RuO_4 thin films	117
4.14	Structural and electrical characterization of a Ru-poor Sr_2RuO_4 thin film . .	119
4.15	Structural and electrical characterization of a Ru-rich Sr_2RuO_4 thin film . .	121
4.16	Signatures of intergrowths in XRD and $R(T)$ data for Sr_2RuO_4 thin films . .	123
4.17	Transport anisotropy in Sr_2RuO_4 induced by oriented defects	127
4.18	Evolution of superconductivity versus substrate-imposed strains	131
5.1	Rutile crystal structure	135
5.2	Low-energy orbital degrees of freedom in RuO_2	139
5.3	Signatures of Fermi liquid behavior in bulk RuO_2	141
5.4	Electrical resistivity of bulk RuO_2 and epitaxially strained RuO_2 thin films .	146
5.5	Electrical resistivity of patterned bridges on $\text{RuO}_2(110)$	148
5.6	Magnetoresistance of three superconducting $\text{RuO}_2(110)$ samples	149
5.7	Structural characterization of epitaxially strained RuO_2 thin films, and thickness-dependent superconductivity for $\text{RuO}_2(110)$	152
5.8	Further electrical and structural characterization of (101)- and (110)- oriented RuO_2 thin films	164
5.9	RSMs and rocking curves for a partially strain-relaxed $\text{RuO}_2(110)$ sample .	165

5.10	Variation in local crystalline quality across a superconducting RuO ₂ (110) sample	165
5.11	HAADF STEM images of a superconducting RuO ₂ (110) sample in the higher strain direction	166
5.12	HAADF STEM images of a non-superconducting RuO ₂ (101) sample	166
5.13	Evolution of crystal structure and electrical transport behavior as a function of film thickness for RuO ₂ (110)	167
5.14	RSMs for RuO ₂ (110) samples with different film thicknesses	168
6.1	Electronic structure of bulk RuO ₂ - DFT	175
6.2	Effects of strain on the electronic structure - DFT	176
6.3	Effects of $+U$ on the electronic structure - DFT	177
6.4	LEED data for RuO ₂ (110)	179
6.5	Angle-integrated valence band spectrum for RuO ₂ (110)	179
6.6	Near- E_F electronic structure of RuO ₂ (110)	181
6.7	k_z determination for RuO ₂ (110)	183
6.8	Signatures of electron-boson coupling in ARPES data for RuO ₂ (110)	185
6.9	Surface lattice constant refinement by LEED spot position analysis	190
6.10	Strain-dependent changes to ARPES data for RuO ₂ (110)	193
6.11	Strain dependence of the near- E_F density of states in RuO ₂	197
6.12	Near- E_F electronic structure of RuO ₂ (101)	200

CHAPTER 1

INTRODUCTION

Solid-state physics is the study of electrons and nuclei interacting quantum mechanically via the Coulomb interaction. It is one of the beautiful aspects of Nature that the same underlying Hamiltonian—which has been known for over 90 years, since the days of Schrödinger, Dirac, and Heisenberg—can give rise to the fantastic diversity of emergent phenomena observed in condensed matter, including crystallinity, metallicity, superconductivity, and magnetism [1]. At the same time, it is rather sobering to realize that this Hamiltonian is utterly insoluble even for simple systems containing few ($N \gtrsim 10$) particles, and so there are no truly *ab initio* theories of condensed matter.

Although it is intractable to find the ground state of an arbitrary collection of electrons and nuclei by brute force calculation, a tried-and-true method for making progress on this problem is perturbation theory: we must recognize (or guess!) the hierarchy of energy scales in the problem, and successively diagonalize terms in the Hamiltonian that contribute less and less to the total energy in increasingly restricted subspaces of the original Hilbert space. In most materials, the largest energy scale involved is usually the cohesive energy that keeps the atoms bonded together in a particular average configuration. If we take this *crystal structure* as a given—*i.e.*, something that can be engineered during materials synthesis, and later measured—then we can focus on accounting for how the electrons propagate in such an environment, or how the atoms vibrate about their mean positions, or even how these two processes are coupled. As we continually downfold the “master Hamiltonian” into more restricted subspaces, the eigenstates become increasing approximations of reality, making experiments that either confirm or deny the validity of these approximations essential.

At an abstract level, the motivation behind this dissertation is to explore the following

questions:

- How do the positions of atoms within a given material influence the tendency of that material to become superconducting?
- What are the mechanisms that link the crystal structure (what is controlled during growth) to the desired electronic property (here, superconductivity)?
- If we understand the relevant structure-property relationships, can we engineer aspects of the structure to enhance aspects of the superconductivity, such as the transition temperature, T_c ?

As alluded to above, the main challenge in answering these questions is that the energy scales involved in superconductivity (typically < 1 meV) are miniscule compared to the accuracy of state-of-the-art methods for computing electronic structures. Therefore, we must employ approximations and effective field theories to rationalize certain aspects of the superconductivity, and indeed there are existing frameworks—such as BCS theory and its extensions—that have historically proven to be immensely successful in this regard. The catch, however, is that appropriate inputs for such theories must be informed by experimental measurements of the normal-state electronic structure from which superconductivity condenses. With close feedback between theory, experimental characterization, and materials synthesis, a new era seems within reach in which the field of superconductivity research progresses beyond the historical discovery-driven mode of research, to a mode where new superconductors are created and enhanced by design. In this chapter, we describe the general conceptual ideas underpinning our approach to this problem in section 1.1, providing some relevant historical background where necessary, and then in section 1.2 we outline how these ideas are applied to the study of two different ruthenium oxide materials, Sr_2RuO_4 and RuO_2 , throughout the remainder of this dissertation.

1.1 From band metals to Fermi liquids to superconductors

1.1.1 Band theory

One-electron band theories are a pillar of introductory solid-state physics courses, with good reason: they explain many of the essential differences of insulators, semiconductors, and metals in a unified framework that can be very accurately computed using modern software packages. The fundamental ideas underpinning this approach date back to the work of Felix Bloch in the late 1920s [2]. Upon considering the physics of an electron propagating through a static periodic potential created by a crystalline lattice of many atoms, Bloch recognized that the periodic nature of the Hamiltonian has two crucially simplifying and important effects, despite the overwhelming number of microscopic degrees of freedom (the number of atoms in a typical crystal is $N_A \approx 10^{23}$). First, the discrete translational symmetries of the lattice ensure that the electron momentum is conserved modulo translations of the reciprocal lattice $\{\mathbf{G}\}$; thus, the most natural basis for diagonalizing the Hamiltonian is \mathbf{k} -space, with \mathbf{k} translated as necessary by integer multiples of $\{\mathbf{G}\}$ to its irreducible value in the first Brillouin zone. Second, when the spectrum of such eigenstates is plotted versus energy, there will be characteristic *bands*—energies where such states exist at some (or all) values of \mathbf{k} in the Brillouin zone—and also *band gaps*—energies where such states do not exist at any value of \mathbf{k} . The existence of band gaps is a consequence of destructive quantum mechanical interference between electron waves moving in the periodic potential. If the Fermi level E_F lies in such a band gap, the material is a *band insulator* that strongly resists the flow of electricity because there are no propagating states at E_F that can transport the applied current; by contrast, if E_F lies within one or multiple bands, the material is usually a metal, unless other interac-

tions render it insulating¹. In the latter case, which is the relevant one for the materials studied in this thesis, details of the $E(\mathbf{k})$ bandstructure—such as the Fermi wavevector(s) \mathbf{k}_F where E_F intersects the band(s), the group velocity(ies) $dE/d\mathbf{k}$ of the current-carrying excitations near E_F , *etc.*—are among the essential ingredients that determine the instability of band metals to forming electronically ordered states at lower temperatures, such as superconductivity.

At a basic level, the “bare” $E(\mathbf{k})$ band dispersion relationships derive from the atomic positions: by maximizing the modulus squared of the electronic wavefunctions near the positively charged ion cores, the energy of a state with a given \mathbf{k} can be reduced. In our studies detailed in this dissertation, band theory calculations are always the starting point, since these provide the essential link between the crystal structure (what is controlled during materials synthesis) and the “bare” normal-state electronic structure, before other higher-order (*i.e.*, smaller) effects such as electron-electron and electron-phonon interactions are taken into account. We utilize commercially available software packages [6, 7, 8, 9, 10] that implement density functional theory (DFT) [11, 12] to perform such calculations. It is largely beyond the scope of this thesis to provide a comprehensive theoretical description of DFT, and many reviews exist elsewhere. From a conceptual perspective, though, we note that DFT treats electron-electron interactions—which we have heretofore ignored—at a *static mean-field level*. Thus, it is not strictly correct to refer to DFT as a “non-interacting” theory; in solving the Kohn-Sham equations for the wavefunction of a given (single) electron, the interaction with the average density of all other electrons is considered self-consistently, via a theoretical construct called the *exchange-correlation potential*. The physics that is neglected in such a treatment are dynamical correlations of the electron fluid: when one electron moves within the solid, the other electrons respond

¹Famous examples include Mott insulators, which invoke strong electronic correlations as the cause of the insulating behavior [3, 4], and magnetically ordered states, which invoke the spin and/or orbital angular momentum of electrons as the cause of the insulating behavior [5]. We omit further discussion of these possibilities here for brevity.

according to the change in Coulomb interaction (usually repulsion) that they experience as a result of this motion. These dynamical interactions can be quite significant in certain materials, and so it is essential to gauge their strength by comparisons of experimental measurements of the electronic structure with the results of static mean-field band theory calculations, as discussed in the next section.

1.1.2 Landau Fermi liquid theory

The concept of a Landau Fermi liquid dates back to the 1950s [13, 14, 15], when Lev Landau first elucidated why band theory was able to account for the electronic structure of a wide class of real metals exceedingly well, despite its complete (in “nearly free-electron”, “tight-binding”, and other phenomenological models) or partial (in DFT) neglect of electron-electron interactions. The key notion is that of *adiabatic continuity* between the wavefunctions of a gas of effectively independent electrons and those of a liquid of weakly interacting quasiparticles. In qualitative terms, the wavefunctions of the independent-electron Hamiltonian will be modified as electron-electron interactions are gradually “turned on”, but as long as the scattering rate between levels remains “low”, the basic structure of the wavefunctions will not change. Thus, eigenstates of the non-interacting Hamiltonian may be identified with (near) eigenstates of the interacting Hamiltonian (*i.e.*, there is a one-to-one mapping between the Hilbert spaces), but the energies of the latter *quasiparticle resonances* will shift (*i.e.*, be *renormalized*) and acquire a finite lifetime (*i.e.*, they are not stationary states of the true many-body Hamiltonian) as a result of the interactions.

The crucial insight of Landau was to realize that the Pauli exclusion principle greatly reduces the scattering rate of electrons near the Fermi level in a metal, in an energy (ϵ)- and temperature (T)-dependent way that becomes increasingly restrictive as $\epsilon \rightarrow E_F$ and

$T \rightarrow 0$ K. This fact greatly expands the regimes of binding energy and temperature over which the “low scattering rate” assumption of Landau Fermi liquid theory is applicable. In particular, at zero temperature and at E_F , even the quasiparticle excitations of strongly interacting metal should be true eigenstates of the many-body Hamiltonian, with infinitely long lifetimes (neglecting impurity scattering); oftentimes we can gain insight into the strength of electronic correlations by gauging how far away in (ϵ, T) from this fixed point a Fermi liquid-like description still applies. Throughout the rest of the text, we refer to this phenomenon as it relates to electrical transport and angle-resolved photoemission measurements as *electron-electron scattering being reduced by phase-space considerations*; we refer interested readers to Ref.[16] for a nice pedagogical exposition of these ideas.

In practical terms, the quasiparticle concept is a more general bridge between “bare” bandstructure calculations and how the low-energy electron-like excitations near E_F propagate in actual solids where the energy-momentum $E(\mathbf{k})$ dispersion relationships are renormalized by electron-electron scattering, electron-phonon interactions, *etc.* A frequently observed consequence of these many-body interactions is that the quasiparticle excitations move slower than would be expected based on the bare band velocities, corresponding to a reduced kinetic energy and increased density of states near E_F (since the total integrated spectral weight over the “squeezed” total bandwidth must be conserved). These effects are typically discussed in terms of increased *effective masses* of the quasiparticles. Although several computational schemes such as dynamical mean-field theory [17, 18] have come online in recent years that are able to compute these many-body mass enhancements (nearly) from first principles, experimental measurements of the renormalized electronic structure remain the ultimate arbiter of how large these effects are in actual materials. We pursue the latter approach in our studies of Sr_2RuO_4 and RuO_2 detailed in this thesis. Finally, as a technical point, we note that whenever we discuss superconductivity and loosely refer to the normal-state bandstructure, we typically

mean the quasiparticle excitation spectrum.

1.1.3 Superconductivity

Superconductivity was first discovered in elemental mercury by Kamerlingh Onnes in 1911 [19]. Onnes was awarded the Nobel Prize for this work shortly thereafter in 1913, and superconductivity in other heavy elements such as tin and lead was observed at around the same time. These original measurements observed the first hallmark of superconductivity: *the electrical resistance rapidly drops to zero as a function of temperature*. It was not until the work of Meissner and Ochsenfeld in 1933 that the second hallmark of superconductivity was realized: namely, *perfect diamagnetism*, in which external magnetic fields are completely expelled from the interior of a superconductor [20]. This phenomenon is now known, fittingly, as the Meissner-Ochsenfeld effect. Zero resistance and perfect diamagnetism are the defining signatures of superconductivity, and together distinguish it from other phases of matter, such as perfect conductors; accordingly, definitive discoveries of new superconductors now rely on the observation of both properties.

In the 100+ years since the initial discovery of superconductivity, many novel superconducting materials have been found, sometimes in seemingly very unlikely places, such as doped Mott insulators [21] and exotic metals where the quasiparticle excitations have effective masses more than 1000 times heavier than bare electrons [22]. While new discoveries continue to challenge existing theories, it appears that certain features of this phase of matter are universal—*i.e.*, applicable to all superconductors—while other features—such as the mechanism whereby superconductivity condenses—are more material-specific. With the benefit of hindsight, we briefly review these ideas here, focusing first on the universal properties and then delving into questions about mechanisms in section 1.1.3. With an eye towards the work presented in later chapters, we also draw

attention to properties of the normal-state electronic structure that are believed to be important in determining the superconducting properties, such as T_c .

Later in the 1930s, the London brothers developed a phenomenological theory describing the electrodynamics of superconducting electrical currents that could account for the Meissner-Ochsenfeld effect [23]. In particular, their work established that external magnetic fields in fact penetrate slightly into the interior of superconductors, but are exponentially suppressed on a characteristic length scale λ , called the London penetration depth. λ is now recognized as a fundamental (and measurable) property of all superconductors that contains information about the density and effective masses of the superconducting electron pairs. In the 1950s, Ginzburg and Landau applied their celebrated phenomenological theory of second-order phase transitions to superconductivity, and were able to deduce a stunning amount of information about the macroscopic properties of superconductors from very general considerations about how the free energy of a complex-valued order parameter field should vary across the superconducting transition [24]. The result of this analysis is a non-linear Schrödinger-like equation for what is now recognized as the superconducting wavefunction, $\Psi \sim \Delta e^{i\phi}$, as well as an expression relating Ψ to the dissipationless electric current density \mathbf{j}_s , that reproduces the predictions of London theory. Ginzburg-Landau theory remains in active use today in computational studies of superconductivity, and can be derived from the more microscopic BCS theory of superconductivity, which we now describe.

Much of our modern understanding of superconductivity originates from the work of Bardeen, Cooper, and Schrieffer (BCS) in the late 1950s, who explained superconductivity as the pairing of individual fermions into *Cooper pairs* [25], and the subsequent condensation of these composite bosons into a charged superfluid state [26, 27]. BCS were awarded the Nobel Prize for their work in 1972. At a conceptual level, this pairing seems rather unintuitive—after all, Coulomb interactions between electrons are naively expected to

be mutually repulsive. However, if we take for granted for the time being that such an effectively attractive interaction V can exist between fermions within a narrow range of energies surrounding the Fermi level ($E_F - \hbar\omega_B < \epsilon < E_F + \hbar\omega_B$, where \hbar is Planck's constant and ω_B is the energy of the pairing boson), then Cooper showed that a bound state of two fermions is lowered in energy compared to two independent states, by an amount δE that scales exponentially with the density of states near the Fermi level $N(E_F)$ and the pairing interaction V . Formally, we have:

$$\delta E = -2\hbar\omega_B \exp[-2/(N(E_F)|V|)] \quad (1.1)$$

The full ground-state wavefunction of a BCS-like superconductor can be expressed as a coherent state of Cooper pairs. It can be obtained by variationally minimizing the total energy of a Hamiltonian that accounts for the kinetic energy of the normal-state quasiparticles and the energy gained by pairing according to Equation 1.1, after applying mean-field decoupling of four-fermion operators in the usual way. In the superconducting state, there is a finite energy gap Δ for single-particle Bogoliubov quasiparticle excitations; this feature in tandem with the macroscopic phase coherence of the superfluid ensures that dissipationless transport occurs, even in the inevitable presence of disorder scattering. The evolution of Δ with temperature and the transition temperature T_c at which $\Delta \rightarrow 0$ can both be solved for analytically within BCS theory; neglecting some factors of order unity (since these depend on the precise gap structure in \mathbf{k} -space and how the effective interaction is modeled), we have:

$$\Delta \sim k_B T_c \sim \hbar\omega_B \exp[-1/(N(E_F)|V|)] \quad (1.2)$$

where k_B is Boltzmann's constant and the other variables have the same meaning as in Equation 1.1. From the structure of Equation 1.2, we see that to substantially enhance T_c ,

we generically need to either increase $N(E_F)$, increase V , or both. Changes to the energy of the pairing boson ω_B will have a much more muted effect on T_c , since this quantity does not appear in the argument of the exponential.

Cooper-pair wavefunctions encode the relevant pairing interactions

A sufficiently generalized description of superconductivity like we have given up to this point—invoking the Bose-Einstein condensation of Cooper pairs, which are formed by some type of effectively attractive interaction between individual fermionic quasiparticles—is widely believed to apply to all superconductors. That being said, there are two qualitatively different classes of superconductors that have been discovered to date; these are differentiated by the structure in \mathbf{k} -space of the superconducting gap function $\Delta(\mathbf{k})$, which ultimately reflects the different mechanisms that produce the effective attraction $V(\mathbf{k}, \mathbf{k}')$ between quasiparticles. The rest of this section is devoted to describing these two different possibilities. For historical reasons, pairing mediated by electron-phonon coupling is often referred to as *conventional superconductivity*, whereas pairing mediated by electron-electron interactions is often called *unconventional superconductivity*. In both cases, an appropriate two-particle wavefunction for a Cooper pair can generically be written as

$$\Psi(\mathbf{r}_1, \sigma_1, \mathbf{r}_2, \sigma_2) = f(\mathbf{r}_1 - \mathbf{r}_2)\chi(\sigma_1, \sigma_2) \quad (1.3)$$

subject to the fundamental requirement that Ψ change sign (*i.e.*, anticommute) under exchange of the two fermions labeled by the subscripts 1 and 2. Since the fermions are individually spin-1/2 particles, the spin component of the wavefunction $\chi(\sigma_1, \sigma_2)$ must either have total spin $S = 0$ (a spin-singlet state that is antisymmetric under exchange of fermions), or $S = 1$ (a spin-triplet state that is symmetric under exchange of fermions).

The orbital component of the wavefunction $f(\mathbf{r}_1 - \mathbf{r}_2)$ is expanded in spherical harmonics Y_m^ℓ with different amounts of relative orbital angular momentum ℓ between the electrons in the Cooper pair, each having well-defined parity $(-1)^\ell$. Conventional superconductors consist of Cooper pairs with $\ell = 0$ bound in spin-singlet states. On the other hand, more strongly interacting unconventional superconductors utilize the higher angular momentum channels available in Equation 1.3—which have larger amplitudes of the wavefunction at finite distances—to minimize the probability that two electrons overlap in the same region of space simultaneously. Unconventional superconducting states with *spin-triplet* pairs must have *odd orbital parity* ($\ell = 1, 3, \dots$), and unconventional states with *spin-singlet* pairs must have *even orbital parity* ($\ell = 2, 4, \dots$), in order to preserve the overall antisymmetry of Ψ under fermion exchange.

Although this picture is intuitively appealing, in reality superconductivity never condenses in media having full $O(3)$ rotational symmetry where ℓ and the electron spin are independently conserved quantum numbers. Rather, to make the above discussion appropriate to crystals where the reduced momentum \mathbf{k} in the first Brillouin zone is the conserved quantity (and there may be non-negligible amounts of spin-orbit coupling), we should represent Ψ and the superconducting gap function Δ in the $(\mathbf{k}, s, \mathbf{k}', s')$ basis that describes two-particle fermionic states that are both in the immediate vicinity of E_F , and we should not presume that \mathbf{k} and spin are quantities that can be specified independently—*i.e.*, multiplied in Ψ irrespective of \mathbf{k} . In this setting², the wavefunction of a Cooper pair with vanishing total momentum ($\mathbf{k} = -\mathbf{k}'$) can be decomposed as $\Psi_{\mathbf{k}s s'} = \phi(\mathbf{k})\chi(s, s')$, and we distinguish the two possibilities for pairing states at each $(\mathbf{k}, -\mathbf{k})$ according to Table 1.1.

The complex-valued superconducting gap function in this more general setting is rep-

²Note that we are still assuming the existence of time-reversal and inversion symmetries, otherwise the single-particle quasiparticle states comprising Cooper pairs with vanishing total momentum need not be degenerate.

Pairing type	orbital component	spin component
even-parity / spin-singlet	$\phi(\mathbf{k}) = +\phi(-\mathbf{k})$	$\chi(s, s') = \frac{1}{\sqrt{2}}(\uparrow\downarrow\rangle - \downarrow\uparrow\rangle)$
odd-parity / spin-triplet	$\phi(\mathbf{k}) = -\phi(-\mathbf{k})$	$\chi(s, s') = c_1 \uparrow\uparrow\rangle + c_2(\uparrow\downarrow\rangle + \downarrow\uparrow\rangle) + c_3 \downarrow\downarrow\rangle$

Table 1.1: Types of Cooper pairing possible in crystalline superconductors invariant under time-reversal and inversion

represented by a 2×2 matrix in spin space at each \mathbf{k} , according to the formula:

$$\Delta(\mathbf{k}) = \begin{pmatrix} \Delta_{\uparrow\uparrow}(\mathbf{k}) & \Delta_{\uparrow\downarrow}(\mathbf{k}) \\ \Delta_{\downarrow\uparrow}(\mathbf{k}) & \Delta_{\downarrow\downarrow}(\mathbf{k}) \end{pmatrix} = i(\Delta_{\mathbf{k}}I + \mathbf{d}(\mathbf{k}) \cdot \sigma)\sigma_y, \quad (1.4)$$

where $\Delta_{\mathbf{k}}$ is a scalar, I is the 2×2 identity matrix, $\sigma = (\sigma_x, \sigma_y, \sigma_z)$ is a vector of Pauli matrices, and $\mathbf{d}(\mathbf{k})$ is a three-component complex-valued vector.

Spin-singlet superconductors correspond to setting $\Delta_{\uparrow\uparrow} = \Delta_{\downarrow\downarrow} = 0$ and $\Delta_{\uparrow\downarrow} = -\Delta_{\downarrow\uparrow} = \Delta_{\mathbf{k}}$ in Equation 1.4—*i.e.*, the \mathbf{d} vector is zero and $\Delta_{\mathbf{k}}$ is finite, leaving:

$$\text{even-parity order parameter: } \Delta(\mathbf{k}) = \begin{pmatrix} 0 & \Delta_{\mathbf{k}} \\ -\Delta_{\mathbf{k}} & 0 \end{pmatrix} \quad (1.5)$$

On the other hand, spin-triplet superconductors correspond to setting $\Delta_{\uparrow\downarrow} = \Delta_{\downarrow\uparrow} = \Delta_0$ and $\Delta_{\mathbf{k}} = 0$ in Equation 1.4. In this case the \mathbf{d} vector specifies all information about the superconducting order parameter—its orbital angular momentum structure in each of the three spin-triplet pairing channels, and also possible nodes in the gap versus \mathbf{k} . The elegant aspect of this notation is that \mathbf{d} transforms just like a vector under spin rotations [28]:

$$\text{odd-parity order parameter: } \Delta(\mathbf{k}) = \begin{pmatrix} -d_x(\mathbf{k}) + id_y(\mathbf{k}) & d_z(\mathbf{k}) \\ d_z(\mathbf{k}) & d_x(\mathbf{k}) + id_y(\mathbf{k}) \end{pmatrix} \quad (1.6)$$

Mechanism of conventional superconductivity

Conventional superconductors have an even-parity (spin-singlet) order parameter, and the sign of the superconducting gap function $\Delta(\mathbf{k})$ is constant irrespective of \mathbf{k} . Until the discovery of heavy-fermion superconductors in 1979, all known superconductors were conventional—and indeed, in its original formulation, BCS theory was constructed to explain the properties of these materials. The non-sign-changing nature and typically weak \mathbf{k} dependence of the magnitude of $\Delta(\mathbf{k})$ reflect the fact that the effective attraction between fermions is mostly local in space, mediated by virtual exchange of phonons. First proposed by Fröhlich in 1950 [29], the key concept in producing this attraction is the separation of time scales between electron and lattice dynamics. As an electron propagates through the lattice, it causes a locally positively charged distortion of the ionic nuclei. This polarization persists long after the electron has left the vicinity, since the lattice relaxation time scales are comparatively slow. During this time, the accumulated positive charge attracts a second electron with opposite momentum, thereby facilitating pairing of the two electrons.

Among the most definitive evidence supporting the BCS mechanism of superconductivity are isotope effect experiments showing that the superconducting transition temperature systematically depends on the average mass M of the ions in the crystal structure. This relationship was demonstrated experimentally [30, 31, 32] before the formulation of BCS theory, and is essentially hard-coded into Equation 1.2: increasing the ionic mass reduces the Debye frequency according to $\omega_D \sim 1/\sqrt{M}$, leading to $T_c \sim 1/\sqrt{M}$. Since its introduction, BCS theory has been refined and extended by many authors, including Migdal and Eliashberg, who fully included the momentum dependence and time retardation aspects of the electron-phonon interaction in a strong coupling generalization of BCS theory [33, 34]. For the purposes of this dissertation, we note that considerably more realistic—although still approximate!—formulas for T_c based on Migdal-Eliashberg the-

ory exist, such as the McMillan-Allen-Dynes equation [35, 36]. These should certainly be considered in any quantitative calculations of T_c , but for discussing qualitative trends in how T_c evolves versus some variable (*e.g.*, strain), we employ the simpler weak-coupling expression in Equation 1.2. To boost the energy scale of superconductivity in conventional superconductors, we must either enhance the density of quasiparticle states near the Fermi level that experience an effective attraction by Fröhlich’s mechanism, and/or increase the magnitude of the electron-phonon coupling. The latter can often be achieved by tuning a material to the brink of a structural phase transition. Somewhat paradoxically, in both of these mechanisms it is usually true that inherently worse (*i.e.*, higher resistivity) single-particle conductors are better (*i.e.*, higher- T_c) two-particle superconductors.

Mechanism of unconventional superconductivity

Unconventional superconductors may have either even-parity (spin-singlet) or odd-parity (spin-triplet) order parameters. A precise definition of unconventional superconductivity is the relationship $\sum_{\mathbf{k}} \Delta(\mathbf{k}) = 0$, where the summation is carried out over all wavevectors on the Fermi surface(s); *i.e.*, $\Delta(\mathbf{k})$ must change sign somewhere in \mathbf{k} -space. Among the most celebrated examples of materials hosting unconventional superconductivity are systems with *f*-electron rare-earth elements (discovered in 1979 [22]), copper oxides (discovered in 1986 [21]), Sr_2RuO_4 (discovered in 1994 [37]), and somewhat more recently, iron-based pnictides and chalcogenides (discovered in 2008 [38]). Partially because of the the newness of these materials, and partially because of fundamental challenges in understanding the physics of systems with strong many-body interactions, the precise mechanism(s) that facilitate Cooper pairing in these materials remains hotly debated and the topic of much active research—see, *e.g.*, chapter 4. At a basic conceptual level, however, it is manifest that phonon-mediated pairing is not responsible: supercon-

ductivity emerges in close proximity to states hosting charge and/or magnetic order³, and the BCS mechanism for producing an effective attraction between quasiparticles in more ordinary metals is not strong enough to overcome the high levels of on-site Coulomb repulsion innate to these systems.

Instead, a scenario that can generate effectively attractive interactions at long ranges from overscreened on-site repulsive interactions between electron-like quasiparticles is the so-called Kohn-Luttinger mechanism of superconductivity [39, 40], first proposed in 1965, several years following BCS theory. The only necessary ingredient in this formalism is a sharply defined Fermi surface⁴; accordingly, it seems very likely to be relevant for rationalizing the low-temperature unconventional superconductivity observed in high carrier density systems such as heavy-fermion materials and Sr_2RuO_4 , where the electronic correlations make the renormalized Fermi liquid coherence scale T_{FL} quite low (in absolute units), but T_{FL} remains substantially larger than the superconducting T_c (in relative units). Computational schemes based on the renormalization group exist for calculating the energy scale of superconducting instabilities that result from this purely electronic mechanism of pairing [41], and have been applied in certain systems where the Fermiology and quasiparticle band dispersions are well parameterized from experiment [42, 43, 44]. Although it is questionable whether any of these calculations have proven capable to date of quantitatively accounting for T_c or Δ in a manner analogous to Equation 1.2, it is qualitatively true that flattened—*i.e.*, non-spherical or non-circular—Fermi surfaces and a high density of states near E_F are generally both favorable conditions for enhancing the energy scale of superconductivity within this framework [39, 40].

³In certain cases, the many-body interactions are strong enough to render the parent materials insulating!

⁴In more practical terms, this means that smearing of the Fermi surface due to thermal effects and impurity scattering must be “small” near T_c , otherwise the effectively attractive interaction drops off exponentially at large distances [39].

1.2 Outline of the text

In this chapter, we described the hierarchy of energy scales relevant to understanding the electronic properties, especially superconductivity, of the ruthenate materials studied in this dissertation. Starting from the periodic potential generated by the ions in the crystal structure, the conduction electrons form *bandstructure*—*i.e.*, energy-momentum dispersion relationships that reflect the atomic positions. Focusing on the eigenstates of the Hamiltonian with energies in the vicinity of E_F , dynamical electron-electron and electron-phonon scattering of these band electrons are accounted for via the concept of Landau's *quasiparticles*—current-carrying excitations of the interacting electron fluid that are in one-to-one correspondence with the eigenstates of band theory, but with renormalized group velocities and finite lifetimes that reflect the many-body interactions. Finally, residual interactions between these quasiparticles can, somewhat surprisingly, be effectively attractive in certain channels at very low energies near E_F , leading to Cooper pairing of the fermionic quasiparticles into composite bosons. When these bosons undergo Bose-Einstein condensation into a charged superfluid state, the material becomes *superconducting*—a novel phase of matter that exhibits both zero electrical resistance and perfect diamagnetism. The mechanisms resulting in an effectively attractive interaction between quasiparticles lead to a division of superconductors into two classes—conventional (electron-phonon mediated pairing) and unconventional (electron-electron mediated pairing).

In both cases, the unifying theme central to the work presented in this dissertation is: how does the arrangement of atoms in the crystal structure ultimately determine the energy scale of superconductivity? Based on the hierarchy of energy scales described above, it is clear that to establish causal connections between the crystal structure and superconductivity, we must understand the states that are intermediate in energy (or temperature)—namely, the $E(\mathbf{k})$ structure of excitations in the band metal, and how these

dispersion relationships are modified by many-body interactions. The remainder of this dissertation is organized as follows: In chapter 2, we describe molecular-beam epitaxy, the technique used to synthesize thin films of the ruthenium oxide materials studied in this work, Sr_2RuO_4 and RuO_2 . In chapter 3, we describe the primary characterization tools we employed to probe where the atoms are located and how the electrons move in these samples: x-ray diffraction, low-energy electron diffraction, electrical transport, and angle-resolved photoemission spectroscopy (ARPES). In chapter 4, we explore how epitaxial strain couples to the electronic structure and unconventional superconductivity in Sr_2RuO_4 thin films. In chapter 5, we demonstrate that epitaxial strain stabilizes (likely conventional) superconductivity in RuO_2 thin films; in chapter 6, we then study the mechanism underlying this phenomenon, utilizing a combination of ARPES measurements and first principles calculations to reveal how the normal-state electronic structure responds to strain in RuO_2 . Lastly, in chapter 7, we summarize our current understanding of how epitaxial strain can be used to engineer aspects of the superconductivity in Sr_2RuO_4 and RuO_2 thin films, and we highlight the most important outstanding open questions resulting from our research, which we hope will guide future investigations of these fascinating materials.

CHAPTER 2

MOLECULAR-BEAM EPITAXY

At the heart of most progress in solid-state physics is the synthesis of new materials exhibiting fascinating properties that challenge existing paradigms and theories for how electrons move in solids. In this dissertation, the technique of choice for materials synthesis is molecular-beam epitaxy (MBE)—colloquially known as atomic spray painting—and the materials under study are epitaxial thin films of multiple different ruthenium oxide compounds. As we will show later, MBE allows for exquisite control over the growth of thin films, atomic layer by atomic layer, in crystal structures and heterointerfaces that are distinctly *artificial*—*i.e.*, not realized in nature. Furthermore, MBE also exposes useful “knobs”, such as the substrate-imposed lattice strain, that can be used to template the crystal structure of the thin films that grow on top and thereby engineer films with enhanced electronic and magnetic properties relative to their bulk counterparts. In this chapter, we first describe the essential components of a modern oxide MBE system (such as those operated by the Schlom group at Cornell), and then we proceed to describe a few of the scientific ideas underlying MBE that are most germane to the synthesis of the ruthenate thin films studied in this work: the concepts of adsorption-controlled growth windows¹ and strain engineering exploiting epitaxy.

2.1 A brief history of MBE

MBE was initially developed in the 1960s by Arthur and Cho at Bell Labs [47]. At that time, the materials *du jour* were compound III-V semiconductors such as (Al,Ga)As, and indeed—after some refining of the art—MBE proved to be among the premier methods for the synthesis of these materials. In the semiconductor arena, the ability of MBE to

¹Some of the results presented in this chapter have been published in Refs. [45, 46].

produce films of high crystalline perfection with controlled compositional (doping) profiles has enabled both the development of functional electrical and optical devices [48], as well as the discovery of fundamental new physics, such as the fractional quantum Hall effect in GaAs/Al_{1-x}Ga_xAs heterostructures [49, 50]. Almost all of the current applications where MBE is used to fabricate commercial products—including field-effect transistors, quantum cascade lasers, light-emitting diodes, and Hall-probe sensors—have been born out of its roots as a method to synthesize semiconductor thin films.

On the condensed matter physics side of things, the field underwent a seismic shift in 1986 following the discovery by Bednorz and Müller of high-temperature superconductivity in copper oxide based compounds [21]. Suddenly there was great motivation to advance methods capable of synthesizing transition metal oxides, and some folks—including one of our advisors, Prof. Darrell Schlom—actively worked on adapting existing semiconductor MBE technologies to the growth of oxide thin films [51]. In the intervening years, the further development of oxide MBE has been a very fruitful scientific endeavor, as it has enabled the creation of new superconductors, (anti)ferroelectrics, (anti)ferromagnets, and even multiferroic materials that display several of these orders simultaneously. Although it remains to be seen whether the inherent complexity of transition metal oxides can be harnessed to create functional devices, the fantastic tunability of these materials (which certainly goes hand in hand with the complexity) means that oxide MBE will continue to be a fertile playground for the synthesis of materials that challenge and advance our understanding of basic solid-state physics.

2.2 Overview of oxide MBE

As the moniker of *atomic spray painting* suggests, MBE involves thermally evaporating atoms from high-purity elemental sources, directing these molecular beams towards a

single-crystal substrate target, and allowing the thus-deposited thin film to crystallize and assemble itself from the bottom up. Film deposition is performed in an ultrahigh vacuum environment to ensure that the elemental fluxes arrive at the substrate largely uncontaminated by foreign atoms, despite the incident beams having low kinetic energies (typically of order a few eV). The atomic fluxes—*i.e.*, number of atoms crossing a unit area per unit time—are measured by a quartz crystal microbalance. One of the primary benefits of using “low” incident fluxes is that the deposition time for a monolayer of atoms is typically tens of seconds, which is “slow” on the timescale of operation of shutters that block the source materials from having line-of-sight to the substrate; this implies that in certain circumstances true atomic layer by atomic layer growth modes can be realized, which enables both the synthesis of ultrathin films with digitally controlled thicknesses [52], as well as the synthesis of artificial heterostructures composed of ultrathin layers of different materials that are stacked in an alternating fashion to create a crystal with longer length-scale *superlattice* periodicities [53]. As any condensed matter physicist is well-aware, many exotic phenomena occur in systems with reduced dimensionality; in practice, MBE is among the most well-established techniques for deliberately introducing dimensional confinement into crystals at the nanometer (*i.e.*, wavefunction) scale that is usually necessary to substantially alter the electronic and magnetic properties of many-body quantum systems.

During film deposition, the substrate target is held by a sample manipulator and maintained at a specific temperature by a radiative heater. For transition metal *oxide* MBE, evaporation of the metal elements occurs simultaneously with a continuous stream of oxygen molecules impinging on the growth front. As we discuss further in subsection 2.3.1, the combination of the substrate temperature (T_s), oxidant partial pressure (p_O), and incident atomic fluxes (f) together determine what phase(s) are locally thermodynamically stable and condense into a solid thin film, and what molecular species are sufficiently volatile to leave the growth front in gaseous form, without incorporating into

the film. By adjusting any one of these three growth conditions (T_s, p_O, f) , the synthesis of one phase can be favored over other possibilities that contain the same source materials, and the regions of stability in parameter space over which specific phases are stable can be calculated from bulk thermodynamic data on the constituent materials.

In reality—especially at lower growth temperatures, where the adatom diffusion length is shorter—kinetic factors are also important in determining the crystal structure and stoichiometry of the thin films deposited by MBE. For this and other reasons, it is desirable to have some type of *in situ* diagnostics for monitoring the film growths. In the MBE systems at Cornell, this objective is achieved via reflection high-energy electron diffraction (RHEED) systems mounted on the growth chambers, which are capable of scattering electrons off the growth front and imaging the resulting diffraction patterns in real time to characterize the surface morphology and crystal structure of the films as they are being deposited. In Figure 2.1, we show a schematic diagram depicting all of these essential components of an oxide MBE system, and in the following subsections we describe each component in further detail.

2.2.1 Effusion cells and electron-beam sources

Most of the metal elements employed in oxide MBE thin film growths are supplied from commercial Knudsen effusion cells [55]. Up to eight effusion cells can be installed on the Cornell MBEs at any given time, and cells are frequently swapped out depending on what compounds users want to synthesize. Each effusion cell consists of high-purity source material (typically 99.99% purity) loaded into a crucible made of a compatible inert material (typically alumina, tungsten, pyrolytic boron nitride, quartz, or graphite) that does not react with the metal at the operation temperatures of the cell. Coiled filaments

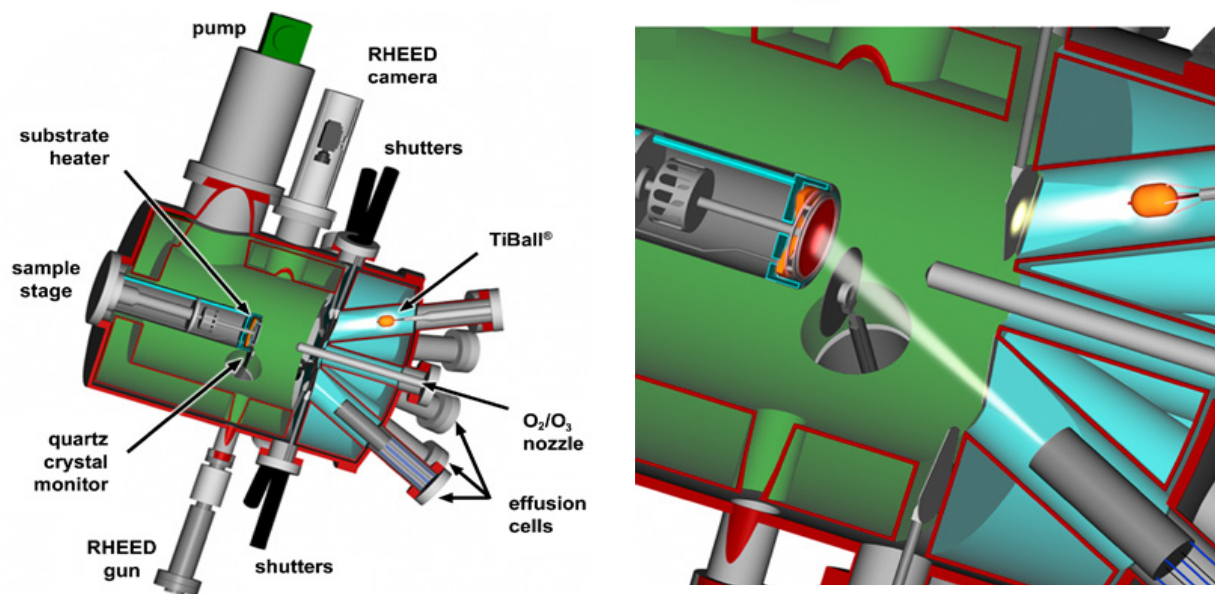


Figure 2.1: Schematic drawing of a typical oxide MBE system, labeling the key components, which are more fully described in the text. Molecular beams of elemental metals are directed from effusion cells towards a single-crystal substrate in the presence of gaseous molecular oxygen (O_2) and ozone (O_3), creating a transition metal oxide epitaxial thin film from scratch. Figure reproduced from Ref.[54].

surrounding the crucible are used to heat the source to operating temperature², which is monitored by an internal thermocouple, and the entire assembly is thermally shielded from other components on the growth chamber by a sheet metal enclosure. This design of the effusion cell, in concert with an active feedback proportional–integral–derivative (PID) temperature controller, can maintain source temperatures up to $\approx 1400^\circ\text{C}$ at values stable to $\approx \pm 0.1^\circ\text{C}$, which can be important if stable atomic fluxes are required for growth of the desired phase(s). Another important consideration in growths requiring a stable flux and high oxidant partial pressures is inadvertent oxidation of the source materials by the oxygen flowing into the main growth chamber: in such cases—as was encountered

²Note that there is no simple correspondence between the source temperatures used in MBE and the melting points of the given elements, because it is ultimately the vapor pressure versus temperature of the element that determines the evaporation rate from the source. Indeed, in some cases (such as La), the source temperature is maintained above the melting point—which can cause rather spectacular effects (and plenty of cracked crucibles) if the temperature is too quickly quenched to below the melting point (*e.g.*, during power outages).

during our growth and study of LaNiO_3 thin films [52, 56, 57]—differentially pumped sources are commonly employed, which keep the effusion cell and its surrounds at a higher level of vacuum than the main growth chamber.

Following evaporation from the effusion cells, the atoms are collimated into a molecular beam directed at the substrate. Computer-controlled programmable shutters determine whether the beams from each source are allowed to reach the substrate. Near the substrate, a quartz crystal monitor (QCM) is used to measure the flux being emitted from the effusion cells; the QCM effectively weighs the atoms that stick to it by measuring the change in resonant frequency of a quartz oscillator. QCM readings are converted to actual atomic fluxes arriving at the substrate via an overall *tooling factor* that absorbs various internal calibrations (of the QCM) and geometrical factors that depend on how the QCM and effusion cell are placed and oriented relative to the substrate. At the end of the day, the accuracy of this method for determining fluxes is limited to $\approx \pm 5\%$, and other methods such as monitoring RHEED oscillations or measuring film thicknesses by x-ray reflectivity are employed if greater accuracy is required.

Although effusion cells work admirably for most elements in the periodic table, they fail to provide sufficient flux for refractory metal elements with very low vapor pressures, such as ruthenium or iridium. In these cases, source temperatures in excess of 2000°C are required. Therefore, instead of resistively heating a crucible containing the source element, an electron beam (e-beam) heater is used to continuously bombard the source element with a stream of high-energy electrons (typical e-beam energies are $\approx 10\text{ keV}$, and typical power consumptions are several kilowatts). To ensure uniform heating, the e-beam is rastered across the source material in specific patterns, usually resembling figure eights. An important consequence of this is that e-beam users must be extremely vigilant to ensure that the beam stays focused on the ruthenium (or iridium, *etc.*); if the e-beam were to stray off target, it would drill (and has previously drilled) a hole in the stainless

steel walls of the MBE vacuum chamber! Setting aside these extra safety precautions, an e-beam source is generally similar to the effusion cell sources, with the caveat that the flux tends to drift considerably more in time. Although this technical constraint largely precludes the growth by MBE of ruthenate or iridate superlattices with atomically abrupt interfaces, it has not severely affected the ruthenate thin films synthesized as part of this thesis, which—by virtue of being grown in an adsorption-controlled regime—are rather tolerant of time-dependent variations in the incident Ru flux.

2.2.2 Oxygen sources

In addition to the effusion cell and e-beam sources for evaporating metals, an oxide MBE must, of course, have an ample supply of oxygen. Over the last ten years, it has become clear that for many transition metal oxides, high oxidant partial pressures are oftentimes required to synthesize the highest quality thin films, especially in materials of interest to the correlated-electron community where the metal-oxygen bonds are rather covalent in character, such as manganites, nickelates, cuprates, ruthenates, and iridates. At face value, this presents something of a conundrum for oxide MBE: on one hand, it is desirable to grow films under highly oxidizing conditions to avoid the detrimental effects of oxygen vacancies on the electrical and magnetic properties of the films; on the other hand, flooding the chamber with too high of a partial pressure of oxygen gas destroys the ultrahigh vacuum environment (threatening the very conception of how film growth proceeds by MBE), and leads to other technical difficulties such as the oxidation of elemental source materials, which leads to unstable fluxes.

A strategy that eliminates most of these problems is to deliver a stream of distilled ozone ($\approx 80\% \text{O}_3 + 20\% \text{O}_2$) through a stainless steel capillary tube positioned near the substrate during film growths by oxide MBE [58, 59]. Ozone is much more reactive than

molecular oxygen (O_2), and thus provides a higher oxidation potential for atoms reaching the thin-film growth front, even when present at partial pressures ($10^{-7} - 10^{-5}$ Torr) that do not totally compromise the ultrahigh vacuum environment inside the MBE chamber. To achieve these high fractional concentrations of O_3 , a 90% O_2 + 10% O_3 mixture produced by a commercial ozone generator is sent through a custom-built ozone still, developed by Tassilo Heeg, an alumnus of Prof. Darrell Schlom's research group. Inside the still, a porous silica gel is cooled by liquid nitrogen and accumulates liquified O_3 over several hours (ozone "charging"), while most of the unwanted O_2 gas is allowed to exhaust. Later, this reserve is controllably boiled off to supply O_3 during film growth, and the exact partial pressure of ozone inside the MBE chamber is controlled by a piezoelectric leak valve located in between the still and the chamber. Like the operation of e-beam sources, the use of distilled ozone for MBE film growths is not for the faint of heart—when present in sufficiently high pressures, O_3 will spontaneously explode. Accordingly, numerous precautions are taken for the ozone system, including housing the still inside a steel blast cabinet, and ensuring that the cryopump on the MBE is always gate valved off from the main vacuum chamber whenever ozone is being delivered into the system.

2.2.3 Substrate heater, pucks, and manipulator

The elements that comprise a thin film synthesized by MBE are, as described in previous sections, literally produced from scratch. However, a machine that merely evaporated various metals in the presence of oxygen would not be a particularly useful tool; we need to provide a template that directs where the atoms eventually settle and crystallize (so as to minimize the free energy of the system), and also need to ensure that the adatoms impinging on the growth front have enough thermal energy to diffuse into the desired locations. In practice, both of these objectives are achieved by inserting single-crystal substrate targets into the MBE sample manipulator and heating the substrates well above

room temperature—sometimes in excess of 1000° C. The selection and preparation of appropriate substrates, as well as the determination of suitable growth temperatures, will be discussed in later sections since they are highly dependent on the type of film being synthesized. Here we simply note a few general technical points, some of them specific to the MBE systems at Cornell.

First, the substrate is heated radiatively from the backside during growth by a silicon carbide heater. The temperature is monitored by a thermocouple connected to the heater, and the temperature setpoint is stabilized and also ramped up/down by a PID algorithm similar to those used to control the temperatures of the elemental sources. To ensure that the energy generated by the heater is efficiently absorbed by the substrates (which are typically wide-band-gap insulators), all substrates are backside coated before growth with thin layers of metals (≈ 10 nm of Ti for adhesion + ≈ 200 nm of Pt) in the Cornell Nanoscale Facility. An optical pyrometer is used to more accurately gauge the absolute temperature of the substrate surface where the film is actually deposited. The discrepancies between the temperatures measured by the thermocouple and pyrometer increase significantly at higher temperatures, which is important to account for in the growths of Sr_2RuO_4 thin films discussed in this thesis, since the windows for realizing adsorption-controlled growth of Sr_2RuO_4 are quite narrow in temperature ($< 50^\circ$ C).

Second, the substrate is held during growth by a Haynes puck that inserts into the end of the sample manipulator. *Haynes 214* is a proprietary high nickel-content alloy that has been engineered to withstand the highly oxidizing conditions and high temperatures that are present during most oxide thin film growths. In order to improve film homogeneity, the entire sample stage is usually continuously rotated during growth to average over atomic flux gradients across the incoming molecular beams. Full 360° sample rotation also allows for the incident RHEED beam to be aligned with arbitrary azimuths of the crystal structure of the film / substrate. The most common size of wafers used for MBE

film growths in our systems are 10 mm \times 10 mm in area, although certain Haynes holders and the substrate heater can accommodate circular wafers with 3 in. diameters.

2.2.4 Reflection high-energy electron diffraction

All of the MBE chambers at Cornell are equipped with RHEED systems to monitor film growth. The basic operating principles underlying RHEED are similar to the other electron and x-ray diffraction methods that will be described more comprehensively in the next chapter: a monochromatic, well-collimated, beam of high-energy electrons (≈ 10 keV) is aimed at the surface of the film / substrate, typically at a grazing angle of incidence ($< 3^\circ$), and the resulting two-dimensional diffraction pattern is detected by a fluorescent phosphor screen on the opposite side of the vacuum chamber, which is in turn imaged by a CCD camera in order to digitize the data. The grazing angles of incidence and exit guarantee a high degree of surface sensitivity despite the large incident energies employed; as a rule of thumb, RHEED is sensitive to scattering from core electrons in the topmost few atomic layers of the film, within < 10 nm from the film surface. Moreover, the grazing scattering geometries and ease of focusing electrons allow RHEED to be a relatively unobtrusive surface structural probe suitable for lab-based MBEs, which can be measured in real time as films are being deposited.

The major drawback of RHEED is that electron diffraction is inherently complicated by the effects of multiple scattering, and so analysis of RHEED data is often guided by anecdotal experiences, rarely with any support from simulations or calculational schemes that have been shown to accurately model RHEED scattering cross sections. For this reason, the author of this dissertation believes that any observations based on RHEED data should be treated skeptically as qualitative *suggestions* rather than definitive *conclusions*, which should be supported by further x-ray diffraction measurements and/or

low-energy electron diffraction measurements³. Nonetheless, there are a few heuristic principles for interpreting RHEED data that we list below, which seem fairly robust in practice:

- The lateral separation between spots and/or streaks in the RHEED pattern are determined by the average in-plane periodicity of the surface crystal structure perpendicular to the propagation direction of the incident and specularly reflected beams. This statement merely expresses the conservation of momentum modulo $\mathbf{q}_{\parallel} = \mathbf{G}$, where \mathbf{G} is a translation of the surface reciprocal lattice, and as such is guaranteed by the discrete translational symmetries of the surface crystal structure in real space, irrespective of the exact details of how high-energy electrons scatter off such a periodic potential. Since a large area of reciprocal space is imaged on a small physical area of the phosphor screen, a precise determination of the surface lattice constants is not possible with RHEED. However, when surface reconstructions are present and “strong” enough to be detected by RHEED—*i.e.*, the extra peaks/streaks clearly rise above the diffuse background, which is usually quite high—the underlying cause is likely a non-stoichiometric surface involving the redistribution of many electrons, rather than some more subtle distortion of the atomic positions in an otherwise stoichiometric surface. In certain cases where the surface chemistries are expected to be similar, such as the SrO-terminated surface of perovskite and Ruddlesden-Popper thin films, it is likely possible (with some personal experience) to establish and recognize the hallmark periodicities and intensity distributions (*i.e.*, “fingerprints”) for electron scattering off of Sr-rich surfaces that are applicable across different material families [60], even if the underlying crystal structures of such surfaces are not known in detail.
- The intensity profiles of the spots and/or streaks along the orthogonal direction in

³Both of these techniques are much better understood theoretically than RHEED, *cf.* chapter 3

RHEED patterns depend primarily on the morphology of the growing film, rather than the surface crystal structure of the film. Strongly islanded film growths generally produce an array of discrete spots, since in this limit RHEED is more akin to transmission electron microscopy than to diffraction measured in a reflection geometry. Smoother surfaces will generally produce streakier RHEED patterns, except in the limit of surfaces with highly perfect crystallinity; in this case, the intensity is very intense and coalesces around single spots along the RHEED streaks due to kinematic constraints on the electron scattering.

- Spots and/or streaks in the RHEED pattern from films that grow in a truly atomic layer by atomic layer fashion will show characteristic oscillations in intensity as progressively more layers of the film are deposited. This can be a useful method for calibration of source fluxes that is accurate to $\approx 1\%$ —one simply must time the period of RHEED oscillations with a stopwatch, and then use the number of atoms in a monolayer of the given crystal structure to obtain the flux impinging on the substrate per unit time. It is not guaranteed, however, that the maximum (or minimum) of RHEED intensity is reached at any special point in the deposition of a given monolayer. For example, contrary to popular belief, it is not necessarily true that the maximum (minimum) of RHEED intensity is reached at the point when a full (half) monolayer of additional material has been deposited [61]. Thus, using RHEED oscillations to purportedly evidence a specific surface termination in the growth of perovskite thin films should be treated with skepticism, in lieu of other supporting measurements.

2.3 Growth of ruthenate thin films by MBE

Perovskite-based ruthenium oxide compounds host a myriad of novel electronic ordering phenomena, including unconventional superconductivity [37] and magnetic field-induced quantum criticality [62], that are extremely sensitive to disorder [63]. As we will discuss at some length in chapter 4, dilute impurity concentrations of only a few hundreds of parts per million can destroy the superconducting ground state in Sr_2RuO_4 [64]. In the case of CaRuO_3 , many experiments conducted over 20+ years suggested the possibility of a non-Fermi liquid behavior, until a set of more recent experiments on cleaner samples evidenced the usual hallmarks of a Fermi liquid ground state, just with an anomalously low coherence scale $T_{FL} \approx 1.5$ K [65, 66]. Because the properties of ruthenates are known to respond dramatically to external perturbations such as uniaxial pressure [67, 68, 69], they represent an ideal system for exploring how these emergent ground states can be manipulated and controlled in thin-film form; however, an obvious prerequisite for any such efforts is the ability to synthesize thin films with extremely low levels of disorder.

A significant issue encountered during the growth of ruthenate thin films is the loss of Ru atoms in the form of volatile RuO_x gas species ($x = 2$ or 3) at temperatures above $\approx 700^\circ$ C. Films grown above this temperature contain significant concentrations of Ru vacancies. On the other hand, films grown below this temperature are generally closer to stoichiometric, but contain significant amounts of quenched structural disorder because of the reduced adatom diffusion length at lower growth temperatures. Thus in both limits, the residual resistivities are well in excess of $10\ \mu\Omega\text{-cm}$ —sometimes even above $100\ \mu\Omega\text{-cm}$ —which are at least 1 - 2 orders of magnitude too large to observe any of the exotic low-energy physics mentioned above.

A significant portion of this dissertation was devoted to assisting our collaborators in the Schlom group develop and conclusively demonstrate a new strategy for the synthesis

of ruthenate thin films by MBE that circumvents both of these issues: grow at high substrate temperatures, where structural disorder is minimized, and flood the growing film with excess ruthenium to mitigate the formation of Ru vacancies. This approach is analogous to the way in which high-quality films of compound semiconductors with volatile constituents, such as GaAs, are grown [70]. In subsection 2.3.1, we describe the concept of adsorption-controlled growth windows as it applies to ruthenate thin films in somewhat more detail, emphasizing how our electrical transport measurements provide a stringent test of the cation stoichiometry. In subsection 2.3.2, we then describe the potential of substrate-imposed epitaxial strains as a knob for tuning the superconducting properties of thin films, an idea which will be revisited and explored throughout the remainder of this thesis in the context of both Sr_2RuO_4 and RuO_2 .

2.3.1 Adsorption-controlled growth windows

The region of substrate temperature, oxidant partial pressure, and atomic fluxes (T_s, p_O, f) over which a particular compound is thermodynamically stable is commonly called a *adsorption-controlled growth window*. For example, at the gross scale this means that by adjusting ($T_s, p_O, f_{\text{Ru}}/f_{\text{Sr}}$), one can favor the condensation of a Sr_2RuO_4 thin film instead of a SrRuO_3 thin film, as illustrated in Figure 2.2. At the finer scale, the finite size of the growth windows in parameter space and the automatic composition control provided by thermodynamics within these windows ensures that when a Sr_2RuO_4 (SrRuO_3) film crystallizes, its stoichiometry is truly 2 atoms (1 atom) of Sr for every 1 atom of Ru, with deviations away from the ideal 2 : 1 (1 : 1) ratio that can be less than 1 part in 1,000.

The crucial insight of Hari Nair (a postdoc in the Schlom group) was to adapt these ideas that are well-known and appreciated among MBE aficionados in the growth of III-V compound semiconductors, to the growth of ruthenate thin films by oxide MBE. Readers

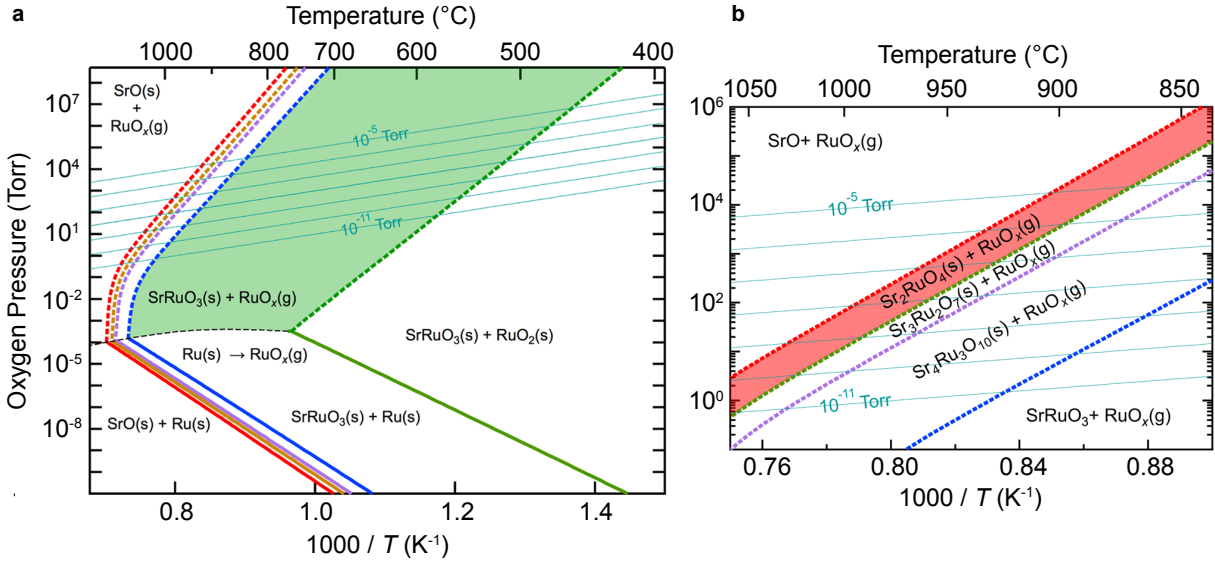


Figure 2.2: Thermodynamics of MBE (TOMBE) diagrams illustrating conditions for which adsorption-controlled growth of Ruddlesden-Popper strontium ruthenate thin films can be realized. The cyan lines represent the equivalent oxygen pressures for the indicated partial pressures of distilled ozone used in MBE growths. Growth in the wide region shaded green in (a) produces SrRuO_3 films, while growth in the narrow region shaded red in (b) produces Sr_2RuO_4 films; in both cases, an excess Ru flux of $\approx 1 - 2 \times 10^{13}$ atoms/cm²s is supplied to avoid the formation of Ru vacancies in the films, which desorbs from the growth front as volatile RuO_x gas species. Note that (b) is essentially a zoomed-in version of (a), but calculated for a slightly lower excess Ru flux so as to expand the width in temperature and pressure over which Sr_2RuO_4 is stable.

interested in a more comprehensive treatment of this topic are referred to Refs. [45, 46], where the synthesis science of CaRuO_3 , SrRuO_3 , and Sr_2RuO_4 is spelled out in considerable detail at an experimental and computational level⁴. To summarize these works in short: by establishing adsorption-controlled growth windows for the growth of several types of ruthenate thin films by MBE, we have been able to reproducibly synthesize films with excellent electrical properties, which is an essential first step towards the study of how the extremely disorder-sensitive ground states in these materials respond to epitaxial strain and dimensionality.

⁴As an aside: after having the privilege of being a co-author on these papers, I am now convinced that there is method to the madness—MBE is not always merely “black magic”.

To substantiate what “excellent” means in this context, Figure 2.3 displays the electrical transport behavior of prototypical CaRuO_3 , SrRuO_3 , and Sr_2RuO_4 thin films synthesized by MBE within adsorption-controlled growth windows for these compounds. Like all perovskite-based ruthenates, these films show large, non-saturating resistivities at elevated temperatures, which reflect the strong electronic correlations in this family of materials. As the temperature is lowered, electron-electron scattering events are successively “frozen out” by phase space constraints, and in the low-temperature limit the residual resistivity $\rho_0 \equiv \rho(T \rightarrow 0 \text{ K})$ provides a metric of the electron-disorder scattering rate (see also section 3.2). Lower values of ρ_0 —or equivalently, higher values of the residual resistivity ratio, $RRR \equiv \rho(300 \text{ K})/\rho(4 \text{ K})$ —indicate lower levels of disorder.

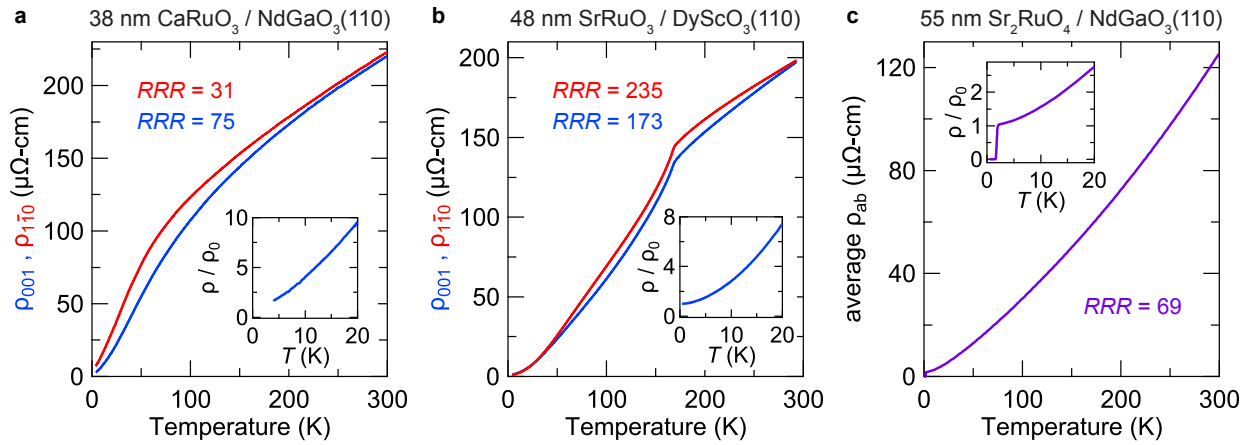


Figure 2.3: Electrical resistivity versus temperature for (a) CaRuO_3 , (b) SrRuO_3 , and (c) Sr_2RuO_4 thin films synthesized by MBE within adsorption-controlled growth windows for these compounds. The resistivity tensor in (a) and (b) is resolved into its two diagonal in-plane components (red and blue), which are not guaranteed to be equal by the orthorhombic crystal symmetry; in (c) we plot the geometric mean of the two in-plane components of the resistivity tensor. Insets show the resistivities at low temperatures normalized to their extrapolated values at $T = 0 \text{ K}$: the data for CaRuO_3 and SrRuO_3 show clear signatures of strong electron-electron scattering down to the lowest measured temperatures, and Sr_2RuO_4 becomes superconducting at $T_c = 1.8 \text{ K}$.

To put the numbers shown here in perhaps more meaningful units, consider the case of Sr_2RuO_4 . An extraordinary amount of information is known about the electronic structure of Sr_2RuO_4 from multiple different probes; thus, it is possible to use the experimen-

tally measured Fermi velocities and Fermi surface topology of this material to quantitatively convert the macroscopic transport scattering rate at low temperatures (gauged by ρ_0) to a more microscopic mean free path for scattering that describes the length scale over which the quasiparticle momentum is relaxed (ℓ). The relationship between these quantities is $\ell = C/\rho_0$, where the coefficient of proportionality $C \approx 1.1 \mu\Omega\text{-cm} * 90 \text{ nm}$ [64]. Therefore, the residual resistivity of $\rho_0 = 1.7 \mu\Omega\text{-cm}$ for the Sr_2RuO_4 film in Figure 2.3 corresponds to $\ell = 60 \text{ nm}$, or about 150 unit cell translations, which is very long by the standards of ternary oxides. Converting ℓ to impurity concentrations n_i requires more microscopic knowledge about the exact nature of the impurities—in technical terms, the impurity scattering cross section(s) Σ_i —which depend on the chemical identities of the defects, their substitution sites, *etc.* Nonetheless, if we assume that the point defect-scattering phenomenology is similar between these Sr_2RuO_4 films and single crystals that have been studied previously⁵, then the observation of superconductivity in these films implies that the Sr:Ru ratio is stoichiometric to better than 1 part in 1,000. This deviation of Sr:Ru from its ideal value of 2 is at least one order of magnitude lower than the $\gtrsim 1\%$ error that can be achieved in MBE via approaches that attempt to explicitly match the fluxes of the source elements in a specific ratio. Finally, we note that a similarly successful adsorption-controlled approach has been applied to the growth of SrVO_3 thin films by hybrid MBE (using a metal-organic precursor for vanadium) to achieve residual resistivities $\rho_0 < 1 \mu\Omega\text{-cm}$ [71], but otherwise this method seems underutilized in the synthesis of correlated metals and superconductors by oxide MBE, so it is hoped that our work spurs more development in this area.

⁵A direct quantitative comparison of ρ_0 values between crystals and films is likely not valid, since extended structural defects from dislocations, anti-phase boundaries, and intergrown phases also contribute to ρ_0 in Sr_2RuO_4 thin films.

2.3.2 Strain engineering exploiting epitaxy

One very appealing aspect of MBE lies in an approach we refer to as *strain engineering exploiting epitaxy*. In this scheme, thin films of a given material are deposited on a substrate whose in-plane lattice constants are chosen to be deliberately mismatched with the in-plane lattice constants the thin film material would adopt if it were a bulk crystal. Up to a certain *critical thickness*, the film will grow pseudomorphically on top of the substrate, essentially inheriting the two in-plane lattice constants of the substrate by the epitaxial templating effect. Along the out-of-plane direction, the film is free to relax however it would like so as to minimize its free energy in this constrained subspace—*e.g.*, if the film lattice constants are under net compression (tension) in the plane, the out-of-plane lattice constant will generally expand (contract), respectively, based on the Poisson effect. In this regime, the film is said to be *coherently strained*, and to controllably alter the crystal structure of the film, we simply need to grow another sample on a different starting substrate that has suitably different in-plane lattice constants. Applied to transition metal oxides, this approach has been employed to create strained thin films of identical chemical formulas that have dramatically different electronic and magnetic properties [72]; these differences in properties ultimately derive from how the magnitudes and symmetries of the substrate-imposed strains couple to the microscopic degrees of freedom in the films, such as orbital polarizations, structural instabilities, *etc.* For a materials scientist, epitaxial strain is thus a very promising route towards creating artificially engineered materials with enhanced properties; for a condensed matter physicist, epitaxial strain is a natural “knob” that can be used to perturb parameters of the effective Hamiltonian of a given material, and thereby gain insight into how competing states of the system depend on (and can be tuned by) these parameters.

In a thermodynamic picture of film growth, the critical thickness t_{crit} is determined by balancing contributions to the free energy from the film-substrate interface (which favors

coherently strained growth) against the accumulation of strain energy within the entirety of the film (which favors relaxation towards the bulk crystal structure of the material). If film growth is continued past $t_{crit.}$, a variety of defects (vacancies, misfit dislocations, twin boundaries, *etc.*) will nucleate to partially relax the interfacial strain. For materials where these mechanisms of strain relaxation are spatially inhomogeneous, it becomes more challenging to interpret the macroscopic electronic and magnetic properties of partially strain-relaxed films in terms of theories that presume periodic crystal structures, so generally data from coherently strained films are preferred whenever possible in studies of how these properties can be tailored by epitaxial strain. Identification of $t_{crit.}$ is thus an important step in epitaxial strain engineering studies. Unfortunately, several of the theoretical estimates—*e.g.*, the Matthews-Blakeslee criterion [73]—that have been proposed in the literature for calculating $t_{crit.}$ based on the lattice mismatches of the film and substrate have been shown to systematically underestimate $t_{crit.}$ in the MBE growth of perovskite-based oxide thin films by as much as an order of magnitude [74]. Without getting into too much detail, these large discrepancies likely reflect a combination of these equilibrium theories ignoring kinetic barriers that can be important in actual thin film growths (especially for growths carried out at lower temperatures), as well as these theories ignoring the internal degrees of freedom in many perovskite-based structures (*e.g.*, metal-oxygen-metal bond angles) that can relax some of the substrate-imposed strain energy without actually changing the film lattice constants. In any case, since these models offer little predictive value, in this thesis we adopt a purely empirical approach towards evaluating $t_{crit.}$: we simply collect x-ray diffraction for different thickness films of Sr_2RuO_4 and RuO_2 synthesized on different substrates, and determine from features of these data beyond what thickness the films start to show hallmarks of partial strain relaxation.

CHAPTER 3

THIN-FILM CHARACTERIZATION TECHNIQUES

In the previous chapter, we introduced the molecular-beam epitaxy (MBE) technique used to synthesize the ruthenate thin-films studied as part of this dissertation. Of course, MBE is only the start of the synthesis + characterization + computation feedback loop that we proposed in the introduction to discover, understand, and ultimately optimize the properties of designer quantum materials, especially novel superconductors. In this chapter, we review the second component of this loop, focusing on the four primary thin-film characterization measurements that have been instrumental to obtain the results presented in this dissertation: x-ray diffraction (section 3.1), electrical transport (section 3.2), *in situ* angle-resolved photoemission spectroscopy (section 3.3), and *in situ* low-energy electron diffraction (section 3.4). Because the scope of these techniques is enormous, and many comprehensive and pedagogical expositions already exist elsewhere, here we provide admittedly myopic descriptions of each topic that discuss only the background and theory needed to understand and interpret data in subsequent chapters of this thesis.

3.1 X-ray diffraction

X-ray scattering occurs via the interaction of x-rays with electrons. In the language of modern condensed matter physics, non-resonant x-ray diffraction probes the Fourier transform of the equal-time spatial correlation function of the electron density ρ : $S(\mathbf{q}) \propto \mathcal{F} \langle \rho(\mathbf{r})\rho(\mathbf{x} + \mathbf{r}) \rangle$. Hence it is an excellent method for obtaining structural information about solids, both ordered and disordered, and is among the most widespread and successful methods for answering one of the most basic questions physicists can ask after synthesizing a new material—namely, *where are the atoms located?* In this section, we first describe the interaction of hard x-rays with matter generally, and then narrow the

scope to configurations of atoms that are frequently encountered in the study of epitaxial thin films grown on top of single-crystal substrates. We discuss the types of diffraction measurements that are typically used to characterize such systems, and where appropriate, include details about how these measurements were performed in this thesis using the lab-based diffractometers and synchrotron-based facilities available at Cornell.

3.1.1 General formalism

When monochromatic x-rays of incident wavevector \mathbf{k}_i and amplitude A_0 elastically scatter off an electron located at position \mathbf{r}_e , the amplitude of the scattered wave at a distance R_0 away is given by the formula

$$A = A_0 \frac{e^2}{mc^2} \frac{1}{R_0} \exp [i(\mathbf{k}_f - \mathbf{k}_i) \cdot \mathbf{r}_e] , \quad (3.1)$$

where e and m are the charge and mass of the electron, and c is the speed of light. Notably, in this expression the Thomson scattering length, $e^2/mc^2 \approx 2.85 \times 10^{-15}$ m, is a *small number* compared with R_0 . This means that interactions between x-rays and electrons are “weak” and accordingly, x-ray scattering from a full crystal containing many unit cells, each of which contains many atoms, each of which contains many electrons, can be easily computed from Equation 3.1 by superposition. We skip the full derivation here and quote the results. The amplitude of the wave elastically scattered by a slab of crystal with unit cell translations $(\mathbf{a}_1, \mathbf{a}_2, \mathbf{a}_3)$ comprised of $N_1 \times N_2 \times N_3$ unit cells is generally given by:

$$A = A_0 \frac{e^2}{mc^2} \frac{1}{R_0} F(\mathbf{q}) \sum_{n_1=0}^{N_1-1} \sum_{n_2=0}^{N_2-1} \sum_{n_3=0}^{N_3-1} \exp [i\mathbf{q} \cdot (n_1\mathbf{a}_1 + n_2\mathbf{a}_2 + n_3\mathbf{a}_3)] , \quad (3.2)$$

where $\mathbf{q} = \mathbf{k}_f - \mathbf{k}_i$ is the momentum transfer, and

$$F(\mathbf{q}) = \sum_{j=1}^{N_a} f_j(|\mathbf{q}|) \exp[i\mathbf{q} \cdot \mathbf{r}_j] \quad (3.3)$$

is the structure factor of the unit cell. All atoms within the unit cell have their own atomic scattering factors $f_j(|\mathbf{q}|)$, which depend primarily on the chemical identity of each atom and are recorded in standard tables [75]. To compute the diffraction intensities I measured experimentally, we simply take the modulus squared of Equation 3.2, *i.e.*, $I \propto |A|^2$.

3.1.2 Application to epitaxial thin films

For epitaxial thin films grown on single-crystal substrates, the penetration depth of x-rays at typical hard x-ray energies (≈ 1 mm at 10 keV) is typically many orders of magnitude larger than the thicknesses of the films being studied ($\approx 10 - 100$ nm). This observation, in combination with the previously mentioned notion that the interaction of x-rays and electrons is weak, means that we can model scattering from this type of “hybrid” crystal as the superposition of scattering from two separate slabs of crystals (in the following, we use f and s subscripts to denote *film* and *substrate* quantities, respectively)¹; *i.e.*,

$$I_{film+sub.} = |A_f + A_s|^2 \quad (3.4)$$

For all practical purposes, the substrates used in our studies are infinitely periodic single crystals in all three spatial dimensions with extremely limited densities of structural defects. Translating this language into the variables of Equation 3.2, this means that one relevant limit of this equation to analyze is $(N_1, N_2, N_3) \rightarrow (\infty, \infty, \infty)$ with single-valued unit-cell translations $(\mathbf{a}_1, \mathbf{a}_2, \mathbf{a}_3)$. In this limit, it can be shown that the scattered inten-

¹For examples and discussion of thin film + substrate systems where multiple scattering effects are important, we refer the interested reader to Ref.[76].

sity becomes very sharply peaked—delta-function-like, with the divergences cut off by absorption of the x-rays, thermal vibrations, and other “real-world” smearing effects—around points in reciprocal space where the three components of \mathbf{q} satisfy the so-called *Laue condition*:

$$\mathbf{q} = \mathbf{G} = H\mathbf{b}_1 + K\mathbf{b}_2 + L\mathbf{b}_3 . \quad (3.5)$$

Here HKL are integers (often called Miller indices of the Bragg peak), and $(\mathbf{b}_1, \mathbf{b}_2, \mathbf{b}_3)$ are the primitive reciprocal lattice translations of the substrate lattice. Writing the primitive translation vectors of the real-space and reciprocal-space lattices as the column vectors of matrices, one can be calculated from the other according to:

$$[\mathbf{b}_1 \ \mathbf{b}_2 \ \mathbf{b}_3]^T = 2\pi [\mathbf{a}_1 \ \mathbf{a}_2 \ \mathbf{a}_3]^{-1} \quad (3.6)$$

To model the contribution to the x-ray diffraction profiles from the thin films grown epitaxially on top of such substrates, a reasonable starting point is to assume that the in-plane lattice constants of the film are matched to those of the substrate by the templating effect discussed in subsection 2.3.2 (*i.e.*, $\mathbf{a}_{1f} = \mathbf{a}_{1s}$ and $\mathbf{a}_{2f} = \mathbf{a}_{2s}$), and that the lattice of the film is also effectively infinite in the plane (*i.e.*, $N_{1f}, N_{2f} \rightarrow \infty$ — we will reexamine this point later in subsection 3.1.4). Along the third direction, although the film will generally have an approximately constant out-of-plane lattice constant a_3 , it will be decidedly finite in extent in this direction: typical values of N_{3f} may range from $\approx 10 - 100$, depending on the thickness of the film.

By similar arguments as above, the scattering from an object with aspect ratios $N_{1f}, N_{2f} \rightarrow \infty \gg N_{3f}$ will be rod-like in nature: highly concentrated in reciprocal space around the locus of points where $\mathbf{q}_{||} = \mathbf{G}_{||} = H\mathbf{b}_{1s} + K\mathbf{b}_{2s}$, and much more extended

along the out-of-plane direction with $\mathbf{q}_\perp \parallel \mathbf{b}_{3f}$. Each feature in diffraction measurements with a specific value of q_\parallel and arbitrary values of q_\perp is referred to as a *crystal truncation rod* (CTR). To appreciate the non-trivial interference effects that can occur along a given CTR due to the finite thickness of the film, suppose that we are simulating data along the specular crystal truncation rod ($q_\parallel = 0$) for an film of $N_{3f} = N$ unit cells in thickness, and just considering scattering from the film, neglecting the contributions of the substrate. In this situation, evaluating Equation 3.2 for the scattered intensity using the well-known formula for a geometric series yields:

$$I \propto |F(q_\perp)|^2 \left| \sum_{n_\perp=0}^{N-1} \exp[iq_\perp a_\perp n_\perp] \right|^2 = |F(q_\perp)|^2 \left| \frac{1 - \exp(iq_\perp a_\perp N)}{1 - \exp(iq_\perp a_\perp)} \right|^2 = |F(q_\perp)|^2 \frac{\sin^2(q_\perp a_\perp N/2)}{\sin^2(q_\perp a_\perp/2)} \quad (3.7)$$

Equation 3.7 is called the *N-slit interference function*, owing to its application in optics (and indeed many areas of physics). A plot of this function—neglecting the structure factor $F(q_\perp)$, which varies gradually on the scale of the oscillations resulting from the \sin^2 terms—is shown in Figure 3.1. There are three salient features of this function that are crucial in interpreting the x-ray diffraction data from the thin films shown later in this thesis:

- The primary maxima of the diffraction pattern are located at integer multiples of $q_\perp = 2\pi/a_\perp$ —exactly the Bragg peak locations that would be realized in the limit of a bulk crystal with $N \rightarrow \infty$. Thus from experimental measurements of these peak locations, we can deduce the out-of-plane lattice constant of the film, a_\perp .
- The width of the primary maxima along q_\perp are inversely proportional to N , the number of unit cells in the film along the out-of-plane direction. This can be thought of as a generalized “uncertainty principle”, whereby the scattering from a finite-sized object (in one dimension) in real space must be spread along a range of values

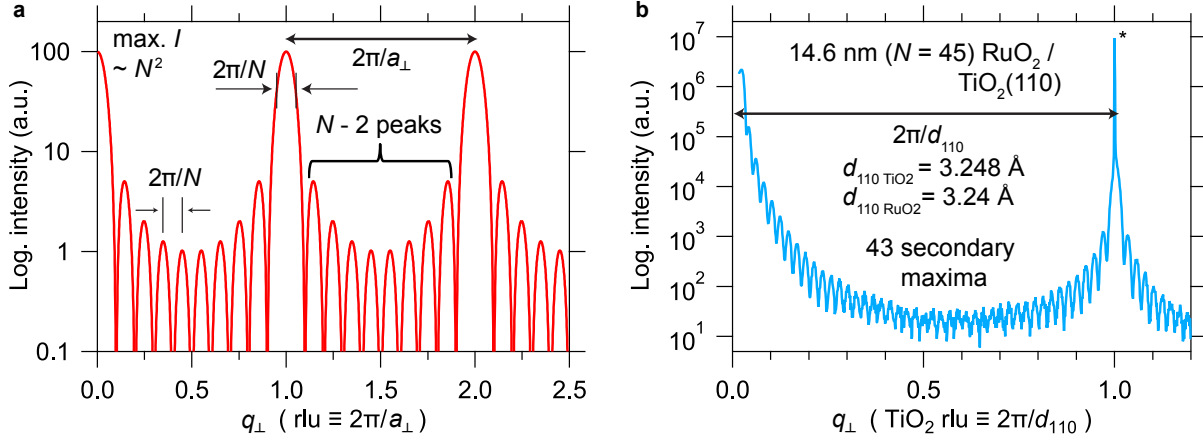


Figure 3.1: (a) Plot of Equation 3.7 simulating the x-ray scattering from a thin film of thickness $N = 10$ unit cells. For simplicity the structure factor is held constant ($F(q_{\perp}) = 1$). The primary maxima of the diffraction pattern are located at integer multiples of $2\pi/a_{\perp}$, and their intensity scales like N^2 . The finite thickness of the film manifests in the width of the primary peaks $2\pi/N$ and the existence of $N - 2$ secondary maxima between the main peaks, which are nearly equally spaced apart by amounts $2\pi/N$. (b) Experimental data for an $N = 45$ film of RuO_2 synthesized on an isostructural $\text{TiO}_2(110)$ substrate, illustrating the features described in (a). The asterisk indicates the 110 Bragg peak of the substrate.

along the same direction in reciprocal space. In practice, it also means that any scattering features in x-ray diffraction data with widths significantly sharper than $1/N$ along q_{\perp} must originate from scattering off the substrate or something besides just the film.

- There are ideally $N - 2$ secondary maxima between each primary maximum of the diffraction pattern. In real experimental data, due to interfacial roughnesses and other instrumental effects, it is usually not possible to resolve all of these secondary maxima and merely *count* their number to obtain the total film thickness; however, because the spacing between between these secondary maxima scales like $1/N$, we can find the positions of several such maxima and from their separations deduce the average coherently scattering crystalline thickness, Na_{\perp} . This is among the most accurate methods for determining the thicknesses of films synthesized by MBE.

3.1.3 X-ray reflectivity

In subsection 3.1.2, we demonstrated how features of the x-ray diffraction profiles measured along the CTRs can be utilized to determine the film thickness. In this modeling, we tacitly assumed that the film had a single-phase crystal structure (with no intergrowths of other phases) and minimal amounts of strain inhomogeneity along the out-of-plane direction, so that we could effectively treat the lattice constant a_{3f} as a single-valued number. In practice, these requirements are often not satisfied in real materials grown by MBE, and it is desirable to have an independent measurement of the film thickness that does not depend on the actual crystal structure of the film conforming to such an idealized model.

Fortunately, there is such a measurement—called x-ray reflectivity—and conveniently, to perform such measurements we can use the same experimental setup as for x-ray diffraction and just change the incident and scattered angles to measure regions of reciprocal space with low values of q_{\perp} . In this region of q -space, the interaction of x-rays with the sample is dominated by refraction effects at the vacuum-film and film-substrate interfaces, rather than on a detailed knowledge of the atomic positions inside the film. By applying wave matching constraints at these interfaces analogous to a generalized form of Snell’s Law, reflectivity profiles can be readily simulated for layered structures of arbitrary complexity, and many software packages exist for precisely this purpose². We refer readers interested in a more thorough theoretical description of x-ray reflectivity to Ref.[78]. For our purposes here, we simply note the following three characteristic features of specular reflectivity curves, which are illustrated in Figure 3.2:

- By far the most important material properties in determining the x-ray reflectivity

²For simulating and fitting x-ray reflectivity and x-ray diffraction profiles in this thesis, we used the X’Pert Reflectivity program (proprietary software from Panalytical) and GenX, an open-source software package [77].

profile are the *electron densities* ρ_{el} of the constituent layers—in our case: air, the film, and the substrate. In fact, because the refractive index inside the film is smaller than that of air ($n_{air} \approx 1$), there will be a *critical angle* of incidence below which x-rays are totally externally reflected, given by the expression:

$$\alpha_{crit.} = \sqrt{\frac{\rho_{el,f} r_0 \lambda}{\pi}} \quad (3.8)$$

where r_0 is the Thomson scattering length and λ is the wavelength of the radiation. While one could imagine inverting Equation 3.8 to deduce $\rho_{el,f}$ from the measured $\alpha_{crit.}$ —*e.g.*, for a film of some unknown material—we do not pursue this approach because the typical beam divergence in lab-based x-ray sources make it challenging to accurately measure $\alpha_{crit.}$.

- Similar to the interference effects observed in diffraction, the finite extent of the film along the out-of-plane direction produces oscillations in the the reflected intensity. The spacings between the maxima of such fringes are almost inversely proportional to the film thickness. This provides a simple (and highly accurate) way of experimentally determining the total film thickness, which can be compared / contrasted with the coherent crystalline thickness obtained from diffraction measurements.
- The peak-to-trough ratio of the finite-thickness fringes are determined by the effective electron density contrast between the constituent layers. “Effective contrast” means that one way to enhance the peak-to-trough ratio is to measure films on substrates with more dissimilar $\rho_{el.}$; the other is to make the interfaces between such layers more abrupt. The latter effect can be used to fit the film roughnesses that always exist at some level at its bounding interfaces.

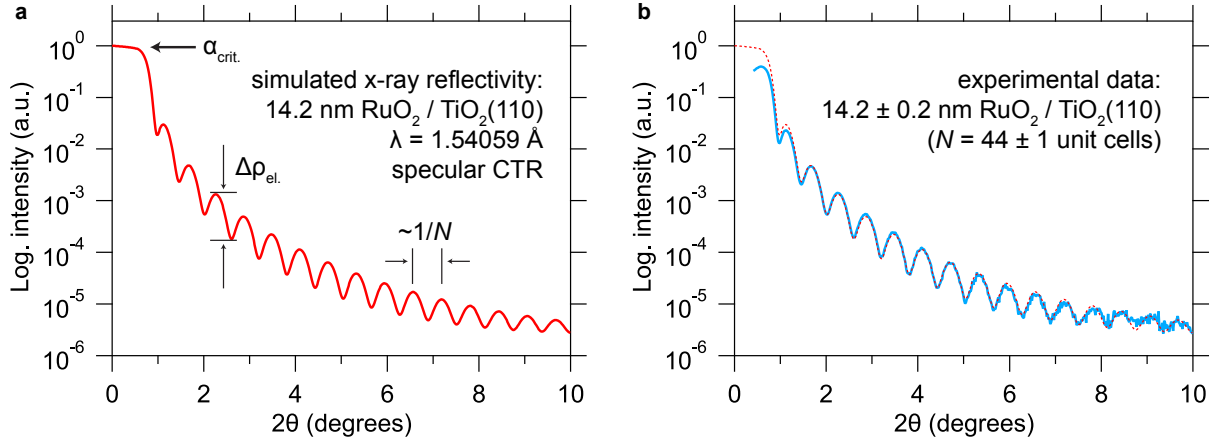


Figure 3.2: (a) Simulated x-ray reflectivity profile along the specular CTR for a 14.2 nm thick $\text{RuO}_2/\text{TiO}_2(110)$ sample, plotted versus the detector angle 2θ . Total external reflection occurs at the surface of the film for angles below $\alpha_{crit.}$, which is set by the electron density of the film, *cf.* Equation 3.8. As in Figure 3.1, interference effects cause finite-thickness fringes that become more closely spaced as the number of unit cells N in the film along the out-of-plane direction increases. The peak-to-trough ratio of the fringes is set by the electron density contrast $\Delta\rho_{el.}$ between the film and substrate. (b) Experimental data plotted in blue, with the simulations from (a) overlaid as a red dashed line. The fit is excellent except at very low incident angles, which is an experimental artifact of the angularly divergent incident beam used in lab-based x-ray machines.

3.1.4 Reciprocal space maps

In subsection 3.1.2, we showed in what regions of reciprocal space appreciable intensities are expected for an epitaxial thin film + substrate system in which the in-plane lattice spacings of the film and substrate are equal and constant over effectively infinite in-plane length scales. While this is a convenient starting point for interpreting experimental data, deviations from this idealized situation are often observed in reality: for examples, the film may form misfit dislocations to relieve the substrate-imposed in-plane strains (*i.e.*, there may be columns and/or sheets of film atoms added or removed to effectively allow $a_{1f} \neq a_{1s}$ and/or $a_{2f} \neq a_{2s}$), or there may be locally non-stoichiometric intergrowths of other phases. With sufficient knowledge about how the atomic arrangements are altered near these regions containing structural defects (*e.g.*, from scanning transmission electron

microscopy), their effects on x-ray diffraction profiles can be simulated by straightforward generalizations of Equation 3.2. As a general rule of thumb, these defects are located in relatively *narrow* regions of real-space, and so their scattering signatures in reciprocal space should be correspondingly *diffuse*.

The most common type of measurements performed to gauge the magnitude of these effects experimentally are called reciprocal space maps (RSMs). In general terms, most RSMs are simply measurements along a specific CTR extended to include some finite region of \mathbf{q} -space surrounding the CTR. These data sets are inherently four-dimensional in nature, with the scattered intensity being measured at many values of (q_1, q_2, q_3) . A common way of visualizing such information is to take two-dimensional slices through the data where the vertical axis is aligned with q_3 (*i.e.*, q_{\perp}), the horizontal axis is aligned with some linear combination of q_1 and q_2 (*i.e.*, q_{\parallel}), and the measured intensity at each $(q_{\parallel}, q_{\perp})$ is plotted using a logarithmic false color scale. By taking line cuts through these data, the spatial correlations of the electron density along different directions with respect to the underlying parent crystal structure can be quantified. Phrased in this way—rather than by appealing to a Bragg’s-Law-type description of diffraction off infinite planes of atoms—it is clear that to assess the role of structural and chemical defects in real materials, the *line shapes* of the measured x-ray intensity profiles are just as important as where the peaks in these intensity profiles are located. Since the information encoded in RSMs is rather specific to the material being measured, we will defer presentation of such data until later chapters where the data can be placed in proper context.

3.1.5 Experimental apparatus

Most of the x-ray scattering data in this thesis were collected using Rigaku SmartLab and Phillips Panalytical Empyrean high-resolution diffractometers. These are commer-

ical products whose design and operation is fully documented elsewhere. Scientifically, the important features of these diffractometers are that they use Cu-K α 1 radiation ($\lambda = 1.54059 \text{ \AA}$), the detectors have a dynamic range of $\approx 10^7$ counts per second, measurements are performed at room temperature ($T = 295 \text{ K}$), and four motorized angles ($\omega, 2\theta, \chi, \phi$) can be swept over wide ranges in a fully automated fashion to access different regions of reciprocal space. For reflectivity and diffraction measurements along the specular CTR ($q_{\parallel} = 0$), the values of χ and ϕ are essentially arbitrary, and ω and 2θ are swept simultaneously in a coordinated fashion ($2\theta = 2\omega$) to continuously vary q_{\perp} . For reciprocal space mapping using these instruments, χ and ϕ are chosen to align the scattering plane with the desired in-plane azimuthal direction of q_{\parallel} , and then ω and 2θ are rocked in an offset fashion (*i.e.*, $2\theta \neq 2\omega$) to measure many independent values of $(q_{\parallel}, q_{\perp})$ in this plane. The transformation from $(2\theta, \omega)$ angular coordinates to $(q_{\parallel}, q_{\perp})$ momentum transfer coordinates are illustrated in Figure 3.3 and are given by the equations:

$$\begin{aligned}\frac{q_{\parallel}}{2\pi} &= \frac{1}{\lambda} (\cos(\omega) - \cos(2\theta - \omega)) \\ \frac{q_{\perp}}{2\pi} &= \frac{1}{\lambda} (\sin(\omega) + \sin(2\theta - \omega))\end{aligned}\tag{3.9}$$

Some of the x-ray scattering data in this thesis were collected at the A2 endstation of the Cornell High Energy Synchrotron Source. Synchrotron measurements used x-ray energies of 14 - 20 keV ($\lambda = 0.620 - 0.886 \text{ \AA}$), were performed at various temperatures between 300 K and 7 K³, and utilized Pilatus 300k or Eiger 1M photon-counting area detectors. These detectors consist of many pixels—300,000 and 1,000,000, respectively—which can be thought of as many independent point detectors performing measurements in parallel. This parallelism, in concert with a very bright incident beam (supplying ≈ 5 orders of magnitude more photons per unit time than the lab-based sources) and the extremely low noise floor of the detectors makes synchrotron-based measurements the tool

³Temperature control is facilitated by a closed-cycle helium cryostat attached to the diffractometer.

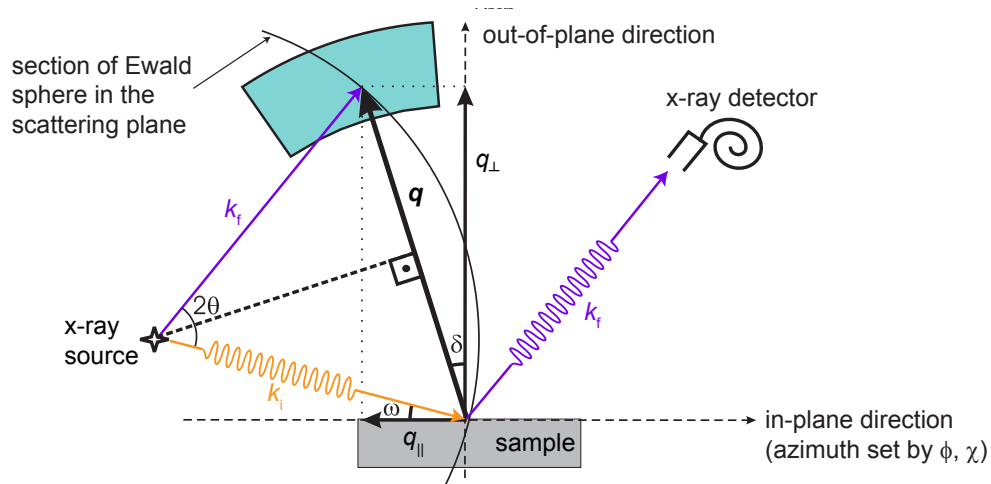


Figure 3.3: Schematic of four-circle x-ray diffraction measurements in the scattering plane spanned by $\{\mathbf{k}_i, \mathbf{k}_f\}$. A monochromatic incident beam of x-rays with initial wavevector \mathbf{k}_i (orange) impinges on the sample at an angle ω , and scatters to a state with final wavevector \mathbf{k}_f (purple) that is detected at an angle 2θ relative to the incident beam. Elastic scattering requires that $\|\mathbf{k}_i\| = \|\mathbf{k}_f\|$, which restricts the scattering to lie on the Ewald sphere. The momentum transfer $\mathbf{q} = \mathbf{k}_f - \mathbf{k}_i$ is resolved into its components parallel (q_{\parallel}) and perpendicular (q_{\perp}) to the sample surface according to Equation 3.9; by changing ω and 2θ in a coordinated fashion, the intensity at all points in the turquoise-shaded region can be measured to record an RSM. Figure adapted from Ref.[79].

of choice for when more exhaustive reciprocal-space mapping of low-intensity features is desired; the qualification, of course, is that synchrotron beamtime is in very limited supply. The diffractometer used for the synchrotron measurements also has four independent angular degrees of freedom that allow access to most regions of reciprocal space reachable in reflection scattering geometries; the naming conventions for these angles are slightly different than on the lab-based machines. The two-dimensional nature of the detector images makes the conversion of the raw data in angle space into histograms of intensity versus (q_1, q_2, q_3) (or HKL) somewhat more complicated, but conceptually the procedure is the same as described above. We omit a full description here for brevity.

3.2 Electrical transport

Once we have used x-ray diffraction to determine where the atoms are located in epitaxial thin films synthesized by MBE, one of the next very fundamental questions we are usually interested in investigating is *how do the electronic excitations move in such a crystal?* Many probes in condensed matter physics exist for answering this question, with varying levels of microscopic detail and experimental complexity. In this chapter we focus on two such techniques that span the gamut of possibilities in this realm: electrical transport measurements and angle-resolved photoemission spectroscopy. In the author's view, these approaches are naturally complementary in several respects, which we outline in the next two sections, and both are thus essential to gaining a complete understanding of a thin film's electrical properties.

3.2.1 Basic phenomenology

Electrical transport probes electronic excitations at their lowest energy scales, within μeV of the Fermi level (E_F). This allows it to be exquisitely sensitive to the electronic structure at E_F , and largely agnostic about anything happening away from E_F . For similar reasons, it is an excellent probe for the study of novel quantum states of matter that generally condense only at low temperatures, such as superconductivity. On the other hand, one of the main drawbacks of transport lies in its lack of a simple connection to the more microscopic aspects of electronic structure that can be calculated by existing theories and computational methods. Therefore, if for example we would like to understand why a superconductor has an enhanced transition temperature (T_c), transport data in isolation will generally offer little insight in this regard, because there are simply too many complicated dependencies involved in the mapping that takes more basic quantities—such as the $E(\mathbf{k})$

dispersion relationships of the near- E_F excitations, or the electron-electron scattering rate, or the electron-phonon scattering rate—to the electrical resistance of real materials.

Glossing over those complications, there is some information that can be gained from electrical transport measurements even if we interpret the data in an overly simplified Drude-esque picture of conduction. In the Drude (or relaxation time) model, the electrical conductivity is given by

$$\sigma = \frac{ne^2\tau}{m} \quad (3.10)$$

where n is the carrier density of the excitations that transport the current, e is their charge, m is their mass, and τ is mean time the carriers travel before scattering and losing any memory of their previous trajectory. In many correlated materials, especially at elevated temperatures, the true current-carrying excitations are not single electrons but rather quasiparticles strongly dressed by electrons, phonons, *etc.* Some of these effects can be accounted for by, *e.g.*, allowing quantities such as the effective mass to be renormalized ($m \rightarrow m^*$); many other effects are more subtle—in some cases, likely the entire picture of quasiparticle transport must be abandoned. Disregarding these complications for now and speaking as if the current-carrying excitations were just bare electrons, the other quantity in Equation 3.10 that deserves further consideration is the scattering time τ . In principle, any type of collision that relaxes the electron momentum will contribute to and should be accounted for in τ . A commonly invoked approximation, called *Matthiessen's rule*, is that these scattering mechanisms are mutually independent, and so the corresponding scattering rates should add independently:

$$\frac{1}{\tau} = \frac{1}{\tau_{el.-ph.}} + \frac{1}{\tau_{el.-el.}} + \frac{1}{\tau_{disorder}} + \dots \quad (3.11)$$

The quantity that is experimentally measured in this thesis is the resistivity, $\rho = 1/\sigma$. Putting together Equation 3.10 and Equation 3.11, we have:

$$\rho = \frac{m}{ne^2\tau} = \frac{m}{ne^2} \left(\frac{1}{\tau_{el.-ph.}} + \frac{1}{\tau_{el.-el.}} + \frac{1}{\tau_{disorder}} + \dots \right) \quad (3.12)$$

Assuming that the effective mass and carrier density of a metal are approximately constant versus temperature, it is clear from Equation 3.12 that decreases in resistivity as the temperature is lowered can be assigned to a reduced scattering rate. Beyond this very basic observation, the normal method of analyzing resistivity versus temperature data is to assume that one of the independent scattering mechanisms in Equation 3.12 dominates over the others. For example, in correlated metals, electron-electron scattering is often the major contributor to ρ , whereas in more classic metals electron-phonon scattering is usually more dominant. Some theories predict certain functional forms for how the scattering rate should scale with powers of temperature—*e.g.*, Fermi liquid theory predicts that $\rho \propto T^2$ for electron-electron scattering—and by fitting the experimentally measured $\rho(T)$ data, some estimates of the relevant scattering rate can be obtained. Nonetheless, in general it is very difficult to guess (or calculate) *a priori* over what temperatures such a description should be valid. One of the most robust statements that can be made in this regard is that all scattering mechanisms are frozen out in the limit of zero temperature (by phase space constraints) *except* elastic electron-disorder scattering. Therefore, at sufficiently low temperatures, we should expect ρ to saturate at a constant value, called the residual resistivity, given by:

$$\rho(T \rightarrow 0 \text{ K}) \equiv \rho_0 = \frac{m}{ne^2} \frac{1}{\tau_{disorder}} \Big|_{T \rightarrow 0 \text{ K}} \quad (3.13)$$

The residual resistivity of a metal is among the most disorder-sensitive characterization measurements one can make: smaller values of ρ_0 imply smaller electron-disorder scat-

tering rates and thus “cleaner” samples with smaller concentrations of defects. For this reason, ρ_0 is very useful in optimizing the growth procedures for metallic thin films synthesized by MBE, and has been used extensively for this purpose during the course of this thesis. In certain unconventional superconductors (such as Sr_2RuO_4 , as we will show in chapter 4), increasing levels of ρ_0 can rapidly suppress the superconducting T_c to zero K; therefore, quantitative measurements of ρ_0 and knowledge of how T_c depends on ρ_0 are essential to quantifying how much other factors, such as epitaxial strain, affect T_c .

The above discussion has focused on how the resistivity of a metal varies in the so-called “normal state”. All metals will superconduct at sufficiently low temperatures⁴, and when the transition from normal metal to superconductor occurs, the resistivity of course abruptly decreases. The mechanism of this drop to zero cannot be rationalized within a Drude-like picture of single-particle conduction (*cf.* chapter 1). As a technical point, we simply note that when we refer to the residual resistivity of a superconductor, such as the RuO_2 and Sr_2RuO_4 films studied in this thesis, we mean the value ρ_0 would take at zero temperature in the absence of superconductivity. Since the T_c s and upper critical fields (H_c s) for these materials are both not large, there are essentially two independent methods for extracting ρ_0 that give very similar results:

1. Extrapolate the $\rho(T)$ behavior measured at zero magnetic field above T_c to zero temperature. This is not a major extrapolation since we typically measure $\rho(T)$ from 300 K all the way down to low temperatures, and then only need to extrapolate how this behavior would (hypothetically) continue from $T_c \approx 2$ K to 0 K.
2. Measure ρ at very low temperatures under an externally applied magnetic field that

⁴This is true in the following philosophical sense: neglecting disorder, dimensionality, and other experimental realities, a Fermi liquid is theoretically unstable towards superconductivity for any arbitrarily weak effective attraction mediated by phonons or other collective excitations of the system. On the other hand, it is clear at a practical level that there is a meaningful distinction between the superconducting T_c of, say, lead (7.2 K) and gold—the latter being astronomically small, much below the detection limits of any refrigerators.

is large enough to fully suppress T_c to 0 K, but that is small enough to not cause too much normal-state magnetoresistance.

3.2.2 Experimental apparatus

Zero-field $\rho(T)$ measurements from 300 K to 4.2 K were measured in this thesis on several hundred ruthenate thin films using a home-built instrument affectionately known as *the dipper*. In this setup, the thin film samples are contacted by four pins, typically placed in the corners of the 10 mm \times 10 mm wafers; two of the pins are used to inject / remove a current I , and the other two are used for voltage measurement ΔV . The four-point resistances $R = \Delta V/I$ for different configurations of the contacts are measured and recorded in a data file as the temperature is manually controlled by the user by lowering the sample into a liquid helium dewar. Resistances are converted to sheet resistances by numerically solving van der Pauw's equation at each temperature, and the sheet resistances can be converted to resistivities using the film thicknesses measured by x-ray reflectivity or x-ray diffraction. The dipper electronics and method of measuring R have undergone several upgrades during the course of this thesis, which are not important for any of the results obtained; the most recent incarnation uses a Keithley 6221 current source and Keithley 2182A nanovoltmeter to perform so-called *delta mode* measurements, in which the current is rapidly toggled between $\pm I$ and the corresponding voltage measurements are appropriately averaged to cancel the non-zero voltage offset measured at zero current (caused by thermoelectric effects and other sources). Importantly, the rapid turnaround time on dipper measurements makes it an invaluable tool for optimizing film growths based on ρ_0 , and allows one to screen out lower-quality samples from higher-quality samples that warrant being measured to lower temperatures to check for superconductivity.

To perform transport measurements on selected samples from 300 K down to lower

temperatures, we used a Quantum Design Physical Properties Measurement System (PPMS) equipped with a He-3 refrigerator. The base temperature of this system is $\approx 350 - 400$ mK. Resistance measurements can also be performed in externally applied magnetic fields of up to 14 Tesla, which is important for conclusively demonstrating the presence of superconductivity. The PPMS and He-3 insert are commercial products whose design and operation are fully documented elsewhere. To contact the samples for PPMS measurements, we wire-bonded aluminum wires from the gold pads on the PPMS sample holders directly to the surfaces of the ruthenate thin films being measured. For measurements at low temperatures < 3 K, we typically used excitation currents of $I = 10 \mu\text{A}$ to mitigate the effects of sample heating. Given that the noise floor of the PPMS electronics is ≈ 10 nV, the noise floor for our low-temperature resistance measurements was $\approx 0.001 \Omega$. The residual normal-state resistances of the superconducting Sr_2RuO_4 and RuO_2 films studied in this thesis were typically $0.1 - 10 \Omega$, so this noise floor was sufficiently low to conclusively establish a zero-resistance state, and no custom add-ons to the PPMS electronics were employed.

3.3 Angle-resolved photoemission spectroscopy

Angle-resolved photoemission spectroscopy (ARPES) is a powerful technique for investigating how the electronic excitations move in crystals at a more microscopic level than transport measurements. One of the beauties of ARPES is that the experimental data directly connects to quantities that can be computed in electronic structure calculations: for example, if we want to know the energy-momentum $E(\mathbf{k})$ dispersion relationship of the near- E_F electrons, we simply eject them from the material and study the energies and angles at which the electrons are photoemitted; similarly, if we want to know the scattering length or scattering rate of these excitations inside the solid, we simply must analyze

the widths of the momentum- or energy-distribution curves measured experimentally. On the other hand, the demanding experimental conditions required for an extremely surface-sensitive probe such as ARPES come with the costs of not being able to perform measurements at low enough temperatures or with sufficiently high energy resolution to directly measure how the near- E_F electronic structure evolves upon entering the superconducting state for most superconductors, including the ruthenate thin films studied in this thesis. In this section we review the basic phenomenology of photoemission and describe some unique aspects of the system at Cornell that allow *in situ* ARPES measurements to be performed on the surfaces of thin films synthesized by MBE.

3.3.1 General formalism

3.3.2 Energy and momentum conservation \implies bandstructure

At its core, photoemission spectroscopy is a descendant of Einstein's celebrated description of the photoelectric effect [80],

$$E_{max} = h\nu - \phi , \tag{3.14}$$

where E_{max} is the maximum kinetic energy E_{kin} a photoelectron can carry, h is Planck's constant, ν is the frequency of the light, and ϕ is the work function of the material. While Equation 3.14 was groundbreaking in its day⁵—owing to its invocation of h and the quantization of light, which spurred the development of quantum mechanics soon thereafter—nowadays it is recognized as a straightforward consequence of energy conservation and the transfer of such energy within the constituent parts of the system: upon shining light

⁵Einstein was awarded the Nobel Prize in 1921 for this work.

on a material, the energy of an incident light packet ($h\nu$) may be absorbed by an electron in the solid, which increases its kinetic energy. If the kinetic energy of the photoelectron exceeds the barrier of the confining potential that kept it bound inside the solid in the initial state (ϕ), the photoelectron may escape into vacuum, but with no more kinetic energy in the final state than the energy it gained from photoabsorption less the energy it “paid” to leave the solid.

After Einstein’s theory of the photoelectric effect was verified by Robert Millikan in 1916 [81]⁶, many years passed before photoemission spectroscopy would again return into the scientific mainstream as an active area of research. During the 1950s and 60s, Kai Siegbahn pioneered a technique now commonly referred to as x-ray photoelectron spectroscopy (XPS) in which the initial-state binding energy of electrons inside a material E_B could be determined by photemitting them from the solid with x-rays and measuring their final-state kinetic energies $E_{kin.}$ using an electron analyzer, according the relation:

$$E_{kin.} = h\nu - \phi_{\text{detector}} - E_B , \quad (3.15)$$

which again is just a statement of energy conservation, but now in a more fully energy-resolved form. Here ϕ_{detector} is the work function of the detector, which is assumed to be in electrical contact with the sample and thus have the same electrochemical potential, μ ⁷. Although Siegbahn was primarily interested in applying XPS to gain information about the chemical identities of the atoms from which and photoelectrons were ejected⁸, multiple independent experiments and theoretical developments happening around the same time realized that Equation 3.15 could also be applied to study the valence bands

⁶This work partially earned Millikan the Nobel Prize in 1923, along with his famed oil drop experiments.

⁷Note that throughout the text we will interchangeably refer to μ as the (electro)chemical potential, the Fermi level, and oftentimes even denote it by E_F . While this last term may be slightly misleading, since the letters suggests that it means the *Fermi energy*—which is a much less general concept than μ , that is strictly well-defined only for metals at zero temperature—in practice our use of E_F follows the standard of many in the photoemission community.

⁸Siegbahn was awarded the Nobel Prize in 1981 for his work on core-level spectroscopy.

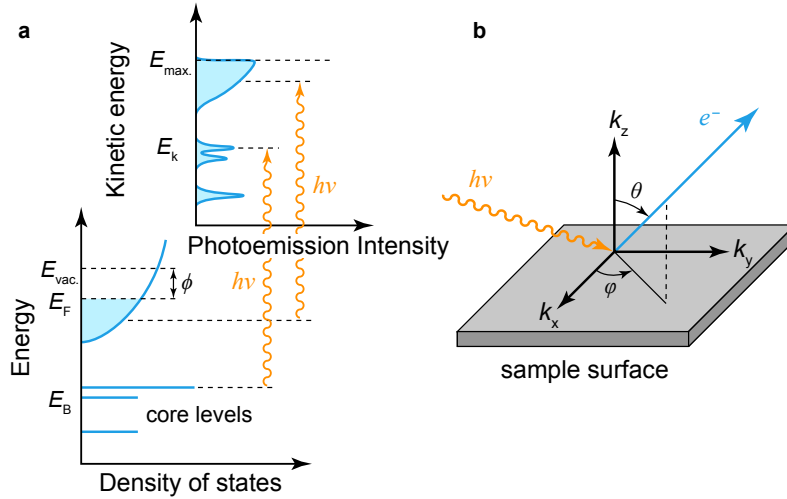


Figure 3.4: Schematic of ARPES showing (a) how the measured intensity and kinetic energy E_{kin} of photoelectrons relate to the density of states and binding energy E_B of the initial states inside the solid, and (b) how the measured angles (θ, ϕ) of the photoelectrons relate to the initial-state momenta (k_x, k_y) inside the solid. Figure adapted from Ref.[87].

of materials—*i.e.*, the electronic structure of electrons having E_B within a few eV of E_F [82, 83, 84]. Moreover, by measuring the angles $\{\theta, \phi\}$ at which these photoelectrons were emitted, the initial-state in-plane momenta $\mathbf{k}_{\parallel} = (k_x, k_y)$ could be determined [85, 86], since the photoemission process from a clean surface conserves the in-plane momenta modulo reciprocal lattice vectors of the surface crystal structure, according to Noether’s theorem. Setting aside several subtleties about the description just given for now, it is clear in principle that angle-resolved photoemission spectroscopy (ARPES) directly measures a quantity proportional to the *energy-momentum dispersion relationship* of electronic excitations inside a solid, $E(\mathbf{k})$ —or in simpler terms, the *bandstructure*. Figure 3.4 contains a schematic of the photoemission process summarizing these points.

3.3.3 From bandstructure to single-particle spectral functions

In the nascent days of ARPES during the 1970s, most systems being studied were classic metals and semiconductors [88, 89] for which the main *ansatz* of *band theory* is remarkably accurate: the electrons near E_F move through solids in a manner that is effectively independent of the motion of all other electrons in the solid, and indeed in a way that is also minimally entangled with any of the dynamical bosonic excitations of the crystal—phonons, magnons, plasmons, *etc.*. In this limit, the single-electron Bloch wavefunctions $\psi^{\mathbf{k}}$ are a natural choice of basis for the Hilbert space of fermionic excitations spanning E_F , and the $E(\mathbf{k})$ bandstructure of these Bloch states are determined by the interaction of the electrons with the static periodic potential formed by the ions in the crystal. The N -electron wavefunctions of the system can be constructed from a Slater determinants of the individual $\psi^{\mathbf{k}}$, which we denote as Ψ^N , and the total energy of each N electron state is denoted by E^N . Using Fermi's golden rule, the probability of an incoming photon with energy $h\nu$ to photoexcite the system from an initial state Ψ_i^N with energy E_i^N to a final state Ψ_f^N with energy E_f^N is given by the expression

$$W_{i \rightarrow f} \propto \left| \langle \Psi_f^N | H_{int} | \Psi_i^N \rangle \right|^2 \delta(E_f^N - E_i^N - h\nu) , \quad (3.16)$$

where H_{int} is the interaction Hamiltonian between the photon and the system. In addition to the delta function in Equation 3.16, which enforces the energy conservation law stressed in the previous section, we see that the probabilities for photoexcitation are modulated by the transition *matrix elements*, $\langle \Psi_f^N | H_{int} | \Psi_i^N \rangle$.

These matrix elements are impossible to calculate directly for real materials, and so we must resort to a series of approximations. The first of these is to assume that the single photoexcited electron does not interact with the system it leaves behind, often called the *sudden approximation*. In this case, the N -electron wavefunctions can be written as ap-

appropriately antisymmetrized product states of a single-electron Bloch state and an $N - 1$ -electron Slater determinant, $\sim \psi^{\mathbf{k}}\Psi^{N-1}$, and Equation 3.16 simplifies to:

$$\langle \Psi_f^N | H_{int} | \Psi_i^N \rangle = \langle \psi_f^{\mathbf{k}} | H_{int} | \psi_i^{\mathbf{k}} \rangle \langle \Psi_f^{N-1} | \Psi_i^{N-1} \rangle \quad (3.17)$$

The first term in Equation 3.17 represents the probability amplitude for an electron to absorb a photon that promotes it from one Bloch state to another. Substituting an interaction Hamiltonian of the form $H_{int} \approx e\mathbf{A}/mc \cdot \mathbf{p}$, where \mathbf{A} is the vector potential of the incident electromagnetic field (we have made the so-called *dipole approximation*, $\nabla\mathbf{A} \approx 0$, and neglected two-photon absorptions, $A^2 \rightarrow 0$), allows us to rewrite this overlap integral as:

$$\langle \psi_f^{\mathbf{k}} | H_{int} | \psi_i^{\mathbf{k}} \rangle \approx \langle \psi_f^{\mathbf{k}} | \frac{e}{mc} \mathbf{A} \cdot \mathbf{p} | \psi_i^{\mathbf{k}} \rangle \equiv M_{\mathbf{k}} \quad (3.18)$$

The second term in Equation 3.17 represents the overlap of the initial-state and final-state $N - 1$ -electron configurations of the system. Note that Ψ_i^{N-1} should not be thought of as a ground state of the $N - 1$ -electron system, but rather the one-hole state reached when one electron is removed from the ground state of the N -electron system, *i.e.*, $\Psi_i^{N-1} = \hat{c}_{\mathbf{k}}\Psi_i^N$, where \hat{c} is the electron annihilation operator. Similarly, there is a choice in what $N - 1$ -electron final state the system is left in after photoexcitation, Ψ_f^{N-1} , and a full model should integrate out all possibilities that conserve the total energy with appropriate amplitudes (this is accomplished via the sum indexed by m below). At the end of the day, we are left with the following expression for the overall photoemission intensity I measured at wavevector \mathbf{k} and kinetic energy E_{kin} . [90]:

$$I(\mathbf{k}, E_{kin.}) \propto \sum_{f,i} W_{i \rightarrow f} = \sum_{f,i} |M_{\mathbf{k}}|^2 \sum_m |\langle \Psi_m^{N-1} | \hat{c}_{\mathbf{k}} | \Psi_i^N \rangle|^2 \delta(E_{kin} + E_m^{N-1} - E_i^N - h\nu), \text{ or} \quad (3.19)$$

$$I(\mathbf{k}, E) \propto |M_{\mathbf{k}}|^2 f(E) A(\mathbf{k}, E)$$

The second half of Equation 3.19 is formally known as the single-particle spectral function for electron removal, $A(\mathbf{k}, E)$, which is the imaginary component of the one-electron removal Green's function. The Fermi-Dirac distribution, $f(E) = (e^{E/k_B T} + 1)^{-1}$, reflects the fact that ARPES only measures occupied electronic states.

The spectral function $A(\mathbf{k}, E)$ for strongly correlated many-body systems will in general be a very complicated object—especially at higher binding energies further removed from E_F —and so the intensity distribution of one-hole excitations measured by ARPES is often difficult to interpret in terms of simple concepts such as quasiparticle resonances. Two important cases that are analytically tractable are illustrated in Figure 3.5: on the left, a gas of effectively non-interacting electrons, and on the right, a Fermi liquid with finite electron-electron interaction strength. In the non-interacting system, the presence of a missing (photoemitted) electron does not affect the other $N - 1$ electrons, by construction, and therefore $A(\mathbf{k}, E)$ consists of delta-function-like peaks that track the single-electron bandstructure at all energies. In a Fermi liquid, qualitatively the same behavior occurs for excitations within some limited range of energies surrounding E_F , leading to well defined quasiparticle peaks having widths Γ along the energy axis much smaller than the binding energies of the peaks⁹. The region in energy over which this behavior persists is often called the *Fermi liquid coherence scale*. In contrast to the non-interacting gas, though, the spectral function of a Fermi liquid also shows *incoherent spectral weight* at larger binding energies; these broad distributions of intensity (signifying larger scattering rates) encode information about more complex many-body excitations.

⁹Note, however, that the peak positions in energy are quantitatively *renormalized* by the interactions.

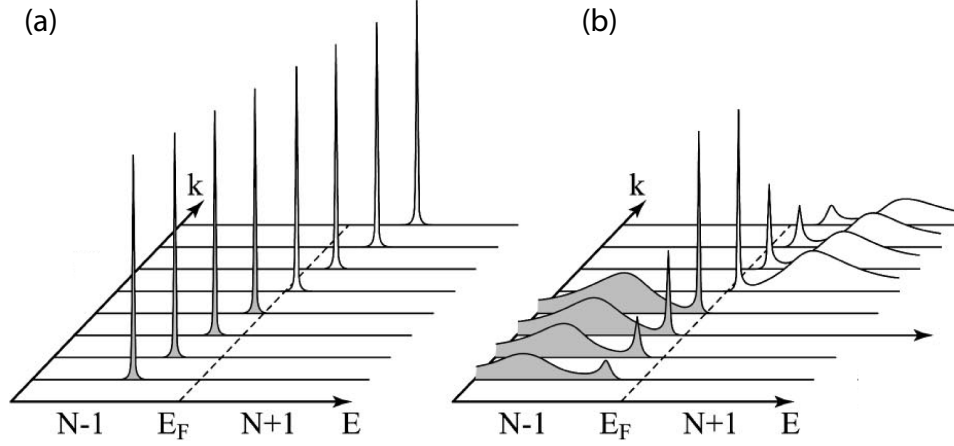


Figure 3.5: Spectral functions of **(a)** a gas of effectively non-interacting band electrons, and **(b)** a Fermi liquid as a function of energy and momentum. In the Fermi liquid, low-energy excitations near E_F experience reduced scattering because of phase-space constraints, and so have long lifetimes with correspondingly sharp (in energy) quasiparticle peaks. Note, however, that these peaks still track a renormalized $E(k)$ dispersion relative to the system of non-interacting excitations. Further removed from E_F , the excitations in the Fermi liquid become strongly damped (*i.e.*, short lived), and more spectral weight is transferred to the incoherent portion. Figure reproduced from Ref.[90].

With these two examples as our guides, it is convenient for comparison to theoretical calculations to parametrize the spectral function in a form that illustrates how the many-body interactions redistribute the intensity in $A(\mathbf{k}, E)$ relative to what the spectral function would be in the absence of interactions. This is typically accomplished by introducing a complex-valued electron self-energy $\Sigma = \Sigma' + i\Sigma''$ to the single-electron Green's function, whose real part (Σ') is related to the renormalization of quasiparticle energies, and whose imaginary part (Σ'') gives the finite quasiparticle lifetime, according to:

$$A(\mathbf{k}, E) = -\frac{1}{\pi} \frac{\Sigma''(\mathbf{k}, E)}{[E - \epsilon_{\mathbf{k}} - \Sigma'(\mathbf{k}, E)]^2 + \Sigma''(\mathbf{k}, E)^2} \quad (3.20)$$

Here $\epsilon(\mathbf{k})$ is the bandstructure in the limit of vanishing interaction strength. When the electron self-energy is “small” ($|\Sigma| \ll E$) and varies smoothly as a function of \mathbf{k} and E , it is clear from Equation 3.20 that $A(\mathbf{k}, E)$ will generally display Lorentzian-shaped

peaks centered at the renormalized quasiparticle energies $\epsilon(\mathbf{k}) - \Sigma'(\mathbf{k}, E)$ with widths $\Gamma \propto 1/\Sigma''(\mathbf{k}, E)$. Formally speaking, in this situation it is common to define a quasiparticle residue $Z_{\mathbf{k}} = (1 - \frac{\partial \Sigma'}{\partial E})^{-1} |_{E=E_{\mathbf{k}}^*}$ and quasiparticle lifetime $\Gamma_{\mathbf{k}} = Z_{\mathbf{k}}|\Sigma''(\mathbf{k}, E_{\mathbf{k}}^*)|$ for the coherent component of $A(\mathbf{k}, E)$, and to label all other intensity as A_{inc} . In terms of these variables, Equation 3.20 can be rewritten as:

$$A(\mathbf{k}, E) = Z_{\mathbf{k}} \frac{\Gamma_{\mathbf{k}}/\pi}{(E - E_{\mathbf{k}}^*)^2 + \Gamma_{\mathbf{k}}^2} + A_{inc} \quad (3.21)$$

Equation 3.21 forms the basis of the modern understanding and interpretation of photoemission data from correlated materials with finite—but not too large—interactions between the electronic excitations and the other degrees of freedom in the system. We start from the spectrum $\epsilon(\mathbf{k})$ of an effectively non-interacting system, which can *e.g.* be calculated from band theory using the computational framework of density functional theory (DFT), as described in chapter 1. Following Landau, we then imagine adiabatically turning on the interactions with other electrons, phonons, *etc.*: turning on these interactions leads to renormalized dispersions of the emergent quasiparticle excitations, finite scattering rates that damp these excitations, and the redistribution of intensity into incoherent spectral weight at higher binding energies, all of which can be directly read off by analyzing ARPES data along the energy axis. Nonetheless, especially near the Fermi level at low temperatures, phase-space constraints on the scattering lead to robust quasiparticle peaks in the excitation spectrum, which are ostensibly the relevant degrees of freedom for novel phases of matter that condense from the Fermi liquid at even lower temperatures, such as superconductivity.

As we will demonstrate in subsequent chapters, for the material systems studied in this thesis, Sr_2RuO_4 and RuO_2 , the hierarchy of energy scales described above appears to be obeyed: the bandstructures resulting from electron-ion and static electron-electron

interactions are expected to have bandwidths of several electron volts, the Fermi liquid coherence scales T_{FL} set by dynamical electron-electron and electron-phonon scattering processes are considerably reduced from these bare bandwidths, and the superconducting T_c s are considerably smaller still than T_{FL} . Therefore, we see that ARPES studies on these materials in the Fermi liquid state at intermediate temperatures and energies are an important logical link between DFT calculations and superconductivity, and essential for any understanding of the latter in terms of the former. Finally, we note in passing that this hierarchy of energy scales need not be realized for more strongly correlated materials in which electron-electron scattering may overwhelm electron-ion interactions, or indeed superconductivity may condense at T_c s substantially exceeding T_{FL} ; however, we leave a description of how ARPES data should be interpreted in these cases to other sources.

3.3.4 Other factors that affect ARPES intensities

Although the spectral function description of ARPES data presented in subsection 3.3.3 is elegant and very appealing for how directly aspects of the experimental data reveal microscopic aspects of the electronic structure (such as the quasiparticle dispersions and scattering rates), ARPES data from real systems are, of course, significantly more complicated. Here we mention a few experimental artifacts that contribute significantly to the ARPES signal measured experimentally besides just the underlying single-particle spectral function of the bulk of the material being studied.

Finite momentum and energy resolution

Experimental ARPES data are collected utilizing electron analyzers with finite angular resolution and finite energy resolution. Commissioning tests of the Scienta R4000 electron

analyzer used in the Cornell ARPES system suggest that our typical settings for collecting ARPES data (pass energy = 5 eV, 0.8 mm slit size, angular range of 30° imaged on the detector) achieve an angular resolution of $\delta Q \approx 1^\circ$ and an energy resolution of $\delta E \approx 10$ meV. When photoemitted with He-I α light, electrons near the Fermi level typically have kinetic energies of ≈ 16.9 eV and $\sqrt{2mE_{kin.}/\hbar^2} \approx 2.1 \text{ \AA}^{-1}$, so near normal emission δQ corresponds to a momentum resolution of $\delta k_{||} \approx 0.018 \text{ \AA}^{-1}$ [90], or $\approx 1\%$ of a typical Brillouin zone dimension for most materials ($2\pi/a$, where $a \approx 4 \text{ \AA}$).

In actual data, any features in $A(\mathbf{k}, E)$ resulting from quasiparticle dispersions and scattering rates are convolved with and smeared out by these instrumental resolutions, δk and δE . While this is not a serious problem in the limit where features in $A(\mathbf{k}, E)$ are intrinsically much broader than δk and δE , back-of-the-envelope estimates of the intrinsic scattering relaxation time τ or scattering length ℓ suggest that \hbar/τ and $1/\ell$ are comparable to δE and $\delta k_{||}$ for many materials of interest. To put some actual numbers behind this statement, consider the case of RuO₂ thin films studied in this work. At low temperatures, the residual resistivities of these films are $\rho \approx 10 \mu\Omega\text{-cm}$, which corresponds to a relaxation time of $\tau \approx 4.6 \times 10^{-14}$ s and an mean free path of $\ell \approx 130 \text{ \AA}$, using the DFT-computed plasma frequency tensor and Fermi velocity averaged over the Fermi surface from Ref.[91]. From these numbers, we would expect the quasiparticle resonance at $A(\mathbf{k} = \mathbf{k}_F, E = E_F)$ to have a width in momentum of $1/\ell \approx 0.008 \text{ \AA}^{-1}$ and a width in energy of $\hbar/\tau \approx 90$ meV, which are comparable in magnitude to the instrumental smearing $\delta k_{||}$ and δE ¹⁰. Therefore, while comparisons of energy distribution curve and momentum distribution curve widths versus temperature (or versus binding energy) can still be instructive to gain insight into *changes* in the electron self-energies Σ as these variables are altered, the absolute magnitudes of Σ should not be overinterpreted without taking care to evaluate the effects of finite instrumental resolution in \mathbf{k} and E [92, 93].

¹⁰Note that for a dispersive feature in an $E(\mathbf{k})$ spectrum, the finite momentum resolution of the analyzer translates to further energy smearing in addition to the instrumental energy resolution, according to $\delta E \approx \delta k \cdot dE/dk = \delta k \cdot v$, where v is the group velocity of the excitations.

Inelastic scattering and k_z broadening

The derivations in subsection 3.3.3 that led to the proportionality relationship $I(\mathbf{k}, E) \propto |M_{\mathbf{k}}|^2 f(E) A(\mathbf{k}, E)$ tacitly assume that each photoelectron escapes the material into vacuum and is detected by the electron analyzer without undergoing any additional scattering events that alter its energy or momentum. In reality, the strong interaction of low-energy electrons with other electrons inside the material provides a facile mechanism whereby the photoelectrons can relax their energy and momentum. When this energy is transferred to other “secondary” electrons—some of which are emitted from the solid, some of which create more secondary electrons—the end result is a cascading sequence of scattering processes that cause the experimentally measured photoemission intensity to grow exponentially in weight at progressively higher (lower) binding (kinetic) energies.

Several phenomenological models of this inelastic background signal have been proposed in the literature [94, 95], and one can attempt to use these models to estimate the magnitude of this background in actual experimental data and subtract it from the total measured intensity to isolate the photoelectrons that were ballistically photoemitted. This is always a bit of an *ad hoc* procedure, however, so care should be taken to ensure that the details of the background subtraction do not appreciably affect the results of any analysis or conclusions that follow it. Perhaps a more troubling consequence of the short inelastic mean free paths L_{imfp} for electron-electron scattering is that it implies that the spectral function measured by ARPES is extremely surface sensitive—*i.e.*, it is dominated by contributions from photoelectrons originating from within some very short distance of the sample surface. Studies of L_{imfp} in a wide range of materials have demonstrated that at the electron kinetic energies 10 – 100 eV typical of most ultraviolet and soft x-ray ARPES experiments, L_{imfp} is less than one nanometer [96].

At a technical level, the small value of L_{imfp} means that ARPES measurements must be performed in an ultrahigh vacuum (UHV) environment ($p \approx 10^{-11} - 10^{-10}$ Torr) on atomically pristine surfaces that have not been exposed to air or any significant dose of gas species that may adsorb onto the surface of the crystal and alter its surface electronic structure. This limits the practical timescale for most ARPES measurements to $\approx 24 - 48$ hours, since there are always residual gases present in any vacuum system that accumulate on the surface and change the measured data in an irreversibly time-dependent fashion.

At a scientific level, the small value of L_{imfp} implies that ARPES data should not (in isolation) be assumed to be representative of the bulk electronic structure of a material. This caveat is particularly relevant in systems where surface reconstructions of the crystal structure and/or polar discontinuities are present at the film-vacuum interface (*cf.* section 3.4), as these can cause manifestly non-bulk-like electronic states and properties to exist over the same near-surface region probed by ARPES. Moreover, the small value of L_{imfp} places a fundamental limit on how precisely the component of the electron's momentum perpendicular to the surface (k_z) can be determined, according to Heisenberg's uncertainty principle. The Fourier transform of a wavefunction for an electron that is exponentially damped in real space over a length scale of L_{imfp} in going from the surface into the bulk of the crystal will necessarily contain contributions from states in k -space with out-of-plane momenta that are spread over a range $\Delta k_z = 1/L_{imfp}$; therefore, the measured photoemission intensity is actually a weighted average of the spectral function over this range in k_z .

In materials with quasi-two-dimensional electronic structures that depend only weakly on k_z (such as Sr_2RuO_4), this " k_z smearing" presents only minor corrections to how the measured quasiparticle scattering rates Γ relate to the values that would be measured in the absence of this final-state broadening. This is not true for electronically three-dimensional materials (such as RuO_2), and a more nuanced k -dependent account-

ing of different contributions to Γ is required, as is nicely described in Ref.[97]. We note that there are no precise or generally applicable methods to determine the central value of k_z probed in ARPES, because k_z is not conserved during the photoemission process. Nonetheless, in this work we employ the so-called *free-electron final-state model* in our studies of RuO_2 , for which kinematic constraints require that:

$$k_z = \sqrt{\frac{2m}{\hbar^2} (E_{kin.} + V_0) - k_{\parallel}^2}, \quad (3.22)$$

where m is the electron mass, $E_{kin.}$ is the kinetic energy of a photoelectron, V_0 is the inner potential, and $k_{\parallel}^2 = k_x^2 + k_y^2$ is the parallel momentum. V_0 is a free parameter that is fit by comparison of the experimentally measured quasiparticle dispersions with DFT calculations at different k_z .

3.3.5 Experimental apparatus

The Cornell ARPES system that allows photoemission measurements to be performed *in situ* on epitaxial thin films synthesized in the oxide MBE systems described in chapter 2 was originally designed, constructed, and commissioned by the first generation of graduate students in the Shen Group: John Harter, Eric Monkman, and Daniel Shai. Various components of the system have been upgraded and refined since their work, but most aspects of the infrastructure for mounting and transferring samples remain conceptually the same, and we refer readers interested in further details to the dissertations of these folks [87, 98, 99]. Here we take for granted—although these are by no means trivial accomplishments!—that substrates can be attached to sample holders (typically with silver paste) on holders compatible with both the MBE and ARPES sample manipulators, loaded into the MBE for film growth (typically at elevated temperatures, sometimes ex-

ceeding 900° C), quickly transferred to the ARPES system under ultrahigh vacuum (without exposing the sample surface to pressures worse than $\approx 10^{-9}$ Torr), and finally measured by ARPES and LEED at cryogenic temperatures (typically ≈ 20 K, although temperatures from $\approx 10 - 300$ K are readily achievable). In this section, we describe some of the technical capabilities of the analysis chambers where ARPES and LEED measurements are performed, which are schematically illustrated in Figure 3.6.

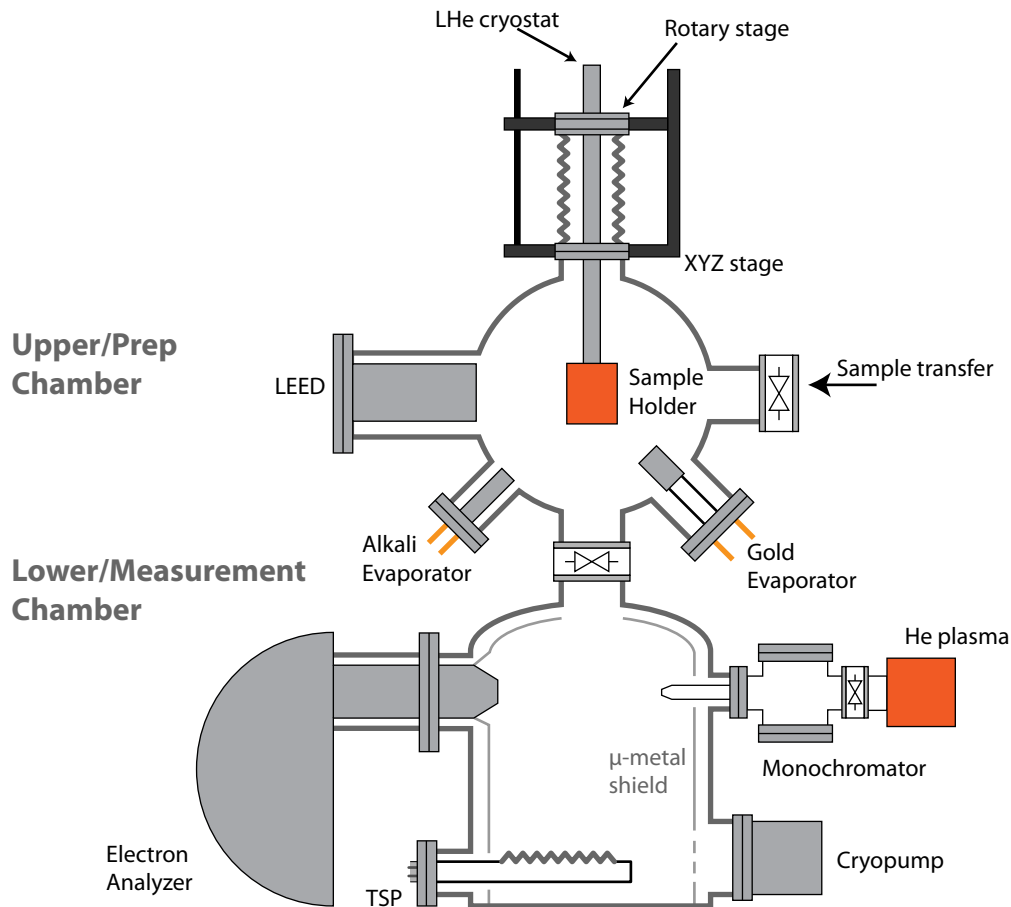


Figure 3.6: Schematic drawing of the Cornell ARPES system, with important components labeled. These are described in more detail in the main text. Image by Haofei Wei, reproduced from Ref.[100].

Sample manipulator

Upon transfer into the ARPES system, samples are inserted into a custom-built 6-axis sample manipulator known affectionately as Mk-III. This manipulator is capable of translating the sample in all three dimensions and rotating the sample about three independent axes, all via fully motorized computer-controlled interfaces. A sizable chunk of time during this dissertation was spent assisting with the design, construction, and testing of Mk-III (under the guidance of Shouvik Chatterjee), and then seeing this project through to completion, installation, and commissioning after Shouvik graduated (with much help from Brendan Faeth and Chris Parzyck, as well as other members of the Shen Group). There are numerous engineering challenges related to the implementation of such a manipulator, most of which derive from the rather demanding requirements that the angular motions operate in ultrahigh vacuum (which greatly limits the types of materials that can be used), and operate at cryogenic temperatures by connection to a liquid helium flow cryostat (where differential thermal contraction of components comprised of different materials makes precise alignment of these components a major headache). We will spare the reader from further details here.

Scientifically, the salient features of such a manipulator are that the (X, Y, Z) translational degrees of freedom allow the sample to be placed in the focus of the electron analyzer for ARPES measurements, while the (θ, ϕ, ω) rotational degrees of freedom allow the sample surface to be rotated relative the analyzer, such that the trajectories of the photoemitted electrons measured by the analyzer at a given kinetic energy $E_{kin.}$ and angle Q (with respect to the analyzer) probe initial states with different in-plane momenta $\mathbf{k}_{||} = (k_x, k_y)$ (with respect to the sample surface). Coordinate transformations from $(\theta, \phi, \omega, E_{kin.}, Q)$ to $(E_B, \mathbf{k}_{||})$ are a straightforward exercise in classical mechanics and linear algebra, the results of which are summarized in Ref.[100]. At the kinetic energies characteristic of near- E_F states for the photon energies used in our system, the angular ranges

of (θ, ϕ, ω) accessible by the manipulator are sufficient to probe ranges of (k_x, k_y) spanning the entire first Brillouin zone of most materials, and occasionally measurements can be extended well into the second Brillouin zone.

Light source and electron analyzer

Arguably the most important components of photoemission spectroscopy measurements are the light source and the electron analyzer. On the Cornell ARPES system, we operate a helium (He) plasma discharge lamp for generating ultraviolet (UV) light at emission lines characteristic of atomic transitions in He, and a hemispherical electron analyzer. Both of these are commercial products purchased from Scienta, whose detailed design, construction, and operation are described elsewhere. For the purposes of understanding data taken with these instruments, we note that the He lamp provides UV light at two energies $h\nu$ in sufficient intensities for ARPES measurements: He-I α ($h\nu = 21.2$ eV) and He-II α ($h\nu = 40.8$ eV). Selecting a specific emission line is facilitated by a compact UV monochromator situated between the lamp and the sample; the intrinsic width in energy of these lines are very sharp ($\delta E < 2$ meV), so the monochromator only needs to crudely distinguish, *e.g.*, He-I α from the other discrete possibilities (He-I β , He-II α , He-II β , ...), which are generally separated by 1 – 10 eV in energy. After UV photons have been generated in the He lamp and monochromatized, they are directed onto the sample surface in a spot size of ≈ 2 mm diameter using a retractable glass capillary.

He-I α light is generally preferred over He-II α , since it is ≈ 30 times brighter. That being said, materials-specific considerations—such as the k_z dependence of the bandstructure being studied, or exploiting the different photoionization cross sections of elements at different energies—sometimes warrant measurements at He-II α . For similar reasons, it is actually desirable to be able to continuously change the photon energy in ARPES experiments, but this generally requires synchrotron radiation. Since ARPES endstations at

synchrotrons are shared among many users, beamtimes are in very short supply and the endstations are optimized for experiments that do not require real-time materials synthesis (à la the *in situ* MBE-grown films studied in this dissertation); therefore, we did not pursue such measurements.

The photoelectrons generated by UV illumination of the sample surface enter a Scienta R4000 electron spectrometer that simultaneously records the angle Q (defined with respect to the analyzer) and kinetic energy $E_{kin.}$ of the electrons. In more detail, the electrons first pass through user-selected mechanical slits that restrict the trajectories of the electrons entering the spectrometer. The electrons are then uniformly slowed down by and focused by electrostatic optics to image them in angle Q at reduced kinetic energies compatible with the user-selected pass energy E_p . Energy resolution is then accomplished by deflecting the electrons through a hemispherical parallel plate capacitor consisting of a positively and negatively charged inner and outer electrode, respectively. The bending radius of the electron trajectories depends on their kinetic energy, such that at the end of the capacitor, the electrons are spread in one dimension based on Q and in the orthogonal dimension based on $E_{kin.}$ Electrons are detected as a function of these quantities using a two-dimensional microchannel plate (MCP). The MCP amplifies the signal from the electrons impinging on it and transduces it to intensities on a phosphor screen, which is visually monitored with a CCD camera outside of vacuum.

From the operational point of view, the energy and angular resolution of the analyzer are determined primarily by the user-selected slit size and pass energy—and to a lesser extent, by inevitable imperfections in the electron optics, hemispherical capacitor, and detector. By opening the slits wider and/or by increasing the pass energy, more electrons are allowed to pass through the analyzer, which increases the count rates on the detector: this improves the statistics of the measured spectrum, but at the expense of poorer instrumental energy and angular resolution. Thus there is a natural tradeoff between the time

required to record a well-sampled spectrum and the resolution of features in $A(\mathbf{k}_{\parallel}, E)$ contained therein; the settings most appropriate to a given measurement depend strongly on the material, photon energy, and even the region of k -space being probed. To determine the actual energy resolution of the Scienta R4000 used in our lab at different combinations of slit sizes and pass energies, reference measurements are performed on the Fermi edge of a clean polycrystalline gold surface at low temperatures (< 20 K). The width of the measured energy distribution curves in this limit are determined primarily by Gaussian instrumental resolution (width ΔE , typically ≥ 10 meV) convolved with the intrinsic thermal smearing of the Fermi-Dirac distribution (width $k_B T$, < 1 meV). Although the R4000 is capable of reaching instrumental resolutions on the order of a few meV, none of the materials studied in this thesis by ARPES experiments required such fine resolution, so unless otherwise specified, we utilized slit widths of 0.8 mm with $E_p = 5$ eV for near- E_F measurements with He-I α ($\Delta E = 10$ meV) and slit widths of 0.8 mm with $E_p = 20$ eV for near- E_F measurements with He-II α ($\Delta E = 40$ meV).

Low-energy electron diffraction

In addition to photoemission measurements, the Cornell ARPES system is equipped with a four-grid low-energy electron diffraction (LEED) optics for analyzing the surface crystal structures of epitaxial thin films synthesized by MBE. A more comprehensive theoretical description of LEED and discussion of how experimental data are interpreted are provided later in section 3.4. Here we simply give a high-level technical description of the apparatus used for these measurements, which is a commercial instrument purchased from SPECS (ErLEED 150): electrons are emitted from a LaB₆ cathode, then accelerated to some modest energy (typically 20 – 500 eV) and collimated by a series of electrostatic lenses to produce a monochromatic plane-wave-like beam of incident electrons impinging on the surface of the sample being studied. Interaction with the periodic arrangement

of atoms in the topmost ≈ 1 nm of material causes a small fraction of the incident beam current to be diffracted into a discrete set of beams that are eventually reflected back towards the LEED gun and screen. Upon striking the phosphor screen, the reflected electron beams are transduced into light intensities, creating a diffraction pattern that is recorded by a CCD camera viewing the LEED screen from the backside, outside of vacuum.

Typical incident beam currents used in this work are $1 - 10 \mu\text{A}$ and typical reflection coefficients are $R \approx 10^{-3}$. The data acquisition parameters used in the camera images—*e.g.*, exposure time, aperture size, ISO level, *etc.*—are determined by the user and should generally be chosen to avoid overexposure/saturation of the most intense spots in the diffraction pattern, unless the user is more interested in establishing the presence/absence of weak spots than in obtaining linear measurements of the intensities of the stronger spots. All parameters of the LEED optics and incident beam characteristics (including the energy) can be controlled from a computer using custom software written by the author of this dissertation. The interface to the CCD camera is also computer-controlled, which allows LEED- $I(V)$ data sets—*i.e.*, diffraction patterns at many different incident energies—to be acquired in a fully automated fashion. Since the same sample manipulator is used for LEED as for ARPES measurements, LEED measurements can also be performed at variable temperatures from $\approx 10 - 300$ K and with the incident electron beam at arbitrary angles of incidence relative to the surface of the sample; however, the sample is usually aligned to near normal incidence for ease of data analysis.

Vacuum pumps and magnetic shielding

Because of the extreme surface sensitivity of ARPES and LEED, all of these experiments must be performed under stringent UHV conditions. Most of the components drawn in Figure 3.6 are indeed different flavors of vacuum pumps—turbomolecular pumps, ion pumps, cryopumps, titanium sublimation pumps, *etc.*—each of which specializes in re-

moving different types of residual gases present in the system at rates that maintain the total pressure in the chamber at levels $p \approx 10^{-11} - 10^{-10}$ Torr. Items such as the helium lamp, which require an active flow of He gas into the lamp head, require a specialized differential pumping scheme to simultaneously allow the UV photons to enter the main chamber and illuminate the sample surface, while also preventing the He gas from severely compromising the chamber's vacuum.

Because the objects under study in ARPES and LEED experiments are slowly moving charged particles, great care must also be taken to eliminate any stray magnetic fields inside the measurement chamber: these will deflect the trajectories of an electron after it has exited the sample, and thereby artificially skew any subsequent measurements of its momentum. In practice, the residual magnetic fields from the Earth and other equipment in the lab are more than strong enough to completely ruin ARPES and LEED measurements, so the measurement chamber must be actively magnetically shielded. On the Cornell system, this is accomplished by having a μ -metal shroud (a material with a very high magnetic permeability) lining the entirety of the lower chamber where ARPES measurements are conducted, and a similar type of shroud on the LEED optics that extends into the upper chamber and shields the area between the sample and the electron gun (source) + screen (detector) during LEED measurements.

3.4 Low-energy electron diffraction

LEED is a powerful technique for performing *surface crystallography*. The basic physical phenomenon is—as in x-ray diffraction—one of quantum mechanical wave interference: by studying how an electron—instead of a photon—elastically scatters upon interaction with a crystalline solid, much information can be gained about the geometrical configuration of atoms within the material. To enhance the angular separation of the diffracted

“beams” induced by this interference, it is desirable to use electrons with wavelengths λ comparable to the typical interatomic spacings in solids; hence, “low-energy” electrons with energies $20 \text{ eV} < E < 500 \text{ eV}$ (corresponding to $2.7 \text{ \AA} > \lambda > 0.55 \text{ \AA}$) are customarily used in LEED experiments. One of the benefits of using low-energy electrons—compared with, *e.g.*, transmission electron microscopy (TEM) or reflection high-energy electron diffraction (RHEED), which typically use electron beams with $E \geq 10 \text{ keV}$ —is that LEED probes the surface crystal structure over a comparable length scale to surface sensitive probes of the near-Fermi-level electronic structure, such as ARPES and spectroscopic imaging scanning tunneling microscopy (SI-STM). Inasmuch as knowledge of the surface atomic positions are a prerequisite to a detailed understanding of the exotic low-energy physical phenomena that emerge from interactions among the electrons moving in this periodic potential, LEED is a complementary technique to ARPES and SI-STM. In this section, we describe the basic setup of LEED experiments and briefly review what information can be extracted from the data collected in such experiments.

3.4.1 General formalism

Figure 3.7 sketches the setup of a typical LEED experiment. An electron initially in a plane-wave eigenstate $|\mathbf{k}_i\rangle = |\mathbf{k}_{\parallel} + \mathbf{k}_{\perp}\rangle$ impinges on a crystal having well-defined translational symmetries parallel to its surface, such that the crystal potential \hat{V} satisfies $V(\mathbf{r}) = V(\mathbf{r} + \mathbf{R}_{\parallel})$ for some discrete set of real-space translations $\{\mathbf{R}_{\parallel}\}$. Interaction with this potential scatters the electron into a final state $|\mathbf{k}_f\rangle = \sum_{\mathbf{G}_{\parallel}} c_{\mathbf{G}_{\parallel}} |\mathbf{k}_{\parallel} + \mathbf{G}_{\parallel}\rangle$, where the sum is over the set of reciprocal lattice translations $\{\mathbf{G}_{\parallel}\} = \mathcal{F}\{\mathbf{R}_{\parallel}\}$ of the crystal parallel to the surface. Since \hat{V} is invariant modulo $\{\mathbf{R}_{\parallel}\}$ (by assumption), the parallel momentum of the initial state must be conserved modulo $\{\mathbf{G}_{\parallel}\}$ in the final state $|\mathbf{k}_f\rangle = \hat{V}|\mathbf{k}_i\rangle$; by a similar argument there is no restriction on the final-state perpendicular momentum, which is not conserved by \hat{V} . Each separate value of $\mathbf{k}_{\parallel} + \mathbf{G}_{\parallel}$ thus defines a diffracted “beam”—

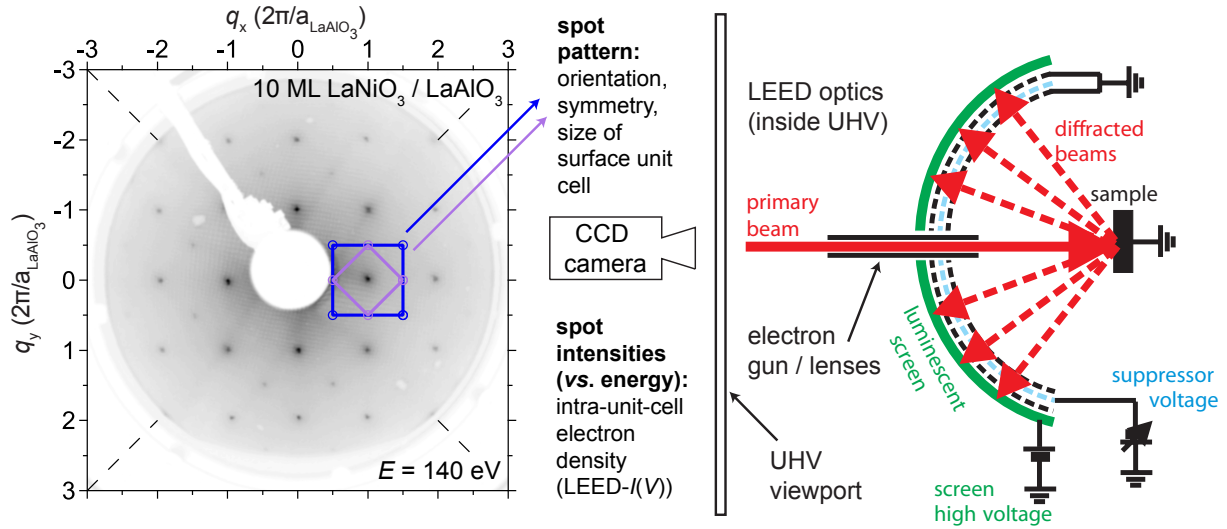


Figure 3.7: Right: schematic diagram of an experimental apparatus for performing LEED measurements, reproduced from Ref.[101]. Left: representative LEED image acquired in the Cornell MBE+ARPES system at 140 eV for a 10 ML epitaxial thin film of LaNiO_3 grown *in situ* on a LaAlO_3 substrate. By analyzing the LEED spot pattern, one can extract information about orientation and size of the surface unit cell, as well as the plane group symmetries of the surface crystal structure. To gain information about the atomic positions within the unit cell, one must analyze the LEED spot intensities versus energy—*cf.*, Figure 3.8.

i.e., direction in momentum space along which the electron can propagate with non-zero probability—with the measured intensity I of a given beam being proportional to $|c_{G_{\parallel}}|^2$. A suppressor voltage allows the LEED optics to detect only electrons with energies in a narrow range about the primary energy E_i , so only scattering channels having $E_f = E_i$ need be considered in the calculation of the $c_{G_{\parallel}}$ coefficients.

Although first realized by Davisson and Germer at a (111)-oriented surface of nickel in 1927 [102]¹¹, LEED did not become commonly employed as a materials characterization tool until the early 1970s. The fundamental reason for this lengthy delay is that *low-energy electrons interact strongly with matter*, which has two major implications:

- As noted in section 3.3.4, characteristic values of the inelastic mean free path for low-energy electrons relevant to LEED and ARPES are $L_{imfp} \approx 5 - 10 \text{ \AA}$ [96]. While

¹¹Davisson and Germer were awarded the Nobel Prize in 1937 for this work.

the precise value of L_{imp} is, of course, material- (and energy-) dependent, this means that the LEED signal (consisting only of elastically scattered electrons) is extremely surface-sensitive. Accordingly, LEED experiments must be conducted in UHV to preserve the nature of the surface being studied and the surface must be prepared *in situ*. Standard preparation methods usually involve some combination of mechanical cleavage, ion bombardment, vacuum annealing, or *in situ* film deposition; however, UHV equipment was not generally available until the 1960s.

- Unlike XRD, the single-scattering approximation is never valid in LEED. Instead, an accurate description of LEED intensities must account for multiple scattering events in computing the $c_{G_{\parallel}}$ coefficients; however, it was not until experimental data were available on well-controlled surfaces that Pendry and others could reach a general consensus regarding the essential ingredients of such a theory—see, *e.g.*, Refs.[103, 104].

In other words, because of the strong interaction of electrons with surface atoms, LEED requires rather demanding experimental conditions and a rather involved theoretical description to interpret the experimental data. Nonetheless, LEED is nowadays among the most well-established techniques in the surface scientist’s toolbox for quantitative structural determination [105], and numerous freely distributed software packages exist for simulating LEED intensities from surfaces of arbitrary complexity [106, 107, 108].

Figure 3.8 graphically represents the standard approach to surface structural determination by LEED analysis. From the description of the scattering process given above, it is clear that the a unique set of diffracted plane waves $\{\mathbf{G}_{\parallel}\}$ corresponds to a unique set of $\{\mathbf{R}_{\parallel}\}$; thus the spatial arrangement of the spots in a LEED pattern can be easily *inverted* to infer the real-space lattice parallel to the surface of the material being studied¹². *Sur-*

¹²There are but *five* two-dimensional Bravais lattices, but these can be non-trivially superposed in the presence of distinct structural domains.

face reconstructions refer to situations where the primitive real-space lattice translations are larger than (and possibly rotated relative to) the translations that would be expected for a bulk-truncated crystal structure. Furthermore, by calibrating the LEED instrument using diffraction patterns recorded for a surface with a known lattice constant, quantitative information about the surface lattice constants of new materials can be obtained from analysis of LEED spot positions. As we show in chapter 6, this can be a useful method to assess the amount of strain relaxation present at the surfaces of epitaxial thin films grown by MBE.

Unfortunately, the same is not true for observables that vary on length scales within the real-space unit cell, such as the electron density ρ_{el} . The measured intensities $I_{G_{\parallel}} \sim |c_{G_{\parallel}}|^2$ contain no phase information about the complex numbers $c_{G_{\parallel}}$ —and even if they did, the importance of multiple scattering in LEED implies that there is no simple operation (*e.g.*, Fourier transformation \mathcal{F}) that could be inverted to recover ρ_{el} (or its autocorrelation) directly. Therefore, in practice LEED structural searches must proceed in the “opposite” direction: first postulating a reference atomic structure with known ρ_{el} , then calculating diffraction intensities $I_G(X)$ for the different beams of this structure as a function of some control parameter X , and finally comparing these simulated intensities with actual data to determine if the model can reasonably explain the experimental observations. This loop is iterated until “good agreement” is reached between simulation and experiment¹³, at which point the surface structure is considered solved.

Readers familiar with so-called *Rietveld refinement* of x-ray and neutron diffraction intensities will note the marked similarities of that method to the procedure just described. The main difference is that LEED studies introduce another variable X that modulates I besides just the reciprocal lattice vectors $\{\mathbf{G}_{\parallel}\}$, so as to generate additional data with which to constrain the theory-experiment comparison. X is usually taken to be the en-

¹³A quantitative definition of “good agreement” is typically expressed in terms of the Pendry *reliability factor* [109].

ergy E of the incident electron, which is readily controlled experimentally by application of an accelerating voltage V to the incident beam and produces a wealth of rich features in LEED intensity *vs.* voltage (LEED- $I(V)$) curves¹⁴. For an example of how the different steps in a LEED- $I(V)$ structural refinement actually play out in the case of electron scattering from the surfaces of complex oxides grown *in situ* by MBE, we refer interested readers to our work on (001)-oriented thin films of the perovskite nickelate LaNiO_3 [57]. This work builds on pioneering LEED- $I(V)$ studies of the cleaved single-crystal surfaces of strongly correlated complex oxides described in Refs.[110, 111, 112, 113]. In the case of $\text{LaNiO}_3(001)$, a polar discontinuity at the film-vacuum interface induces large bucklings of the LaO layers nearest the surface [57, 114]; at a structural level, these distortions cause a dramatic redistribution of the intensities in LEED- $I(V)$ curves, and at an electronic level, these distortions likely play a crucial role in why ultrathin films of LaNiO_3 undergo film-thickness-dependent metal-insulator transitions [52, 114, 115].

¹⁴More pedantically these might be called $I(E)$ curves, where $E = eV$ is related to the applied voltage by the elementary electronic charge e .

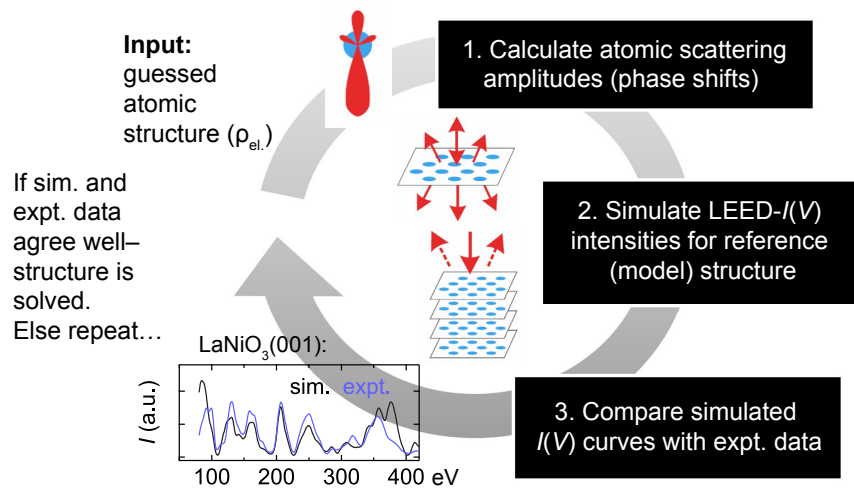


Figure 3.8: Abstract depiction of the LEED- $I(V)$ structural refinement process. A guess for the atomic structure—more pedantically, the intra-unit-cell electron density $\rho_{el.}$ —is used as input to the simulations, and the black boxes at stages (1.) and (2.) of the loop entail separate calculations that can be done with freely distributed software packages to model how low-energy electrons scatter off such a periodic potential. If the simulated and experimentally measured data agree well in stage (3.), the structure is considered solved; otherwise the process is repeated with a different guess for the atomic structure. Example data shown here is for the $(H, K) = (2, 0)$ $I(V)$ curve for the (001)-oriented surface of LaNiO_3 thin films [57].

CHAPTER 4

EPITAXIAL STRAIN TUNING OF SUPERCONDUCTIVITY IN Sr_2RuO_4

Sr_2RuO_4 is in many ways the archetypal strongly correlated material, offering opportunities to study:

- A bad metal at intermediate to high temperatures ($T \sim 100 - 1000$ K) in which strong Hund's rule interactions among the electrons cause large non-saturating resistivities, with scattering rates well in excess of the Mott-Ioffe-Regel limit and the notion of coherent quasiparticle transport ceases to exist.
- A strongly renormalized Fermi liquid at low temperatures ($T \sim 10$ K) which—despite inheriting large effective masses from the strong correlations in the parent state and a quasi-two-dimensional nature from the layered crystal structure—nonetheless displays all of the canonical signatures of a *bona fide* Fermi liquid.
- An unconventional superconductor condensing from the Fermi liquid at even lower temperatures ($T \sim 1$ K), mediated by collective spin fluctuations—*i.e.*, an effectively attractive interaction of quasiparticles near the Fermi level resulting from bare Coulomb repulsion.

Moreover, because single crystals of Sr_2RuO_4 are among the purest ternary materials in existence, all of these phenomena can be studied without the additional complications of disorder. Interestingly, although enormous amounts of experimental and theoretical progress have been made over the last two decades in quantitatively understanding the first two states of matter, many questions about the unconventional superconductivity remain unresolved. These open questions range from basic facts, such as the symmetry of the superconducting order parameter, to more detailed questions about the mechanisms that set the condensation energy scale of the superconductivity.

In the author’s opinion, this confusion likely reflects that Nature has been (un)kind in arranging for multiple superconducting states with different order parameters to be nearly degenerate in bulk Sr_2RuO_4 . To a physicist, this is unkind in the sense that the ultimate ground state depends on rather subtle details in the effective Hamiltonian for the low-energy physics, which are generally not known with sufficient precision for theory to provide robust predictions that can reliably guide the interpretation of experimental data. To a more materials-minded physicist, however, this is kind in the sense that it also implies that the superconductivity should respond quite sensitively to external perturbations—and by studying the behavior in nearby regions of phase space, one can gain insight into which superconducting properties are “fundamental” (applicable to all superconducting variants of Sr_2RuO_4), and which are more “accidental” or “fine-tuned” (applicable in more limited regions of phase space). In this chapter we present studies towards this goal carried out during this dissertation, aimed at using substrate-imposed epitaxial strains to perturb and thereby better understand the unconventional superconductivity in thin films of Sr_2RuO_4 . In section 4.1 and section 4.2 we introduce salient features of the normal-state electronic structure and superconductivity in Sr_2RuO_4 that were known from previous work, to place the current results and discussion given in section 4.3 and section 4.4 in proper context. Along the way we provide relevant technical details where appropriate regarding the experimental and computational methods used in our work, so that the foundations and approximations on which the conclusions rest are transparent.

4.1 Introduction to Sr_2RuO_4

4.1.1 Crystal structure

The parent crystal structure of Sr_2RuO_4 , without any symmetry lowering structural distortions, belongs to space group #139, $I4/mmm$. The conventional unit cell is tetragonal ($a = b \neq c$) and contains two formula units related by a body-centering translation of $(1/2, 1/2, 1/2)$. Ruthenium (Ru) cations sit on the vertices of the lattice at fractional coordinates $(0, 0, 0)$ and $(1/2, 1/2, 1/2)$ and are octahedrally coordinated by six nearly equidistant oxygen (O) anions at $\pm(1/2, 0, 0)$, $\pm(0, 1/2, 0)$, and $\pm(0, 0, z_{apO})$. Owing to the tetragonal symmetry, the Ru-O bond lengths are actually split into 2 + 1 inequivalent lengths, giving rise to so-called equatorial oxygens eq.O within the RuO_2 planes perpendicular to the c axis, and apical oxygens ap.O perpendicular to these planes. Strontium (Sr) cations are positioned in spacer layers at $\pm(1/2, 1/2, 1/2 - z_{Sr})$ and $\pm(0, 0, z_{Sr})$ that are 9-fold coordinated to the oxygen anions; these cations provide structural integrity and extra electrons to the RuO_6 octahedral network, but play no direct role in the electronic and magnetic properties. The lattice constants (a, c) and internal parameters (z_{apO}, z_{Sr}) are thus the four basic structural degrees of freedom that parametrize the crystal structure of Sr_2RuO_4 .

A powerful way of visualizing and thinking about the structure of Sr_2RuO_4 as it relates to both the solid-state chemistry (*cf.* subsection 4.3.4) and low-energy physics aspects of this material is as the single-layer ($N = 1$) end member of the Ruddlesden-Popper series of homologous structures, $(\text{SrO})(\text{SrRuO}_3)_N$ [116]. In this picture, drawn schematically in Figure 4.1, rocksalt-type (SrO) layers are interleaved with N layers of perovskite-type (SrRuO_3) slabs in a *natural superlattice*. The rocksalt layers disrupt the connectivity of the RuO_6 octahedral network along the c axis, leading to progressively more two-dimensional electronic properties as N is reduced from the three-dimensional limit

$N \rightarrow \infty$ (SrRuO_3) to the two-dimensional limit $N = 1$ (Sr_2RuO_4). Interestingly, the magnetic behavior in this series evolves from ferromagnetism for $N \rightarrow \infty$ [117, 118, 119, 120], to quantum-critical metamagnetism for $N = 2$ (antiferromagnetic spin-density wave order can be stabilized in $\text{Sr}_3\text{Ru}_2\text{O}_7$ under modest externally applied magnetic fields, $B \approx 8$ T [62, 121]), to unconventional superconductivity for $N = 1$ [37, 64].

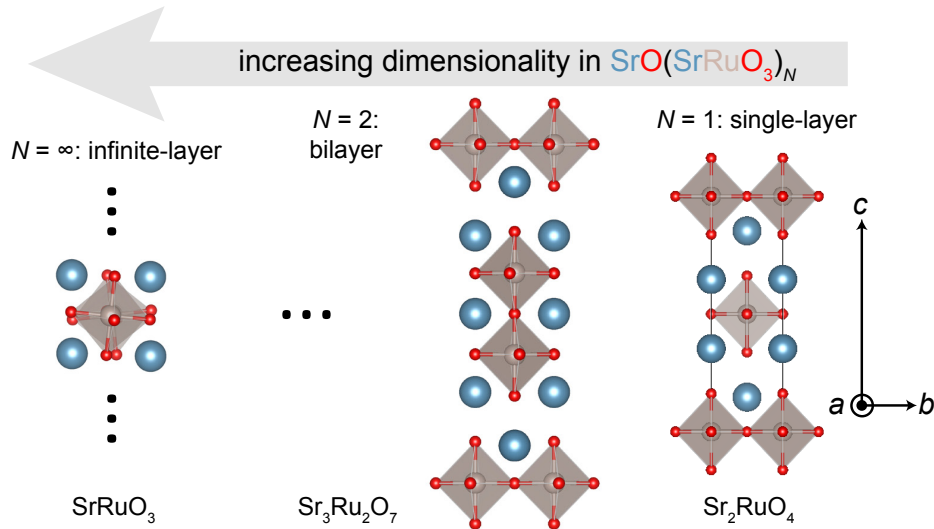


Figure 4.1: Crystal structures of the Ruddlesden-Popper series of strontium ruthenates, $(\text{SrO})(\text{SrRuO}_3)_N$ ($N = 1, 2, \dots, \infty$). Increasing N increases the connectivity of the RuO_6 octahedra along the c -axis, and thus the effective dimensionality of the electronic structure.

Sr_2RuO_4 is rather unique among Ruddlesden-Popper materials inasmuch as it does not show any evidence for any structural phase transitions that may reduce the symmetry from the ideal $I4/mmm$ structure. A comprehensive series of temperature-dependent neutron and x-ray diffraction measurements have proven that the structure remains tetragonal with 180° Ru-O-Ru bond angles from 0–300 K [122, 123, 124, 125]; furthermore, inelastic neutron scattering measurements evidence weakly temperature-dependent electron-phonon coupling [126]. By contrast, the isovalent Ca_2RuO_4 and $N \neq 1$ members of $(\text{SrO})(\text{SrRuO}_3)_N$ all exhibit coordinated tilts and/or rotations of the RuO_6 octahedral network that evolve non-trivially with temperature [127, 128]; similarly, the parent $N = 1$ Ruddlesden-Popper compound of the cuprate superconductors, $(\text{La,Sr})_2\text{CuO}_4$, exhibits a

zoo of symmetry lowering structural distortions to low-temperature tetragonal and orthorhombic phases [124, 126]. As we discuss further in subsection 4.3.2, the relative structural simplicity of Sr_2RuO_4 makes it an excellent candidate for strain tuning studies in which distortions of the unit cell are externally imposed, since this reduces the number of internal degrees of freedom whereby the strain can be accommodated.

4.1.2 Charge, orbital, and spin degrees of freedom

Each O atom in Sr_2RuO_4 requires two electrons to completely fill its $2p$ shell, and each Sr atom has two loosely bound $5s$ electrons that are readily ionized. With formal valences of Sr^{2+} and O^{2-} , the formal valence of the ruthenium cations is Ru^{4+} , which leaves four electrons filling states with primarily $4d$ orbital character near the Fermi level, E_F . Despite the large carrier densities $n \approx 4 \times 10^{28}/\text{m}^3$ that result from this charge configuration (the typical volume of a conventional unit cell containing two Sr_2RuO_4 formula units is $\approx 200 \text{ \AA}^3$), Sr_2RuO_4 is a *resistively challenged “bad” metal* at elevated temperatures, with room-temperature values of $\rho_{ab}(300 \text{ K}) \approx 120 \mu\Omega\text{-cm}$ that continue to increase without saturation as the temperature is raised. Naively applying the Drude model would associate this level of $\rho_{ab}(300 \text{ K})$ with in-plane mean free paths $\ell_{ab} \approx 8 \text{ \AA}$, which is the same order of magnitude as the interatomic distances, casting much doubt on the validity of any theory that presumes the current-carrying quasiparticle excitations are only weakly scattered.

At a fundamental level, these large values of ρ at intermediate to high temperatures in Sr_2RuO_4 are a manifestation of strong electron-electron scattering that originates from local atomic-like Hund’s rule interactions between electrons when they simultaneously occupy d orbitals on the same Ru site. We leave a more complete theoretical exposition of this phenomenology to the many excellent articles that have been written recently on so-

called *Hund's metals* [129, 130, 131, 132]. It has been one of the many triumphs of single-site dynamical mean-field theory (DMFT) to recognize the Hund's rule interaction J as the primary source of electronic correlations in ruthenates, Fe-based superconductors, and many other multi-orbital systems of current interest¹.

Despite this representing a highly non-trivial conceptual advance in our understanding of the *bad metal* state of ruthenates, for our purposes in this dissertation, we take for granted that the ansatz of DMFT calculations is correct: the interplay of U and especially J produces high-spin configurations of four electrons that are essentially localized on individual RuO_6 clusters on “short” time scales, but do still fluctuate (*i.e.*, exchange electrons) on “long” time scales. The octahedral crystal-field splitting $10Dq \approx 3 - 4$ eV that splits the five d orbitals into a triplet of t_{2g} states and a doublet of e_g states at higher energies is appreciably larger than both $U \approx 1 - 3$ eV and $J \approx 0.2 - 0.7$ eV. Thus, high-spin here means four electrons occupying the t_{2g} shell, for an effective Curie-Weiss-like spin moment of $\approx 2\mu_B$ (Bohr magnetons) per Ru at elevated temperatures [133], as depicted in Figure 4.2. Note that in Sr_2RuO_4 and other ruthenates with tetragonally distorted octahedra, there is also a small intra- t_{2g} crystal-field splitting of $\delta < 0.1$ eV between states with d_{xz}/d_{yz} and d_{xy} orbital character; however, because δ is usually lower than J and the spin-orbit coupling $\lambda \approx 0.1 - 0.2$ eV, which both favor equal t_{2g} orbital occupancies, we ignore it except when discussing fine details of the low-energy electronic structure in subsequent sections.

4.1.3 Fermi liquid regime

As the temperature is lowered further, the Hund's rule spin correlations described in subsection 4.1.2 and drawn in Figure 4.2 are eventually fully screened and an emergent

¹None of these materials are close to hosting an effectively half-filled manifold of electronic states near E_F , so the usual Mott-Hubbard-like mechanism of producing electronic correlations based on the on-site Coulomb repulsion U suppressing double occupancy of this level is not particularly operative.

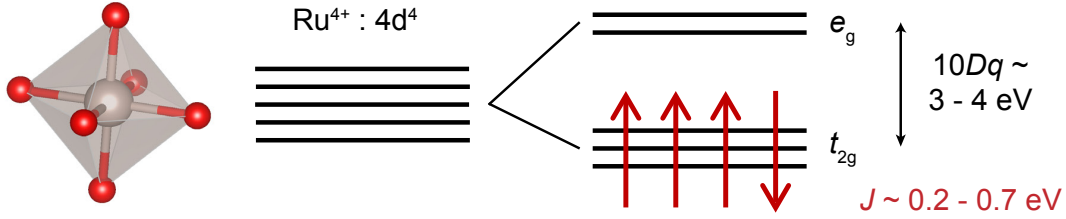


Figure 4.2: Local orbital level structure of Sr_2RuO_4 within individual RuO_6 octahedra. The octahedral crystal-field splitting $10Dq$ and Hund's rule interaction J together favor four electrons occupying the t_{2g} shell in high-spin configurations having slowly fluctuating magnetic moments of magnitude $\approx 2\mu_B$.

Fermi liquid of strongly dressed but long-lived quasiparticle excitations forms below a coherence scale of $T_{FL} \approx 25$ K. Early indications of Fermi liquid behavior at low temperatures in Sr_2RuO_4 came from measurements of the temperature dependence of the specific heat ($C/T = \gamma + AT^2$, with a large Sommerfeld coefficient of $\gamma = 38 \text{ mJ mol}^{-1}\text{K}^{-2}$) [134], a temperature-independent Pauli spin susceptibility ($\chi_s = 1.7 \times 10^{-4}$, corresponding to a Wilson ratio of $R_W = m_{susc.}^*/m^* = 1.5$) [134, 135], and a characteristic T^2 temperature dependence of the in-plane component of the resistivity resulting from quasiparticle-quasiparticle Umklapp scattering events ($\rho_{ab} = \rho_0 + A_{ab}T^2$, with $A_{ab} \approx 6 \text{ n}\Omega\text{-cm}/\text{K}^2$) [136]. Note that the out-of-plane component of the resistivity ρ_c also varies as T^2 below T_{FL} ($A_c \approx 5.5 \mu\Omega\text{-cm}/\text{K}^2$), despite being about 3 orders of magnitude larger than ρ_{ab} , as expected based on the quasi-two-dimensional crystal and electronic structure of Sr_2RuO_4 [136].

At a more microscopic level, the four valence electrons in the t_{2g} orbitals are distributed among three bands in momentum space in the Fermi liquid state, historically labeled the $\{\alpha, \beta, \gamma\}$ sheets as indicated in Figure 4.3. Extensive characterization of all three Fermi surfaces by quantum oscillations [136, 137, 138], angle-dependent magnetoresistance measurements [136], and angle-resolved photoemission spectroscopy (ARPES) [139] have provided an extremely detailed parametrization of the Fermi surface topographies as well as the quasiparticle dispersions near E_F . Readers interested in more details along these

lines are referred to the comprehensive review article by Bergemann *et al.* [136]

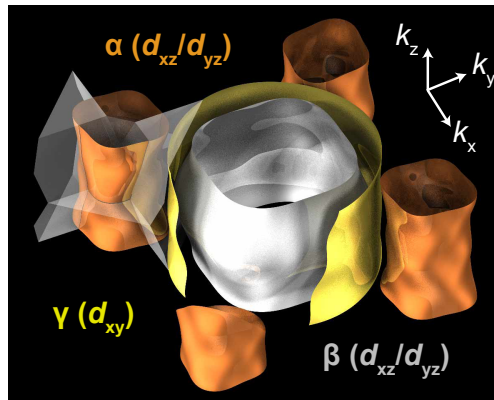


Figure 4.3: $\{\alpha, \beta, \gamma\}$ Fermi surfaces of bulk Sr_2RuO_4 , as measured experimentally by quantum oscillations and angle-dependent magnetoresistance measurements. The dominant orbital character $\{d_{xz}/d_{yz}, d_{xy}\}$ of wavefunctions on each sheet are also indicated in parentheses. Note that the corrugations and warpings of the otherwise cylindrical Fermi surfaces along k_z have been exaggerated by a factor of 15 for clarity—the electronic structure is, to an excellent approximation, two-dimensional. Figure reproduced from Ref.[136].

As expected for state born out of a soup of strong electron-electron scattering, the effective masses m^* of the charge- and spin-carrying quasiparticle excitations in the Fermi liquid regime are rather large. Fitting the decay of the quantum oscillation amplitudes as temperature is increased gives $m_\alpha^*/m_e = 3.3$, $m_\beta^*/m_e = 7.0$, and $m_\gamma^*/m_e = 16$, where the subscript on m^* labels the band index and m_e is the bare electron mass [136]. The sum of the contributions of the three Fermi surfaces to the total electronic component of the specific heat can be calculated using these masses as a consistency check, and excellent agreement is found with independent measurements of the Sommerfeld coefficient γ listed above [137]. Finally, recent high-resolution ARPES experiments measured sheet-averaged effective masses for the β - and γ -band carriers that are in quantitative agreement with these cyclotron masses obtained from quantum oscillations [140]. Comparisons of these values of m^*/m_e with the band masses m_b/m_e predicted by computational schemes that treat electron-electron interactions at a static mean-field level, such as density functional theory (DFT), suggest that the masses in all bands are enhanced by factors

of $m^*/m_b \approx 3 - 4$ due to dynamical many-body interactions [130]. Taken together, there is a wealth of evidence that strongly renormalized Fermi liquid behavior exists in Sr_2RuO_4 below temperatures T_{FL} that are quite low compared with the bare bandwidths of the material, but still about an order of magnitude larger than the temperature scale T_c at which superconductivity condenses. Moreover, because the Fermi liquid state in Sr_2RuO_4 is exceedingly well characterized—certainly known much better than in any other unconventional superconductor!—it seems like a detailed understanding of the superconductivity in terms of properties of the normal-state electronic structure should be within reach.

4.1.4 Superconductivity in bulk Sr_2RuO_4

Superconductivity in Sr_2RuO_4 was first discovered by Y. Maeno and coworkers in 1994 [37]. Much of the research into the superconductivity in the intervening 25 years since then has been motivated by an early suggestion of Rice and Sigrist [141], who noted that the Fermi liquid parameters of Sr_2RuO_4 —*e.g.*, the enhancements of the specific heat and spin susceptibility noted above—are similar to those observed for ^3He ; *ergo*, perhaps the superconductivity in Sr_2RuO_4 is an electronic (*i.e.*, charged superfluid) analogue of the superfluidity observed in ^3He . If true, this would represent an essentially new phase of matter: all superconductors known to date, both conventional and unconventional, consist of electrons bound in spin-singlet Cooper pairs with anti-aligned spins, whereas the fermionic nuclei in ^3He are bound in spin-triplet pairs with co-aligned spins. While many experiments conducted over many years were interpreted as providing evidence for spin-triplet superconductivity in Sr_2RuO_4 [142, 143, 144], the results of recent experiments conclusively refute this possibility [145].

Many comprehensive reviews of what is known—and what outstanding mysteries remain—regarding the superconducting order parameter in bulk Sr_2RuO_4 exist else-

where [146, 147, 148]. It is largely outside the scope of this thesis to add content to these discussions of the pairing symmetry in a direct way. Therefore, we briefly list several features of the order parameter below that are suggested by some of the major experiments that have been performed in this realm, and we leave a deeper analysis of what candidate order parameters are (in)compatible with what pieces of experimental data to other sources. Because the exploration of strain effects on the superconductivity *is* much more germane to the results presented in this thesis, we defer a discussion of these measurements to section 4.2, even though in certain cases these experiments weigh in on the order parameter question as well.

Evidence for unconventional superconductivity in Sr_2RuO_4

Recall from chapter 1 that a precise definition of unconventional superconductivity is the relationship:

$$\sum_{\mathbf{k}} \Delta(\mathbf{k}) = 0 \quad , \quad (4.1)$$

where $\Delta(\mathbf{k})$ is the superconducting gap function, and the summation is carried out over all wavevectors on the Fermi surface(s). Equation 4.1 has the important consequence of implying that sufficiently strong elastic scattering, which mixes quasiparticle states with different \mathbf{k} , can average the superconducting order parameter to zero [146]. In other words, even non-magnetic disorder can destroy unconventional superconductivity when the scattering rate is approximately equal to the \mathbf{k} -averaged $|\Delta(\mathbf{k})|$ —or equivalently, when the elastic mean free path ℓ equals the superconducting coherence length ξ . This is in marked contrast to conventional *s*-wave superconductors, which are relatively insensitive to non-magnetic disorder by virtue of Anderson’s theorem [149].

Turning this statement around, measurements of strongly disorder-dependent superconductivity are very compelling evidence for an unconventional origin of the superconductivity. Perhaps the most universally agreed upon aspect of the superconducting order parameter in Sr_2RuO_4 is that it is indeed unconventional, because of how sensitively the superconductivity responds to disorder. This observation traces back to early measurements by A. P. Mackenzie, Z. Q. Mao, *et al.* showing that the superconducting transition temperature T_c varies systematically with changes in the residual resistivity ρ_0 , as illustrated in Figure 4.4 [64, 150, 151]. We will continue to revisit this phenomenon throughout the remainder of this chapter, so it is worth quoting some actual numbers here for reference: in bulk Sr_2RuO_4 , residual resistivities of less than $\rho_0 \approx 1.1 \mu\Omega\text{-cm}$ are required to observe superconductivity, corresponding to in-plane mean free paths of $\ell_{ab} \approx 90 \text{ nm}$. This extreme sensitivity to dilute concentrations of impurities motivated the growth of exceptionally clean single crystals, which now routinely have $\rho_0 < 0.1 \mu\Omega\text{-cm}$, or $\ell_{ab} > 1 \mu\text{m}$, and $T_c = 1.5 \text{ K}$ [152, 153].

Not purely spin-triplet

As mentioned above, the early realization that the superconductivity in Sr_2RuO_4 was unconventional, together with some apparent similarities in its Fermi liquid parameters to those of ^3He , led to speculation that the superconducting order parameter may be odd-parity. Arguably the most convincing way to demonstrate this property is using an experimental probe that directly measures the spin susceptibility in the superconducting condensate: spin-singlet Cooper pairs are inherently non-magnetic objects that should have vanishingly small magnetic susceptibility—*i.e.*, ability to be polarized by a small external magnetic field—whereas spin-triplet Cooper pairs should retain the full susceptibility of two unpaired electrons. Any macroscopic measurements of the magnetic susceptibility will of course measure strongly diamagnetic response upon entering the superconducting

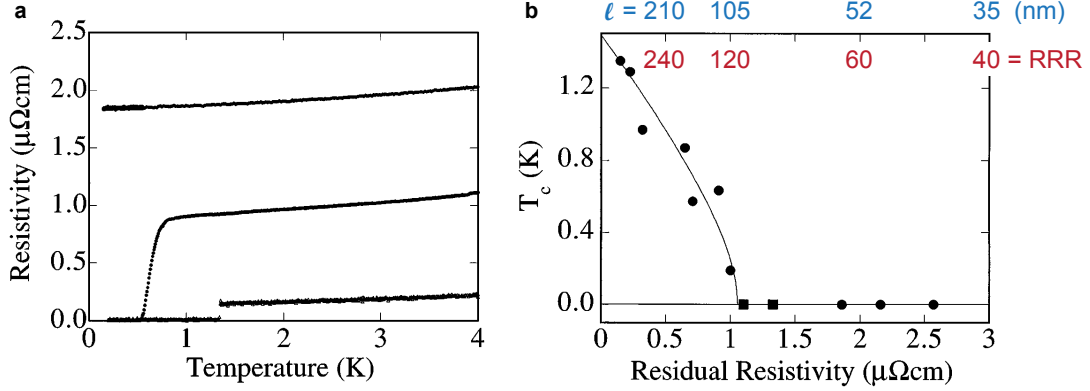


Figure 4.4: Disorder dependence of superconductivity in bulk Sr_2RuO_4 . **(a)** Low-temperature $\rho(T)$ behavior for three single crystals of Sr_2RuO_4 with different residual resistivities of $\rho_0 = 1.85, 0.85, \text{ and } 0.15 \mu\Omega\text{-cm}$. In the cleanest sample, a very sharp superconducting transition of width $\approx 10 \text{ mK}$ is observed at $T_c = 1.35 \text{ K}$. As ρ_0 increases, T_c is suppressed and the transition broadens. **(b)** T_c versus ρ_0 for twelve single crystals of Sr_2RuO_4 . Solid markers are crystals with different purity levels and hence different T_c s; the solid line is the result of fitting the data to the expectations of Abrikosov-Gor'kov pair-breaking theory. To put the data in more natural units, the corresponding residual resistivity ratios ($RRR \equiv \rho_{300\text{K}}/\rho_0$) and mean free paths ℓ are indicated on the top horizontal axis in red and blue; the latter is calculated from the expression $\ell = 2\pi\hbar d/e^2\rho_0\sum_i k_F^i$, where d is the interlayer spacing of 6.4 \AA and the sum runs over the three $\{\alpha, \beta, \gamma\}$ Fermi surface sheets of Sr_2RuO_4 , whose average Fermi radii k_F are known from quantum oscillations [137]. All data and figures are reproduced from Ref.[64].

state, due to Meissner screening; nonetheless, nuclear magnetic resonance (NMR) Knight shift measurements can still be sensitive to changes in just the spin susceptibility of the electrons via their hyperfine coupling to the nuclear magnetic moments. A celebrated early experiment by K. Ishida *et al.* measured a null result for the Knight shift upon cooling through the superconducting T_c in Sr_2RuO_4 : no changes in the spin susceptibility were resolved, strongly suggesting the presence of odd-parity superconductivity [142]. However, more recent experiments by the research group of S. Brown conclusively demonstrated that the Knight shift does indeed change upon cooling through T_c , and moreover, does so by an amount that indicates most of the spin susceptibility vanishes in the superconducting state [145], consistent with the behavior expected for an even-parity order

parameter. Upon learning of these new developments, K. Ishida repeated his original experiments using the measurement protocols suggested by S. Brown *et al.*, and confirmed that the previous null result was an artifact of the radio frequency pulses used in NMR transiently heating the crystals above the superconducting T_c [154]. At the time of writing this thesis, there remain quantitative open questions about the interpretation of the newer Knight shift results in terms of candidate order parameters [155], but it seems inescapable that the old Knight shift results—which long formed the basis of the argument in favor of an odd-parity order parameter—are not valid.

Time-reversal symmetry breaking

Muon spin relaxation (μ SR) and polar Kerr effect (PKE) measurements have both observed internal magnetic fields in Sr_2RuO_4 single crystals that form upon cooling below the superconducting T_c [156, 157]. In isolation, these experiments provide strong evidence for a chiral superconducting order parameter that breaks time-reversal symmetry (TRS). Historically, in the context of a putatively odd-parity order parameter (as suggested by the old NMR Knight shift results), these data were used to argue for a d vector of the form $\mathbf{d} = \Delta_0 \hat{z}(k_x \pm ik_y)$. With an odd-parity order parameter now ostensibly off the table of possibilities, it is much more difficult to reconcile the μ SR and PKE observations with candidate even-parity order parameters without invoking some theoretical fine tuning of degeneracies. The only even-parity d -wave order parameter guaranteed by the tetragonal point group symmetry of Sr_2RuO_4 to have two degenerate components that could be mixed in a TRS-breaking chiral state is of the form $d_{xy} \pm id_{yz}$, which would feature horizontal line nodes and Cooper pairs formed between electrons in different RuO_2 planes [148]. While not impossible, interplane pairing seems intuitively very unlikely in a material with a highly two-dimensional crystal and electronic structure such as Sr_2RuO_4 . In passing, we also note that the size of the volume-averaged internal magnetic fields measured

by μSR (≈ 0.5 G) are several orders of magnitude larger than the upper limit on internal fields (< 0.001 G) established by scanning SQUID and Hall probe microscopy measurements [158, 159]. Until these quantitative discrepancies are resolved and/or the temperature at which the TRS-breaking signal onsets is shown to respond in a sensible way to externally applied rectangular fields that lift the degeneracy between different components of the superconducting order parameter, it seems prudent to treat these indications of a chiral superconducting order parameter as *suggestive*, but perhaps not *conclusive*.

Low-lying quasiparticle excitations

The electronic specific heat $C_{el.}$ versus temperature T within the superconducting phase depends on how the quasiparticle density changes with T . In a fully-gapped superconductor, all excitations are suppressed at low temperatures, so $C_{el.} \rightarrow 0$ as $T \rightarrow 0$ K. As the temperature is raised, thermal activation of carriers across the superconducting gap Δ causes an exponential increase in $C_{el.}$. In contrast, the specific heat $C_{el.}/T$ of Sr_2RuO_4 exhibits linear scaling that persists from $\approx T_c/2 = 750$ mK down to the lowest measured temperatures, $T < 100$ mK [160]. Early measurements of this behavior on dirtier samples were clouded by the possibility that the heat was being transferred in this regime to excitations that would have been fully gapped out, were it not for the extreme disorder dependence of superconductivity; however, subsequent measurements since then have confirmed that this behavior is an intrinsic effect that is observed even for crystals in the clean limit. The only logical explanation capable of accounting for these results is that the superconducting order parameter has (near) nodes in the gap structure $\Delta(\mathbf{k})$, which produce ungapped excitations at all temperatures below T_c . Near nodes means that if $\Delta(\mathbf{k})$ does not contain symmetry-enforced zeroes—as would necessarily occur, *e.g.*, for any d -wave order parameter—then some amount of “accidental” fine-tuning occurs in regions of \mathbf{k} space that produce very deep minima in Δ there. Besides specific heat, there are a

litany of other probes that suggest low-lying quasiparticle excitations exist deep into the superconducting state, including thermal conductivity [161, 162, 163], London penetration depth [164], ultrasound attenuation [165], and scanning tunneling microscopy [166]. Although there is firm consensus for the existence of nodes in $\Delta(\mathbf{k})$ along extended regions *somewhere* in \mathbf{k} -space, there is considerable disagreement from different measurements about the specifics of where these nodes are located and how they are oriented—*e.g.*, vertically (along the c axis) [163] or horizontally (perpendicular to c) [161, 162].

4.2 Strain tuning of superconductivity and the normal-state electronic structure in Sr_2RuO_4

As stressed in the introduction, a powerful approach that may help to resolve some of these outstanding puzzles regarding the superconducting order parameter in Sr_2RuO_4 is to venture away from the single fixed point in phase space provided by thermodynamics—namely, to stabilize artificial forms of this material with subtly different crystal and electronic structures, and to measure how the superconductivity responds to these perturbations. The most common methods of achieving this objective are to apply hydrostatic pressure and to chemically dope the material. Both of these approaches have been applied to Sr_2RuO_4 ; however, the results are somewhat underwhelming. Hydrostatic pressure causes modest reductions in both the superconducting transition temperature ($\delta T_c/\delta P \approx -0.2$ K/GPa) as well as the quasiparticle mass enhancements ($\approx 5 - 10\%$ decreases in m^* per GPa) [167]. On the other hand, because of the extreme sensitivity of the superconductivity to disorder, essentially any type of chemical doping rapidly suppresses T_c to zero before enough dopant atoms can be introduced to appreciably change the electronic structure. For examples, alloying strontium with calcium (Ca) sterically induces transitions to a slew of interesting magnetically ordered and even-

tually insulating states in $(\text{Ca,Sr})_2\text{RuO}_4$ [168], but the concentrations of Ca required are $> 50\%$ and thus the superconductivity has long disappeared for other reasons before the more innate response of superconductivity to these structural distortions can be gauged². Similarly, replacing strontium with $\approx 10 - 15\%$ of lanthanum has been used to electron-dope Sr_2RuO_4 and traverse a van Hove singularity in the electronic structure [169], but the dopant-induced disorder renders these crystals non-superconducting long before the effects on the superconductivity of approaching this Lifshitz transition can be assessed.

Fortunately, there is a tuning parameter that is both “clean” and efficacious in modulating the superconducting and normal-state properties of Sr_2RuO_4 : externally applied *uniaxial pressure*. In a set of pioneering experiments conducted over the last five years, researchers in the group of C. Hicks and A.P. Mackenzie at the Max Planck Institute for the Chemical Physics of Solids have advanced this technique to the point where elastic strains of up to $\approx -1\%$ can be applied to single crystals of Sr_2RuO_4 at cryogenic temperatures [67, 68, 170, 171]. Besides being an impressive technical achievement for a brittle metal oxide such as Sr_2RuO_4 , these levels of strain are also sufficient to cause profound changes to the underlying low-energy physics, as we will describe in the next two subsections.

4.2.1 Strain effects on superconductivity

In Figure 4.5, we show how the superconducting T_c in Sr_2RuO_4 evolves as the crystal structure is mechanically compressed along one of the in-plane Ru-O-Ru bond directions, reproduced from Ref.[68]. In these experiments, single crystals of Sr_2RuO_4 are oriented, cut, and polished into long slender bars that are glued between the jaws of a piezoelectrically actuated vice; measurements of the AC magnetic susceptibility and electrical resis-

²Note that this substitution is isovalent “structural doping,” since Ca and Sr occupy the same column in the periodic table, but are differentiated by their ionic sizes.

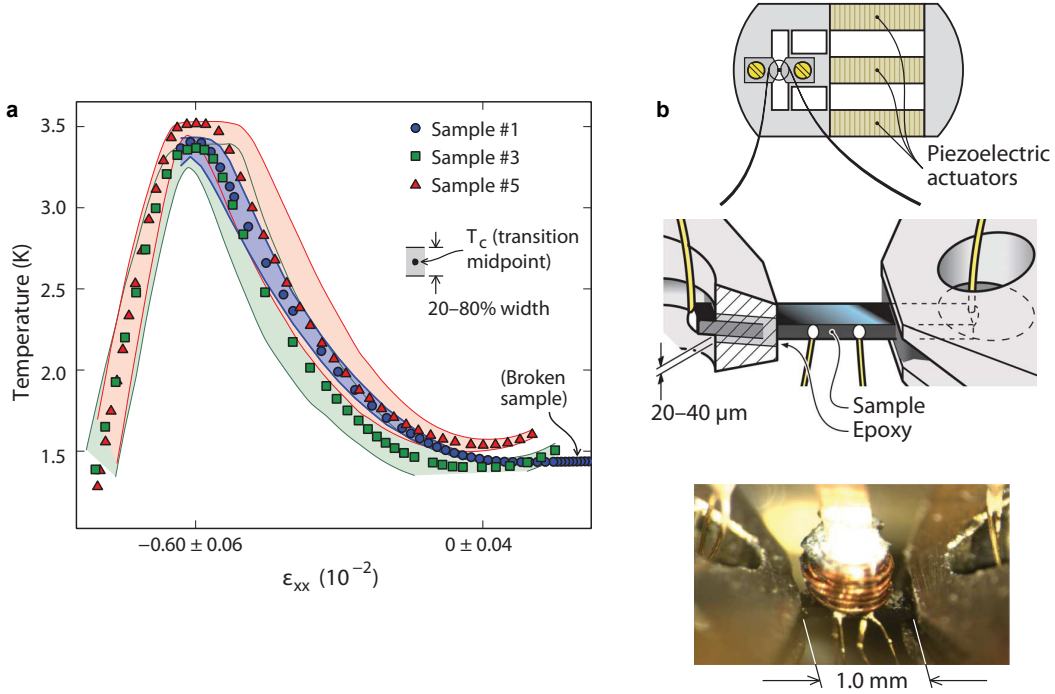


Figure 4.5: (a) Evolution of superconducting T_c with [100]-oriented uniaxial pressure in Sr_2RuO_4 . Negative values of ϵ_{xx} indicate compression along one of the in-plane Ru-O-Ru bond directions; the crystal expands along the orthogonal in-plane direction and along the c axis according to the Poisson effect. (b) Experimental apparatus for applying uniaxial pressure at cryogenic temperatures, using piezoelectric actuators. Four-point electrical resistivity and AC magnetic susceptibility measurements are performed versus temperature and pressure to gauge the response of superconductivity to these externally applied distortions of the crystal structure. Figures reproduced from Ref.[68].

tivity versus temperature are then performed on the crystals as their length is elastically shrunk by the vice—*cf.* the schematic diagram in Figure 4.5(b). Note that the aspect ratios of the bars are chosen such that uniaxial pressure along the “long” axis of the bar (under compressive strain) produces expansion (tensile strain) along the two orthogonal directions, according to the Poisson ratios of Sr_2RuO_4 . T_c rises rapidly as the compressive strain ϵ_{xx} is increased away from zero, reaches a maximum of $T_c \approx 3.5$ K at $\epsilon_{xx} \approx -0.6\%$ (representing an enhancement of ≈ 2.3 over the 1.5 K T_c of bulk unstrained Sr_2RuO_4), and then decreases as the strain is increased further. The widths of the superconducting transitions versus temperature exhibit a non-monotonic dependence on strain as well, which

mostly result from residual strain inhomogeneities in the experimental setup; the non-monotonic behavior then follows from the non-monotonic slope of the T_c versus strain curve evaluated at each strain.

Subsequent work has conclusively demonstrated that this maximum in T_c is associated with traversing a Van Hove singularity in the electronic structure. Further attention will be given to the interpretation of this point in later sections. Several other features of these data that provide important clues into the order parameter and mechanism of the superconductivity in Sr_2RuO_4 are summarized below:

- T_c increases under compressive and tensile strain (*i.e.*, negative and positive ϵ_{xx}), but there is no apparent cusp in T_c around the point of zero strain. It was originally suggested that extrinsic strain inhomogeneities could be rounding off and thereby obscuring a cusp in the intrinsic $T_c(\epsilon_{xx})$ behavior; however, more local micron-scale measurements of T_c by scanning SQUID have not measured such a cusp, either [172]. Additionally, specific heat measurements conducted under uniaxial pressure have not measured any signatures of the superconducting transition splitting into two separate transitions as the in-plane rectangularity of the crystal structure is increased [173]. Taken together, these observations are strong evidence against any multi-component chiral order parameter having x - and y -oriented components that are only degenerate at the point of zero strain (*i.e.*, when the structure is truly tetragonal).
- The response of T_c to uniaxial pressure along [110] is much smaller than the response to pressure along [100] displayed in Figure 4.5. Original measurements reported a change in T_c of ≈ -0.02 K at $\epsilon_{xx} \approx -0.2\%$ of [110]-oriented strain [67], about 20 times smaller in magnitude than the increase in T_c over the same range for [100]-oriented strain. [110]- and $[1\bar{1}0]$ -oriented compressive/tensile strains also break the C_4 rotational symmetry of the parent crystal structure, but this mode of strain alters

the Ru-Ru next-nearest-neighbor distances rather than the Ru-Ru nearest-neighbor distances.

- The upper critical magnetic fields applied along the c -axis, $H_{c2||c}$, increase more rapidly than T_c^2 as the peak in T_c is approached. Within a BCS-like picture of superconductivity, dimensional analysis shows that if the energy scale of superconductivity is uniformly raised by a factor of X , then any orbitally limited upper critical field will increase by a factor of X^2 . Therefore boosting T_c by a factor of 2.3 in going from zero strain to the peak in T_c would be expected to boost $H_{c2||c}$ by a factor of $2.3^2 = 5.3$; in reality, $H_{c2||c}$ at the peak in T_c is about a factor of 20 larger than its value at ambient conditions [171]. This *superquadratic* enhancement of $H_{c2||c}$ as T_c increases is strong evidence for a non-trivial change in the normal-state electronic structure as the Van Hove singularity is approached.

4.2.2 Strain effects on the normal-state electronic structure

In addition to the strain-dependent behavior of the superconducting upper critical fields, several other probes have shown that the peak in T_c coincides with traversing a Van Hove singularity in the normal-state electronic structure. Strain-dependent electrical transport measurements performed simultaneously with the AC susceptibility measurements shown in Figure 4.5 exhibit a maximum in the low-temperature normal-state resistivity ρ at the maximum in T_c [170]; this is naturally interpreted as ρ tracking the density of carriers near E_F , which is maximized as the Van Hove point(s) cross E_F . Furthermore, the temperature scale T_{FL} below which ρ shows canonical Fermi liquid-like scaling behavior ($\rho = \rho_0 + AT^2$) is *minimized* as the Van Hove point(s) cross E_F [170]. Finally, ARPES measurements conducted under uniaxial pressure are able to directly visualize how the γ -band Fermi surface transforms from being electron-like to hole-like as the Lifshitz transition

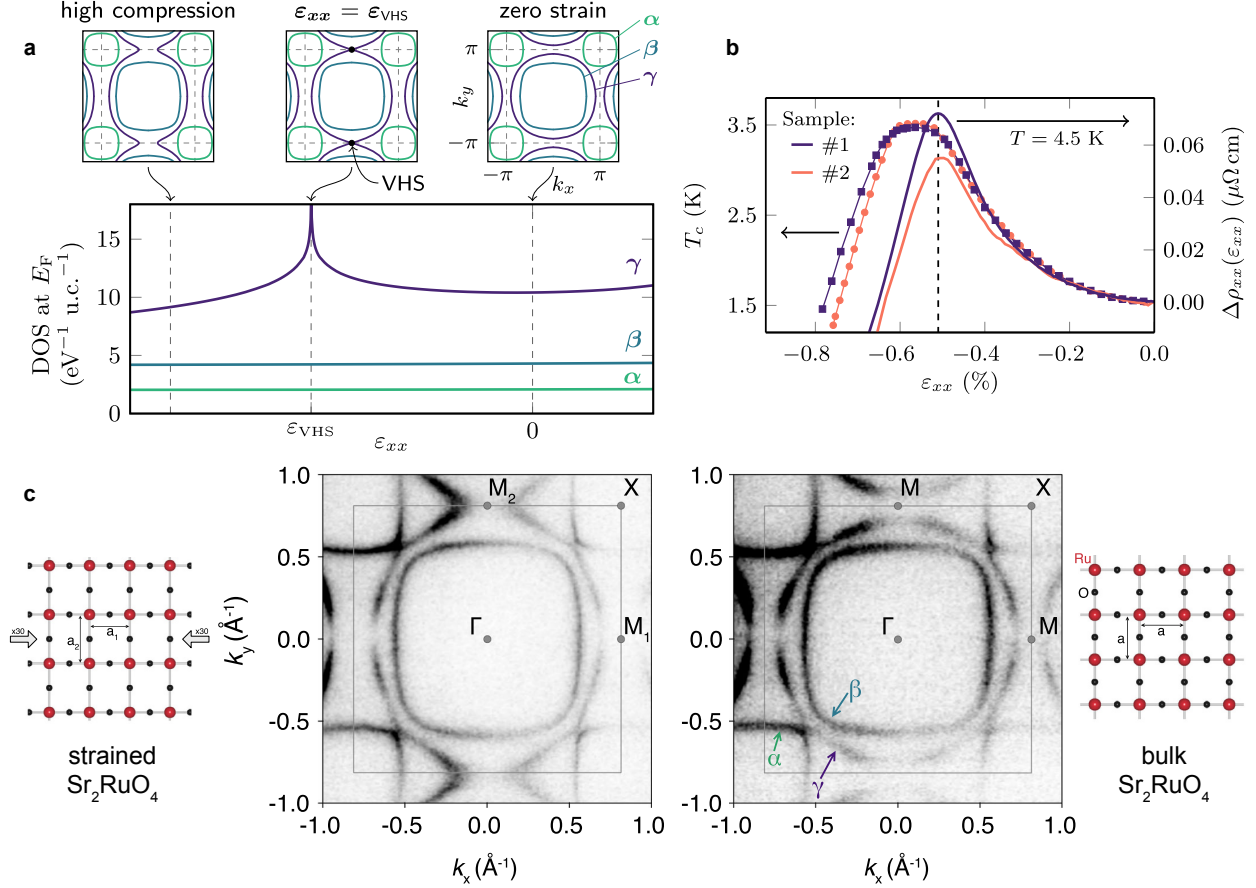


Figure 4.6: (a) Tight-binding model of near- E_F electronics structure for Sr_2RuO_4 subject to variable amounts of [100]-oriented uniaxial pressure. At some critical value of compression along the a axis, $\epsilon_{xx} = \epsilon_{VHS}$, the accompanying expansion along the b axis causes a Lifshitz transition in the topology of the γ band. Tuning this Van Hove singularity in the electronic structure towards the Fermi level enhances the density of states (DOS) at E_F . (b) The superconducting T_c (left axis) and the change in normal-state resistivity at $T = 4.5 \text{ K}$ (right axis) both show peaks around $\epsilon_{xx} = -0.6 - -0.5\%$, suggesting that these values of ϵ_{xx} are sufficient to realize ϵ_{VHS} experimentally. (c) Fermi surfaces in Sr_2RuO_4 under [100]-oriented uniaxial pressure, as measured by ARPES. The right panel is for bulk (unstrained) Sr_2RuO_4 , and the left panel is data for strained Sr_2RuO_4 ($\epsilon_{xx} = -0.7\%$), showing that a Lifshitz transition has indeed been traversed: the γ sheet Fermi surface becomes open along k_y , in excellent agreement with the expectations of (a, b). Figures reproduced from Refs.[170, 174].

occurs, as shown in Figure 4.6 [174]. Neglecting some quantitative discrepancies in the levels of strain required to reach this point in the electronic structure, this change in Fermi surface topology is precisely what first principles band theory calculations expect to occur

when Sr_2RuO_4 is subject to the types of structural distortions that are imposed in these experiments.

4.3 Synthesis and characterization of epitaxially strained Sr_2RuO_4 thin films

The existing body of work on uniaxially pressurized single crystals of Sr_2RuO_4 indicates that tuning the normal-state electronic structure towards a Van Hove singularity significantly enhances the energy scale of superconductivity. Qualitatively, this trend can be rationalized in terms of a weak-coupling (BCS-like) description of the superconductivity where

$$T_c \sim \Delta \sim \omega_B \exp[-1/N(E_F)V] \quad (4.2)$$

Here ω_B is the energy of the pairing boson (likely magnons in Sr_2RuO_4 , instead of phonons as in conventional superconductors), $N(E_F)$ is the density of fermionic states near the Fermi level, and V is the effectively attractive interaction between fermions mediated by the bosonic degrees of freedom. In this interpretation, the proximity to the Van Hove point determines how much $N(E_F)$ increases relative to unstrained Sr_2RuO_4 , which in turn determines how much Δ and T_c increase according to Equation 4.2.

On the other hand, given the enigmatic nature of the superconductivity in Sr_2RuO_4 —with possibly nearly degenerate order parameters and, at a minimum, a highly \mathbf{k} -dependent superconducting gap structure $|\Delta(\mathbf{k})|$ that should be averaged over in a more realistic generalization of Equation 4.2—it is not *a priori* obvious that this Occam’s razor explanation of the strain-induced T_c enhancement is correct in detail. Competing

instabilities such as spin-density wave order may develop as the Lifshitz transition is approached, which could effectively “cut off” an underlying enhancement in the superconducting T_c that is caused more by anisotropic strain than by proximity to the Van Hove point [175]. Even if superconductivity remains the leading instability of the Fermi liquid throughout the structural phase diagram, the inherently multi-band nature of the electronic structure (including inter-orbital interactions driven by Hund’s coupling) also allows for strain-dependent modifications to the effective pairing potential V in Equation 4.2 that may contribute more readily to the T_c enhancement than increases in $N(E_F)$.

To gain further insight into the mechanism(s) of strain-induced changes to T_c , we synthesized Sr_2RuO_4 epitaxial thin films on several different perovskite oxide substrates that impose different modes and magnitudes of biaxial in-plane strains. In the remainder of this chapter we discuss the growth of these films by molecular-beam epitaxy (MBE), characterization of the superconductivity by electrical transport measurements, and characterization of the crystal structures by x-ray diffraction (XRD) and scanning transmission electron microscopy (STEM) measurements. Finally, we provide some interpretation and discussion of these results in terms of strain-induced changes to the normal-state electronic structure. The effects of biaxial strain on the electronic structure of Sr_2RuO_4 are experimentally well-known from MBE + ARPES studies performed by previous members of our research groups [176], which demonstrated that first principles calculations account for strain-dependent trends in the electronic structure quite well; therefore, we employed DFT calculations to model the quasiparticle bandstructures specific to the strain states studied here.

4.3.1 Film growth by molecular-beam epitaxy

Epitaxial thin films of Sr_2RuO_4 were synthesized on various perovskite oxide substrates using the Veeco GEN10 reactive oxide MBE systems described in chapter 2. All films discussed in this dissertation were grown by Hari Nair and Nate Schreiber, a postdoc and a graduate student in the Schlom group. Prior to growth, commercially available substrates of NSAT(001), $\text{NdGaO}_3(110)$, $\text{NdGaO}_3(001)$, LSAT(001), $\text{LaGaO}_3(110)$, and $\text{SrTiO}_3(001)$ were cleaned with organic solvents, etched in acid, and annealed in air to produce starting surfaces with step-terrace morphology, following materials-specific preparation recipes described elsewhere. Elemental ruthenium (supplied using an electron-beam evaporator) and strontium (supplied using an Knudsen effusion cell) were co-deposited in a background oxidant partial pressure of $p_O = 1 \times 10^{-6}$ Torr of distilled ozone ($\approx 80\% \text{O}_3 + 20\% \text{O}_2$) at substrate temperatures of $T_S > 850^\circ \text{C}$, as measured by a optical pyrometer. For the high growth temperatures used in this work, we found that thermometry using a pyrometer gauged the true value of T_S more reliably than using a thermocouple directly attached to the substrate heater.

As described in chapter 2, the primary challenge in the growth of ruthenate thin films with low defect concentrations is the volatility of RuO_x ($x = 2$ or 3) gas species at high temperatures. This problem can be overcome in MBE by flooding the growth front with excess Ru flux—*i.e.*, $f_{\text{Ru}}/f_{\text{Sr}} \gg 1/2$ —and accessing an adsorption-controlled growth window. In this approach one needs to perform electrical and structural measurements on many samples grown under different conditions to determine where the boundaries of this growth window exist in the parameter space of $\{p_O, T_S, f_{\text{Ru}}/f_{\text{Sr}}\}$. A significant portion of this thesis was spent characterizing over 100 Sr_2RuO_4 thin films towards this end; these results are summarized in detail in Ref.[46]. Although the experimental validation of an adsorption-controlled growth window for realizing superconducting Sr_2RuO_4 thin films

represents a significant scientific and technical advance in its own right³, for the remainder of this chapter we eschew further presentation of this point, and take for granted that Sr₂RuO₄ thin films having sufficiently low levels of disorder to exhibit superconductivity can now be reproducibly synthesized.

As discussed in subsection 4.1.1, bulk Sr₂RuO₄ crystallizes in a quasi-two-dimensional tetragonal crystal structure with lattice constants at 295 K of ($a = 3.870 \text{ \AA}$, $c = 12.743 \text{ \AA}$)⁴. In Figure 4.7, we summarize the in-plane lattice mismatches of (001)-oriented Sr₂RuO₄ thin films with the six perovskite substrates on which we have been able to synthesize superconducting samples to date. For our discussion of results obtained for films grown on different substrates, we assume that the primary differences between these samples are caused by the different amounts of coherent substrate-imposed epitaxial strains present in each case—*i.e.*, we do not consider the roles played by other possibly relevant factors such as structural defects, dimensional confinement, cation interdiffusion, charge transfer, or interfacial mode coupling between the substrates and films. Lastly, we note that the film-substrate lattice mismatches are inherently temperature-dependent because of differences in the coefficients of thermal expansion between the metallic films and insulating substrates (and in certain cases, structural phase transitions in the substrate that occur at intermediate temperatures); for internal consistency, we quote the lattice mismatches at 295 K throughout our work, and leave a further exploration of these more subtle temperature-dependent effects to future studies.

³To wit: the growth of superconducting Sr₂RuO₄ thin films by MBE and pulsed laser deposition had been attempted by various members of the Schlom group and other groups around the world for over 20 years [177, 178], but has only recently yielded success [46, 179, 180, 181].

⁴The lattice constants at 295 K reported for bulk single crystals of Sr₂RuO₄ in Refs.[122, 123] are significantly different ($\gtrsim 0.01 \text{ \AA}$). We do not understand the systematic errors that cause these discrepancies, so we just take the arithmetic average of the reported values for a and c .

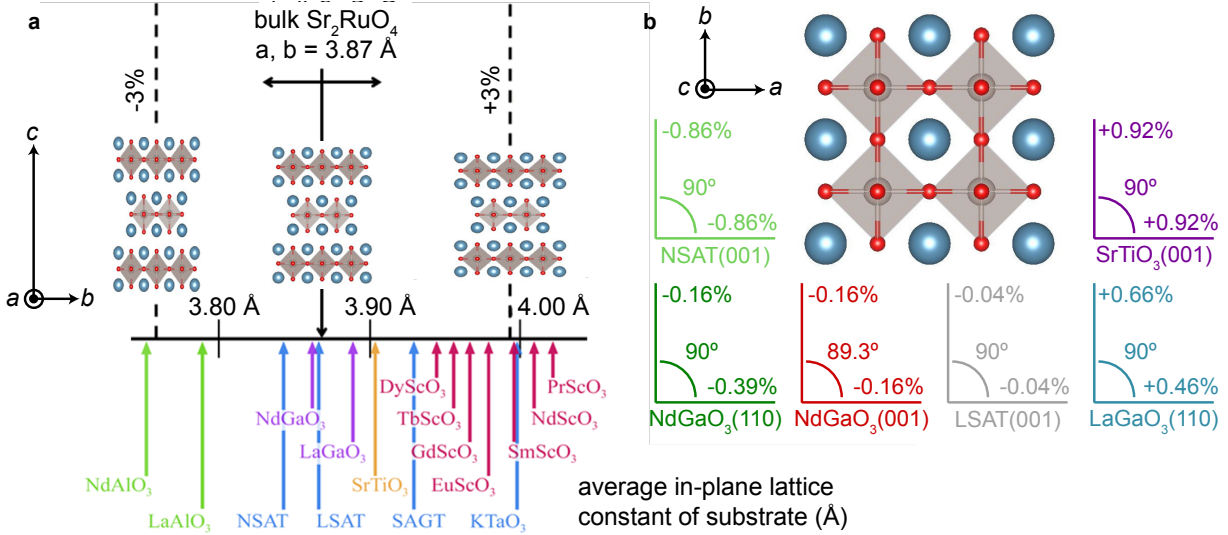


Figure 4.7: (a) Substrates available for growth of perovskite-based oxide thin films, plotted from left to right as a function of increasing pseudocubic lattice constant. Cartoons (not to scale) depict how these substrate-imposed strains couple to the crystal structures of (001)-oriented Sr_2RuO_4 thin films. (b) Schematic diagrams indicating the in-plane lattice mismatches with Sr_2RuO_4 of the six substrates on which we have been able to synthesize superconducting Sr_2RuO_4 thin films to date. To aid in comparison with previous work, we quote the mismatches between the Ru-Ru nearest-neighbor distances in bulk Sr_2RuO_4 and the corresponding distances between transition metal cations in the substrates; negative (positive) signs denote that the Ru-O-Ru bonds are under compression (tension), respectively. The Ru-Ru-Ru angle is also indicated; in the case of films synthesized on (001)-oriented orthorhombic substrates (such as NdGaO_3), this number deviates slightly from the 90° observed in bulk Sr_2RuO_4 and films synthesized on (001)-oriented cubic or tetragonal substrates (NSAT, LSAT, SrTiO_3), as well as on (110)-oriented orthorhombic substrates (NdGaO_3 , LaGaO_3).

4.3.2 DFT calculations

To model the crystal and electronic structures of epitaxially strained Sr_2RuO_4 thin films within the framework of DFT, we proceeded in three steps:

1. Constrained structural relaxations of the out-of-plane lattice parameter c and internal coordinates ($z_{\text{Sr}}, z_{\text{ap.O}}$) were performed using the Vienna Ab Initio Software Package (VASP) [9, 10] to minimize the DFT-computed total energy of Sr_2RuO_4 in

structures compatible with the in-plane biaxial strains imposed by each substrate—*cf.* Figure 4.7. Specifically, the body-centered tetragonal crystal structure of bulk Sr_2RuO_4 (space group #139, $I4/mmm$) is preserved for films grown on (001)-oriented cubic or tetragonal substrates (NSAT, LSAT, SrTiO_3), just with quantitatively different values of the lattice constants $a = b$ and c as compared with bulk. On the other hand, growth on (110)-oriented orthorhombic substrates (NdGaO_3 , LaGaO_3) stabilizes a body-centered orthorhombic structure (space group #71, $Immm$) in which the Ru-eq.O in-plane bond lengths are split into two slightly unequal values $a/2 \neq b/2$. Finally, growth on (001)-oriented orthorhombic substrates (NdGaO_3) stabilizes a face-centered orthorhombic structure (space group #69, $Fmmm$) in which the **a** and **b** principal axes of the conventional unit cell are rotated by 45° relative to the other cases and elongated by a factor of $\approx \sqrt{2}$. The Ru-eq.O in-plane bond lengths are set by $\sqrt{a^2 + b^2}/4$ and thus remain equal despite $a \neq b$; the effect of orthorhombicity here is to make the in-plane Ru-Ru-Ru angles *not* equal to 90° . Forces were converged in all structural relaxations to $< 1 \text{ meV}/\text{\AA}$. The numerical values of lattice constants and internal coordinates used as inputs to (or obtained as outputs from) these structural relaxations are summarized in Table 4.1.

2. Self-consistent field (SCF) DFT calculations were performed using the Quantum ESPRESSO software package [6] using fully relativistic ultrasoft pseudopotentials for Sr, Ru, and O [182]. Spin-orbit coupling (SOC) was included in the SCF cycles and in all subsequent calculations of band energies and other quantities for the converged charge density thus obtained. The inclusion of SOC in DFT calculations for Sr_2RuO_4 and related $4d$ compounds, such as Sr_2RhO_4 , significantly improves the agreement of the computed Fermi surfaces with experimental photoemission data; this has been appreciated in the literature as far back as Ref.[183], and nicely validated in the more recent ARPES and DFT+DMFT studies of Refs.[140, 184, 185]. Although SOC can be incorporated into SCF calculations performed with VASP, the

VASP to Wannier90 interface is not compatible at present with DFT results that include SOC—this is why we switched from using VASP for structural relaxations to using Quantum ESPRESSO for SCF calculations.

3. After obtaining self-consistent Kohn-Sham eigenstates via DFT, we used the pw2wannier and Wannier90 codes [186] to construct six maximally localized Wannier functions spanning the manifold of eigenstates surrounding E_F . We referenced the trial orbitals employed in the Wannierisation routine to three t_{2g} -like states centered on the Ru sites ($6 = 3 \times 2$, accounting for spin degeneracy). The more computationally efficient Wannier basis was used to calculate quantities that required very dense \mathbf{k} meshes to be properly converged, such as the the Fermi surfaces in Figure 4.8 and the near- E_F density of states traces in Figure 4.9 ($101 \times 101 \times 101$ \mathbf{k} -meshes).

For both structural relaxations and SCF calculations, Perdew, Burke and Ernzerhof’s parametrization of the generalized gradient approximation (GGA) was employed as the exchange-correlation functional [187], and Brillouin zone integrations were carried out on an $11 \times 11 \times 11$ \mathbf{k} -mesh. We represented the Kohn-Sham wavefunctions in a basis set of plane waves extending up to a kinetic energy cutoff of 65 Ry in SCF cycles (44 Ry in structural relaxations), and used a cutoff of 280 Ry in SCF cycles for representing the charge density (176 Ry in structural relaxations). We confirmed that crystal and electronic structures calculated within the local density approximation (LDA) exhibit the same strain-dependent *trends* as the results of GGA calculations—albeit with quantitatively wider bandwidths (since LDA favors crystal structures having reduced unit cell volumes), and to a much lesser extent, slightly different band fillings than the GGA results.

All of the crystal structures employed in the calculations described above are referenced to a “bulk Sr_2RuO_4 - DFT” crystal structure that we obtained by DFT structural relaxations of all lattice constants and internal coordinates for Sr_2RuO_4 within space

group #139. The actual lattice parameters and bond lengths for this structure that minimizes the DFT-computed total energy overestimate the experimentally measured values for bulk single crystals of Sr_2RuO_4 (“bulk Sr_2RuO_4 - expt.”) by $\approx 1\%$, due to well-established deficiencies of the GGA—*cf.* the first two rows of Table 4.1. With the former as the bulk reference structure, we simulated biaxial in-plane strains to different substrates by scaling these theoretical lattice constants of Sr_2RuO_4 by amounts appropriate to the experimentally measured lattice mismatches quoted in Figure 4.7. For example, to simulate the $(-0.39\%, -0.16\%)$ strains along a and b corresponding to Sr_2RuO_4 films grown on $\text{NdGaO}_3(110)$, we held a and b fixed in the DFT structural relaxations at $a = (1 - 0.0039) \times a_{\text{bulk-DFT}}$ and $b = (1 - 0.0016) \times a_{\text{bulk-DFT}}$, respectively.

Name	Space group	a	b	c	z_{Sr}	Ru - apical O bond length(s)	Ru - equatorial O bond length(s)
bulk Sr_2RuO_4 - expt.	#139	3.870	3.870	12.743	0.3532	2.057	1.935
bulk Sr_2RuO_4 - DFT	#139	3.877	3.877	12.913	0.3523	2.095	1.939
$\text{Sr}_2\text{RuO}_4/\text{NSAT}(001)$	#139	3.844	3.844	12.983	0.3518	2.104	1.922
$\text{Sr}_2\text{RuO}_4/\text{NdGaO}_3(110)$	#71	3.862	3.871	12.936	0.3521	2.098	1.931, 1.936
$\text{Sr}_2\text{RuO}_4/\text{NdGaO}_3(001)$	#69	5.440	5.510	12.926	0.3522	2.096	1.936
$\text{Sr}_2\text{RuO}_4/\text{LSAT}(001)$	#139	3.875	3.875	12.916	0.3523	2.095	1.938
$\text{Sr}_2\text{RuO}_4/\text{LaGaO}_3(110)$	#71	3.895	3.903	12.867	0.3525	2.089	1.948, 1.951
$\text{Sr}_2\text{RuO}_4/\text{SrTiO}_3(001)$	#139	3.913	3.913	12.838	0.3528	2.086	1.956

Table 4.1: Crystal structures used in DFT simulations of Sr_2RuO_4 . All units of length are given in Å. The fractional coordinate z_{Sr} is given in units of the c -axis lattice constant.

Figure 4.8 shows the DFT-computed Fermi surfaces for the six epitaxially strained variants of Sr_2RuO_4 studied in this work. At the Brillouin zone scale, the differences in Fermiology are quite subtle: all of the strain states display the three-band $\{\alpha, \beta, \gamma\}$ Fermi surfaces characteristic of bulk Sr_2RuO_4 (*cf.* Figure 4.3), with typical shifts in the Fermi wavevectors of $\delta k_F \lesssim 0.01\pi/a$. In particular, none of the Fermi surfaces have undergone a Lifshitz transition that changes its topology, which gives us confidence that the normal-state electronic structure can be considered to be in a “linear response” type of regime for all of the strain states studied in this work. These results are fully consistent with

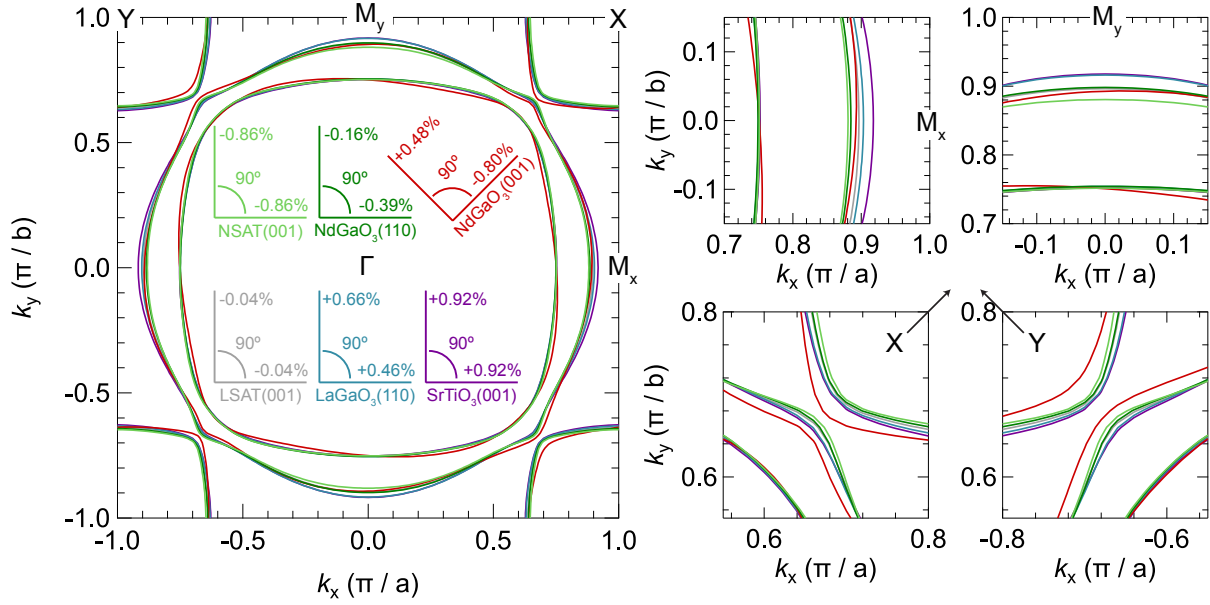


Figure 4.8: Left: DFT-computed Fermi surfaces in the $k_z = 0$ plane for Sr_2RuO_4 thin films subject to different amounts of epitaxial strain. Very similar results are obtained in the $k_z = 2\pi/c$ plane, consistent with the quasi-two-dimensional electronic structure measured experimentally—*cf.* Figure 4.3. Right: zoomed-in versions of the plot on the left, highlighting how the Fermi wavevectors in different regions of \mathbf{k} -space evolve with strain.

experimental ARPES data reported for the most heavily strained sample shown here, $\text{Sr}_2\text{RuO}_4/\text{SrTiO}_3(001)$, which showed that +0.92% biaxial tension along a and b is not sufficient to pin the Van Hove points in the electronic structure at (or below) E_F [176].

Figure 4.9 shows the DFT-computed \mathbf{k} -integrated density of states (DOS) on the energy axis for the same six epitaxially strained variants of Sr_2RuO_4 . Clear peaks in the DOS are observed above E_F ; these are the signatures of a Van Hove “singularity” in the electronic structure, which becomes not a true—*i.e.*, not logarithmically divergent—singularity when the full three-dimensional character of the electronic structure is properly accounted for. Note that for films synthesized on (110)-oriented orthorhombic substrates where the Ru-eq.O bond lengths are split into two unequal values, the Van Hove singularity splits into two separate peaks, which are each of slightly diminished intensity to ensure that the total amount of spectral weight is conserved. The absolute val-

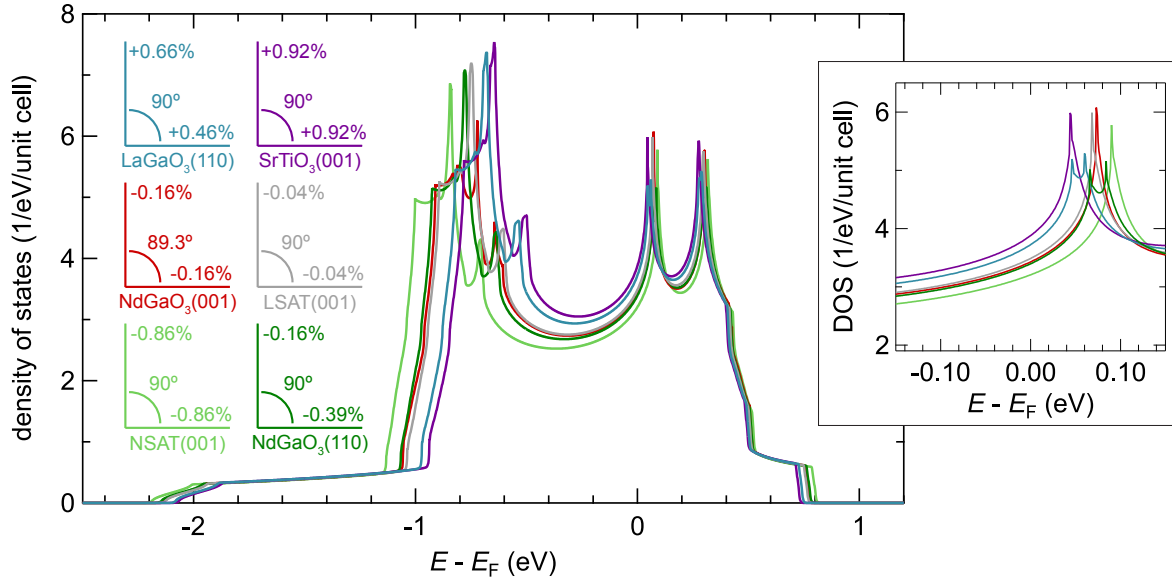


Figure 4.9: DFT-computed density of states for epitaxially strained Sr_2RuO_4 thin films. The total bandwidth scales inversely with the unit cell volume, and $N(E_F)$ generally increases as the total bandwidth shrinks, as expected. The inset shows the proximity of the Van Hove singularity(ies) to E_F .

ues of $|E - E_F|$ where these peaks in the DOS exist should not be interpreted too literally, since moderately strong electron-electron interactions are known to renormalize the bare bandwidths predicted by static mean-field theories such as DFT by factors of $\approx 3 - 4$ in Sr_2RuO_4 . Nonetheless, assuming that the effective masses of different bands evolve smoothly with strain—which is supported by experimental data [176] and also by more realistic calculations that incorporate the effects of dynamical many-body interactions [188]—the strain-dependent *trends* anticipated by DFT for how proximate the Van Hove singularity is to E_F should be a very robust prediction. In good agreement with previous computational studies and with the experimental data described in Figure 4.6 and Ref.[176], we see that the center of mass of the Van Hove peak(s) in the DOS essentially tracks the average in-plane strain, $(\epsilon_{xx} + \epsilon_{yy})/2$, moving closer to E_F under net in-plane tension; on the other hand, the amount of anisotropy in the in-plane strains, $|\epsilon_{xx} - \epsilon_{yy}|$, determines how far apart the Van Hove peak(s) in the DOS are split in energy. Thus there are two conceptually rather different—although not mutually exclusive—mechanisms

whereby the DOS at E_F can be increased relative to bulk Sr_2RuO_4 : either increase the A_{1g} component of strain, $(\epsilon_{xx} + \epsilon_{yy})/2$, or make the rectangular B_{1g} component of strain $|\epsilon_{xx} - \epsilon_{yy}|$ large enough so that one of the Van Hove-derived peaks shifts close enough to E_F to overcome (or further enhance) the changes in the DOS at E_F effected by $(\epsilon_{xx} + \epsilon_{yy})/2$.

4.3.3 Electrical transport measurements

We now turn to our investigations of how these epitaxial strains couple to the superconductivity in Sr_2RuO_4 thin films. Figure 4.10 shows the electrical resistivity versus temperature of a 55 nm thick $\text{Sr}_2\text{RuO}_4/\text{NdGaO}_3(110)$ sample overlaid on bulk single crystal results from Ref.[64]. Despite having a substantially larger residual resistivity than single crystals of Sr_2RuO_4 , the zero-field superconducting T_c of the Sr_2RuO_4 film is clearly higher than bulk (1.8 K *vs.* 1.5 K), and the upper critical field $H_{c2||c}$ is higher than bulk as well (2.0 kOe at $T = 0.45$ K *vs.* 0.75 kOe as $T \rightarrow 0$ K). Note that the quoted single-crystal results are measured on samples in the clean limit, so the measured $\{T_c, H_{c2||c}\}$ are basically saturated, whereas the thin-film sample is likely not in the clean limit, so the measured $\{T_c, H_{c2||c}\}$ should be considered *lower bounds* for what their values would be in the absence of disorder.

These results demonstrate that the energy scale of superconductivity is significantly enhanced in $\text{Sr}_2\text{RuO}_4/\text{NdGaO}_3(110)$ relative to bulk Sr_2RuO_4 . A more detailed accounting of what “significantly enhanced” means in this context is complicated by the following observation: strain (and possibly other factors) are known to enhance T_c in Sr_2RuO_4 , while dilute amounts of disorder are known to rapidly suppress T_c . Therefore, to disentangle the strain-induced enhancement of T_c from the disorder-induced suppression, one must have a quantitative handle on the magnitude of the latter effect. To show how this manifests in actual data, Figure 4.11 illustrates the ambiguities that disorder

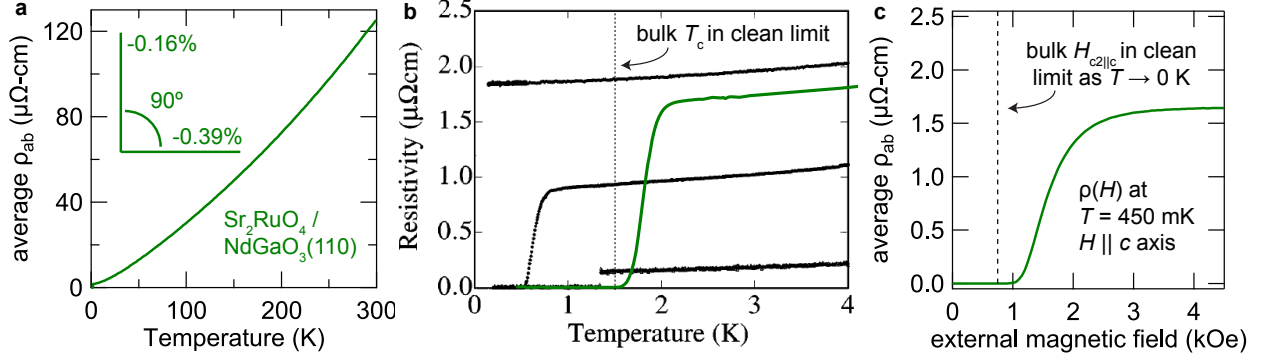


Figure 4.10: (a) Zero-field electrical resistivity versus temperature of a 55 nm thick film of Sr_2RuO_4 synthesized on a $\text{NdGaO}_3(110)$ substrate. (b) Thin-film transport data from (a) overlaid on results for bulk Sr_2RuO_4 , reproduced from Ref.[64]—*cf.* Figure 4.4. (c) Magnetoresistance data on the same thin-film sample from (a,b) acquired at a fixed temperature $T = 450$ mK. Despite not being in the clean limit, $\text{Sr}_2\text{RuO}_4/\text{NdGaO}_3(110)$ exhibits a significantly enhanced superconducting T_c and $H_{c2||c}$ relative to the bulk results.

effects contribute to any naive evaluation of how T_c depends on different modes of epitaxial strain. The two different $\text{Sr}_2\text{RuO}_4/\text{LSAT}(001)$ thin-film samples are both under minimal amounts of strain that do not create inequivalent Ru-eq.O bond lengths, since LSAT has a cubic crystal structure that is very well lattice matched to Sr_2RuO_4 ($\epsilon_{xx} = \epsilon_{yy} = -0.04\%$ at 295 K); thus, these results should be the most representative of bulk Sr_2RuO_4 among the data we have collected for thin films synthesized on different substrates. By contrast, the two different $\text{Sr}_2\text{RuO}_4/\text{NdGaO}_3(110)$ thin-film samples are both coherently strained to the substrates, placing Sr_2RuO_4 under a modest amount of net in-plane compression ($(\epsilon_{xx} + \epsilon_{yy})/2 = -0.28\%$) that is also somewhat anisotropic ($|\epsilon_{xx} - \epsilon_{yy}| = 0.23\%$). Depending on the disorder levels present in the samples, we either measure $T_c \text{ Sr}_2\text{RuO}_4/\text{NdGaO}_3(110) > T_c \text{ Sr}_2\text{RuO}_4/\text{LSAT}(001)$, as in Figure 4.11(a), or vice versa, as in Figure 4.11(b).

Relative comparisons of the superconducting T_c s between samples in the clean limit are arguably the simplest to interpret, theoretically, but preparing such crystals is highly non-trivial, experimentally—mean free paths $\ell \gtrsim 500$ nm are required, *cf.* Figure 4.4. None of the Sr_2RuO_4 thin films grown by MBE in our research group or by other groups

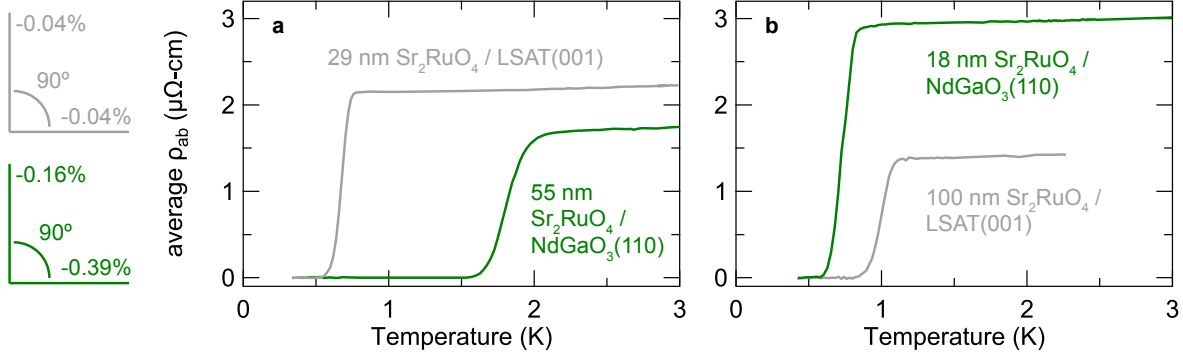


Figure 4.11: (a) Zero-field electrical resistivity versus temperature of Sr_2RuO_4 thin films synthesized on $\text{NdGaO}_3(110)$ and $\text{LSAT}(001)$ substrates. Superconducting transitions are observed at $T_c = 1.80 \pm 0.13$ K for the film on NdGaO_3 and at $T_c = 0.67 \pm 0.05$ K for the film on LSAT . (b) Same as (a), but for different thin-film samples in both cases that have different residual resistivities and hence different superconducting T_c s: $T_c = 0.73 \pm 0.07$ K for $\text{Sr}_2\text{RuO}_4/\text{NdGaO}_3(110)$ and $T_c = 1.00 \pm 0.08$ K for $\text{Sr}_2\text{RuO}_4/\text{LSAT}(001)$. In all cases, T_c is extracted as the temperature at which ρ drops to 50% of its residual normal-state value ρ_0 , and the error bars on the quoted T_c s refer to the temperature interval over which ρ drops from 90% to 10% of ρ_0 .

around the world are close to approaching these levels of purity: the cleanest samples we have been able to synthesize to date have residual resistivities $\rho_0 \approx 1 \mu\Omega\text{-cm}$, corresponding to mean free paths $\ell \approx 100$ nm. In the author’s opinion, this length scale of ℓ likely reflects the presence of some essentially unavoidable anti-phase boundaries that nucleate at step edges on the substrates in the heteroepitaxial growth of $N = 1$ Ruddlesden-Popper films on $N = \infty$ Ruddlesden-Popper substrates—*cf.* subsection 4.1.1 and Figure 4.17. Setting aside for now the precise origin of the defects that contribute to ρ_0 , it is clear that any careful comparison of superconducting T_c s for differently strained variants of Sr_2RuO_4 must attempt to account for the disorder dependence of T_c .

Figure 4.12 displays our efforts towards this goal at the time of writing this dissertation. We performed $R(T)$ measurements on over 40 Sr_2RuO_4 thin film samples synthesized on different substrates (indicated by different colored markers) using a ^3He refrigerator with a base temperature of 350 – 400 mK (indicated by horizontal dashed lines). Following Ref.[64], we plot the superconducting T_c s for these samples as a function of

the inverse residual resistance ratio, $R(4\text{ K})/R(300\text{ K})$. Assuming that the measured resistances are directly proportional to the resistivities and that the resistivities of all samples at 300 K are similar, this is essentially equivalent to a graph of T_c versus ρ_0 ⁵. Samples with T_c s less than the base temperature of our refrigerator are marked as having $T_c = 0\text{ K}$; although this is likely accurate for certain samples, it would of course be desirable to extend measurements to lower temperatures in the future. At the other extreme, for reference we also delineate the superconducting T_c of bulk Sr_2RuO_4 in the clean limit by a horizontal dashed line at 1.5 K.

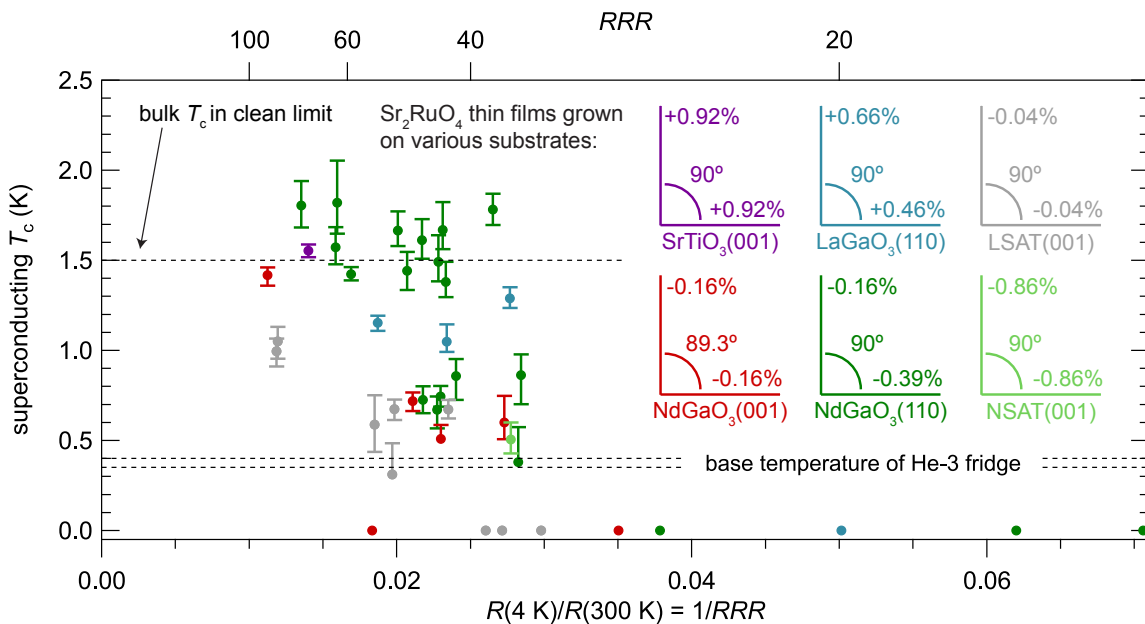


Figure 4.12: Superconducting T_c versus $1/RRR \equiv R(4\text{ K})/R(300\text{ K})$ for many Sr_2RuO_4 thin-film samples synthesized on different substrates. Error bars on the extracted T_c s have the same meaning as in Figure 4.11.

The purpose of Figure 4.12 is to present an unbiased survey of all data we have collected to date, and to guide the planning and interpretation of future experiments that will more clearly elucidate the “intrinsic” strain-dependent changes to T_c that are buried in this data. Strain states where we have synthesized multiple superconducting samples generally show the expected trend of increasing T_c with decreasing ρ_0 , albeit with signifi-

⁵The benefit of taking a ratio between two experimentally measured quantities in $R(4\text{ K})/R(300\text{ K})$ is that some quantitative uncertainties in the factors that convert $R \rightarrow \rho$ for a given contact geometry cancel out.

cant amounts of scatter. This scatter is not altogether surprising, given that the synthesis of superconducting Sr_2RuO_4 films by MBE is a rather immature field (only ≈ 2 years old), and multiple technical aspects about how the films are grown have been continually changed (in most cases, improved!) during this time period; we emphasize that Figure 4.12 does *not* attempt to control for these “historical” changes.

To give the reader a sense of some of these historical changes, in Figure 4.13 we show XRD acquired along the specular crystal truncation rod (CTR) and zero-field $R(T)$ data for seven $\text{Sr}_2\text{RuO}_4/\text{NdGaO}_3(110)$ samples of different film thicknesses. The samples shown in panels (a) and (b) were grown in 2017 using NdGaO_3 substrates that were backside coated with titanium and platinum (Ti + Pt) metal layers in the “usual” fashion; on the other hand, the samples shown in panels (c) and (d) were grown in 2018 using NdGaO_3 substrates that were backside coated with a thick (> 100 nm) amorphous layer of SrRuO_3 in addition to Ti + Pt. The addition of SrRuO_3 allows the heat radiated by the MBE sample heater to be more efficiently absorbed by the substrates, which enables the same (or higher) growth temperatures to be achieved at lower heater powers; this method also allows for more stable control of the growth temperature, which is crucial to remain within the adsorption-controlled windows for Sr_2RuO_4 thin-film growth outlined in chapter 2. Comparing the XRD data in Figure 4.13(a, c), the newer generation of films grown on substrates backside-coated with SrRuO_3 exhibit noticeably higher structural quality; perhaps unsurprisingly, these newer films also exhibit systematically higher RRRs and higher superconducting T_c s, as shown in Figure 4.13(b, d).

Finally, for completeness we note that the transport data shown in Figure 4.13 also display a clear correlation between T_c and the film thickness, as indicated by the gray arrows, despite similar RRR values across samples within the individual data sets. We do not claim to fully understand this empirical observation at the time of writing this dissertation, but we believe there are several facts that suggest this trend is mainly extrinsic in

origin, rather than implying anything especially fundamental about the symmetry of the superconducting order parameter in dimensionally confined variants of Sr_2RuO_4 [189]. The superconducting coherence length of Sr_2RuO_4 is $\xi_c \approx 3$ nm along the crystallographic c -axis [152]—*i.e.*, along the direction that points out of the plane of these thin films—while the total film thicknesses t of all samples shown here are around one order of magnitude larger than ξ_c . Therefore, superconducting fluctuation effects becoming more pronounced in reduced dimensions and thereby intrinsically reducing T_c in films with smaller t could only be relevant here if there are sizable discrepancies between t and the effective superconducting layer thicknesses. Future measurements of the superconducting critical fields versus the direction of the externally applied magnetic field relative to the surface normal may help to shed light on this possibility, following similar measurements described in Ref.[190]. If the superconducting layer thicknesses do turn out to be much less than t , it would then beg the question: what causes the “dead layers”? Given that the thickness dependence of T_c is considerably less pronounced in more recent Sr_2RuO_4 thin films that are objectively higher quality samples by all structural and electrical figures of merit, it seems likely that the answer may have more to do with materials science than with the underlying physics of the superconductivity.

In the following section, with the aid of more extensive structural characterization by XRD and STEM, we consider what the plot in Figure 4.12 suggests about the different types of defects that are natively present in Sr_2RuO_4 thin films, and how these affect superconductivity. Based on this understanding, we utilize a cherry-picked subset of the data shown in Figure 4.12 to evaluate how the T_c s of the different strain states compare when disorder effects are (somewhat) controlled for; in section 4.4, we then proceed to discuss how these strain-dependent changes in T_c may be interpreted in terms of the normal-state electronic structures shown in Figure 4.8 and Figure 4.9. Because subsection 4.3.4 is admittedly heavy on materials science and light on physics content, we invite readers more interested in the latter to skip ahead to section 4.4.

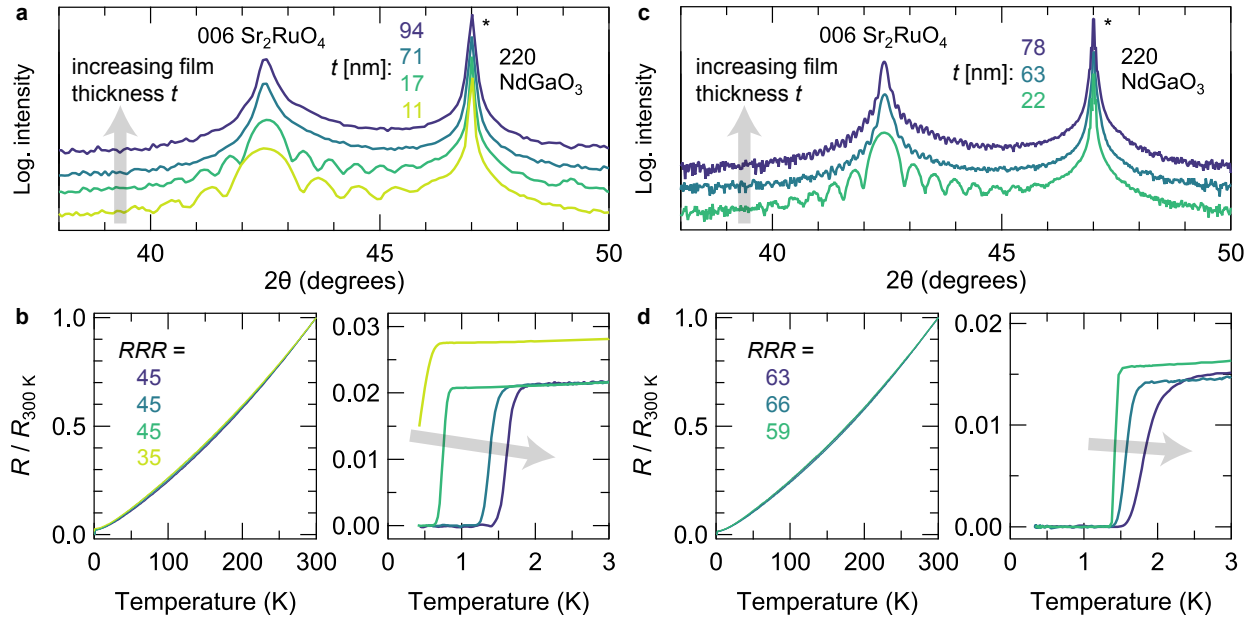


Figure 4.13: (a) XRD data collected with Cu-K α radiation along the specular CTR for four Sr₂RuO₄/NdGaO₃(110) samples of different film thicknesses, synthesized in 2017 using substrates with just Ti + Pt backside coatings. (b) $R(T)$ data for the samples from (a), normalized to the film resistances at 300 K. Despite similar scaling behavior and RRRs over wide temperature scales, the superconducting T_c s monotonically increase by over a factor of 2 with increasing film thickness, as indicated by the gray arrows. (c - d) Same measurements as in (a - b), but for three Sr₂RuO₄/NdGaO₃(110) samples of different film thicknesses, synthesized in 2018 using substrates with Ti + Pt + SrRuO₃ backside coatings. The improved thermal stability at high growth temperatures afforded by the SrRuO₃ results in Sr₂RuO₄ films with significantly enhanced structural and electrical properties. This newer generation of samples still generically shows higher T_c s for thicker films (other factors being nearly equal), but the magnitude of the trend is much reduced compared with the older generation of samples.

4.3.4 XRD and STEM measurements

During our studies of Sr₂RuO₄ thin films, we have observed three qualitatively different types of defects in Sr₂RuO₄ thin films: (1) point-like defects (possibly Ru vacancies), (2) locally higher- N Ruddlesden-Popper intergrowths (*cf.* subsection 4.1.1), and (3) anti-phase boundaries between regions of otherwise pure Sr₂RuO₄ (these are often nucleated at step edges on the substrate). All of these defects contribute to ρ_0 , but empirically speaking (1)

and (3) degrade the superconducting properties much more readily than (2); therefore, comparing samples with different concentrations of (1), (2), and (3) is a major source of scatter in Figure 4.12.

To illustrate how these defects appear to different probes and how they couple to the superconductivity, we focus on structural and electrical characterization measurements for a few specific thin-film samples of Sr_2RuO_4 grown on $\text{NdGaO}_3(110)$ substrates. It should be noted that type (1) and type (2) defects are not overly dependent on the substrate; rather, the relative concentrations of (1) and (2) depend much more sensitively on the exact growth conditions—*viz.*, temperature, oxidant partial pressure, and Ru flux—used to synthesize each sample, and the proliferation of one type of defect often comes at the expense of the other. On the other hand, the density of type (3) defects can be limited to the $\gtrsim 100$ nm scale by employing substrates with similarly low miscut angles.

Figure 4.14 shows data for a 36 nm thick Sr_2RuO_4 film that presumably contains a non-negligible density of point defects⁶. The structural data for this sample are extremely clean: STEM measurements give no evidence of extended defects over wide fields of view ($\gg 10$ nm), and XRD data acquired along the specular crystal truncation rod (CTR) can be simulated exceedingly well by a simple slab model consisting of 28 unit cells Sr_2RuO_4 stacked along the out-of-plane direction. In other words, the coherently diffracting film thickness is equal to the total film thickness, indicating that there is a negligible density of stacking faults. Note that the average *c*-axis lattice constant obtained from this fit is $c = 12.771 \pm 0.004 \text{ \AA} = 1.0022 \pm 0.0003 c_{\text{bulk Sr}_2\text{RuO}_4}$, in good agreement with the 0.18% expansion relative to bulk Sr_2RuO_4 expected from DFT structural relaxations for a film subject to

⁶The nature and identity of these point defects remains unknown at the time of writing. Ru vacancies are one natural candidate, given the volatility of RuO_x gas species at the high temperatures used to synthesize the films. This possibility was recently suggested by Raman scattering measurements [191], but vacancies can only exist up to a certain small concentration before they will manifest as a measurable expansion of the average lattice constants [192], which we do not observe. Therefore, it may be true that some other similarly sized ion actually *replaces* Ru and preserves the integrity of the lattice—*e.g.*, Cr, Ni, or Al, which are all present in the Haynes sample holders used for most MBE growths.

the levels of in-plane compressive strains imposed by $\text{NdGaO}_3(110)$; therefore, the point defect concentration must still be “low” in absolute terms ($< 1\%$)—or if greater than this amount, be some type of substitutional defect that preserves the integrity of the lattice. Nonetheless, the residual resistivity from transport measurements is $\rho_0 \approx 8 \mu\Omega\text{-cm}$, corresponding to a mean free path of $\ell \approx 13 \text{ nm}$; since ℓ is significantly smaller than the in-plane superconducting coherence length ξ_{ab} , this film is non-superconducting down to $T < 0.4 \text{ K}$, and likely has $T_c = 0 \text{ K}$.

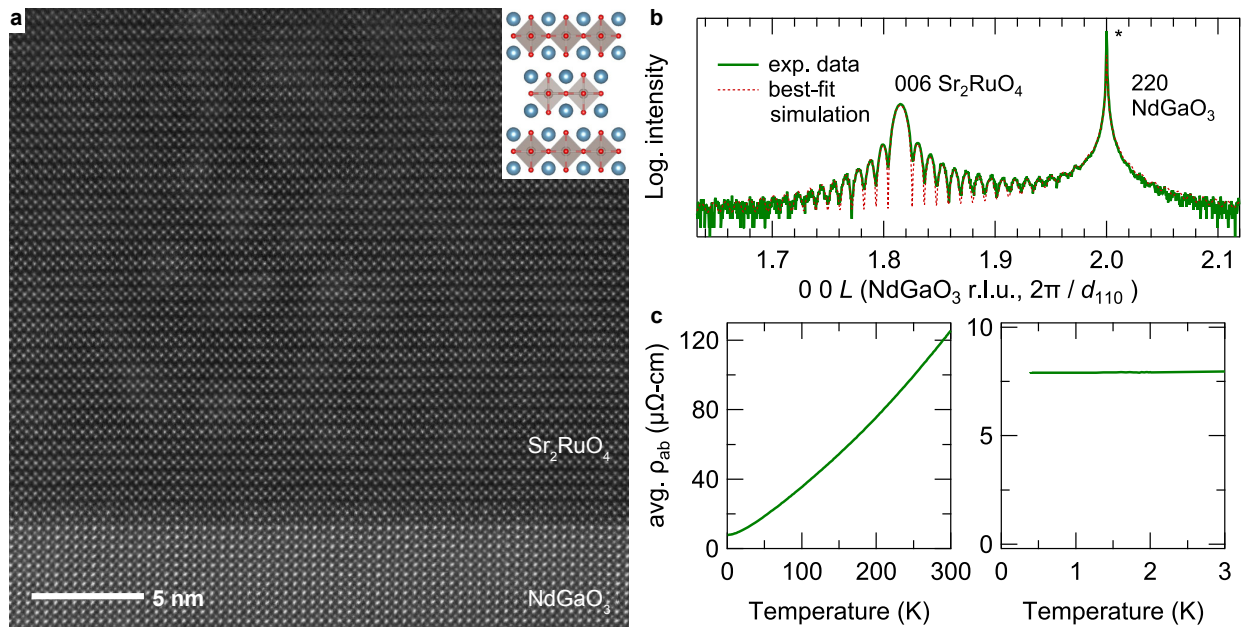


Figure 4.14: (a) Cross-sectional STEM image of a $\text{Sr}_2\text{RuO}_4/\text{NdGaO}_3(110)$ sample, viewed in projection along the $[100]$ direction of Sr_2RuO_4 , courtesy of Berit Goodge and Prof. Lena Kourkoutis. Sr and Ru atoms in the film appear similarly bright, due to their similar atomic numbers. No stacking faults are visible over large fields of view. (b) XRD data collected along the specular CTR with $\text{Cu-K}\alpha$ radiation (green), overlaid with simulated data (dashed red) for a finite-sized slab of pure $\text{Sr}_2\text{RuO}_4/\text{NdGaO}_3(110)$. (c) Electrical resistivity versus temperature for this sample. Despite the excellent structural quality, the residual resistivity remains rather large ($RRR = 16$), and superconductivity is not observed down to 400 mK.

Figure 4.15 shows analogous data for a 73 nm thick Sr_2RuO_4 film containing a multitude of higher- N Ruddlesden-Popper intergrowths. STEM measurements clearly resolve that the structure and local Sr:Ru stoichiometry throughout a sizable fraction of the film is

not 2:1 (with two layers of Sr atoms cladding each Ru layer, and a darker “gap” of lower electron density between each Sr-Ru-Sr triple layer), but rather closer to 1:1 (with alternating Sr and Ru layers, as in perovskite SrRuO_3). Moreover, the XRD data are not well described by scaling up the same slab model used to fit the data in Figure 4.14 to have a total thickness of 73 nm: the coherently diffracting film thickness is much less than this (based on the inverse width of the central 006 film peak), the measured peak location is displaced to slightly larger values of out-of-plane momentum transfer (this would imply a smaller c axis lattice constant, if the material were pure Sr_2RuO_4), and the stacking disorder evidenced in STEM makes this peak asymmetric and washes out any finite-thickness interference fringes that would result from scattering off an object with abrupt bounding interfaces. Despite these extended structural defects existing on length scales less than or comparable to the characteristic length scale of superconductivity ($\xi_{ab} \approx 70$ nm in bulk Sr_2RuO_4), the sample is superconducting at $T_c = 1.49 \pm 0.13$ K. The residual resistivity is also much lower than the sample in Figure 4.14: $\rho_0 \approx 2.6 \mu\Omega\text{-cm}$, which would correspond to a mean free path of $\ell \approx 36$ nm if the material were pure Sr_2RuO_4 .

After synthesizing and characterizing many Sr_2RuO_4 thin films, it seems clear by now from the growth side of the equation that the possible types of defects shown in these two figures are largely mutually exclusive: Ru-poor samples like in Figure 4.14 result when drifting out of the adsorption-controlled growth window on the {high temperature, low Ru flux} side of parameter space, and at the other extreme, Ru-rich samples like in Figure 4.15 result when drifting out of the adsorption-controlled growth window on the {low temperature, high Ru flux} side of parameter space. From the physics side of the equation, the effect of the former type of defect on superconductivity should be much more amenable to a description in terms of Abrikosov-Gor’kov pair-breaking theory than the latter type of defect. Point defects are isotropic scattering centers, presumably uniformly distributed throughout the entirety of the film, and so it is valid to employ the residual resistivity ρ_0 as a proxy for the concentration of these impurities—irrespective

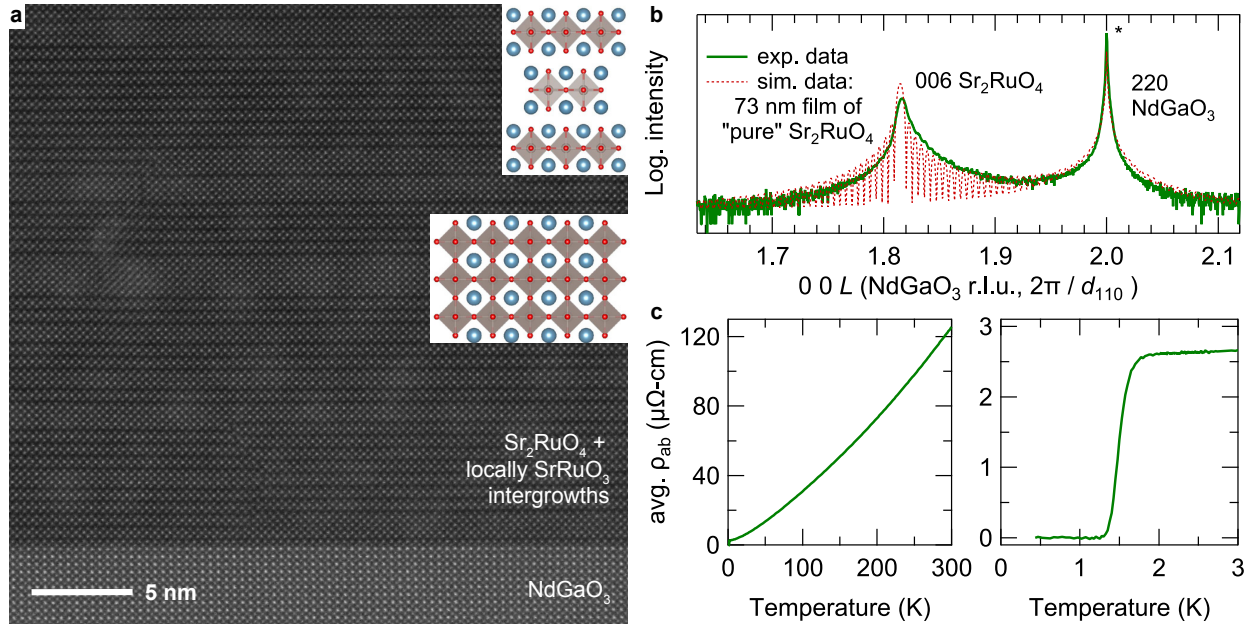


Figure 4.15: Same measurements as in Figure 4.14, but for a heavily non-stoichiometric (nominally Sr_2RuO_4) thin film containing many intergrowths where the stacking of the Sr and Ru layers is locally like SrRuO_3 instead of Sr_2RuO_4 . These stacking faults manifest obviously in (a) cross-sectional STEM images and (b) XRD measurements near the 006 peak of Sr_2RuO_4 , which can not be fit by a slab model where the total film thickness (73 nm) is assumed to be equal to the coherent crystalline thickness of the Sr_2RuO_4 regions. (c) Despite the high density of extended defects, the film has a relatively low residual resistivity ($RRR = 46$), and superconductivity is observed at $T_c = 1.49 \pm 0.13$ K.

of knowing their exact chemical identity. On the other hand, in the case of extended defects, we believe that the global (measured) resistivity is set by more complicated mechanisms. Roughly speaking, there is some network of resistors with microscopically different resistivities—in the present case, interpolating between the values appropriate for Sr_2RuO_4 and SrRuO_3 —and these resistors are sometimes connected in “series” and sometimes connected in “parallel”, depending on the morphology of the defects; the global resistivity is then determined by some coarse-grained effective resistance between nodes of this network. Most importantly, it is not guaranteed that the global ρ is proportional to the microscopic resistivity of the Sr_2RuO_4 regions. The scattering rate of the latter (if it could be isolated) may be significantly smaller than the value implied by the global ρ , since the higher- N members of $(\text{SrO})(\text{SrRuO}_3)_N$ generically have larger values of ρ at elevated tem-

peratures, and at low temperatures, ρ_0 is probably dominated by contact resistances at the interfaces between chemically different regions of the film. At the same time, it seems likely that the Sr_2RuO_4 regions are the relevant parts of this resistor network for determining the superconducting properties, since no members of the $(\text{SrO})(\text{SrRuO}_3)_N$ series with $N \neq 1$ are known to be superconducting. In Figure 4.12, plotting a quantity on the vertical axis (*i.e.*, T_c) that directly reflects the properties of the Sr_2RuO_4 regions in a given film versus a quantity on the horizontal axis (ρ_0) that does not directly reflect the properties of the Sr_2RuO_4 regions will, of course, lead to scatter in any ostensible correlation between these two variables.

While the above discussion has focused on the role of Ruddlesden-Popper intergrowths in skewing straightforward connections between the measured RRRs and superconducting T_c s of Sr_2RuO_4 thin films, we have also observed that such intergrowths affect the XRD patterns and normal-state electrical transport behavior of these films in easily detectable, quantifiable, and sensible ways. Figure 4.16 displays the relevant phenomenology for four different $\text{Sr}_2\text{RuO}_4/\text{NdGaO}_3(110)$ samples, all of nearly the same total film thickness, but containing different densities of intergrowths. In x-ray scattering measurements along the specular CTR shown in Figure 4.16(a), the nearly equal total film thicknesses ($t \approx 17 - 19$ nm) manifest as nearly equal spacings between intensity fringes at low values of q_{\perp} ; by contrast, an increasing volume fraction of intergrowths manifests as a shift of the primary 002 Bragg peaks of Sr_2RuO_4 (004 Bragg peaks) to larger (smaller) values of 2θ , respectively. Note that this shift of different 00L Bragg peaks in opposite “directions” is a hallmark of stacking faults along the out-of-plane direction that disrupt the periodicity of the pure Sr_2RuO_4 lattice—*cf.* the STEM images in Figure 4.15—and is *not* indicative of homogeneous strain relaxation within the Sr_2RuO_4 regions, which would cause all peaks to shift in a monotonic fashion. This effect can be quantified as oscillations in the nominal out-of-plane “lattice constants” extracted from the positions of different Bragg peaks in Nelson-Riley plots [193], and can be simulated by sufficiently

more complex slab models consistent with the true crystal structures of the films [194]. Although the measurements and analysis described here are well-known among certain folks working in the thin-film growth community⁷, these effects appear to be largely undocumented in the literature to the best of the present author's knowledge, except for a few somewhat oblique references to likely the same phenomenon [180, 195].

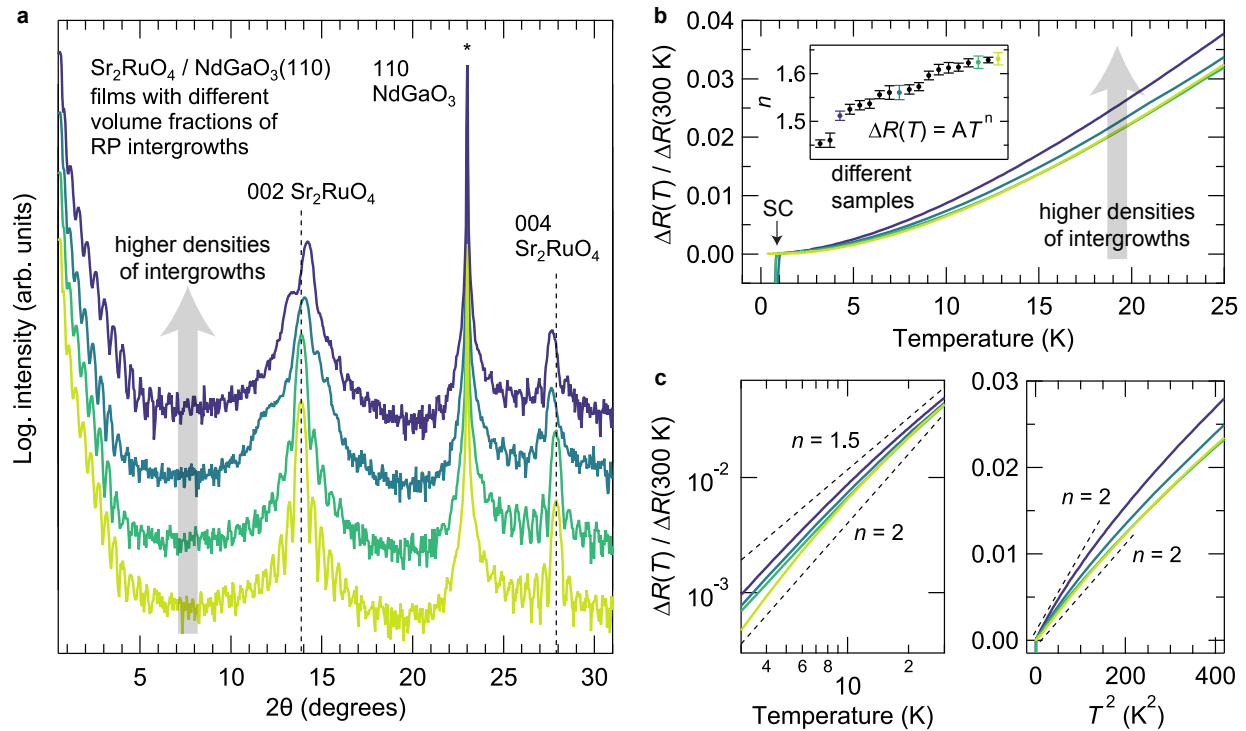


Figure 4.16: (a) XRD data collected with Cu-K α radiation along the specular CTR for four Sr₂RuO₄/NdGaO₃(110) samples of nearly the same total film thicknesses, containing different densities of Ruddlesden-Popper intergrowths. (b) Low-temperature $\Delta R(T) \equiv R(T) - R_0$ data for the four samples from (a), normalized to $\Delta R(300 \text{ K})$. All of the samples except the film showing the smallest density of intergrowths become superconducting below $T_c \approx 0.7 - 0.9 \text{ K}$. The inset shows the exponents n obtained by fitting transport data from 4 K to 25 K for 19 different Sr₂RuO₄/NdGaO₃(110) samples to the power-law expression $R(T) = R_0 + AT^n$. (c) Same data as in (b), plotted in log-log and linear versus T^2 forms. Samples with higher volume fractions of intergrowths and correspondingly smaller values of n cross over to the more gradual $\Delta R(T) \sim T^2$ Fermi-liquid-like scaling of the inelastic component of the scattering rate at progressively lower temperatures T_{FL} .

From the transport perspective, higher densities of Ruddlesden-Popper intergrowths

⁷Matt Barone and Hari Nair, private communication.

manifest as *steeper decreases* in the electrical resistance at low temperatures. In Figure 4.16(b, c), we plot $\Delta R(T) \equiv R(T) - R_0$ (R_0 is the extrapolated residual resistance at 0 K in the absence of superconductivity), normalized to $\Delta R(300 \text{ K})$, for the same four $\text{Sr}_2\text{RuO}_4/\text{NdGaO}_3(110)$ films measured by XRD in Figure 4.16(a). As mentioned in subsection 4.1.3, bulk Sr_2RuO_4 exhibits canonical Fermi-liquid-like scaling of all components of the resistivity tensor—*i.e.*, $R(T) = R_0 + AT^2$ —below $T_{FL} \approx 25 \text{ K}$; higher- N members of the Ruddlesden-Popper series $(\text{SrO})(\text{SrRuO}_3)_N$ all exhibit *lower* values of T_{FL} [63]. Therefore, we fit $R(T)$ data from 4 K to 25 K acquired for 19 different (nominally) Sr_2RuO_4 thin films, all synthesized on $\text{NdGaO}_3(110)$ substrates, to a power law of the form $R(T) = R_0 + AT^n$, allowing R_0 , A , and n to vary. The results of this analysis for the exponents n are summarized in the inset to Figure 4.16(b), with results for the raw data shown elsewhere in this figure indicated by appropriately color-coded markers. As the density of intergrowths increases, n smoothly evolves towards lower values, corresponding to the steeper decreases in $\Delta R(T)$ noted above. As illustrated by the graphs in Figure 4.16(c), we believe that these progressively lower values of n —including the fact that $n \neq 2$ for any of the samples—should be understood as the (average) Fermi liquid crossover scale of these Sr_2RuO_4 thin-film samples ($T_{FL} \approx 4 - 8 \text{ K}$, depending on the density of intergrowths) being suppressed to lower temperatures than bulk Sr_2RuO_4 , rather than as evidence of stabilizing a state that is truly not a Fermi liquid above the superconducting T_c . Although T_{FL} and n have previously been shown to decrease versus uniaxial pressure in bulk Sr_2RuO_4 single crystals upon approaching a Van Hove singularity [170], the largest variations in T_{FL} and n we have observed during our studies of Sr_2RuO_4 thin films are caused primarily by extrinsic factors—such as the dependence on intergrowths illustrated here for samples all subject to the same amount of biaxial epitaxial strains—rather than by any intrinsic strain-induced alterations to the normal-state electronic structure and/or to the spin fluctuation spectrum⁸. The fragile, strongly disorder-dependent nature of T_{FL} has been well

⁸Indeed, if E_F being in close proximity to a Van Hove singularity were the cause of the low values of n and T_{FL} observed in our strained Sr_2RuO_4 thin films, then n and T_{FL} would also be expected to change

documented in many perovskite-based ruthenate compounds [63, 65, 151]; based upon our work, it appears that similar phenomenology is realized even in Sr_2RuO_4 thin films that are electrically “clean” enough to superconduct.

Finally, for completeness we note that when the densities of type (1) and type (2) defects are both small enough to not be limiting ρ , and the temperature is low enough that electron-electron scattering is also not dominating ρ , the effects of type (3) defects appear in electrical transport measurements, as shown schematically in Figure 4.17(a - b). Prior to film growth, the substrates are polished, etched, and annealed to produce starting surfaces with large, atomically flat terraces separated by single perovskite unit cell step heights $h \approx 4 \text{ \AA}$. The average lateral width w of the terraces perpendicular to the step edges is determined by the miscut angle δ of the polishing procedure, according to $\tan(\delta) = h/w$; for typical miscut angles of $\delta \approx 0.05^\circ - 0.10^\circ$, we thus have $w \approx 200 - 400 \text{ nm}$. Because the unit cell of Sr_2RuO_4 along the out-of-plane direction is *incommensurate* with the unit cell step heights of the perovskite substrates, Sr_2RuO_4 crystallites that nucleate on different terraces cannot be connected in a continuous fashion. The exact atomic structure of how the film grows across the step edges is not precisely known; however, on very general grounds we can be sure that the continuity of the RuO_2 planes is interrupted across the step edges. The resulting defects will either scatter the charge carriers in transport measurements, or force the carriers to briefly move along the c axis of the crystal structure in the course of hopping to a crystallite on an adjacent terrace. Since the electrical resistivity of Sr_2RuO_4 is known to be much higher along the out-of-plane direction than along the in-plane directions⁹, both mechanisms cause an extrinsic anisotropy between measurements of the diagonal in-plane components of the resistivity tensor (ρ_a, ρ_b), as we describe in detail below.

rapidly under externally applied magnetic fields that cause meV-scale Zeeman shifts of E_F for electrons with different spin orientations [62, 196]. We have not observed any such effects in magnetoresistance measurements conducted up to 14 Tesla.

⁹Recall from subsection 4.1.3 that $\rho_c > 1000 \times \rho_{ab}$ in Sr_2RuO_4 at low temperatures.

At the atomic (nm) scale, the step edges are aligned with one of the two orthogonal metal-metal nearest-neighbor in-plane directions. On the mesoscopic (μm) and macroscopic (mm) scales relevant for transport measurements, the step edges are meandering, and their average direction can be aligned with essentially any in-plane azimuth depending on how the substrate was polished and prepared. This direction can be easily detected and referenced to the crystallographic axes using XRD or atomic force microscopy (AFM) measurements. For ease of discussion, suppose that the step edges—or equivalently, the longer dimension of the atomically flat terraces—are nearly aligned with the a axis of Sr_2RuO_4 ; *i.e.*, along the orthogonal b axis, the terraces are shorter before a discontinuous unit cell step is encountered. Although the diagonal in-plane components of the resistivity tensor (ρ_a, ρ_b) are guaranteed to be equal by tetragonal crystal symmetry in bulk Sr_2RuO_4 , the enhanced scattering off defects for electron transport perpendicular the step edges, and/or ρ_c becoming admixed in putative measurements of ρ_b , will inevitably lead to an apparent anisotropy $\rho_b > \rho_a$ in experimental data, as illustrated in Figure 4.17(c).¹⁰

While we mention the presence of these type (3) defects that are induced by—or at least, oriented by—step edges on the substrate in the interest of full disclosure, we do not believe that they play a major role in the data shown in Figure 4.12 for two reasons. First, as a means of averaging over this defect-induced transport anisotropy, we performed two complementary four-point resistance versus temperature measurements $R_{\text{vert.}}(T)$ and $R_{\text{horiz.}}(T)$ having the current injection/removal and voltage detection contacts rotated by 90° between measurements. We then numerically solved van der Pauw’s equation [198] to obtain the sheet resistance versus temperature, $R_s(T)$:

$$\exp[-\pi R_{\text{vert.}}(T)/R_s(T)] + \exp[-\pi R_{\text{horiz.}}(T)/R_s(T)] = 1 \quad (4.3)$$

¹⁰The resulting temperature-dependent anisotropy between ρ_a and ρ_b has been interpreted by certain authors in the literature as the hallmark signature of an exotic phase of quantum matter known as an *electron nematic* [197]; the author of this thesis believes it has a much more mundane defect-induced origin in the case of Sr_2RuO_4 thin films.

The RRRs used in Figure 4.12 are calculated as $R_s(300\text{ K})/R_s(4\text{ K})$. Note that in the limit of small to intermediate anisotropies between ρ_a and ρ_b , R_s is essentially the geometric mean of these quantities, times the thickness t of the film—*i.e.*, $R_s = t\sqrt{\rho_a\rho_b}$. Second, all samples shown in Figure 4.12 were synthesized on substrates with similarly low miscut angles $\delta \approx 0.05^\circ - 0.10^\circ$, corresponding to terrace widths $w \approx 200 - 400\text{ nm}$. As stressed in Figure 4.14 and Figure 4.15, in many Sr_2RuO_4 thin-film samples there are defects existing on much smaller length scales than w , which we expect to be more dominant in governing the observed T_c versus ρ_0 behavior.

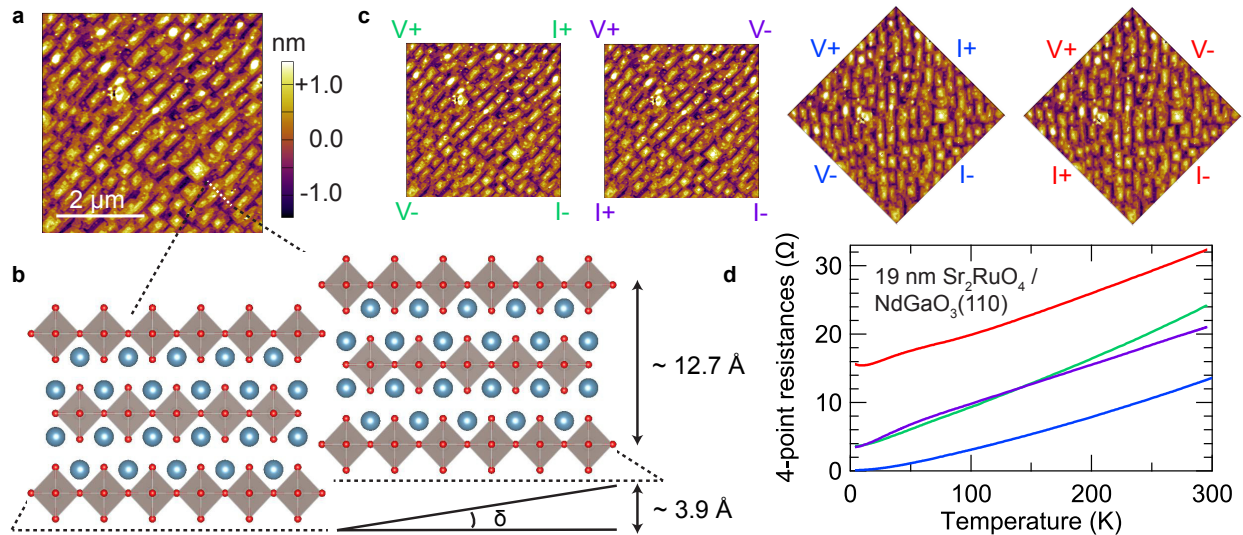


Figure 4.17: (a) Atomic force microscopy image of the morphology of a 19 nm thick $\text{Sr}_2\text{RuO}_4/\text{NdGaO}_3(110)$ sample. (b) Schematic diagram illustrating how the continuity of the RuO_2 planes in a Sr_2RuO_4 film is necessarily disrupted across a step edge on any perovskite substrate, since the c axis lattice constants of film and substrate are incommensurate. (c) Macroscopic electrical transport data for four different van der Pauw contact geometries, having the current injection/removal ($I+$, $I-$) and voltage measurement probes ($V+$, $V-$) oriented differently with respect to the substrate step edge direction measured in (a). Perhaps unsurprisingly, the RRRs for these data sets are very different: 2.1 (red), 6.1 (purple), 6.8 (green), and 151 (blue).

Taken together, these considerations allow us to interpret several features in the T_c versus ρ_0 behavior displayed in Figure 4.12. As the point defect concentration is reduced in

Ru-poor Sr_2RuO_4 thin films, markers move *up and left* on this plot; *i.e.*, T_c responds quite sensitively to decreases in ρ_0 , as expected from the Abrikosov-Gor'kov scaling theory exhibited by bulk single crystals in Figure 4.4. As the volume fraction of Ruddlesden-Popper intergrowths is reduced in Ru-rich Sr_2RuO_4 thin films, markers move *mostly horizontally (to the left) and slightly upward*; *i.e.*, T_c does not respond as sensitively to decreases in ρ_0 , because the decreases in ρ_0 are more reflective of an increasing volume fraction of Sr_2RuO_4 regions in such samples, rather than of a decreased scattering rate in these Sr_2RuO_4 regions. The collection of $\text{Sr}_2\text{RuO}_4/\text{NdGaO}_3(110)$ samples (dark green markers) provide the clearest examples of this behavior, since we have synthesized and measured the largest number of samples for this strain state. Clusters of films exist at $T_c = 1.4 - 1.8$ K and also at $T_c = 0.7 - 0.9$ K that appear to form nearly horizontal “bands” for which T_c does not depend strongly on ρ_0 ; these are samples where the primary differences between samples are the volume fractions of Ruddlesden-Popper intergrowths.

Based on these observed trends, we are left with several possible options moving forward to more conclusively map out the disorder dependence of superconductivity in differently strained Sr_2RuO_4 thin films. These are not mutually exclusive approaches, but for clarity we list and discuss them as separate items:

- **Synthesize many more superconducting samples on each substrate, and discard results for any samples that show an appreciable density of Ruddlesden-Popper intergrowths in XRD and STEM.** The downside of this approach is that the success rate of growing such “Goldilocks” samples that are not overly Ru-rich but also not too Ru-poor—and thus non-superconducting—has historically been quite low. For example, of the 41 samples shown in Figure 4.12, Nelson-Riley analysis of XRD measurements (not shown) indicates that only 18 samples do not contain obvious signatures of such intergrowths. Of these 18 samples, only 11 samples have low enough residual resistivities to show superconductivity. With a success rate of \approx

25%, and assuming we would like to measure around 10 samples per substrate to trace out an Abrikosov-Gor'kov scaling curve of how T_c varies with ρ_0 , we would need to synthesize and characterize around 40 samples *per substrate*. The investment of time and money that would be involved in such efforts seems to quickly get out of hand, as we may have already witnessed for $\text{Sr}_2\text{RuO}_4/\text{NdGaO}_3(110)$.

- **Take one “Goldilocks” sample per substrate, having a natively high T_c and low density of Ruddlesden-Popper intergrowths, and externally introduce additional point-like defects to this film that degrade the superconductivity in a controllable way.** By progressively measuring the decreases in T_c that occur as the disorder level is ramped up, effectively the same sample could be used to trace out an Abrikosov-Gor'kov scaling curve of how T_c varies with ρ_0 . We have not pursued such experiments at the time of writing this thesis, but preliminary discussions with Andy Mackenzie's group at the Max Planck Institute in Dresden suggest that high-energy electron irradiation may be a feasible route to achieve this objective.
- **Employ some other proxy besides ρ_0 to quantify the disorder level inherent to the pure Sr_2RuO_4 regions in superconducting samples that show an appreciable density of Ruddlesden-Popper intergrowths.** One metric that may serve this purpose is the decay rate of quantum oscillation amplitudes, as quantified by the Dingle temperature¹¹. Focusing on the decay of oscillation amplitudes at the characteristic frequencies of quasiparticles orbiting the $\{\alpha, \beta, \gamma\}$ Fermi surfaces of Sr_2RuO_4 should naturally isolate the contributions of the pure Sr_2RuO_4 regions in any given sample, and be largely agnostic to the presence of intergrowths. Indeed, preliminary Shubnikov-de Haas measurements being conducted by Prof. Brad Ramshaw's

¹¹Dingle showed that electron-disorder scattering has phenomenologically the same effect as raising temperature in quantum oscillation experiments: this additional scattering broadens the Landau levels that appear in high magnetic fields, and reduces the amplitude of oscillations observed in resistivity, magnetization, *etc.* The discrepancy between the so-called *Dingle temperature*—extracted from analysis of the oscillation amplitudes—and the measured sample temperature thus measures the strength of electron-disorder scattering.

group on superconducting Sr_2RuO_4 thin films grown by our group suggest mean free paths extracted from the Dingle temperatures in excess of $\ell > 100$ nm, which are significantly higher than the values of ℓ implied by our zero-field measurements of the global ρ_0 . The drawback of this approach is that quantum oscillation experiments do not have a quick turnaround time and often require time at national user facilities specializing in the creation of large magnetic fields; thus, performing these measurements on ≈ 10 samples per substrate is likely not feasible, unless multiple measurements can be performed simultaneously.

4.4 Discussion and Conclusions

Based on the considerations explained in subsection 4.3.4 regarding how different types of defects couple to the superconductivity in Sr_2RuO_4 thin films, we analyzed XRD data for all of the samples shown in Figure 4.12 and discarded transport results for all films showing an appreciable concentration of Ruddlesden-Popper intergrowths. Figure 4.18(a) displays the T_c versus ρ_0 behavior for this smaller subset of samples. Because the highest- RRR (and highest- T_c) Sr_2RuO_4 films grown on $\text{NdGaO}_3(001)$ and $\text{SrTiO}_3(001)$ shown here do contain a discernible volume fraction of intergrowths, we include left-pointing arrows indicating how we believe these strain states would move on the plot if these intergrowths were eliminated¹².

With the perspective offered by the plot in Figure 4.18(a), we then chose one thin-film sample for each strain state for which the disorder-induced suppressions of T_c are likely to be similar. These samples are indicated in Figure 4.18(a) by the gray-shaded ellipse, and zero-field transport data for these samples are shown in Figure 4.18(b).

¹²These arrows are based on our experience with $\text{Sr}_2\text{RuO}_4/\text{NdGaO}_3(110)$ samples, but are not in any way intended to be quantitative.

Note that it is not possible with the current data set to include $\text{Sr}_2\text{RuO}_4/\text{LaGaO}_3(110)$ or $\text{Sr}_2\text{RuO}_4/\text{NSAT}(001)$ in this type of analysis, so we neglect results for these strain states moving forward¹³. Finally, in Figure 4.18(c) we plot the superconducting T_c for this select group of four films versus the DFT-computed DOS near E_F , $N(E_F)$, normalized to the value appropriate for bulk Sr_2RuO_4 .

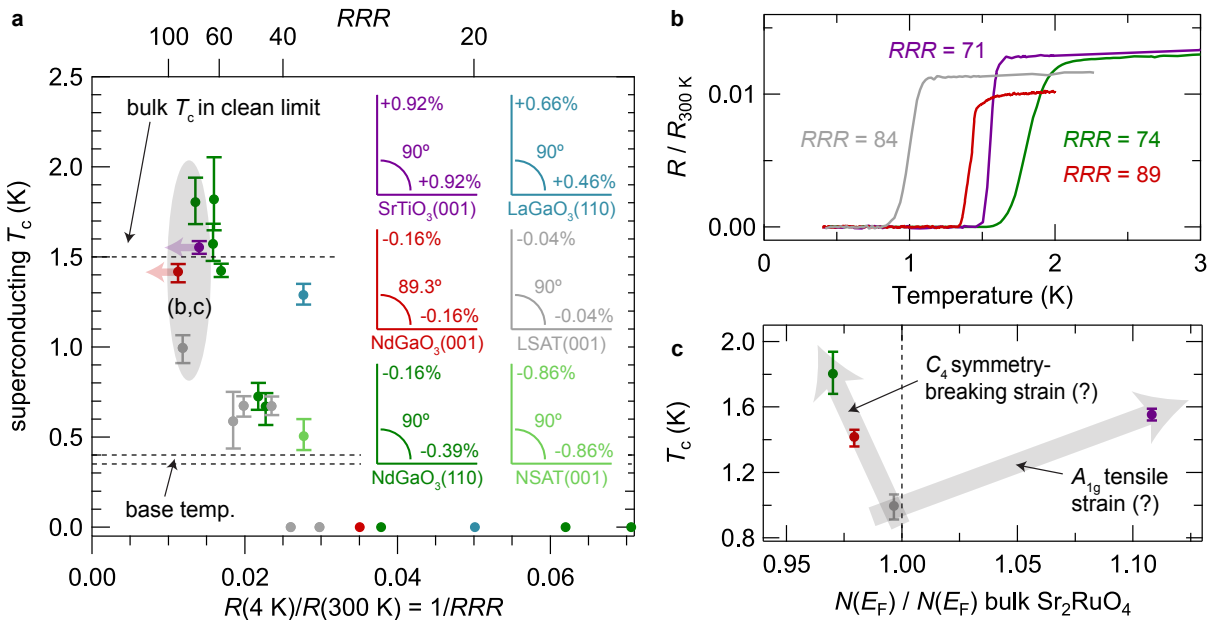


Figure 4.18: (a) Superconducting T_c versus $1/RRR$ for a subset of Sr_2RuO_4 films from Figure 4.12 that do not contain significant densities of Ruddlesden-Popper intergrowths (as quantified by XRD). (b) Low-temperature transport data for four select films that lie in the gray-shaded ellipse in (a). Based on the similar RRR s, we believe that the disorder-induced suppressions of T_c are similar across all of these samples, so that *relative* comparisons between the measured T_c s should primarily reflect strain-induced variations. (c) Superconducting T_c s of the four samples from (b), plotted versus the DFT-computed density of states $N(E_F)$ (normalized to the value appropriate for bulk Sr_2RuO_4). Clearly T_c does *not* merely track $N(E_F)$, as would be expected based on a simple-minded application of Equation 4.2.

These data clearly demonstrate that T_c does *not* merely track $N(E_F)$ in the regime of

¹³The electrical quality of the single superconducting film on NSAT(001) is too different to make a meaningful comparison with the other strain states. On $\text{LaGaO}_3(110)$, the microscopic film quality on the length scales relevant for superconductivity (10 - 100 nm) is likely comparable to the other strain states; however, the macroscopically measured RRR is significantly lower, likely due to enhanced scattering off defects near structural twin boundaries that form in this substrate (on the 10 - 100 μm scale) upon cooling down from growth temperature. Since this complication muddles any direct comparison with films on other substrates, we omit results for $\text{Sr}_2\text{RuO}_4/\text{LaGaO}_3(110)$ from the subsequent discussion.

low strains explored in this work, as would be expected based on a simple-minded application of Equation 4.2. A heuristic interpretation of these data—hence the question marks!—is indicated schematically by the gray arrows Figure 4.18(c): A_{1g} tensile strains that preserve the tetragonal symmetry of Sr_2RuO_4 cause subtle increases in T_c in going from LSAT(001) \rightarrow SrTiO₃(001), despite comparatively large increases in $N(E_F)$; by contrast, strains that break the four-fold rotational symmetry of the crystal structure induce more dramatic increases in T_c , even though $N(E_F)$ slightly *decreases* in going from LSAT(001) \rightarrow NdGaO₃(001) \rightarrow NdGaO₃(110). Since these are early days for superconducting Sr_2RuO_4 thin films, and there remain numerous subtleties and open questions regarding how seriously the experimentally measured T_c s should be interpreted (as this chapter hopefully illustrated), it is probably wise to treat these observations as *suggestive* at the moment rather than *conclusive*. Nonetheless, assuming that these correlations between how T_c responds to different modes of biaxial strain survive further scrutiny in future synthesis and characterization efforts, their explanation certainly warrants further computational studies, and may shed some light on the nature of the enigmatic superconductivity in Sr_2RuO_4 .

CHAPTER 5

STRAIN-STABILIZED SUPERCONDUCTIVITY IN RuO_2

For the remainder of this dissertation, we focus on our discovery, characterization, and current understanding of superconductivity in epitaxial thin films of rutile RuO_2 synthesized on $\text{TiO}_2(110)$ substrates, having transition temperatures up to $T_c \approx 2$ K. Since bulk single crystals of RuO_2 are not known to superconduct at experimentally accessible temperatures ($T_c < 300$ mK), this observation naturally begs the question: what variables and mechanisms conspire to significantly enhance the energy scale of superconductivity in $\text{RuO}_2/\text{TiO}_2(110)$? In section 5.2, we utilize a combination of thin film synthesis by molecular-beam epitaxy (MBE) and extensive electrical and structural characterization of these RuO_2 thin films by multiple techniques—including electrical transport, x-ray diffraction, and scanning transmission electron microscopy—to demonstrate that $\text{RuO}_2/\text{TiO}_2(110)$ is the first reported example of a *strain-stabilized superconductor*, in which substrate-imposed epitaxial strains boost the instability of a Fermi liquid towards superconductivity by (at least) an order of magnitude relative to bulk RuO_2 . In chapter 6, we present experimental measurements of the electronic structure of RuO_2 thin films by *in situ* angle resolved photoemission spectroscopy (ARPES), supported by density functional theory (DFT) calculations, to provide an interpretation of this phenomenon in terms of strain-induced changes to the normal-state electronic structure¹. Although we emphasize the generality of this approach and believe it may open the door to strain engineering of superconductivity in a wide variety of other multi-orbital systems, in section 5.1 we first introduce some specific features of rutile materials and RuO_2 that were known from prior work, highlighting properties that we believe are most relevant to understanding

¹Some of the results presented in these chapters have been submitted in a manuscript to *Nature Physics*.

the effective low-energy physics in this system.

5.1 Introduction to the rutile family of materials

RuO_2 is one of many binary transition metal oxides MO_2 that crystallize in the rutile structure (or distorted variants of this structure), which is drawn in Figure 5.1. Similar to the perovskite-based structures discussed in previous chapters, the rutile structure is known to host a wide range of interesting electronic and magnetic properties, including metal-insulator transitions (VO_2 , NbO_2), half-metallic ferromagnetism (CrO_2), and large spin-Hall conductivities (IrO_2)². Furthermore, numerous such compounds are extensively employed in photocatalytic applications (especially TiO_2), so rutiles are among the most practically useful transition metal oxides. While it is well beyond the scope of this thesis to explain how all of these properties and functionalities derive from the fundamental building blocks—namely, the structure and coordination of the MO_6 octahedral network, and how many carriers occupy the d -electron states near the Fermi level derived from this network [199, 200]—here we provide a brief overview of the structural, electronic, and magnetic degrees of freedom to put what is known about bulk RuO_2 (and what may be possible to realize in appropriately strained RuO_2) in proper context.

5.1.1 Structural degrees of freedom

The parent structure of the rutile family of materials, without any symmetry lowering structural distortions, belongs to space group #136, $P4_2/mnm$. The primitive unit cell in this case is tetragonal ($a = b \neq c$) and contains two MO_2 formula units: two metal cations sit on the vertices of a body-centered tetragonal lattice at fractional coordinates $(0, 0, 0)$

²Perhaps notably, this list *does not include superconductivity*—although as we will show later, superconductivity can be realized in artificially engineered rutile structures.

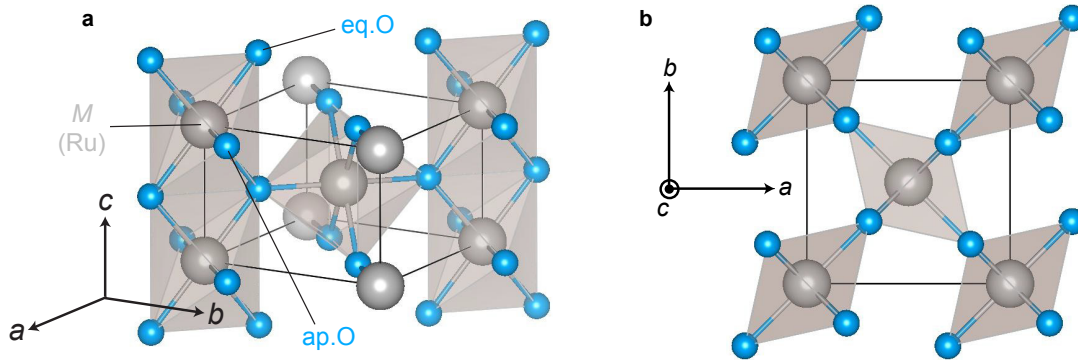


Figure 5.1: Drawings of the parent rutile crystal structure. Gray spheres represent transition metal atoms M (such as Ru), and the blue spheres represent O atoms. The structure is viewed from different crystallographic perspectives in the two panels (as indicated by the $\{a, b, c\}$ triads) to emphasize the mixed (a) edge-sharing and (b) corner-sharing nature of the MO_6 octahedral network.

and $(1/2, 1/2, 1/2)$, and are surrounded by four independent oxygen anions at $\pm(u, u, 0)$ and $\pm(1/2 - u, 1/2 + u, 1/2)$, where u is a freely adjustable parameter. Translations of this primitive unit cell by integer multiples of $\{\mathbf{a}, \mathbf{b}, \mathbf{c}\}$ dictate that each metal cation is locally coordinated by an octahedral cage of six approximately equidistant oxygens. On longer length scales, the octahedra form a connected network in all three directions with mixed edge-sharing and corner-sharing character, as illustrated in Figure 5.1.

The lattice constants (a, c) and internal parameter u are the three basic structural degrees of freedom that parametrize the rutile structure. The interplay of u with the c/a ratio determines how close the octahedra are to a regular octahedron. In general the octahedra are not regular: there are two inequivalent M-O bond lengths, and for a given oxygen anion, the M-O-M bonds are split to 2 + 1 inequivalent angles, not all equal to 120° . By analogy with perovskite-based structures, it is common to further differentiate the oxygen anions into two apical oxygens ap.O and four equatorial oxygens eq.O. The apical axis of the octahedron centered at $(0, 0, 0)$ points along $[110]$, and rotates to being directed along $[\bar{1}10]$ for the octahedron centered at $(1/2, 1/2, 1/2)$. The equatorial oxygens are located in planes perpendicular to these apical axes (*i.e.*, the ap.O-M-eq.O bond angles

are 90°); however, note that within a given equatorial plane, the eq.O-M-eq.O bond angles are generally not equal to 90° .

Besides these local deviations from regular octahedra, another important distinction that differentiates rutile structures from perovskite-based structures is the mixed edge-sharing and corner-sharing nature of the octahedral network—recall that in perovskite-based structures, the octahedra are purely corner-sharing in all three directions. This distinction has two important consequences. First, the higher connectivity of the rutile structure precludes the existence of any normal modes of vibration involving purely octahedral rotations: to rotate the octahedra in a coordinated fashion, the M-O bond lengths must distort as well, and/or the M cations must be displaced. Second, the edge-sharing octahedra create much shorter M-M distances, typically closer to $\approx 3 \text{ \AA}$ instead of $\approx 4 \text{ \AA}$ characteristic of perovskites. This allows for direct M-M interactions that can lead to the formation of covalent bonds between the cations, instead of indirect M-M interactions solely mediated by electrons first hopping onto an adjacent oxygen site in the intermediate state. Indeed, most of the distorted variants of the parent rutile structure observed in Nature involve some kind of *dimerization* of paired metal cations³, which is often referred to in the literature as an *embedded Peierls instability* [201, 202, 203].

5.1.2 Charge and orbital degrees of freedom

Along with the structural degrees of freedom discussed above, the effective d electron count is a crucial variable in determining the wide diversity of ground states realized in rutile-like compounds. Without delving into too many materials-specific details, this number is usually determined as follows: since each oxygen ion requires two electrons to completely fill its $2p$ shell, the formal valence of the metal cation is taken to be M^{4+} ,

³In slightly different language: alternating M-M bond lengths along the rutile c axis.

and then the number of electrons filling states near the Fermi level (E_F) derived from the transition-metal d orbitals is determined the chemical identity of M. For examples, M = Ti results in a zero $3d$ electrons near E_F —and thus a band insulator—whereas M = Ru leaves four $4d$ electrons near E_F —and thus highly metallic behavior with relatively large carrier densities $n \approx 10^{29}/\text{m}^3$ (the typical volume of a rutile unit cell containing two MO_2 formula units is $\approx 60 \text{ \AA}^3$).

At a more detailed level, the shapes of the relevant d orbitals spanning E_F are also essential in determining the electronic and magnetic properties of rutile-like compounds. The largest energy scale in the problem is the octahedral crystal-field splitting $10Dq \approx 3 - 4 \text{ eV}$ that splits the five d orbitals into a lower-energy triplet of states with primarily t_{2g} orbital character and a higher-energy doublet of states with primarily e_g orbital character. Since all metal cations that crystallize in a rutile structure have an electron count less than or equal to six when present as M^{4+} , the e_g -like states are generally not populated and can be safely ignored in any discussion of the effective low-energy physics. On the other hand, an important factor in determining how the electrons are distributed amongst the remaining t_{2g} -like states is that the d_{xy} , d_{xz} , and d_{yz} orbitals comprising this manifold are *not* nearly degenerate, as is commonly observed in perovskite-based structures. Instead, the orbitals are further split by $\Delta \approx 0.1 - 0.4 \text{ eV}$ into states with so-called $d_{||}$ orbital character and states with mixed (d_{xz} , d_{yz}) orbital character. The $d_{||}$ -derived states are generically lower in energy and thus are filled *before* the (d_{xz} , d_{yz})-derived states.

Besides Δ and the total electron filling, the exact $d_{||}$ and (d_{xz} , d_{yz}) orbital occupancies also depend on several other energy scales we have neglected thus far: the bandwidths W of these states, the mutual Coulomb repulsion U between electrons (which can substantially renormalize W in correlated systems), the Hund's rule coupling J (which generally favors equal orbital occupancies), and the spin-orbit coupling λ_{soc} . A proper accounting of the interplay between W , U , J , and λ_{soc} —which can all be of comparable strength in actual

materials such as RuO_2 —is of course necessary for a full understanding of the effective low-energy physics, and is highly material-dependent. We we will revisit this point in further detail for RuO_2 in the next chapter using ARPES measurements of the electronic structure in concert with first-principles calculations. Nonetheless, ignoring for now these additional considerations, a schematic diagram of the on-site level structure realized in rutile structures is sketched in Figure 5.2, along with plots of how the lobes of the $d_{||}$ and (d_{xz}, d_{yz}) orbitals are oriented relative to the crystallographic axes. Many of the ground states observed in rutile compounds—as well as their evolution versus different modes of strain—can be rationalized in terms of a simple picture like this that invokes unequal $d_{||}$ and (d_{xz}, d_{yz}) orbital occupancies, as we will illustrate later for RuO_2 .

5.1.3 Structural, electronic, and magnetic properties specific to RuO_2

Bulk single crystals of RuO_2 were first synthesized in the 1960s by multiple different groups [205, 206]. All measurements of the crystal structure to date suggest that the crystal structure belongs to the ideal high-symmetry rutile space group #136, $P4_2/mnm$, with no evidence for any symmetry-lowering structural distortions at any temperatures up to 1000 K [207]. At 295 K, the lattice constants are $(a, c) = (4.492 \text{ \AA}, 3.106 \text{ \AA})$ and the internal oxygen parameter $u = 0.3056$, corresponding to apical oxygen-ruthenium bond length of 1.94 \AA and an equatorial oxygen-ruthenium bond length of 1.98 \AA [204].

Bulk RuO_2 (formal valence Ru^{4+} , with a corresponding electronic configuration of $4d^4$) exhibits metallic conduction at all temperatures, in agreement with the simplest expectations for a material with four electrons in partially filled bands crossing E_F . Early experimental studies by Ryden *et al.* reported room-temperature resistivities of $\rho(300 \text{ K}) = 35 \pm 1 \mu\Omega\text{-cm}$ that were approximately isotropic with respect to the crystallographic axes [208, 209], even though different components of the resistivity tensor such as

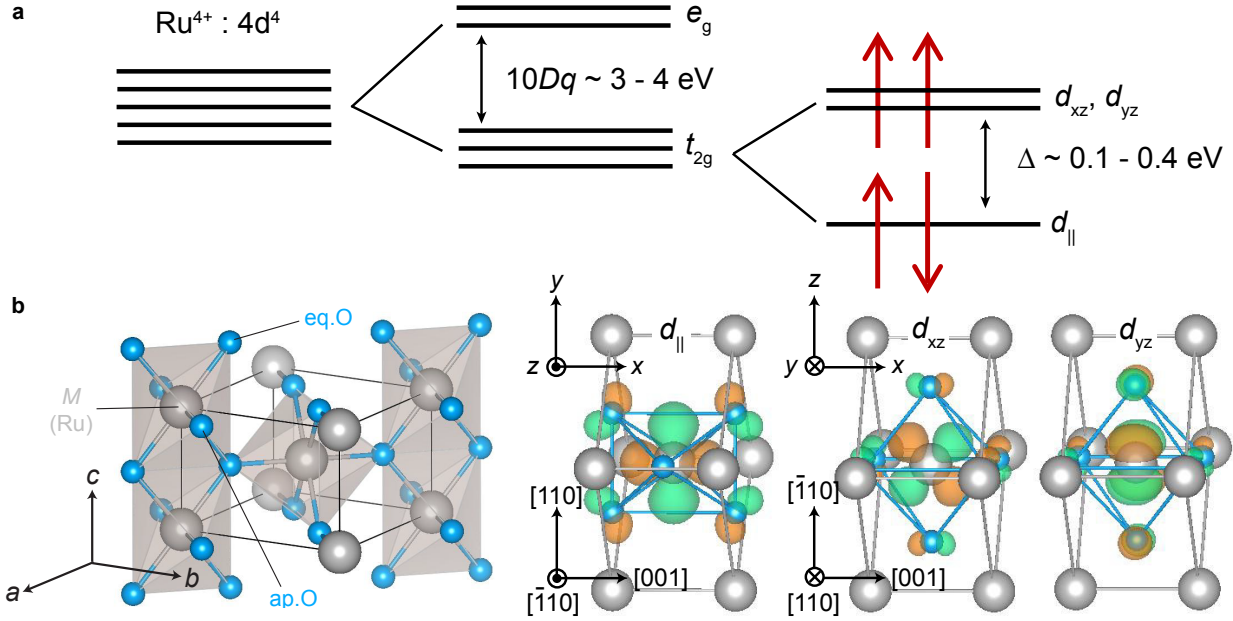


Figure 5.2: (a) Schematic diagram of the low-energy orbital degrees of freedom in RuO_2 . In addition to the usual octahedral crystal field splitting $10Dq$, there is a sizable splitting Δ between the on-site energies of the $d_{||}$ and (d_{xz}, d_{yz}) orbitals that comprise the “ t_{2g} ” manifold. For RuO_2 , this leaves an effectively half-filled manifold of (d_{xz}, d_{yz}) -derived states spanning E_F , which strongly favors antiferromagnetic correlations between neighboring Ru sites, as first noted in Ref. [204]. (b) Plots of the $d_{||}$, d_{xz} , and d_{yz} Wannier functions that span the low-energy Hilbert space for RuO_2 , calculated using DFT. Results are shown for Wannier functions centered on the Ru atoms at $(1/2, 1/2, 1/2)$; the corresponding Wannier functions centered at $(0, 0, 0)$ can be generated by rotating and translating the local $\{x, y, z\}$ axes according to the glide plane symmetry operation of the rutile space group. The on-site crystal-field splitting Δ follows from how the lobes of these orbitals (colored orange and green) are oriented relative to directions for which the octahedra have edge- and corner-sharing character, respectively.

ρ_{100} and ρ_{001} are not required to be equal by the tetragonal symmetry of the crystal structure. Later computational studies of the transport properties of RuO_2 obtained values for different components of the plasma frequency tensor that were in good agreement with the observed isotropy of ρ [91]. Moreover, these studies used the Fermi surfaces and Fermi velocities calculated within band theory to estimate that the experimentally measured magnitude of $\rho(300 \text{ K})$ corresponds to an inelastic mean free path of $\ell \approx 36 \text{ \AA}$. Since this value of ℓ is well in excess of the characteristic interatomic distances such as (a, c) , it was

suggested that a Boltzmann-type description of transport—*i.e.*, a theory assuming the existence of long-lived quasiparticle excitations that are only weakly scattered—should be sufficient to describe the transport properties of RuO₂ at all intermediate temperatures between 0 and 300 K. In particular, there are no indications in RuO₂ of strong electron-electron correlations causing a crossover at elevated temperatures to a “bad metal” regime with incoherent excitations that display linear in temperature scaling of $\rho(T)$, and the absolute values of ρ are always much lower than the Motte-Ioffe-Regel limit. This is in marked contrast to what is observed in perovskite-based ruthenates with the same formal valence of Ru⁴⁺, where local atomic-like Hund’s rule correlations destroy the coherence of quasiparticle excitations at very low temperatures $T \ll 300$ K—*cf.* chapter 4 for the case of Sr₂RuO₄.

Like most traditional metals, the primary contribution to $\rho(300\text{ K})$ in RuO₂ is from electron-phonon scattering [91]. As the temperature is reduced, these scattering channels become progressively frozen out by phase-space considerations. At sufficiently low temperatures, electron-electron scattering becomes dominant, and in this regime all of the traditional hallmarks of a Landau Fermi liquid are observed, including $\rho \sim \rho_0 + AT^2$ scaling of the electrical resistivity [208], $C/T \sim \gamma + BT^2$ scaling of the specific heat capacity [210], and (under large externally applied magnetic fields) quantum oscillations of observables such as the magnetization and resistivity that result from quantization of the near- E_F quasiparticle orbits into well-defined Landau levels [211, 212, 213]. Figure 5.3 summarizes some of these canonical signatures of Fermi liquid behavior. Focusing on the electronic component γT of the heat capacity as $T \rightarrow 0$ K, more recent calculations [91] have shown that the experimentally measured value of γ is enhanced by a factor of 1.45 over the value expected from the DFT-computed density of states at E_F , suggesting that the quasiparticle excitations in the Fermi liquid state have only modestly enhanced effective masses.

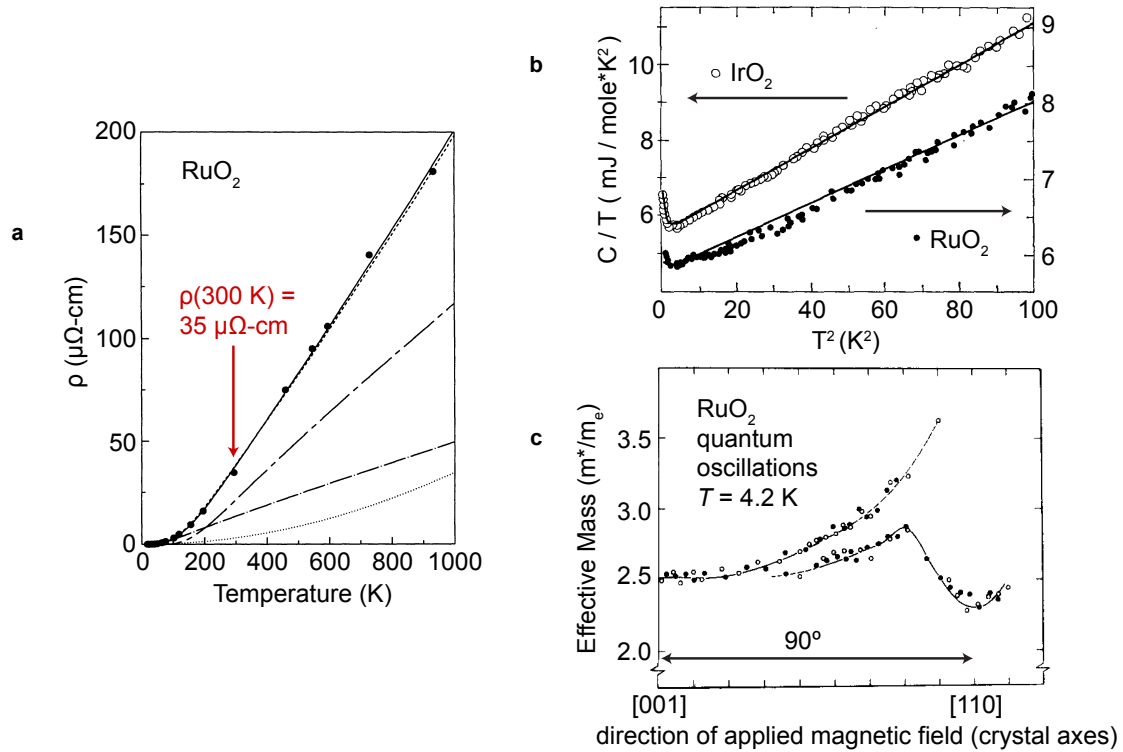


Figure 5.3: (a) Electrical resistivity versus temperature of bulk RuO_2 single crystals, reproduced from Refs.[91, 208]. (b) Low-temperature specific heat of bulk RuO_2 single crystals (right axis), reproduced from Ref.[210]. (c) Cyclotron effective masses (in units of the free-electron mass m_e) extracted from quantum oscillations measurements at $T = 4.2$ K, reproduced from Ref.[212]. All of these probes evidence a canonical Fermi liquid ground state in bulk RuO_2 .

In short, Figure 5.3 is intended to show that the known transport behavior of bulk RuO_2 places it firmly in “vegetable” territory—*i.e.*, thoroughly characterized and understood in terms of well-established theories. Clear signatures of electron-phonon scattering are present at higher temperatures, but a Fermi liquid state is eventually reached at low enough temperatures, and the wide temperature range over which conventional metallic transport properties are measured suggest that none of this phenomenology should depend too sensitively on disorder that may be present in different experimental incarnations of RuO_2 , such as epitaxial thin films⁴. Turning this argument around, how-

⁴As an aside, we note that disorder effects are almost certainly negligible in single crystals of RuO_2 : residual resistivities of $\rho_0 < 0.3 \mu\Omega\text{-cm}$ are routinely measured, corresponding to mean free paths in excess of 400 nm.

ever, we should definitely expect superconductivity to condense from a Fermi liquid at some finite transition temperature T_c , and if we furthermore presume that the modest quasiparticle mass enhancements measured by specific heat are primarily the result of electron-phonon coupling λ —*i.e.*, $m^*/m_{DFT} = 1.45 \approx 1 + \lambda$ —then one might even expect that the T_c for electron-phonon mediated superconductivity should not be astronomically low. Following this line of reasoning, Ref.[91] estimated that T_c for RuO₂ could be as large as a few Kelvin, based on the weak-coupling BCS expression $T_c \sim \hbar\omega_D \exp[-1/\lambda]$. Unfortunately, subsequent electrical transport measurements on single crystals of RuO₂ down to lower temperatures gave no evidence of superconductivity down to temperatures $T < 300$ mK [214].

Although we do not claim to understand what mechanism is operative in limiting the superconducting T_c of bulk RuO₂—or whether the errors in the T_c estimate of Ref.[91] can be merely explained by quantitative uncertainties in the appropriate values of λ , ω_D , *etc.*—we believe that several of the properties emphasized above suggest that RuO₂ is a model system for exploring how epitaxial strain affects superconductivity. The starting point (bulk RuO₂) is a robust Fermi liquid with non-negligible electron-phonon coupling and—as we will demonstrate in the next chapter—an electronic structure that responds sensitively to strain. The remainder of this chapter is devoted to showing that appropriately strained RuO₂ is indeed a superconductor with experimentally accessible T_c s, and to establishing the modes of strain to which superconductivity responds most sensitively.

Before proceeding to investigate strain-induced changes to the superconductivity, we note one experimental reality that may complicate the interpretation of these effects is the presence of commensurate spin-density wave (SDW) order at $\mathbf{q}_{SDW} = (1\ 0\ 0)$ that was recently discovered in bulk RuO₂ single crystals and RuO₂ thin films synthesized on perovskite SrTiO₃(001) substrates to persist up to temperatures $T_{N\acute{e}el} > 400$ K [204, 215]. Recent resonant x-ray scattering measurements conducted by Dan Weinstock, a graduate

student in Andrej Singer's group at Cornell, have confirmed that SDW order at the same \mathbf{q}_{SDW} exists in *both* of the thin-film variants of RuO_2 that we describe in later sections, $\text{RuO}_2/\text{TiO}_2(110)$ and $\text{RuO}_2/\text{TiO}_2(101)$, with similarly high ordering temperatures as in single crystals⁵—in all cases, well above the temperatures that can be accessed experimentally. The origin of robust *commensurate* antiferromagnetic correlations in a system that shows many other signatures of itinerant electrons remains somewhat mysterious, both experimentally and theoretically, and is an active area of research. The small values of the ordered magnetic moment measured experimentally ($M < 0.05\mu_B$, where μ_B is the Bohr magneton) and the high Néel temperature might suggest that it is appropriate to view RuO_2 as a system in which a small fraction of magnetically ordered electrons are largely decoupled from a much larger fraction of the electron fluid that carries current and primarily determines the low-temperature electrical properties. On the other hand, while the coexistence of antiferromagnetism and superconductivity in strained RuO_2 thin films would not be unprecedented—having been previously observed in heavy-fermion compounds [216] as well as electron-doped cuprates [217]—it may alternatively imply that some exotic physics is operative in RuO_2 that may invalidate our basic working hypothesis of conventional superconductivity mediated by electron-phonon coupling. For the remainder of this dissertation, we adopt the former perspective, although we believe the latter viewpoint deserves further consideration in future work, especially considering the recent resurgence of interest in materials that support Cooper-pair density waves [218, 219].

⁵Unpublished work by Dan Weinstock and Andrej Singer.

5.2 Synthesis and characterization of RuO₂ thin films

5.2.1 Film growth by molecular-beam epitaxy

Epitaxial thin films of RuO₂ were synthesized on various orientations of rutile TiO₂ substrates using the Veeco GEN10 reactive oxide MBE systems described in chapter 2. All films discussed in this dissertation were grown by two postdocs and a graduate student in the Schlom group: Hanjong Paik, Hari Nair, and Nate Schreiber. Prior to growth, commercially available TiO₂ substrates were cleaned with organic solvents, etched in acid, and annealed in air to produce starting surfaces with step-terrace morphology, following the methods in Ref.[220]. Elemental ruthenium of 99.99% purity was evaporated using an electron-beam evaporator in background oxidant partial pressures of $p_{\text{O}_3} = 1 \times 10^{-6} - 5 \times 10^{-6}$ Torr of distilled ozone ($\approx 80\% \text{ O}_3 + 20\% \text{ O}_2$)⁶ at substrate temperatures of $T_s = 250 - 400^\circ \text{ C}$, as measured by a thermocouple⁷. Reflection high-energy electron diffraction was used to monitor the surface crystallinity of the films *in situ* and showed characteristic oscillations in intensity during Ru deposition, indicating a layer-by-layer growth mode.

As discussed in subsection 5.1.3, bulk RuO₂ crystallizes in the ideal tetragonal rutile structure with room-temperature lattice constants of ($a = 4.492 \text{ \AA}, c = 3.106 \text{ \AA}$) [204]. To investigate the strain dependence of superconductivity, RuO₂ thin films in distinct epitaxial strain states were synthesized using MBE by employing different orientations of isostructural TiO₂ substrates, ($a = 4.594 \text{ \AA}, c = 2.959 \text{ \AA}$) [221]. As shown in Figure 5.4(a),

⁶In certain films grown at $p_{\text{O}_3} = 1 \times 10^{-6}$ Torr, electron microscopy measurements evidenced unoxidized Ru metal inclusions existing within ≈ 5 nm of the film-substrate interface. These inclusions do not qualitatively affect the superconducting properties of thicker strained RuO₂(110) samples, but to avoid the presence of these intergrowths, later films were deposited at higher oxidant partial pressures.

⁷ T_s appreciably affects the superconducting properties of RuO₂(110) films, as summarized in Table 5.1. We believe that these trends in how superconductivity depends on T_s likely reflect the fact that higher growth temperatures promote epitaxial strain relaxation at smaller film critical thicknesses. We leave a more systematic investigation of this point to future studies.

the surfaces of (101)-oriented substrates are spanned by the $[\bar{1}01]$ and $[010]$ lattice vectors of TiO_2 , which ideally impart in-plane tensile strains on RuO_2 (at 295 K) of +0.04% and +2.3%, respectively. On $\text{TiO}_2(110)$, the lattice mismatches with RuO_2 are larger: -4.7% along $[001]$ and $+2.3\%$ along $[1\bar{1}0]$.

5.2.2 Electrical transport measurements

Figure 5.4(b) shows the electrical resistivity $\rho(T)$ of RuO_2 films, along with bulk RuO_2 single crystals from Ref. [214]. To compare with bulk RuO_2 , for the thin-film samples we plot the geometric mean of ρ along the two in-plane directions; the intrinsic resistivity anisotropy is known to be small in bulk, consistent with our findings, which are shown in further detail in Figure 5.5. The $\rho(T)$ data for the lightly strained $\text{RuO}_2 / \text{TiO}_2(101)$, which will henceforth be referred to as $\text{RuO}_2(101)$, is nearly indistinguishable from bulk RuO_2 , exhibiting metallic behavior with low residual resistivities $\rho(0.4 \text{ K}) < 2 \mu\Omega\text{-cm}$. In contrast, a clear superconducting transition is observed in the more highly strained $\text{RuO}_2 / \text{TiO}_2(110)$ sample, referred to as $\text{RuO}_2(110)$, at $T_c = 2.0 \pm 0.1 \text{ K}$. Magnetoresistance measurements with H_\perp applied along $[110]$ show a suppression of T_c with increasing fields, with an extrapolated zero temperature value of $H_{c\perp}(T \rightarrow 0 \text{ K}) = 13.3 \pm 1.5 \text{ kOe}$, corresponding to an average in-plane coherence length of $\xi = 15.8 \pm 0.9 \text{ nm}$. In Fig. 1d, we show a superconducting $V(I)$ curve measured on a lithographically patterned resistivity bridge, and extract a critical current density $J_c = (9.5 \pm 1.2) \times 10^4 \text{ A/cm}^2$ at $0.3 T_c$. This large value of J_c (over one order of magnitude larger than values reported on typical elemental superconductors with comparable T_c s) indicates that the superconductivity does not arise from a filamentary network, structural defects, or from some other minority phase, which would all yield much smaller values of J_c .

In Figure 5.5, we show how the electrical transport properties of an $\text{RuO}_2(110)$ sample

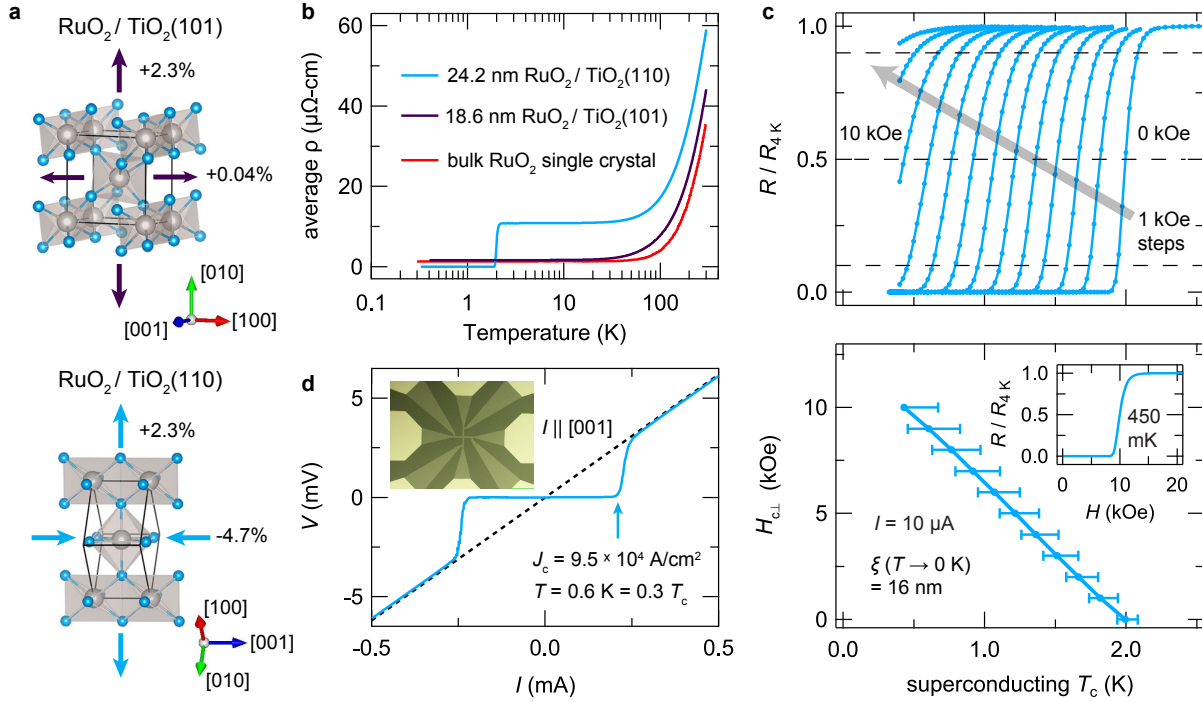


Figure 5.4: (a) Schematic diagrams of the crystal structures and in-plane lattice mismatches with TiO₂ of RuO₂ thin films synthesized in (101)- and (110)-orientations. (b) Average resistivity versus temperature curves for 24.2 nm thick RuO₂(110) and 18.6 nm thick RuO₂(101) films and bulk RuO₂ single crystals reproduced from Ref.[214]. For clarity the results for bulk RuO₂ have been rigidly shifted upward by 1 $\mu\Omega\text{-cm}$ ($\rho_0 \approx 0.3 \mu\Omega\text{-cm}$). (c) Upper critical magnetic fields $H_{c\perp}$ versus superconducting T_c s extracted from magnetoresistance measurements for the RuO₂(110) sample in **b**, along with (inset) a characteristic $R(H)$ sweep taken at $T = 0.45$ K. Superconducting T_c s are taken as the temperatures at which the resistance drops to 50% of its residual normal-state value R_0 ; error bars on these T_c s delineate drops to 90% and 10% of R_0 , respectively—cf. the horizontal dashed lines in the top panel. (d) $V(I)$ curve measured at 0.6 K on a resistivity bridge lithographically patterned on the RuO₂(110) sample from **b** and **c**, with the direction of current flow parallel to $[001]_{\text{rutile}}$. Similarly large critical current densities are obtained with $I \parallel [1\bar{1}0]$ —cf. Figure 5.5.

depend on the direction of current flow in the film when it is confined to flow along the orthogonal in-plane crystallographic axes, $[001]$ and $[1\bar{1}0]$. Prior to lithographically patterning resistivity bridges on the film, we measured the resistance versus temperature of the entire $10 \text{ mm} \times 10 \text{ mm} \times 24.2 \text{ nm}$ thick film by wire bonding four contacts directly to the surface of the sample in an in-line contact geometry. Such a contact geometry

probes the geometric mean of the two diagonal components of the in-plane resistivity tensor, $\sqrt{\rho_{001}\rho_{1\bar{1}0}}$, neglecting small finite-size corrections that depend on how the contacts are oriented relative to the edges of the wafer [222]. The results of these measurements are shown by the blue traces in Figure 5.5(a-b); these are the same data plotted on a logarithmic temperature scale in Figure 5.4(b).

Since RuO₂ has a tetragonal crystal structure in bulk—and orthorhombic or perhaps monoclinic in (110)-oriented films— ρ_{001} and $\rho_{1\bar{1}0}$ are not guaranteed by symmetry to be equal. The intrinsic transport anisotropy in bulk RuO₂ is known to be small, with differences between ρ_{100} and ρ_{001} that are less than 10% at 300 K [208, 91]; however, in thin films it is common for highly oriented structural defects—*e.g.*, those nucleated at step edges on the substrate—to induce sizable extrinsic anisotropies in the different in-plane components of ρ . To investigate this possibility, we used standard lithographic techniques to pattern the same RuO₂(110) sample into four-point resistivity bridges with dimensions 55 μm (length) \times 10 μm (width) \times 24.2 nm (thickness), where the direction of current flow is confined (via lithography) to be aligned with specific crystallographic directions. In the course of performing the lithography, we noticed that the TiO₂ substrates became mildly conducting, possibly due to oxygen vacancies formed during ion milling, as has been reported to occur for SrTiO₃ [223]. Therefore, we annealed the wafer containing the patterned resistivity bridges in air at elevated temperatures until the substrate again read open-circuit two-point resistances ($> 100 \text{ M}\Omega$); 2 hours at 500° C was found to be sufficient.

The results of electrical measurements on these patterned resistivity bridges are shown by the green and orange traces in Figure 5.5(a-c). The temperature dependence of $\rho(T)$ is qualitatively consistent with the control measurements performed on the entire film before patterning, and the absolute magnitude of the resistivity anisotropies at 300 K and 4 K are both $< 20\%$. Furthermore, the superconducting $\rho(T)$ and $V(I)$ behavior do not de-

pend strongly on the direction of current flow; this is contrary to what might be expected if the superconductivity arose from oriented structural defects. In Figure 5.5(b), we ascribe the substantial decrease in low-temperature resistivities observed in the patterned resistivity bridge data relative to the entire film data to the aforementioned annealing involved in preparing the bridges. We confirmed on other $\text{RuO}_2(110)$ samples not containing bridges that post-growth annealing in air generically causes the low-temperature values of ρ to drop, by as much as a factor of four. Because of these complications and additional uncertainties involved in lithographically patterning resistivity bridges on films on TiO_2 substrates, unless otherwise noted, all other electrical transport data presented in this dissertation were acquired by wire bonding directly to the surfaces of as-grown samples that were not subject to any post-growth annealing treatments.

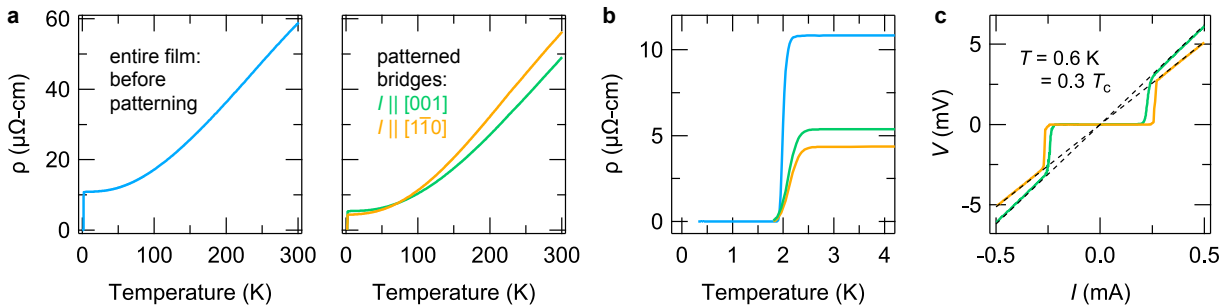


Figure 5.5: (a - b) Zero-field $\rho(T)$ data measured on an entire as-grown 24.2 nm thick $\text{RuO}_2 / \text{TiO}_2(110)$ sample (blue), and after lithographically patterning four-point resistivity bridges (green and orange). (c) Superconducting $V(I)$ curves measured on patterned resistivity bridges with the directions of current flow parallel to $[001]$ and $[1\bar{1}0]$.

In Figure 5.6, we present the results of magnetoresistance measurements for three samples of $\text{RuO}_2(110)$ with different film thicknesses; the data in Figure 5.6(a,b) are reproduced from Figure 5.4(c). Each $R(T)$ trace is taken at discrete values of the externally applied field H_\perp (applied perpendicular to the surfaces of the films, along $[110]$) upon slowly warming the samples up from base temperature through the superconducting transitions. All resistances are normalized to their zero-field values at 4 K, well above the superconducting transitions; since the normal-state $R(T, H)$ behavior of $\text{RuO}_2(110)$ in the

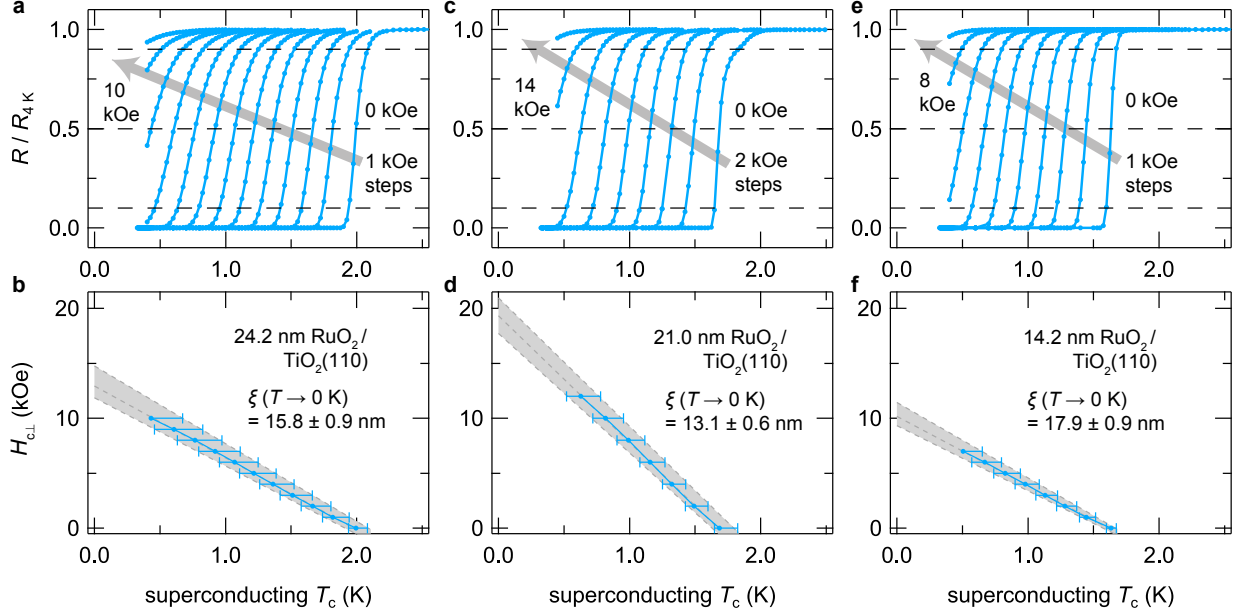


Figure 5.6: Magneto-resistance measurements for three superconducting $\text{RuO}_2(110)$ samples with different film thicknesses. All raw data traces in **(a, c, e)** are normalized to a common value $R_{4\text{K}} \equiv R(T = 4\text{ K}, H = 0\text{ kOe})$ for ease of visualization and analysis. The extracted scaling behavior of the upper critical fields versus superconducting T_c are plotted in **(b, d, f)**, along with the superconducting coherence length ξ corresponding to the extrapolated zero-temperature $H_{c\perp}$.

absence of superconductivity is negligible in this regime of low temperatures and fields, the choice of a single normalization factor $R_{4\text{K}}$ for all data does not appreciably affect any of the results that follow. Because percolation effects imply that resistive measurements of critical fields inherently contain some ambiguity about the definition and meaning of $H_{c\perp}$ relative to truly bulk-sensitive measurements of superconductivity [224], here we adopt the same convention employed in Figure 5.4: the temperature at which R drops to 50% of $R_{4\text{K}}$ is taken as T_c for the given $H_{c\perp}$, and the error bars on the extracted T_c are the temperatures at which R drops to 90% and 10% of $R_{4\text{K}}$, respectively [225].

While there are considerable quantitative discrepancies in the values of $H_{c\perp}$ and T_c for the different thickness samples in Figure 5.6, the scaling behavior seems to be remarkably linear for all three samples, with no signs of saturation down to reduced temperatures

$T/T_c \approx 0.2 - 0.3$. This is unlike what is expected in, *e.g.*, Werthamer-Helfand-Hohenberg (WHH) theory [226]. For example, evaluating the right side of the WHH expression

$$H_{c\perp}(T \rightarrow 0 \text{ K}) \leq -0.693 \left. \frac{dH_{c\perp}}{dT} \right|_{T=T_c} T_c \quad (5.1)$$

places upper bounds of 9.0, 13.5 and 7.1 kOe on $H_{c\perp}(T \rightarrow 0 \text{ K})$ for these three samples; however, the experimentally measured critical fields at 0.45 K (*i.e.*, $T/T_c = 0.23, 0.27, 0.28$) are already larger than these bounds: 10.0, 13.7 and 7.4 kOe, respectively. Therefore, to extrapolate $H_{c\perp}$ down to zero temperature, we performed linear Ginzburg-Landau-type fits to all available data and propagated the systematic uncertainties in the definition of $H_{c\perp}$ according to the gray dashed lines. The quoted zero-temperature values of the average in-plane superconducting coherence lengths $\xi(T \rightarrow 0 \text{ K})$ are obtained from the relation

$$\xi(T \rightarrow 0 \text{ K}) = \sqrt{\frac{\Phi_0}{2\pi\mu_0 H_{c\perp}(T \rightarrow 0 \text{ K})}} \quad (5.2)$$

where Φ_0 is the superconducting flux quantum and μ_0 is the magnetic permeability of free space.

Notably, these values of $\xi(T \rightarrow 0 \text{ K})$ are less than values reported for traditional elemental superconductors with comparable T_c s by almost an order of magnitude, corresponding to critical fields that are $\approx 1 - 2$ orders of magnitude greater. While an explanation and understanding of these sizable critical field enhancements are beyond the scope of the present work, they are internally self-consistent with the large critical current densities noted in Figure 5.4(d) and Figure 5.5(c). These results may motivate future real-space measurements of the superconducting condensate by scanning-probe techniques. In particular, an interesting question to address is whether the structural defects in RuO_2 act

as pinning sites for the vortices that form under applied fields, similar to what has been observed in numerous other thin-film superconductors [227], or whether the defects host regions of enhanced superfluid density that effectively act as barriers to vortex motion, akin to twin boundaries in bulk single crystals of iron-based superconductors [228, 229].

5.2.3 X-ray diffraction and scanning transmission electron microscopy measurements

In order to disentangle the effects of epitaxial strain on the emergence of superconductivity from other possible interfacial or dimensional confinement effects—*e.g.*, cation interdiffusion [230], charge transfer from the substrate [231], and/or non-stoichiometry in the film or substrate [232]—we compare results for RuO₂ films both as functions of strain as well as film thickness. In Figure 5.7(a), we plot representative x-ray diffraction data from RuO₂(101) and RuO₂(110), showing that the films are strained as expected along the out-of-plane direction based on the average in-plane lattice mismatches with TiO₂. The primary 101 and 202 film peaks of RuO₂(101) are shifted to larger angles than bulk RuO₂ (dashed red lines) [204], corresponding to a 1.1% compression of d_{101} , while Nelson-Riley analysis of the primary 110, 220 and 330 (not shown) peak positions for RuO₂(110) evidence a 2.0% expansion of d_{110} relative to bulk. In Figure 5.7(b,c), we plot normalized resistance versus temperature data as a function of film thickness t for RuO₂(110), which show that the superconducting T_c rises above our measurement threshold between $t = 5.8$ nm and 11.5 nm, excluding the possibility that the superconductivity is highly localized to the substrate-film interface [231, 233], or that it arises from oxygen vacancies in the TiO₂ substrates or RuO₂ films. Note that since d^0 titanates are prone to becoming (super)conducting upon oxygen reduction [232], we also measured the $R(T)$ behavior of a bare TiO₂(110) substrate that was treated identically to substrates having RuO₂ films

grown on them, and did not observe superconductivity. Finally, in Figure 5.7(d), we show a scanning transmission electron microscopy image of RuO₂(110), which confirms uniform growth of the film over lateral length scales exceeding those expected to be relevant for superconductivity (*e.g.*, ξ), with no evidence of minority phases.

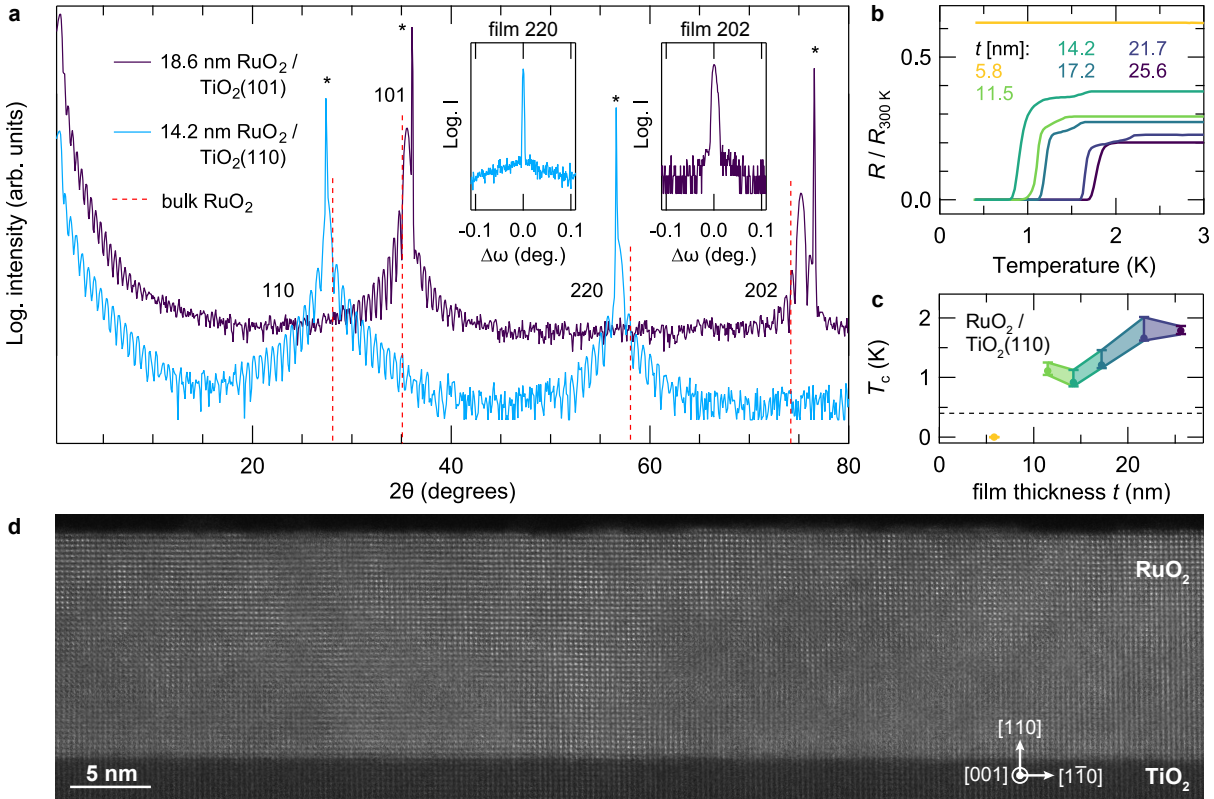


Figure 5.7: (a) X-ray diffraction measurements taken with Cu-K α radiation along the specular crystal truncation rods for 18.6 nm thick RuO₂(101) and 14.2 nm thick RuO₂(110) samples. Bragg peaks arising from the TiO₂ substrates are marked with asterisks, and the peak positions that would be expected for unstrained bulk RuO₂ are indicated by red dashed lines. Insets display rocking curves with FWHMs < 0.01° taken at the 2θ values corresponding to the central 220 and 202 film peaks. Here $q_{||}$ is aligned with TiO₂[1 $\bar{1}$ 0] for the (110)-oriented sample, and with TiO₂[$\bar{1}$ 01] for the (101)-oriented sample. (b - c) Resistance versus temperature curves for RuO₂(110) samples with different film thicknesses t , normalized to their values at 300 K. Error bars on the plotted superconducting T_c s have the same meaning as in Figure 5.4. The horizontal dashed line represents the base temperature attainable in our refrigerator, 400 mK. (d) Scanning transmission electron microscopy image of the same 14.2 nm thick RuO₂(110) sample from (a - c), courtesy of Berit Goodge and Prof. Lena Kourkoutis. More comprehensive structural and electrical characterization of the samples shown here are included in subsequent figures in this chapter.

In Figure 5.8, we include electrical characterization and more comprehensive lab-based x-ray diffraction measurements for the same $\text{RuO}_2(101)$ and $\text{RuO}_2(110)$ films of comparable thickness shown in Figure 5.7. Figure 5.8(a, e) show the zero-field $\rho(T)$ behavior for the two films: the 18.6 nm thick $\text{RuO}_2(101)$ film is non-superconducting down to < 0.4 K with a residual resistivity $\rho_0 < 1.7 \mu\Omega\text{-cm}$, whereas the 14.2 nm thick $\text{RuO}_2(110)$ film is superconducting at $T_c = 0.92 \pm_{0.07}^{0.21}$ K with a residual resistivity $\rho_0 < 32 \mu\Omega\text{-cm}$. Figure 5.8(b,f) show rocking curves for the films overlaid on rocking curves for the TiO_2 substrates they were synthesized on: in all cases the coherent components of the film peaks exhibit narrow full width at half maximum (FWHM) values that are limited by the underlying substrate FWHM, as expected for isostructural film growths. In our studies we found that the rocking curve shapes and widths of the TiO_2 substrates supplied by CrysTec, GmbH can vary significantly depending on how the in-plane momentum transfer q_{\parallel} is oriented relative to the crystal axes of a given wafer, which may be due to the Verneuil process used to synthesize the crystals; to give some idea of the magnitude of this asymmetric mosaic spread, we show scans with q_{\parallel} oriented along azimuths separated by 90° for each sample.

In Figure 5.8(c, d) and Figure 5.8(g, h) we show off-specular $(q_{\parallel}, q_{\perp})$ reciprocal space maps (RSMs) for both samples in regions surrounding HKL Bragg peaks that have q_{\parallel} purely aligned with the crystallographic directions indicated in the labels on the horizontal axes. For reference, the peak positions that would be expected for bulk RuO_2 and bulk TiO_2 at 295 K [204, 221] are shown as red and white squares, respectively; the orange squares represent the central peak positions expected for commensurately strained RuO_2 thin films, calculated using appropriately constrained density functional theory structural relaxations (chapter 6). To give a more quantitative sense of the logarithmic false color scale used here, the solid white lines overlaid on each plot represent the scattered intensity along the crystal truncation rods (CTRs)—*i.e.*, the one-dimensional cuts through the RSMs with q_{\parallel} equal to that of the substrate. These results show that the 18.6 nm

thick RuO₂(101) film is coherently strained to the substrate along both in-plane directions, within the $\approx 0.1\%$ resolution of the measurements. The variable widths of the CTRs versus q_{\parallel} in different RSMs are an artifact of instrumental resolution effects—namely, the “tall” incident beam profile convolved with the scattering geometries used to measure each RSM—which we do not attempt to correct for in this work. On the other hand, the 14.2 nm thick RuO₂(110) film is partially strain-relaxed, as evidenced by the more diffuse distribution of scattered intensity versus q_{\parallel} and less prominent finite-thickness fringes versus q_{\perp} along the CTRs. The diminished (or non-existent) contrast between thickness fringes in the CTRs for RuO₂(110) is likely a manifestation of crystalline disorder in the film interplanar spacings, since all (110)-oriented films have atomically abrupt bounding interfaces, *cf.* the x-ray reflectivity data in Figure 5.13(a).

To further substantiate the partial strain relaxation observed in RuO₂ / TiO₂(110) samples, we measured RSMs around several Bragg peaks along the specular CTR. Figure 5.9 summarizes the results of such measurements for the same 14.2 nm thick RuO₂(110) sample for which off-specular RSMs are shown in Figure 5.8, which was also characterized by x-ray diffraction, transport, and scanning transmission electron microscopy in Figure 5.7. By taking line cuts averaged over the dashed boxes—which span ranges of q_{\perp} where the measured intensities are predominantly due to scattering from the film—we obtained the three rocking curves plotted in Figure 5.9(d). Each rocking curve shows a sharp central peak that is resolution-limited in width (or substrate-limited, *cf.* Figure 5.8), superimposed on a much broader, nearly Lorentzian (FWHM = 0.003 – 0.005 Å⁻¹), component of the scattering that is also centered at $q_{\parallel} = 0$. Furthermore, the integrated intensity of the former coherent component of the scattering decays relative to that of the diffuse component as the magnitude of $|\mathbf{q}| = q_{\perp}$ increases in progressing from (a) to (c).

The non-zero intensity of the diffuse component in the film rocking curves, and the scaling behavior of how the total integrated intensity is distributed between the coherent

and diffuse components as $|\mathbf{q}|$ is varied, are both completely consistent with published data for numerous epitaxial thin films grown on lattice mismatched substrates where the films are thick enough to exhibit some form of strain relaxation [234, 235, 236, 237, 238, 74]. In principle, by analyzing the diffuse scattering profiles around multiple Bragg peaks with \mathbf{q} that project differently onto the Burgers vectors of the relevant misfit dislocations that relax the strain, one can obtain quantitative information on the types of dislocations that exist, the dislocation densities, *etc.* [239, 79]. We leave a more systematic analysis of this type to future synchrotron x-ray diffraction studies, where the measurement noise floor is significantly lower and the strongly \mathbf{q} -dependent instrumental resolution effects observed here are mitigated by having a more point-like incident beam profile. We note, however, that the similar FWHM values of the diffuse scattering versus q_{\parallel} around the 110, 220, and 330 peaks imply that the structural defects responsible for this scattering are more translational in nature than rotational (which in typical mosaic crystals, produce rocking curves of constant *angular* widths) [234, 235]. Whether the inverses of these FWHM values for the fitted Lorentzians can be directly interpreted as the Fourier transform of a real-space correlation length (200 – 300 Å) depends on whether the film is in the limit of *weak disorder*, in the formalism of Refs.[235, 239].

To visualize how the partial strain relaxation evidenced by XRD manifests in real-space images of the crystal structure, our collaborators in one of the electron microscopy groups at Cornell (Berit Goodge and Prof. Lena Kourkoutis) imaged select RuO₂(110) samples that we had characterized previously. Specimens suitable for cross-sectional scanning transmission electron microscopy measurements were prepared using the standard focused ion beam (FIB) lift-out process on a Thermo Scientific Helios G4 X FIB. High-angle annular dark-field scanning transmission electron microscopy (HAADF-STEM) images were acquired on an aberration-corrected FEI Titan Themis at 300 keV with a probe convergence semi-angle of 21.4 mrad and inner and outer collection angles of 68 and 340 mrad, respectively.

In Figure 5.10, we show additional HAADF-STEM data from the same 14.2 nm thick RuO₂(110) sample characterized in Figure 5.7, Figure 5.8, and Figure 5.9. In Figure 5.10(a), the RuO₂ film appears continuous and epitaxial to the TiO₂ substrate over several hundred nm. At the lattice scale, different regions from the same film exhibit varying degrees of crystalline coherence under the epitaxial strain applied by the TiO₂ substrate. The in-plane direction is the $[1\bar{1}0]$ axis of the RuO₂ film, subject to +2.3% tensile strain from the TiO₂ substrate. Some regions, such as that shown in Figure 5.10(b), exhibit exceptionally “clean” crystalline quality, so that all of the atomic columns of Ru stack nicely in the projection of the STEM image, giving rise to clear and ordered atomic contrast. In other regions of the same film, local strain effects in the film distort the RuO₂ lattice away from the idealized rutile structure such that the columns of Ru atoms are misaligned to the electron beam projection direction. This local misalignment of the lattice causes the apparent blurring and somewhat mottled contrast of the STEM image seen in Figure 5.10(c).

In Figure 5.11, the same film is also studied with HAADF-STEM in the orthogonal projection direction. This orientation allows us to assess the crystalline response of the RuO₂ film along the [001] direction, which is subject to a larger lattice mismatch with the TiO₂ substrate, −4.7% compressive strain. Again, Figure 5.11(a) confirms the continuous and epitaxial growth of the RuO₂(110) thin film. Effects of the large compressive strain along the in-plane direction of this projection are clearly apparent in Figure 5.11(a, b) as characteristic V-shaped contrast in the RuO₂ film. Contributions from electron channeling in ADF STEM imaging gives rise to this bright/dark contrast in regions of local crystallographic strain; such contrast is a common signature of epitaxial lattice strain in many other oxide systems. Figure 5.11(c) shows the same structural response at atomic resolution, where—similar to Figure 5.10(c)—the apparent blurring of atomic columns indicates regions where the film lattice has been locally distorted.

For completeness, the structural quality of the same non-superconducting 18.6 nm

thick $\text{RuO}_2(101)$ film characterized in Figure 5.7 was also measured in similar HAADF-STEM experiments. The non-superconducting film shown in Figure 5.12(a) appears comparably continuous and epitaxial to the superconducting films also studied, showing no signs of any long-range defects or inclusions that might otherwise alter the properties of the film. Unsurprisingly, the $\text{RuO}_2(101)$ film shows somewhat more coherent crystalline order than the more drastically strained superconducting films, even over relatively large fields of view as shown in Figure 5.12(b). The lattice appears largely defect-free down to the atomic scale, as shown in Figure 5.12(c), lacking many of the signatures of larger strain observed in the $\text{RuO}_2(110)$ samples. This agrees well with the observation that the residual resistivities of $\text{RuO}_2(101)$ samples are consistently much lower than those of $\text{RuO}_2(110)$ samples.

5.2.4 Dependence of superconductivity on film thickness for $\text{RuO}_2(110)$

Figure 5.7 shows that the superconducting T_c s of RuO_2 thin films synthesized on $\text{TiO}_2(110)$ substrates depend sensitively on the thickness of the films, t . We do not purport to completely understand this empirical observation at the time of writing this dissertation, but Figure 5.13 and Figure 5.14 include several additional pieces of structural and electrical characterization data for this same thickness series of $\text{RuO}_2(110)$ samples that constrain possible explanations.

In Figure 5.13(a, b), we plot x-ray reflectivity data taken at low incident angles, and x-ray diffraction data taken near the 110 Bragg peaks of the film and substrate, both acquired along the specular CTRs with $\text{Cu-K}\alpha$ radiation. Finite-thickness fringes are present over a wide range of angles in both data sets, evidencing (from reflectivity) atomically abrupt interfaces of the films with the substrates and with vacuum, and (from diffraction) comparable levels of crystallinity along the out-of-plane direction across samples; further-

more, the spacings between secondary maxima on either side of the primary film Bragg peaks match the spacings between the low-angle reflectivity fringes, suggesting that the crystal structures of all films are essentially homogeneous along the out-of-plane direction. The film thicknesses t quoted here and elsewhere are obtained by directly fitting the reflectivity data in Figure 5.13(a) using a genetic algorithm, which yields sub-nanometer roughnesses in all cases in the refined models.

Given that there are no obvious differences in film morphology or out-of-plane crystallinity between $\text{RuO}_2(110)$ samples with different t , an alternative explanation that may account for the thickness-dependent superconducting T_c s is the proliferation of misfit dislocations in thicker films that progressively relax the epitaxial—*i.e.*, in-plane—strains; in this scenario, it may be true that partially strain-relaxed $\text{RuO}_2(110)$ films have higher (average) superconducting T_c s compared with fully commensurately strained $\text{RuO}_2(110)$ films. To investigate this possibility, in Figure 5.13(c - e) we plot line cuts of the intensity versus q_{\parallel} extracted from RSMs near the 220, 310, and 332 Bragg reflections of the $\text{RuO}_2(110)$ thin films and TiO_2 substrates. The raw data for all RSMs are plotted in Figure 5.14 using logarithmic false color scales; the line cuts in Figure 5.13 are averaged over the ranges of q_{\perp} between the dashed white lines in Figure 5.14. All of the samples except the thinnest film exhibit diffuse scattering surrounding the CTRs, indicating that partial strain relaxation onsets between film thicknesses of 5.8 nm and 11.5 nm for the growth conditions used in this work to synthesize $\text{RuO}_2 / \text{TiO}_2(110)$ samples. Since the in-plane lattice mismatches between RuO_2 and TiO_2 are highly anisotropic for the (110) orientation, it might also be expected that the substrate-imposed compressive strain along $[001]$ (-4.7%) starts to relax at smaller film thicknesses than the tensile strain along $[\bar{1}\bar{1}0]$ ($+2.3\%$) [236, 238]. The off-specular RSMs in Figure 5.14(b, c) qualitatively agree with this expectation, inasmuch as finite-thickness fringes can still be observed along the CTRs in the RSMs near 310 for films up to at least $t = 17.2$ nm, whereas only the $t = 5.8$ nm film shows a contribution to the coherent CTR scattering in the RSMs near 332 that clearly

rises above the contributions of the substrate.

Although signatures of scattering from partially strain relaxed $\text{RuO}_2(110)$ are manifestly present in the data for all of the superconducting samples in Figure 5.13—namely, broader distributions of intensity versus q_{\parallel} that asymmetrically gain weight towards the positions expected for bulk RuO_2 as the film thickness increases—it remains somewhat ambiguous whether this data can be interpreted in a straightforward manner to gain insight into what levels of strain optimize the superconducting T_c s in RuO_2 . Strain relaxation in oxide thin films often occurs inhomogeneously, with a mixture of commensurately strained and partially relaxed material [240]. The STEM images in Figure 5.10 and Figure 5.11 of $\text{RuO}_2(110)$ may indicate that similar phenomenology is realized here. Indeed, examining the transport data for these same samples, it is tempting to ascribe the multi-stage behavior of the superconducting transitions to temperature-dependent Josephson coupling of regions of the films under different amounts of strain with correspondingly different “local” T_c s; similar behavior has been described theoretically [241] and observed experimentally in patterned Nb islands on gold substrates [242]. Nonetheless, because of the close proximity of the substrate peaks along q_{\perp} ($d_{110} = 3.248 \text{ \AA}$) with the positions expected for commensurately strained $\text{RuO}_2(110)$ ($d_{110} = 3.241 \text{ \AA}$), it is difficult to disentangle their respective contributions to the total scattering observed in x-ray diffraction.

Despite these complications in quantitatively analyzing the x-ray diffraction results, we can use the values of t obtained from the x-ray reflectivity data to alternatively plot the normalized resistance versus temperature curves from Figure 5.7(b) in terms of absolute resistivities, as shown in Figure 5.13(f). From these data, a robust *correlation* between the superconducting T_c s and the residual resistivities immediately becomes apparent, as displayed in Figure 5.13(g); this may suggest that the primary effect of reducing t is to enhance the relative importance of elastic scattering off disorder near the film-substrate

interfaces, which can cause a decrease of T_c by smearing out and reducing the average value of an otherwise anisotropic superconducting gap function $\Delta(\mathbf{k})$.

5.3 Discussion and Conclusions

In this chapter we employed substrate-imposed epitaxial strains to transmute a normal metal into a superconductor. Specifically, we synthesized rutile RuO_2 thin films by MBE on isostructural but deliberately lattice-mismatched TiO_2 substrates to increase the superconducting transition temperatures from $T_c < 0.4$ K for lightly strained $\text{RuO}_2(101)$ films (or $T_c < 0.3$ K for bulk single crystals of RuO_2) to $T_c > 2.0$ K for more heavily strained $\text{RuO}_2(110)$ films. Utilizing a comprehensive set of electrical and structural characterization measurements for many such samples, we demonstrated that the enhanced superconductivity is a strain effect that occurs within a sizable volume fraction of the films; in particular, the superconductivity is not filamentary or interfacial in origin, and thus is unlikely to result from structural defects, unintentional non-stoichiometry in the film (or substrate), dimensional confinement, charge transfer, or interfacial mode coupling between the substrate and film.

Table 5.1 summarizes the electrical and structural properties we measured for over 30 RuO_2 thin-film samples as part of this dissertation. For all samples listed here we performed XRD measurements along the specular CTR to obtain the film thicknesses, and $R(T)$ measurements from 300 K down to 0.4 K to obtain the RRRs and superconducting T_c s. For select samples we also performed magnetoresistance measurements of the superconducting upper critical fields $H_{c\perp}$, as well as RSMs to gauge the strain status of the films, as indicated by the rightmost two columns. Some representative examples of these data are presented throughout the figures displayed in this chapter.

Sample ID	TiO ₂ substrate orientation	T_s (°C)	film thickness (nm)	RRR	90%, 50%, 10% SC T_{cs} (K)	SC $H_{c\perp}$?	RSMs?
HP2261	(110)	350	24.2	5.43	2.08, 2.00, 1.94	yes	yes
HP2263	(110)	350	12.4	2.51	0.87, 0.69, 0.60	no	no
HP2832	(110)	350	14.4	6.04	1.67, 1.63, 1.60	yes	yes
HP2833	(110)	350	13.0	2.47	0.95, 0.87, 0.82	yes	no
180830A	(110)	350	33	3.06	1.31, 0.75, < 0.4	yes	no
180830B	(110)	350	5.5	1.40	all < 0.4	n/a	no
180830C	(110)	350	11	2.05	0.68, 0.55, 0.50	yes	no
180830D	(110)	350	22	3.18	1.98, 1.75, 0.56	yes	no
180920A	(110)	320	21.0	4.52	1.82, 1.69, 1.65	yes	no
180924A	(110)	400	22.9	3.89	1.92, 1.33, < 0.4	yes	no
181108A	(110)	300	22.8	3.88	1.65, 1.53, 1.48	yes	no
181108A anneal2	(110)	600 for 135 min.	22.8	6.58	1.65, 1.56, 1.50	yes	no
181108A anneal3	(110)	700 for 240 min.	22.8	7.45	1.70, 1.60, 1.54	yes	no
181108B	(110)	250	23.4	2.93	1.68, 1.13, 1.08	yes	no
181108B anneal1	(110)	600 for 300 min.	23.4	10.9	2.05, 1.91, 1.82	yes	no
181203A	(110)	320	21.0	5.20	1.79, 1.73, 1.68	yes	yes
181204D	(001)	320	62	5.76	all < 0.4	n/a	no
181204E	(100)	320	21.8	4.53	1.06, 0.84, 0.72	yes	no
181204E anneal1	(100)	600 for 300 min.	21.8	4.51	0.62, < 0.4, < 0.4	yes	no
181205A	(101)	320	18.6	26.9	all < 0.4	n/a	yes
190103A	(110)	320	21.7	4.40	2.01, 1.66, 1.62	yes	yes
190103B	(110)	320	11.5	3.43	1.25, 1.11, 1.04	yes	yes
190103C	(110)	320	5.8	1.61	all < 0.4	n/a	yes
190209A	(110)	320	48	3.41	all < 0.4	n/a	no
190213C	(110)	320	25.6	4.98	1.86, 1.79, 1.73	yes	yes
190213D	(110)	320	17.2	3.68	1.46, 1.21, 1.16	yes	yes
190222A	(110)	320	14.2	2.64	1.13, 0.92, 0.85	yes	yes
190426A	(101)	320	19.3	27.7	all < 0.4	n/a	yes
HP-ARPES-1	(110)	300	30.2	7.67	2.49, 2.40, 2.33	no	no
HP-ARPES-2	(110)	300	14.6	3.74	1.66, 1.56, 1.48	no	no
HP-ARPES-3	(110)	300	8.3	2.76	0.45, < 0.4, < 0.4	no	yes

Table 5.1: Electrical and structural properties of over 30 RuO₂ thin films synthesized on TiO₂ substrates that were measured as part of this dissertation. For samples that were subject to post-growth annealing (the temperatures and durations in minutes of the annealing treatments are listed in the table under the T_s column), the annealing was carried out in a tube furnace with the film surface exposed to ambient atmosphere.

In more microscopic detail, the data presented in this chapter indicate that compression along the rutile c -axis likely plays a key role in stabilizing superconductivity under strain in RuO_2 . XRD measurements on superconducting $\text{RuO}_2(110)$ samples show that the rutile a and b axes are under modest amounts of tensile strain (up to +2.3% at 295 K), with small amounts of orthorhombic splitting between $[1\bar{1}0]$ (in-plane) and $[110]$ (out-of-plane), whereas the rutile c -axis lies purely in plane and is subject to a large lattice mismatch with the c -axis of the TiO_2 substrates (up to -4.7% at 295 K). By contrast, XRD measurements on non-superconducting $\text{RuO}_2(101)$ samples show that the rutile b -axis lies purely in plane and is under almost the same amount of tension as in $\text{RuO}_2(110)$ samples, but the rutile a and c axes both point partially out-of-plane and are free to relax their lengths to adopt nearly bulk-like values, only subject to the combined constraint that $\sqrt{a^2 + c^2}$ match that of the TiO_2 substrates along $[\bar{1}01]$. Our attempts to quantify the precise levels of c -axis compression that optimize the superconducting T_c in partially strain-relaxed $\text{RuO}_2(110)$ samples were hampered by overlapping contributions from the substrate and film to the total measured XRD signal. Nonetheless, we note that even the thickest (*i.e.*, most strain-relaxed) superconducting $\text{RuO}_2(110)$ samples in Figure 5.13 and Figure 5.14 only show appreciable amounts of scattering (when q_{\parallel} is aligned with $\text{TiO}_2[001]$) for $|q_{\parallel}| \gtrsim 0.66 \text{ \AA}^{-1}$, corresponding to average c -axis lattice spacings of $\lesssim 3.03 \text{ \AA}$. Since all c values in this range are much less than $c = 3.11 \text{ \AA}$ measured for bulk RuO_2 , our claim that large ($\gtrsim 2.6\%$) c -axis compressions are necessary to significantly enhance the energy scale of superconductivity in RuO_2 appears to be firmly established.

Because RuO_2 is known to be a rather conventional metal from the standpoint of charge transport, it seems likely that the strain-stabilized superconductivity observed here can be rationalized in terms of established theories for conventional (electron-phonon mediated) superconductors. In such materials, T_c is usually parameterized according to the Bardeen-Cooper-Schrieffer (weak-coupling) limit of the McMillan-Allen-Dynes formula [35, 36],

$$T_c \sim \omega_{\text{ln}} \exp\left(-\frac{1}{\lambda}\right) = \omega_{\text{ln}} \exp\left(-\frac{M \langle \omega^2 \rangle}{N(E_F) \langle I^2 \rangle}\right) \quad (5.3)$$

where ω_{ln} is a suitable average phonon frequency and λ is the dimensionless electron-phonon coupling strength that appears in Migdal-Eliashberg theory. In the isotropic regime, the average λ can be further decomposed into the ionic mass(es) M , $\langle \omega^2 \rangle$, the electron-phonon matrix element averaged over the Fermi surface $\langle I^2 \rangle$ and the density of states (DOS) near the Fermi level (E_F), $N(E_F)$ [243]. Changes to T_c are commonly discussed in terms of how quantities in the argument of the exponential vary, which can be roughly separated into two channels:

- **Phonon softening:** a shift of the phonon spectrum to lower frequencies *decreases the numerator* of the argument of the exponential in Equation 5.3, thereby increasing T_c .
- **Hopfield parameter:** increases in the product $\eta \equiv \langle I^2 \rangle N(E_F)$, often called the Hopfield parameter [243, 244], *increases the denominator* of the argument of the exponential in Equation 5.3, thereby increasing T_c .

One of the main advantages of strain engineering exploiting epitaxy is that it allows for the use of sophisticated spectroscopic probes such as ARPES or STM that require access to the sample surface [176], which in turn enable direct experimental measurements of normal-state electronic properties that appear on the right side of Equation 5.3. In chapter 6, we pursue this approach for strained RuO_2 thin films to better understand the mechanism underlying the T_c enhancement. We show that c -axis compression naturally leads to an increase in $N(E_F)$, which likely contributes to stabilizing superconductivity under strain.

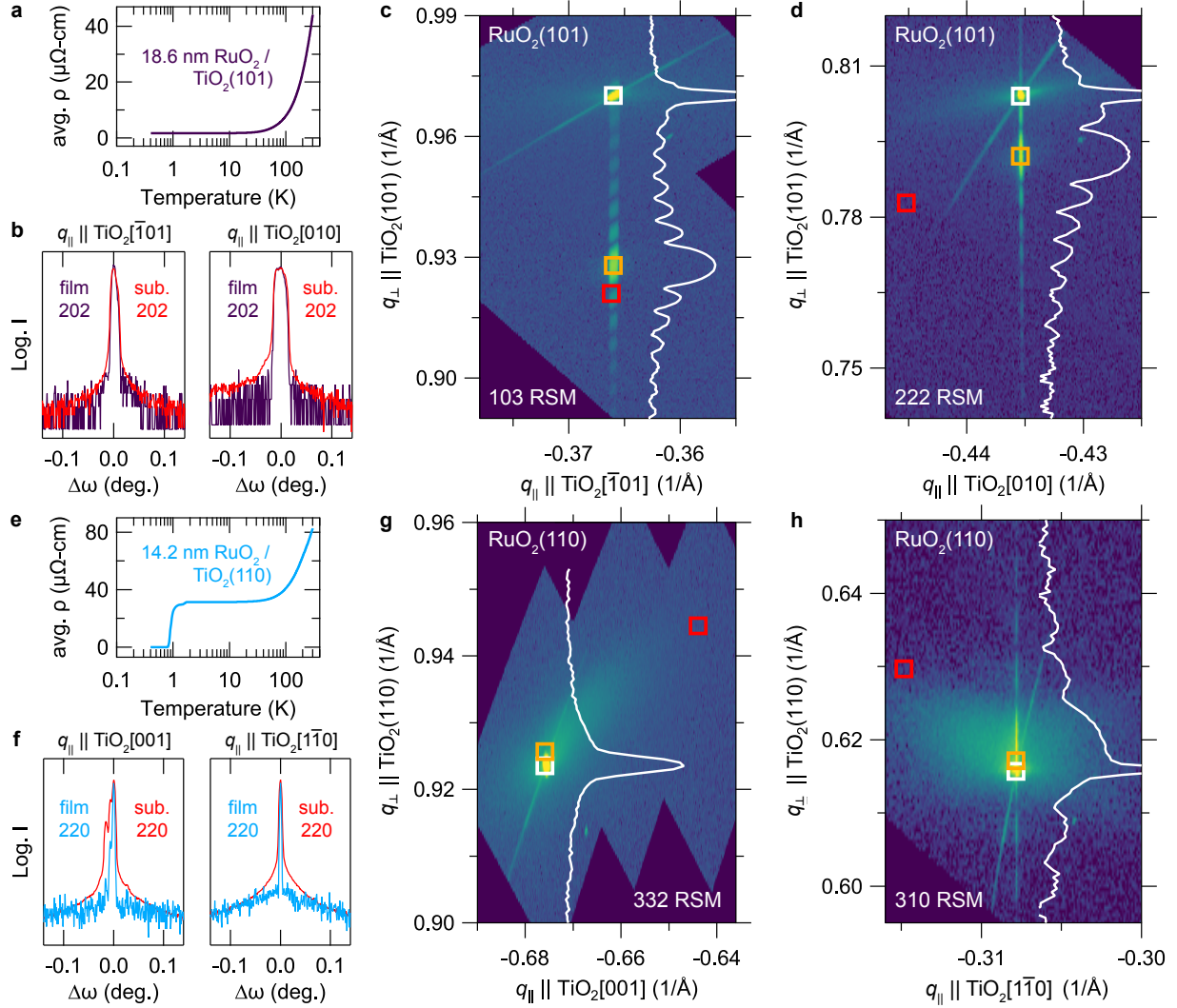


Figure 5.8: (a) Zero-field $\rho(T)$ (geometric mean) data for a non-superconducting 18.6 nm thick RuO₂(101) sample. (b) Rocking curves for this sample, taken at 2θ values corresponding to the primary film and substrate 202 reflections. The FWHMs are 0.0081° (0.021°) with $q_{||} \parallel [\bar{1}01]$ ($q_{||} \parallel [010]$). (c - d) RSMs for this sample near the 103 and 222 reflections. Solid white lines are the scattering profiles along the CTRs. White, red, and orange squares represent the central peak positions expected for bulk TiO₂, bulk RuO₂ and commensurately strained RuO₂ thin films, respectively. The in-plane lattice mismatches of TiO₂ with bulk RuO₂ can be read off directly from the lateral offsets of the white and red squares: $+0.04\%$ (tensile) along $[\bar{1}01]$ in (c) and $+2.3\%$ along $[010]$ in (d). (e - h) Analogous electrical and structural data for a superconducting 14.2 nm thick RuO₂(110) sample. The rocking curve FWHMs at 220 are 0.0042° (0.0036°) with $q_{||} \parallel [001]$ ($q_{||} \parallel [1\bar{1}0]$), although are clearly multiple peaks present in the former data sets. RSMs for RuO₂(110) at this film thickness show clear signatures of partial strain relaxation, because of the larger absolute levels of in-plane lattice mismatch with TiO₂: -4.7% along $[001]$ in (g) and $+2.3\%$ in (h).

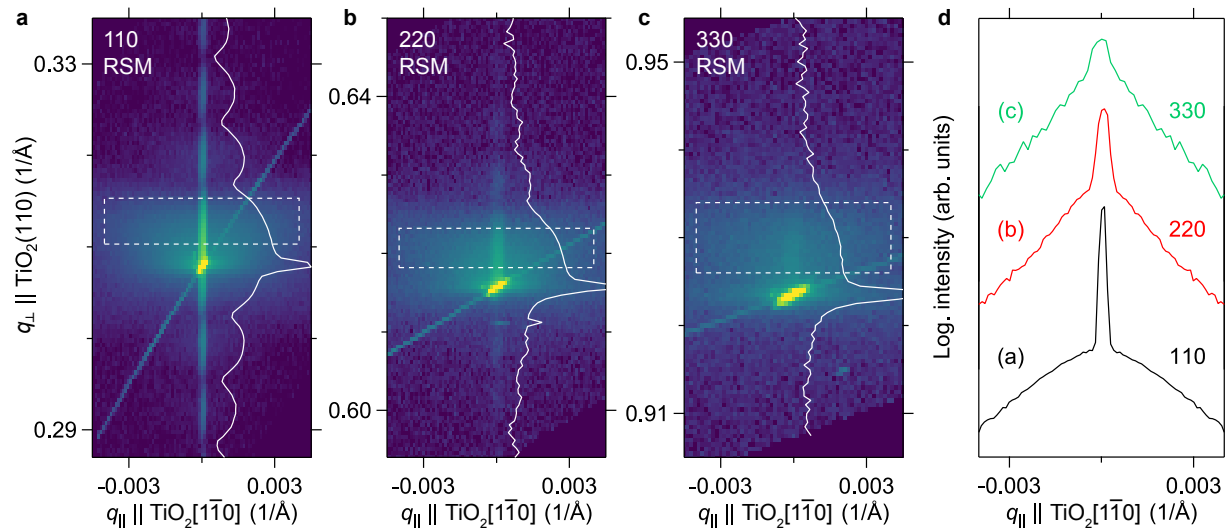


Figure 5.9: (a - c) RSMs measured near the 110, 220, and 330 Bragg reflections for a 14.2 nm thick $\text{RuO}_2 / \text{TiO}_2(110)$ sample. Solid white lines are the scattering profiles along the specular CTR. (d) Line cuts of the intensities averaged over the dashed boxes in (a - c) show rocking curves with a two-component narrow plus broad structure characteristic of partially strain relaxed epitaxial thin films. The in-plane momentum transfer q_{\parallel} is aligned with $\text{TiO}_2[1\bar{1}0]$ in all panels; similar results are obtained with q_{\parallel} along $\text{TiO}_2[001]$ —cf. Figure 5.14.

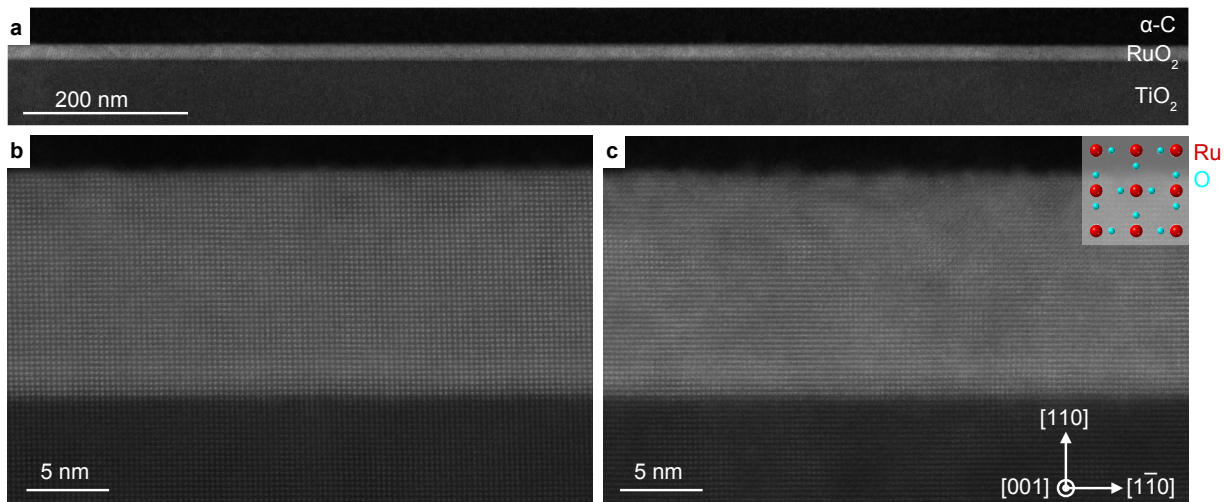


Figure 5.10: STEM images showing variation in local crystalline quality across a superconducting 14.2 nm thick $\text{RuO}_2 / \text{TiO}_2(110)$ sample. (a) Confirmation of continuous film growth over μm length scales. (b) A crystallographically coherent region of the superconducting film shown in Figure 5.7. (c) A relatively less-ordered region of the same film shown in the same projection. Inset shows the expected structure for this projection (not to scale).

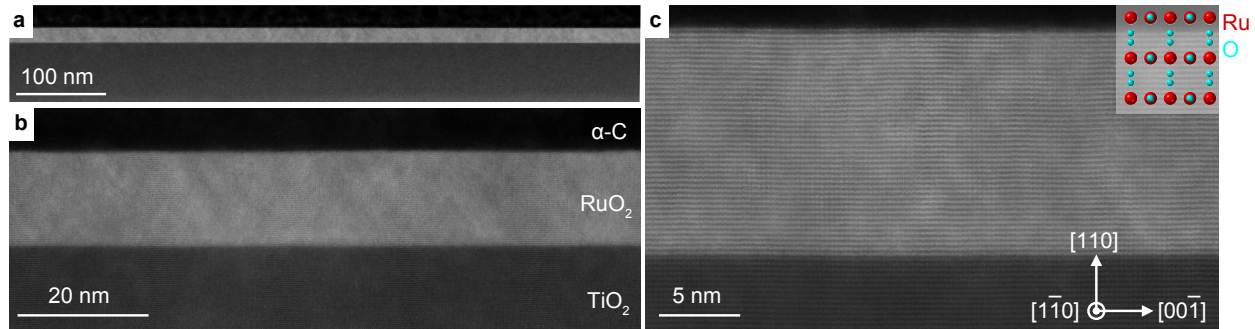


Figure 5.11: STEM images acquired along the $[1\bar{1}0]$ projection for a superconducting 14.2 nm thick $\text{RuO}_2 / \text{TiO}_2(110)$ sample demonstrate the effects of the 4.7% compressive strain applied by the $[001]$ axis of the TiO_2 substrate. **(a)** Continuous film growth is observed across the full length of the STEM lamella, shown here without interruption over several hundreds of nm. **(b)** Epitaxial film growth observed in the orthogonal projection is again confirmed. **(c)** Atomic-resolution image shows the crystalline quality of the strained RuO_2 film. Inset shows the expected structure for this projection (not to scale).

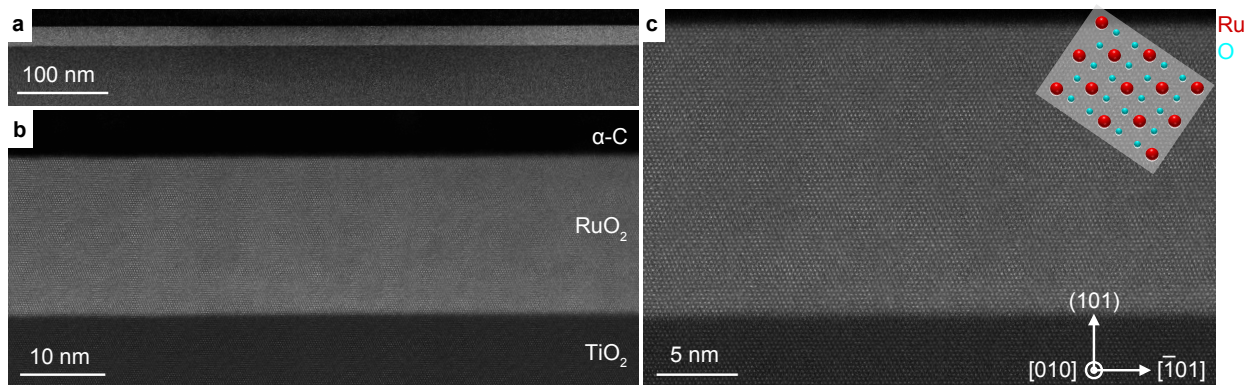


Figure 5.12: STEM structural characterization of a non-superconducting 18.6 nm thick $\text{RuO}_2 / \text{TiO}_2(101)$ sample. **(a)** As in the superconducting $\text{RuO}_2(110)$ samples, continuous film growth is observed across the length of the STEM lamella. **(b)** Epitaxial growth between the RuO_2 film and TiO_2 substrate is again confirmed. Here, however, the observed contrast is comparatively smooth across the film without the clear signs of high strain observed in the $\text{RuO}_2(110)$ sample. **(c)** Atomic-resolution STEM image demonstrating the high crystalline quality of the $\text{RuO}_2 / \text{TiO}_2(101)$ film. Inset shows the expected structure for this projection (not to scale).

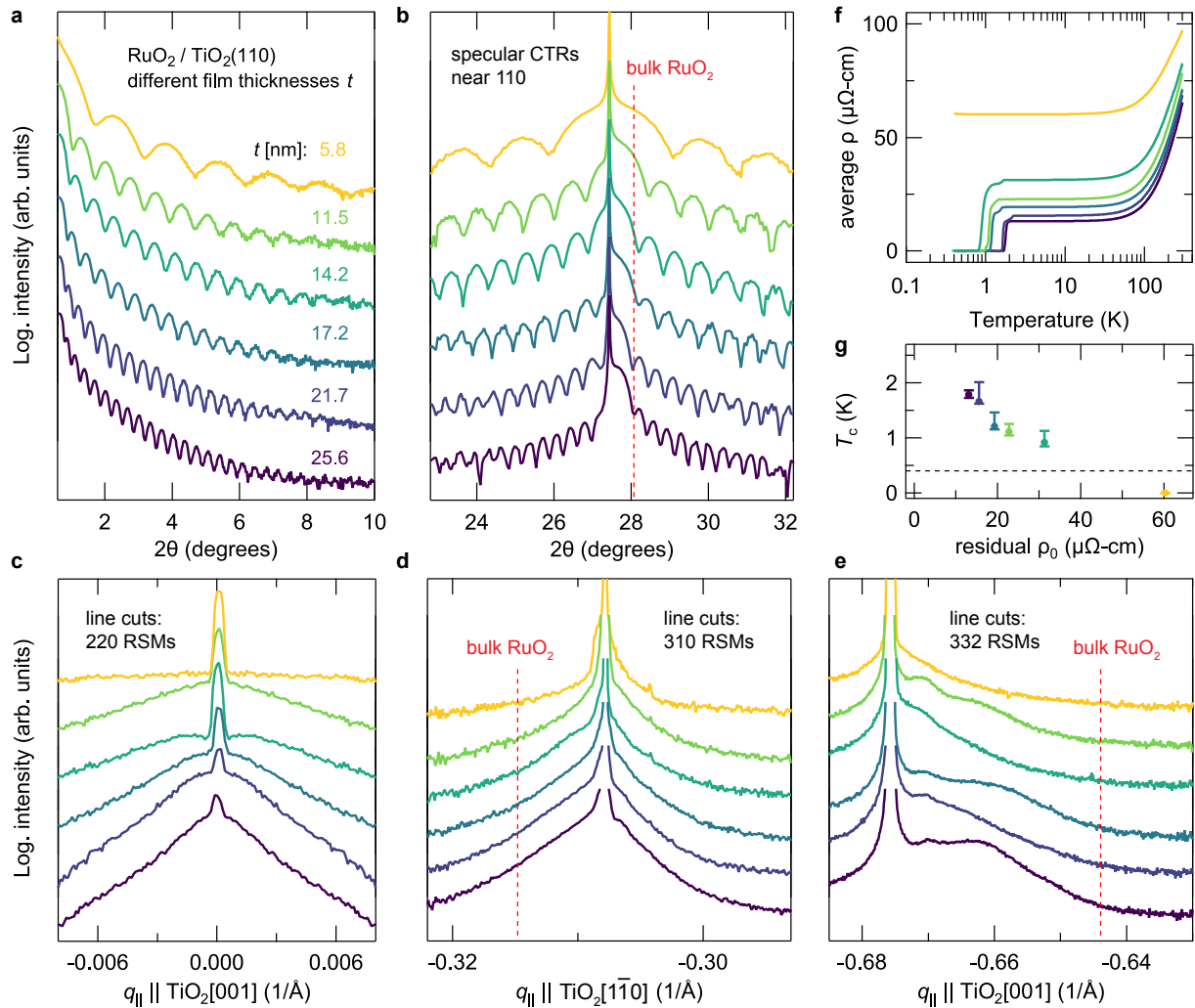


Figure 5.13: (a) X-ray reflectivity and (b) x-ray diffraction data along the specular CTR show comparable levels of flatness and crystalline order along the out-of-plane direction for all $\text{RuO}_2(110)$ samples of different film thicknesses, t . (c - e) Average line cuts versus q_{\parallel} through the 220, 310, and 332 RSMs (fully \mathbf{q} -resolved data are shown in Figure 5.14) indicate that all samples with $t > 5.8$ nm exhibit partial strain relaxation. (f - g) Zero-field $\rho(T)$ data show that thinner films generally have higher residual resistivities and lower superconducting T_c s. The horizontal dashed line in (g) represents the base temperature attainable in our refrigerator, 400 mK.

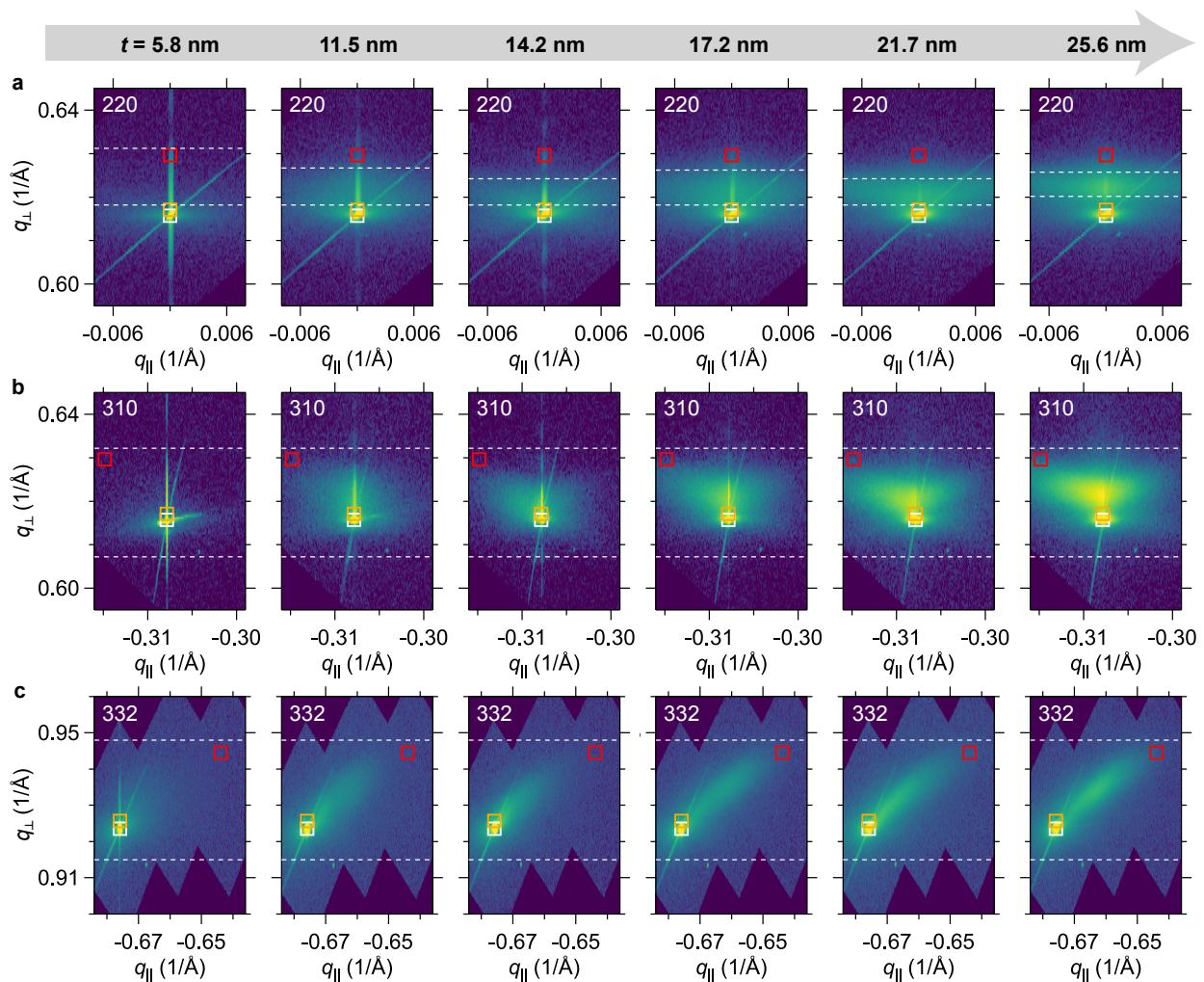


Figure 5.14: (a) RSMs along the specular CTR near the 220 Bragg reflections for $\text{RuO}_2 / \text{TiO}_2(110)$ samples with increasing film thicknesses t , moving from left to right. q_{\parallel} is aligned with $[001]$ in all panels, although the phenomenology is similar with q_{\parallel} along $[1\bar{1}0]$ —cf. Figure 5.9. (b) Thickness-dependent RSMs near the off-specular 310 Bragg reflections where q_{\parallel} is purely along $[1\bar{1}0]$. (c) Same as (b), but near the 332 Bragg reflections where q_{\parallel} is purely along $[001]$. White, red, and orange squares represent the central peak positions expected for bulk TiO_2 , bulk RuO_2 , and commensurately strained $\text{RuO}_2(110)$, as in Figure 5.8. The line cuts plotted in Figure 5.13(c - e) are averaged over the ranges of q_{\perp} of the RSMs between the horizontal white dashed lines.

CHAPTER 6

STRAIN-INDUCED CHANGES TO THE ELECTRONIC STRUCTURE OF RuO_2

Having established the epitaxial strain-induced origin of the superconductivity in $\text{RuO}_2/\text{TiO}_2(110)$ thin films in chapter 5, we now explore its underlying explanation in this chapter using a combination of density functional theory (DFT) calculations and experimental measurements of the electronic structure by angle-resolved photoemission spectroscopy (ARPES). Since the superconducting T_c of strained $\text{RuO}_2(110)$ is about an order of magnitude lower than the base temperature achievable in our ARPES system (and the single-particle excitation gap Δ in the superconducting phase is about an order of magnitude smaller than the highest energy resolution achievable with our electron spectrometer), all of the ARPES data shown here are taken in the normal metal state at temperatures $T \gg T_c$. Thus our goal is not to directly measure features of the superconductivity in ARPES, but rather to understand strain-induced changes to features of the normal-state electronic structure that could plausibly lead to enhanced superconducting properties, according to the theoretical framework for understanding conventional superconductivity described in previous chapters. Perhaps most importantly, we seek to benchmark how accurately DFT captures strain-dependent changes to the normal-state electronic structure, in order to determine if computational schemes built on DFT—such as *ab initio* Migdal-Eliashberg calculations—can be reliably used as a tool to engineer aspects of the superconductivity in strained RuO_2 and other artificially designed material systems.

The outline of the chapter is as follows: In section 6.1, we describe the expectations of DFT for the electronic structure of bulk RuO_2 and two of its epitaxially strained variants studied in chapter 5, $\text{RuO}_2(110)$ and $\text{RuO}_2(101)$. In section 6.2, we present the experimentally measured electronic structure of nearly coherently strained $\text{RuO}_2(110)$ samples and compare the results with DFT. Finally, in section 6.3, we show how the experimentally

measured electronic structure evolves with strain by comparing data from section 6.2 with results for partially strain relaxed RuO₂(110) samples and results for coherently strained RuO₂(101) samples, and we assess the extent to which DFT calculations correctly account for these strain-dependent trends.

6.1 Electronic structure calculations

6.1.1 Technical details

Non-magnetic density functional theory (DFT) calculations for RuO₂ were performed using the Quantum ESPRESSO software package [6] using fully relativistic ultrasoft pseudopotentials for Ru and O [182]. We represented the Kohn-Sham wavefunctions in a basis set of plane waves extending up to a kinetic energy cutoff of 60 Ry, and used a cutoff of 400 Ry for representing the charge density. Brillouin zone integrations were carried out on an $8 \times 8 \times 12$ k -mesh with 70 meV of Gaussian smearing. Perdew, Burke and Ernzerhof's parametrization of the generalized gradient approximation (GGA) was employed as the exchange-correlation functional [187], supplemented by an on-site correction of $+U_{\text{eff.}} = U - J = 2$ eV within spheres surrounding the Ru sites, following Ref.[204]. Spin-orbit coupling (SOC) was included in the self-consistent field cycles and in all subsequent calculations of band energies and other quantities for the converged charge density thus obtained.

After obtaining self-consistent Kohn-Sham eigenstates via DFT, we used the pw2wannier and Wannier90 codes [186] to construct 20 Wannier functions spanning the manifold of eigenstates surrounding E_F (20 = 10 Kramers-degenerate d -orbitals per Ru atom \times 2 Ru atoms per unit cell). Following Ref.[202], to account for the non-symmorphic space group symmetries of rutile-like crystal structures, we referenced the trial orbitals

employed in the Wannierisation routine to locally rotated coordinate systems centered on the two Ru sites within each unit cell. Orbital designations employed later in this chapter such as $d_{||}$ and (d_{xz}, d_{yz}) refer to projections onto this basis of Wannier functions. The more computationally efficient Wannier basis was used to calculate quantities that required denser k meshes to be properly converged, such as the the projected Fermi surface in Figure 6.6 ($51 \times 51 \times 51$ k -mesh) and the near- E_F density of states traces in Figure 6.1, Figure 6.2, and Figure 6.3 ($32 \times 32 \times 48$ k -meshes).

Finally, because the RuO_2 samples studied in this dissertation are thin films subject to biaxial epitaxial strains imposed by differently oriented rutile TiO_2 substrates, we performed DFT + Wannier calculations for several different crystal structures of RuO_2 as summarized in subsection 6.1.2. We used the ISOTROPY software package [245] to study distortions of the parent tetragonal rutile crystal structure that are induced in biaxially strained thin films. Crystal structures and Wannier functions were visualized using the VESTA software package [246].

6.1.2 Structural relaxations

One of the central themes of this work is the exploration of strain-induced changes to the electronic structure in epitaxial thin films of RuO_2 subject to biaxial epitaxial strains imposed by differently oriented rutile TiO_2 substrates. To model this situation computationally within the framework of DFT, we started by using the Vienna Ab Initio Software Package [9, 10] to perform full structural relaxations (of lattice parameters and internal coordinates) to minimize the DFT + U -computed total energy of RuO_2 in the ideal tetragonal rutile crystal structure (space group #136, $P4_2/mnm$). Structural relaxations employed the same exchange-correlation functional and calculational parameters as for the DFT + U ($U = 2$ eV) calculations described in subsection 6.1.1, and forces were converged to

$< 1 \text{ meV}/\text{\AA}$.

Throughout the remainder of this chapter, we refer to DFT results for this minimum energy structure as “bulk RuO_2 ”. The actual lattice parameters for this structure, ($a_{\text{bulk}} = 4.517 \text{ \AA}$, $c_{\text{bulk}} = 3.130 \text{ \AA}$), overestimate the experimentally measured lattice parameters at 295 K for RuO_2 single crystals of ($a = 4.492 \text{ \AA}$, $c = 3.106 \text{ \AA}$) by $< 1\%$, due to well-established deficiencies of the generalized gradient approximation. With the former as the bulk reference structure, we then simulated biaxial epitaxial strains to (110)-oriented TiO_2 substrates by performing constrained structural relaxations for RuO_2 in which the in-plane lattice parameters $c = (1 - 0.047) \times c_{\text{bulk}}$ and $d_{1\bar{1}0} = (1 + 0.023) \times d_{1\bar{1}0, \text{bulk}}$ were held fixed, while the out-of-plane lattice constant d_{110} and all other internal coordinates of the structure were allowed to relax so as to minimize the total energy. The fixed compression and expansion of c and $d_{1\bar{1}0}$, respectively, correspond to the experimentally measured lattice mismatches between TiO_2 and RuO_2 single crystals at 295 K [204, 221].

Within this scheme, DFT + U predicts that commensurately strained $\text{RuO}_2(110)$ thin films will have an out-of-plane lattice constant $d_{110} = (1 + 0.017) \times d_{110, \text{bulk}}$, which compares reasonably well with the 2.0% expansion of d_{110} measured experimentally on a 5.8 nm thick $\text{RuO}_2(110)$ film. Because the splitting of d_{110} and $d_{1\bar{1}0}$ in strained $\text{RuO}_2(110)$ breaks the non-symmorphic glide plane symmetry of the parent rutile structure, we used a base-centered orthorhombic structure (space group #65, $Cmmm$) with lattice constants of $c \times 2d_{1\bar{1}0} \times 2d_{110}$ for DFT simulations of $\text{RuO}_2(110)$. The primitive unit cell of this $Cmmm$ structure contains the same number of atoms as the parent rutile unit cell, so there is no apparent doubling and/or folding of the bands in spaghetti plots that compare the bandstructures of $\text{RuO}_2(110)$ and bulk RuO_2 , such as in Figure 6.2 or Figure 6.3.

To simulate the electronic structure of commensurately strained (101)-oriented RuO_2 thin films, we adopted a slightly different approach, since it is not straightforward to perform constrained structural relaxations with DFT in such a low-symmetry situation.

Specifically, we took the rutile b axis to be under 2.3% tension, $b = (1 + 0.023) \times b_{\text{bulk}}$, as dictated by the lattice mismatch of RuO_2 with TiO_2 along this direction. On the other hand, the lengths of the rutile a and c axes are free to adjust their lengths, but are subject to the simultaneous constraints:

$$\sqrt{a^2 + c^2} = \sqrt{(a_{\text{TiO}_2})^2 + (c_{\text{TiO}_2})^2} = 5.464 \text{ \AA} \quad (6.1)$$

$$|\mathbf{q}_{202}| = \sqrt{\left(\frac{2}{a}\right)^2 + \left(\frac{2}{c}\right)^2} = 0.792 \text{ \AA}^{-1} \quad (6.2)$$

$$|\mathbf{q}_{103}| = \sqrt{\left(\frac{1}{a}\right)^2 + \left(\frac{3}{c}\right)^2} = 0.998 \text{ \AA}^{-1} \quad (6.3)$$

$$|\mathbf{q}_{402}| = \sqrt{\left(\frac{4}{a}\right)^2 + \left(\frac{2}{c}\right)^2} = 1.114 \text{ \AA}^{-1} \quad (6.4)$$

Equation 6.1 ensures that the film is lattice matched to the substrate along $[\bar{1}01]$, and the remaining three equations ensure that the d -spacings for the $HKL = 202, 103,$ and 402 Bragg reflections reproduce the values measured experimentally for epitaxially strained $\text{RuO}_2(101)$ films¹—a proper lattice constant refinement would, of course, include data for many more reflections. Nonetheless, finding the best-fit solution to this system of four equations gives lattice constants of ($a = 4.501 \text{ \AA}, c = 3.077 \text{ \AA}$) in absolute units; dividing through by the experimentally measured lattice constants of bulk RuO_2 yields $a = (1 + 0.002) \times a_{\text{bulk}}$ and $c = (1 - 0.009) \times c_{\text{bulk}}$ as appropriately scaled inputs for DFT simulations. With $a \neq b \neq c$ and all angles between the primitive unit cell translations equal to 90° , the crystal structure for $\text{RuO}_2(101)$ DFT simulations was taken as the primitive orthorhombic

¹Note that in deriving these equations, we assumed for simplicity that the angle between the rutile a and c axes remains 90° in epitaxially strained films; small deviations away from this limit should be expected in reality, since this orthogonality is not guaranteed by any symmetry or constraint of the system.

space group #58, $Pnmm$. Table 6.1 summarizes all parameters of the crystal structures used in DFT simulations for bulk RuO_2 , $\text{RuO}_2(110)$, and $\text{RuO}_2(101)$.

Name	Space group	a_{rutile}	b_{rutile}	c_{rutile}	$d_{1\bar{1}0}$	d_{110}	Ru - apical O bond length(s)	Ru - equatorial O bond length(s)
bulk RuO_2 - expt.	#136	4.492	4.492	3.106	3.176	3.176	1.941	1.984
bulk RuO_2 - DFT	#136	4.517	4.517	3.130	3.194	3.194	1.945	2.002
$\text{RuO}_2(110)$ - DFT	#65	4.606	4.606	2.982	3.266	3.249	1.946, 1.957	1.980, 1.984
$\text{RuO}_2(101)$ - DFT	#58	4.525	4.618	3.101	3.233	3.233	1.969	2.000

Table 6.1: Crystal structures used in DFT simulations of RuO_2 (all units of length are given in Å)

6.1.3 Basic electronic structure of RuO_2

In Figure 6.1, we present the electronic structure of $\text{RuO}_2(110)$ calculated by DFT+ U ($U = 2$ eV), following the methods of Berlijn *et al.* [204]. Despite being constructed of RuO_6 octahedra with the same d^4 configuration as $(\text{Ca}, \text{Sr}, \text{Ba})\text{RuO}_3$, the electronic structure of RuO_2 is noticeably different from perovskite-based ruthenates. These distinctions arise from a sizable crystal-field splitting of the t_{2g} orbitals, such that the most natural description of the low-energy electronic structure is in terms of states derived from two distinct types of orbitals: $d_{||}$ and (d_{xz}, d_{yz}) , as illustrated by plots of Wannier functions in Figure 6.1(c). Viewed in the band basis, the differentiation in k -space between these orbitals becomes apparent: the near- E_F $d_{||}$ states form mostly flat (*i.e.*, non-dispersive) bands that are concentrated around the $k_{001} = \pi/c$ (ZRA) plane, whereas the (d_{xz}, d_{yz}) states form more isotropically dispersing bands that are distributed uniformly throughout the Brillouin zone. Notably, the much reduced bandwidths of the $d_{||}$ -derived states produce a large peak in the density of states (DOS) that responds sensitively to strain, as we illustrate in more detail below.

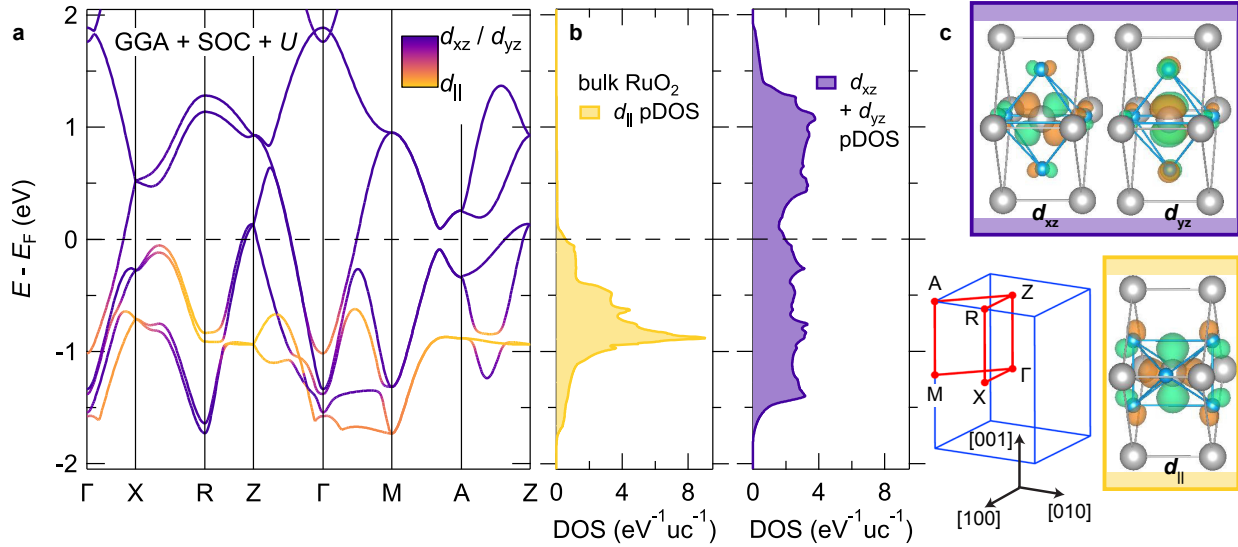


Figure 6.1: Non-magnetic electronic structure of bulk RuO_2 , calculated with DFT in the GGA, including spin-orbit coupling and a static $+U = 2$ eV correction on the Ru sites. The $E(\mathbf{k})$ bandstructure in (a) is calculated along the high-symmetry contour through the Brillouin zone colored red in (c), and the yellow-purple color scale indicates the magnitudes of projections onto Ru-centered Wannier functions with $d_{||}$ and (d_{xz}, d_{yz}) orbital characters, respectively. These Wannier functions are constructed from the near- E_F Kohn-Sham eigenstates and plotted in drawings of the crystal structure in (c). The \mathbf{k} -integrated partial density of states (PDOS) for these $d_{||}$ and (d_{xz}, d_{yz}) orbitals are shown in the middle panels in (b). The lower on-site energy and reduced bandwidth of the $d_{||}$ -derived states makes them nearly fully filled, leaving the (d_{xz}, d_{yz}) -derived states approximately half-filled, as noted previously in Figure 5.2.

6.1.4 Effects of strain on the electronic structure

In Figure 6.2(a), we show the strain dependence of the DFT-computed bandstructure (left panel) and corresponding DOS for $\text{RuO}_2(110)$, $\text{RuO}_2(101)$, and bulk RuO_2 (right panel). While the electronic structure for lightly strained $\text{RuO}_2(101)$ is almost identical to bulk, the calculations for $\text{RuO}_2(110)$ exhibit significant differences. The large, $d_{||}$ -derived peak in the DOS centered around a binding energy of 800 meV for bulk RuO_2 is split into multiple peaks for $\text{RuO}_2(110)$, several of which are shifted closer to the Fermi level, thereby increasing density of states near the Fermi level, $N(E_F)$. In our studies, we confirmed that this strain-dependent trend was robust against details of the DFT calculation, such

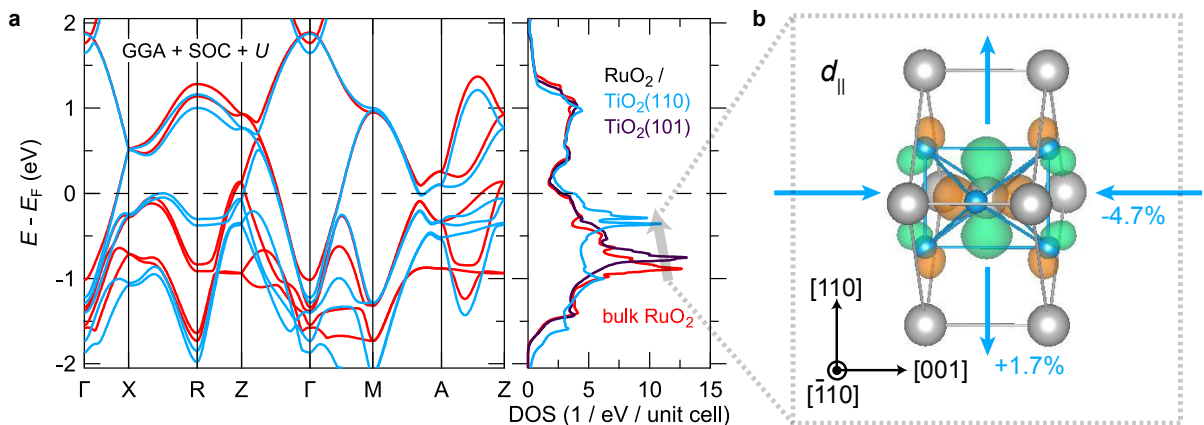


Figure 6.2: (a) DFT + U bandstructures and corresponding density of states traces for bulk RuO_2 and epitaxially strained $\text{RuO}_2(110)$ and $\text{RuO}_2(101)$. The $\text{RuO}_2(101)$ results are omitted from the spaghetti plot for clarity since they are very similar to bulk. (b) Plot of the d_{\parallel} orbital reproduced from Figure 6.1, indicating how the epitaxial strains imposed by the TiO_2 substrates on $\text{RuO}_2(110)$ films (blue arrows) cause the on-site energy of the d_{\parallel} states to *increase*: this shift of the d_{\parallel} -derived peak in the DOS towards E_F generates a concomitant enhancement of the DOS near E_F .

as whether U was finite—*cf.* Figure 6.3. Rather, by selectively turning certain distortions of the crystal structure “on” and “off” in the calculations, we found that the essential ingredient in producing an enhanced $N(E_F)$ is *c-axis compressive strain*. This mode of distortion generally moves the d_{\parallel} orbitals up in energy, making them closer to degenerate with the (d_{xz}, d_{yz}) states in a purely on-site picture of crystal-field splittings, as should be expected based on inspection of Figure 6.1(c) and how the lobes of these orbitals are oriented relative to the crystallographic axes.

6.1.5 Effects of $+U$ on the electronic structure

In Figure 6.3, we show the effects of including an *ad hoc* static mean-field $+U$ term on the Ru sites in DFT calculations. Adding such a phenomenological term to the Kohn-Sham Hamiltonian shifts the bands relative to each other (up/down in energy) so as to force the

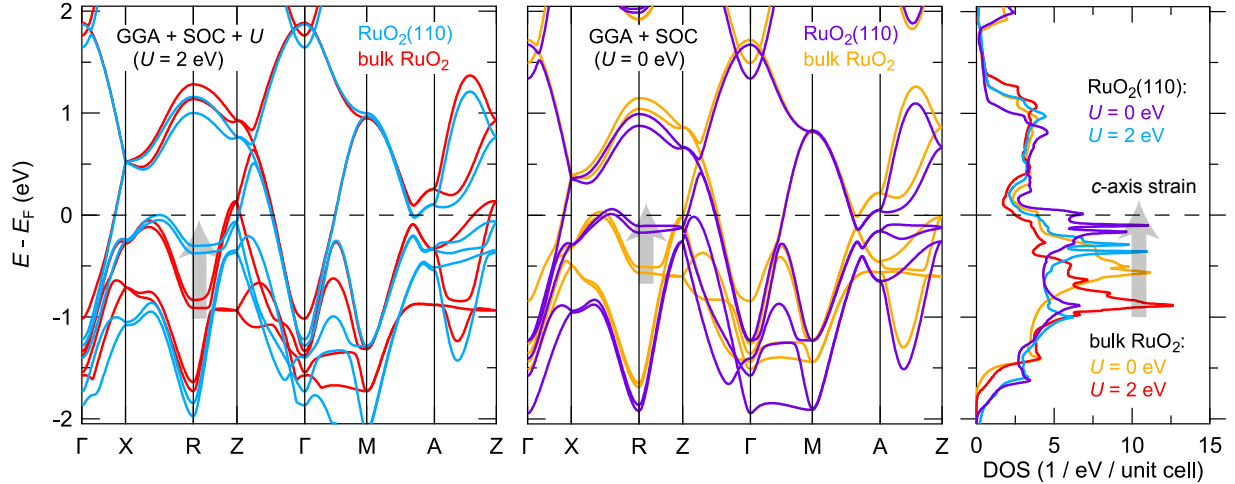


Figure 6.3: Strain dependence of the electronic structure of RuO_2 , according to DFT (+ U). Irrespective of whether U is finite (left panel) or zero (right panel), increasing the amount of c -axis compression upon going from bulk RuO_2 (red, orange) to $\text{RuO}_2(110)$ (blue, purple) causes the $d_{||}$ -derived peak in the DOS to shift towards E_F , as indicated by the gray arrows.

orbital occupancies towards integer fillings, rather than also shrinking the bandwidths, as would occur in a more realistic theory that includes dynamical electron-electron interactions. The blue and red traces are reproduced from the non-magnetic DFT + U ($U = 2$ eV) results presented in Figure 6.2. The purple and orange traces are the results of repeating GGA + SOC calculations for the same $\text{RuO}_2(110)$ and bulk RuO_2 crystal structures, but now setting $U = 0$ eV. The same shift of the $d_{||}$ flat bands towards E_F (indicated by gray arrows) observed in the $U = 2$ eV calculations and concomitant enhancement of the DOS near E_F are observed here when the c -axis compressive strain is increased upon going from bulk RuO_2 to $\text{RuO}_2(110)$. Although these strain-dependent *trends* in the electronic structure are robust against details of the calculations, Figure 6.3 also suggests that the calculated energy positions of the peaks in the DOS and the exact value of $N(E_F)$ should not be taken too seriously, as there are considerable theoretical uncertainties in these quantities based on what value of U is chosen. Lastly, we note that the minimum energy solution according to DFT is actually antiferromagnetically ordered when finite values of $U \gtrsim 1$ eV are employed [204]. While this qualitatively agrees with the recent ex-

perimental observations of commensurate spin-density wave (SDW) order in RuO₂ single crystals and thin films [204, 215], it is not possible in static mean-field based approaches such as DFT to stabilize self-consistent solutions with the small values of the ordered moment ($m < 0.05 \mu_B/\text{Ru}$) that are measured experimentally [204]. Therefore—since $m = 0$ is in some sense much closer to $m < 0.05 \mu_B/\text{Ru}$ than the values $m_{\text{DFT}} \approx 2 \mu_B/\text{Ru}$ obtained in self-consistent magnetic solutions to the Kohn-Sham equations—in all of our DFT simulations we enforce non-magnetic configurations, irrespective of U . More realistic treatments of the effects of $\mathbf{q}_{\text{SDW}} = (1\ 0\ 0)$ antiferromagnetic order on the electronic structure are left to future studies [247].

6.2 ARPES and LEED results for strained RuO₂(110) samples

In many other d^4 ruthenates, such as Sr₂RuO₄ or Ca₂RuO₄, incorrect electronic structures or even ground states are often predicted by purely DFT-based approaches owing to local many-body interactions not captured by these calculations [130, 248]. Therefore, it is imperative to directly compare the calculated electronic structure with experiment, in order to establish the reliability of any theoretically predicted dependence of the electronic structure on strain.

ARPES and low-energy electron diffraction (LEED) measurements on epitaxial thin films of RuO₂ synthesized by MBE were performed using the integrated Cornell MBE + *in situ* ARPES system described in chapter 2 and chapter 3. Unless specified otherwise, ARPES spectra and LEED data were collected at sample temperatures of $T = 10 - 20$ K and chamber pressures of $p = 5 - 10 \times 10^{-11}$ Torr. ARPES spectra were taken with energy resolutions of $\Delta E = 10$ meV for data acquired with He-I α photons ($h\nu = 21.2$ eV), and $\Delta E = 40$ meV for data acquired with He-II α photons ($h\nu = 40.8$ eV).

6.2.1 LEED images and angle-integrated valence band spectrum

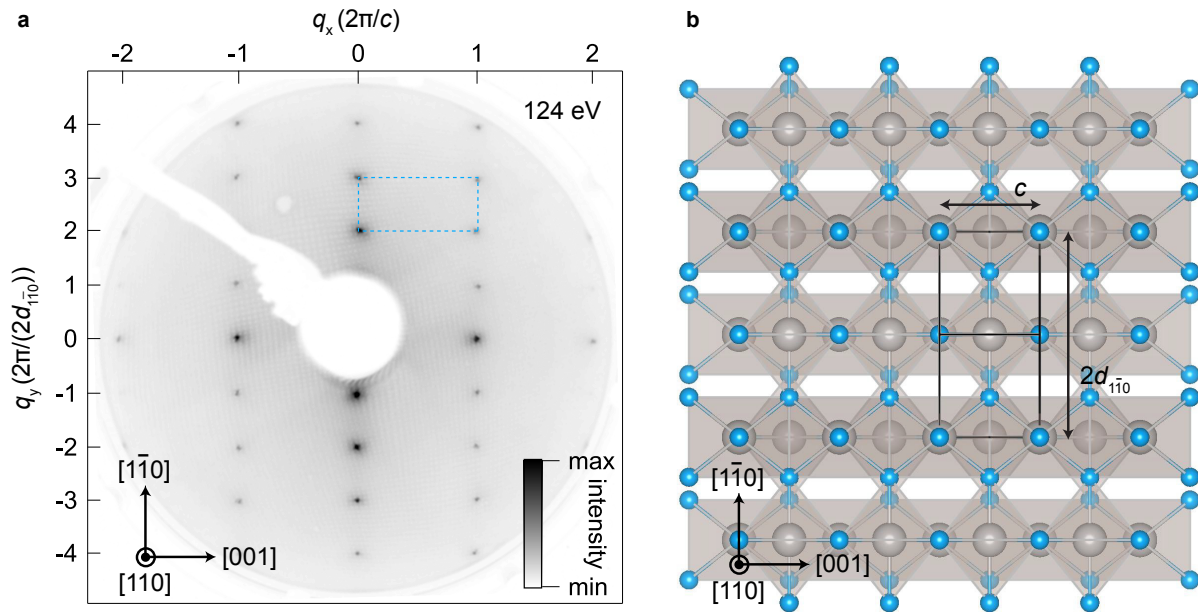


Figure 6.4: (a) LEED data acquired for a 7 nm thick $\text{RuO}_2(110)$ film at an incident beam energy of $E = 124$ eV. The primitive unit cell in reciprocal space (dashed blue outline) has the size and orientation expected for an bulk-truncated (*i.e.*, unreconstructed) (110)-oriented slab of RuO_2 in real space, as drawn in (b).

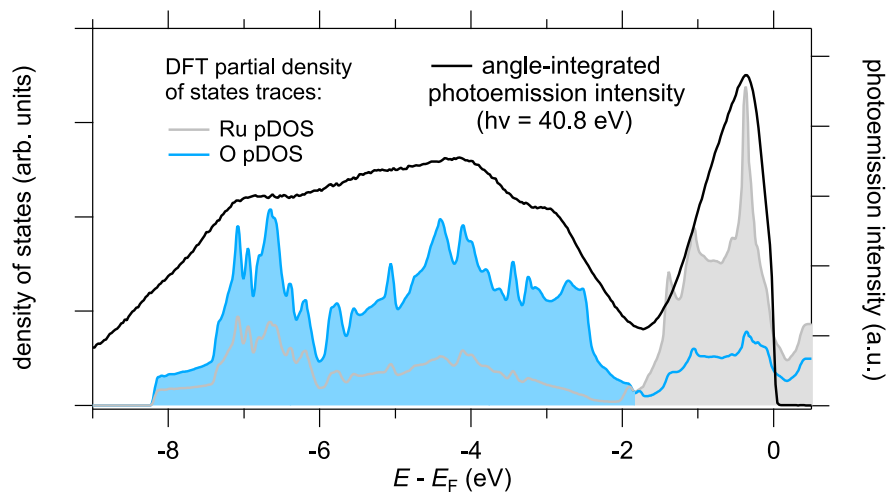


Figure 6.5: Angle-integrated valence band spectrum for $\text{RuO}_2(110)$ measured with He-II α light (black, right axis), compared with the DFT partial density of states (left axis) for oxygen 2p states (shaded blue) and ruthenium 4d states (gray), respectively.

In Figure 6.4(a), we show representative LEED data acquired for a 7 nm thick

RuO₂(110) film at an incident beam energy of $E = 124$ eV. The sharpness of the LEED spots suggests a high degree of surface crystallinity and an atomically flat surface morphology, in good agreement with the x-ray reflectivity results presented in chapter 5. Moreover, the spot pattern has the periodicities expected for an unreconstructed (110)-oriented rutile surface along both the [001] (horizontal) and $[1\bar{1}0]$ (vertical) in-plane crystallographic directions. To illustrate this, Figure 6.4(b) displays the crystal structure of RuO₂ viewed along [110]: in this orientation, the bulk unit cell (outlined in black) projects to a rectangular surface unit cell with dimensions c and $2d_{1\bar{1}0}$.

In Figure 6.5, we show an angle-integrated valence band spectrum recorded on the same 7 nm thick RuO₂(110) film with He-II α light (black, right axis), compared with the GGA + SOC partial density of states (left axis) for oxygen 2*p* states (shaded blue) and ruthenium 4*d* states (gray), respectively. All major features of the measured spectrum are well reproduced by the DFT calculations. The near- E_F states have primarily Ru character and the O-derived states mostly exist at higher binding energies, in good agreement with the usual trends for transition metal oxides. Note, however, that there are significant amounts of covalent mixing in both energy ranges: this is also indicated by the plots of the near- E_F Wannier functions in Figure 6.1, which show appreciable amounts of electron density on the oxygen sites.

6.2.2 Fermi surface and near- E_F quasiparticle dispersions

To further demonstrate the close agreement between theory and experiment, in Figure 6.6 we now zoom in on the region near E_F in a fully energy- and momentum-resolved fashion. Figure 6.6(a) shows the results of non-magnetic GGA + SOC + U ($U = 2$ eV) calculations for RuO₂(110) (similar to Figure 6.1, but now simulating strain to TiO₂(110)), highlighting the k -space differentiation stressed previously between states with primarily $d_{||}$

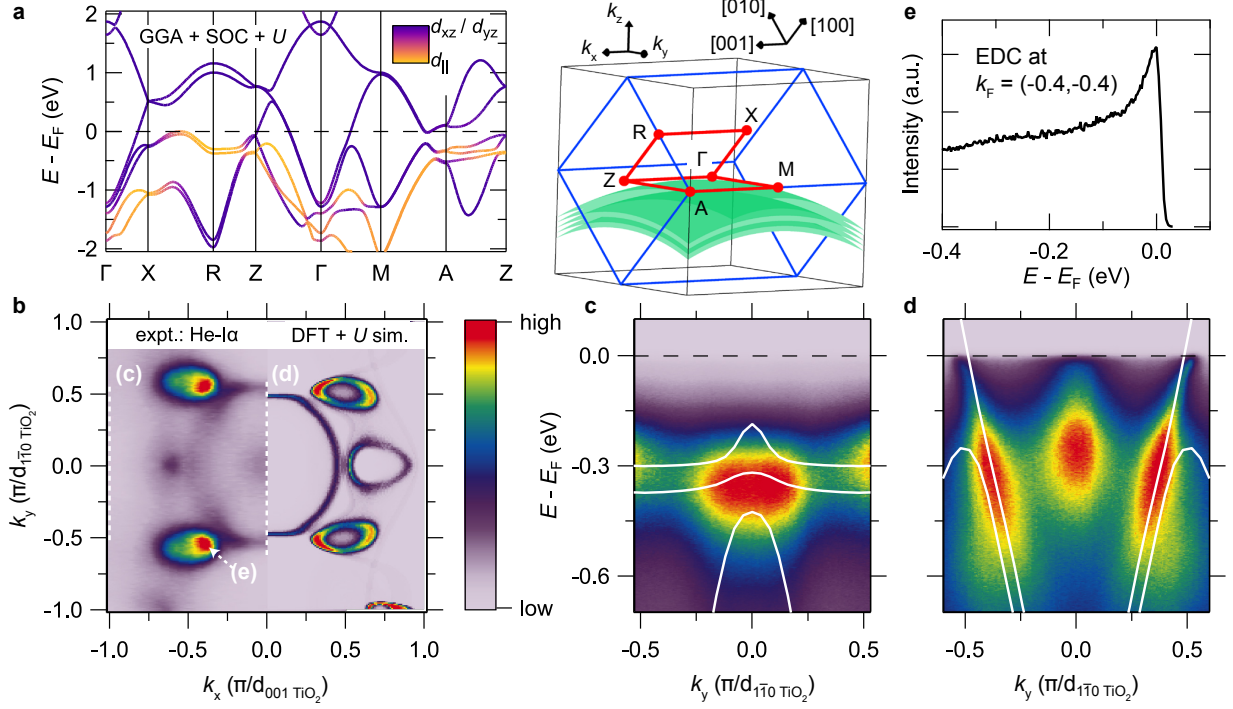


Figure 6.6: (a) Non-magnetic bandstructure of RuO₂(110) according to DFT. The color scale indicates the magnitudes of projections onto Ru-centered Wannier functions with d_{\parallel} and (d_{xz}, d_{yz}) orbital characters. The schematic in the middle shows the Brillouin zone of the parent tetragonal rutile structure in blue, the high-symmetry contour for the spaghetti plot in red, and the region probed on (110)-oriented surfaces at the experimental photon energy in green. (b) Slice through the Fermi surface measured on a 7 nm thick RuO₂(110) film (left), compared with the DFT Fermi surface (right) projected onto the green region of the Brillouin zone. (c - d) $E(\mathbf{k})$ spectra along the one-dimensional cuts indicated in b, showing flat bands with d_{\parallel} orbital character and more dispersive bands with (d_{xz}, d_{yz}) character, consistent with DFT expectations (solid white lines). (e) Energy distribution curve at the Fermi wavevector $k_F = (-0.4, -0.4)$ indicated in (b), showing the existence of sharply defined quasiparticle excitations near E_F .

and (d_{xz}, d_{yz}) orbital characters. The region of \mathbf{k} -space that is probed on (110)-oriented surfaces at the experimental photon energy ($h\nu = 21.2$ eV) is indicated by the curved green planes in the Brillouin schematic in Figure 6.6—for further details, see section 6.2.2. Projecting the DFT electronic structure onto this region produces the simulated Fermi surface shown on the right half of Figure 6.6(b), which agrees well with the experimentally measured Fermi surface of a 7 nm thick RuO₂(110) sample shown on the left half.

Figure 6.6(c, d) shows energy versus momentum spectra taken along the dashed lines indicated in Figure 6.6(b). In cut (c)—taken at $k_x = k_{001} = \pi/c$ —the spectrum is dominated by the flat $d_{||}$ -derived bands around a binding energy of 300 meV, whereas in cut (d)—taken at $k_x = k_{001} = 0$ —the (d_{xz}, d_{yz}) -derived bands are much more steeply dispersing and can be tracked down to several hundred meV below E_F . Both of these features are well reproduced by the bandstructure expected from DFT, which are overlaid on the experimentally measured spectra as white lines. The reasonable agreement of the experimental and DFT-calculated band velocities is consistent with earlier specific heat measurements of the Sommerfeld coefficient in RuO₂ single crystals, which indicate a relatively modest momentum-averaged quasiparticle mass renormalization of $\gamma_{\text{exp.}} = 1.45\gamma_{\text{DFT}}$ [210, 91]. Again, we note that this is in marked contrast with more strongly correlated d^4 perovskite-based ruthenates, where static mean-field theories that neglect local atomic-like Hund’s rule spin correlations predict effective masses that are many times smaller than experimentally measured [130, 137, 140, 249, 250].

Determination of $k_z = k_{110}$

Figure 6.6 compares ARPES data collected for a 7 nm thick RuO₂(110) sample with the results of DFT + U simulations. To make this comparison, it is necessary to determine what range of out-of-plane momenta $k_z = k_{110}$ in the initial state are probed by ARPES at a given final-state kinetic energy and momentum. This was established by plotting the DFT-computed $E(\mathbf{k})$ dispersions on top of the experimentally measured spectra along several one-dimensional cuts through momentum space measured over a small range of kinetic energies corresponding to near- E_F states at the given photon energy (21.2 eV), and allowing k_z to vary in the calculations so as to best match the experimental data.

Figure 6.7 shows representative examples of this procedure for experimental spectra taken along the one-dimensional cuts shown in Figure 6.6(d) (top row, $k_x = k_{001}$ fixed

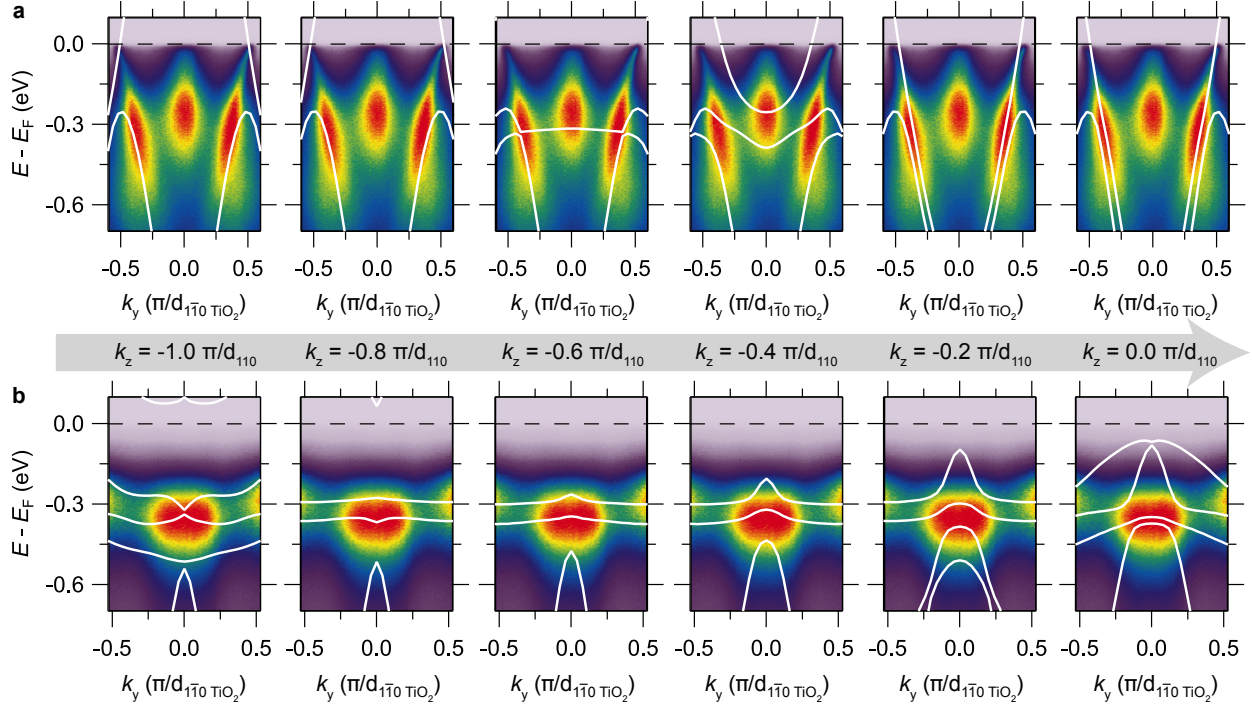


Figure 6.7: Determination of k_z probed by ARPES for RuO₂(110). Experimental ARPES spectra for a 7 nm thick RuO₂(110) sample are reproduced from Figure 6.6(d) in **(a)** and from Figure 6.6(c) in **(b)**; in both cases, the band dispersions from DFT + U ($U = 2$ eV) calculations are overlaid on the experimental data as white lines. For the data in **(a)** $k_x = k_{001}$ is fixed at zero and in **(b)** $k_x = \pi/c$. Moving from left to right, k_z is incremented in the DFT simulations in steps of $0.2 \pi/d_{110}$ starting from $-1.0 \pi/d_{110}$.

at zero) and in Figure 6.6(c) (bottom row, $k_x = \pi/c$). Moving from left to right, k_z is incremented in the DFT simulations in steps of $0.2 \pi/d_{110}$ starting from $-1.0 \pi/d_{110}$. For the panels in Figure 6.7(a), the magnitude of the Fermi wavevectors (k_F) and electron-like character of the band crossing E_F are best fitted by calculations with k_z in the range $-0.2 \rightarrow 0.0 \pi/d_{110}$. Likewise, for the panels in Figure 6.7(b), k_z values in the range $-0.6 \rightarrow -0.3 \pi/d_{110}$ best reproduce the measured spectra, although the results here are more ambiguous because of the insensitivity of the flat-band energies to the precise value of k_{110} . Therefore, we took the range of reduced initial-state out-of-plane momenta probed at normal emission ($k_x = k_y = 0$) to be $k_{z,i} = -0.1 \pm 0.1 \pi/d_{110}$. Assuming a free-electron-like model of final states, the final-state $k_{z,f}$ is given by the expression

$$k_{z,f} = \sqrt{\frac{2m_e(E_{kin.} \cos^2 \theta + V_0)}{\hbar^2}} = \frac{2\pi}{2d_{110}}N + k_{z,i} , \quad (6.5)$$

where m_e is the free electron mass, $E_{kin.}$ is the kinetic energy of the photoelectrons, θ is the emission angle relative to the surface normal, V_0 is the inner potential, and $2d_{110}$ is the spacing between equivalent lattice points along the out-of-plane direction (N can adopt any integer value). Substituting $E_{kin.} = 16.6 \pm 0.3$ eV, $\theta = 0^\circ$, $k_{z,i} = -0.1 \pm 0.1 \pi/d_{110}$, and $d_{110} = 3.23$ Å into Equation 6.5, we find that an inner potential of 13.7 ± 2.3 eV is compatible with our determination of $k_{z,i}$. Taking this same value of V_0 and setting $\theta = 30 - 35^\circ$ in Equation 6.5—as is appropriate for the experimental data in the panels displayed in Figure 6.7(b)—yields $k_{z,i} = -0.35 \pm 0.17 \pi/d_{110}$; visual inspection of the DFT bands for this range of $k_{z,i}$ show that the calculations also reasonably reproduce the experimental spectrum in this region of the Brillouin zone. The curved green planes drawn in the Brillouin zone schematic in Figure 6.6 are constructed by evaluating Equation 6.5 with $V_0 = 13.7$ eV and $N = 3$ for all (k_x, k_y) , and accounting for an intrinsic uncertainty of $\approx 0.2 \pi/d_{110}$ in k_z owing to the finite elastic escape depth of photoelectrons, which we take to be ≈ 5 Å.

Signatures of electron-boson coupling

Although we emphasized above that the Kohn-Sham quasiparticle dispersions from DFT + U calculations account well for the experimentally measured electronic structure of RuO₂(110), close inspection of the spectra reveals that more pronounced deviations from the DFT results occur below a characteristic energy scale $|E - E_F| < \omega_B$. In Figure 6.8(a), we show the spectrum from Figure 6.6(d) zoomed in on the region near the Fermi level, again overlaid with the DFT bands at the k_z determined in Figure 6.7. The presence of a well-isolated single band crossing E_F at $k_y \approx 0.5$ Å⁻¹, along with minimal dependence of

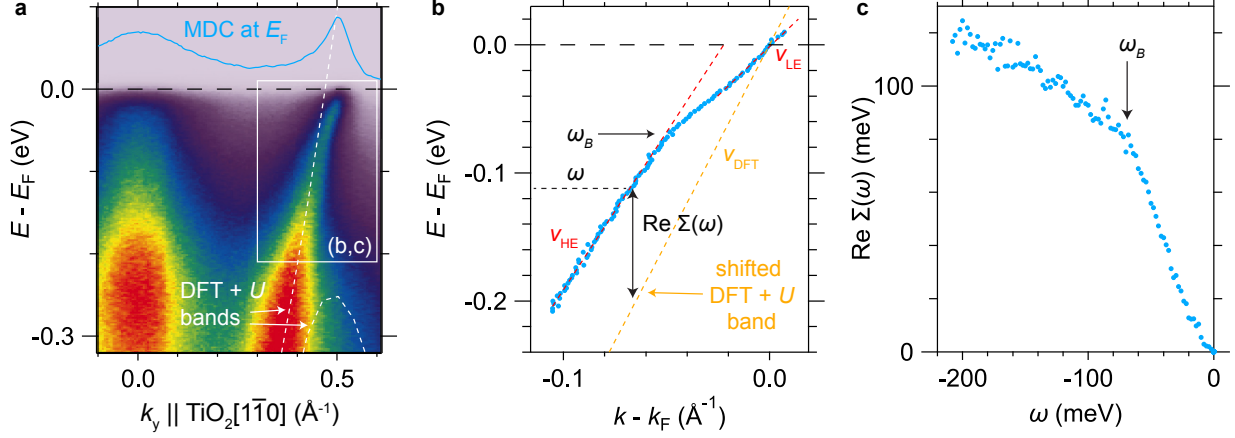


Figure 6.8: (a) $E(\mathbf{k})$ spectrum measured by ARPES along the $k_{001} = 0$ cut from Figure 6.6(d) for a 7 nm thick $\text{RuO}_2(110)$ sample. The DFT + U ($U = 2$ eV) bands are overlaid on the data as dashed white lines, and a representative momentum distribution curve (MDC) at E_F is shown in blue. By fitting individual MDCs to Lorentzians plus a linear background, we obtained the experimental $E(k - k_F)$ dispersion indicated by blue markers in panel (b), which exhibits a clear kink in the group velocities v of the quasiparticle excitations at the characteristic boson energy $|E - E_F| = \omega_B \approx 70$ meV. (c) The real part of the self-energy extracted from (b) as the difference between the the experimentally measured dispersion and the the shifted DFT + U band dispersion also shows an anomaly at ω_B .

the DFT-computed band velocities on the precise value of k_z (not shown)², together make this region of \mathbf{k} space suitable for a detailed analysis of the quasiparticle dispersions. In Figure 6.8(b), we plot the experimentally measured dispersion using blue markers; these points are obtained as the maxima of Lorentzian fits (plus a linear background) to the momentum distribution curves at each energy in the $E(\mathbf{k})$ spectrum from Figure 6.8(a). Using the experimental data at different binding energies as an internal reference, it is clear that the group velocity (*i.e.*, slope) of the quasiparticle excitations changes most abruptly at $\omega_B \approx 70$ meV: a linear fit to $E(\mathbf{k})$ of the high-energy (HE) excitations with $-210 \text{ meV} \leq E - E_F \leq -100 \text{ meV}$ gives $v_{HE} = 2.45 \pm 0.03 \text{ eV} \cdot \text{\AA}$, whereas a linear fit to $E(\mathbf{k})$ of the low-energy (LE) excitations with $-40 \text{ meV} \leq E - E_F \leq +10 \text{ meV}$ gives

²Recall that the out-of-plane momentum is not conserved in photoemission, so the experimentally measured data should be considered as a weighted average over initial states with a distribution of different k_z —*cf.* section 3.3.

$v_{LE} = 1.53 \pm 0.03 \text{ eV} \cdot \text{\AA}$; thus, $v_{HE}/v_{LE} = 1.61 \pm 0.04$. Comparing the experimental dispersion with the DFT + U band dispersion yields the real part of the self-energy plotted in Figure 6.8(c), which also shows an anomaly at ω_B . Note that because DFT + U underestimates the size of the electron-like pocket measured here, we rigidly shifted the DFT + U results to larger \mathbf{k} (or equivalently, to lower E) to align the calculations with the k_F measured experimentally.

Kinks in the $E(\mathbf{k})$ quasiparticle dispersion relationships extracted from ARPES data—and the corresponding anomalies in $\text{Re}[\Sigma(\omega)]$ —are commonly observed at energies characteristic of bosonic excitations of a given material—including phonons, magnons, and plasmons [92, 140, 251, 252, 253, 254]. It is not strictly possible to distinguish between these scenarios from ARPES data in isolation; we must appeal to other experimental measurements of the bosonic modes—and possibly computations that include (or neglect) the coupling of electrons to different types of excitations—to identify what the relevant bosons are and to assess how much of the corresponding renormalizations of v noted above can be ascribed to different types of electron-boson coupling. In the case of RuO_2 , high-resolution electron energy loss spectroscopy measurements supported by DFT calculations have previously identified a surface oxygen optical phonon mode at 69 meV [255]. The close agreement in energy of this phonon with the value of ω_B observed above suggests that electron-phonon coupling is responsible for most of the velocity renormalization near E_F shown in Figure 6.8. This assignment can be further quantified by comparing v_{HE} and v_{LE} with the band velocity obtained from DFT + U calculations, $v_{DFT} = 3.08 \pm 0.04 \text{ eV} \cdot \text{\AA}$. The Kohn-Sham quasiparticles of DFT account for electron-electron interactions at a static mean-field level, but neglect dynamical electron-electron correlations and also neglect electron-phonon coupling. In this interpretation, $v_{DFT}/v_{HE} = 1.26 \pm 0.05$ likely reflects the dressing of the electron-like excitations by other electrons, and $v_{HE}/v_{LE} = 1.61 \pm 0.04$ reflects the further dressing of these excitations by phonons, resulting in a total Fermi velocity renormalization of $v_{DFT}/v_{LE} = 2.02 \pm 0.05$.

In a modestly correlated material such as RuO_2 , dynamical electron-electron correlations might reasonably be expected to persist over a wider range in binding energy than the effects of electron-phonon coupling—so that doing “perturbation theory” in this order is valid—but it would be interesting to address this assumption in future studies by, *e.g.*, DFT + DMFT calculations [247]. On the experimental side of the equation, it would be enlightening to check whether the phonon-induced self energies and mass renormalizations display any appreciable momentum dependence in ARPES, and also whether the coupling strengths of the electrons to lower-energy phonon modes (which may be more important for enhancing the instability towards superconductivity) display any non-trivial dependence on strain in RuO_2 .

6.3 Evolution of electronic structure with strain

The results presented in section 6.2 illustrate that the experimentally measured electronic structure of thin, nearly commensurately strained $\text{RuO}_2/\text{TiO}_2(110)$ samples are well described by DFT+ U across multiple energy scales, even down to fine details of the low-energy physics such as the \mathbf{k} -resolved Fermi surface and $E(\mathbf{k})$ quasiparticle dispersions. This agreement, taken together with similar findings for lightly Ir-doped bulk RuO_2 single crystals [256]³, suggests that DFT calculations should be a reasonable starting point to explore and understand how epitaxial strains can be employed to engineer features of the bandstructure to enhance superconductivity in RuO_2 . In this section, we benchmark how the calculated strain-dependent changes to the electronic structure shown in subsection 6.1.4 compare to “reality”—*i.e.*, ARPES measurements on RuO_2 thin films under different amounts of epitaxial strain.

³Note that because Ir lies one column to the right of Ru in the periodic table, the ARPES studies of $(\text{Ru}_{0.93}\text{Ir}_{0.07})\text{O}_2$ reported in Ref.[256] also tacitly include the effects of 7% electron doping on the electronic structure, which amounts to a chemical potential shift of $\Delta E_F \approx +36$ meV in a rigid-band picture, using the DFT-computed DOS from Figure 6.1.

There are two conceptually rather distinct strategies for producing RuO₂ thin-film samples subject to different amounts of epitaxial strain that are suitable for ARPES studies:

1. Grow progressively thicker films on the same substrate—*e.g.*, TiO₂(110)—with film thicknesses t spanning across the critical thickness $t_{crit.}$ at which epitaxial strain relaxation onsets.
2. Grow commensurately strained films (*i.e.*, $t < t_{crit.}$) on different substrates. Here *different substrates* more abstractly means *templates for epitaxial film growth with different in-plane lattice constants*; thus, substrates of the same chemical formula but polished to expose different orientations of the crystal structure—*e.g.*, TiO₂(101) versus TiO₂(110)—can also be used to accomplish this result.

Both of these methods have certain advantages and drawbacks, so it is not *a priori* clear which is preferable for studying how strain couples to the electronic structure. Therefore, we took both approaches in our studies of RuO₂ thin films. The results from both methods are in qualitative agreement with each other; however, some systematic uncertainties present in both methods limit our confidence with which quantitative comparisons to DFT calculations can be made, as explained in further detail below.

6.3.1 Results on RuO₂(110) films of different thicknesses

The large in-plane lattice mismatches present for RuO₂ film growth on TiO₂(110) substrates (−4.7% along $[001]_{rutile}$ and +2.3% along $[\bar{1}\bar{1}0]_{rutile}$ at 295 K) imply small critical thicknesses $t_{crit.}$ for epitaxial strain relaxation. As detailed in subsection 5.2.3, high-resolution x-ray diffraction (XRD) measurements place $t_{crit.}$ in the range of 5.8 – 11.5 nm

for the growth conditions used in this work to synthesize RuO₂/TiO₂(110) samples⁴. Therefore, to measure strain-dependent changes to the electronic structure, we collected ARPES data on RuO₂(110) films of different thicknesses ranging from $t = 7 \text{ nm} \approx t_{crit.}$ to $t = 48 \text{ nm} \gg t_{crit.}$

In chapter 5, we utilized XRD to characterize the crystal structures of RuO₂(110) films of different thicknesses, and attempted to relate these thickness-dependent changes observed in XRD to the thickness-dependent superconducting properties observed in electrical transport measurements. The rationale there was that XRD and electrical transport measurements are both *bulk-sensitive* techniques that probe—and in some sense, average over—the crystal and electronic structure throughout the entire thickness of the films. By a similar argument, ideally we should utilize a very *surface-sensitive* probe of the crystal structure, such as LEED, in order to properly interpret strain-dependent changes to the surface electronic structure measured by ARPES. Accordingly, in this section we first present the results of a LEED surface lattice constant refinement for two RuO₂(110) films spanning the range of film thicknesses t studied by ARPES, before proceeding to discuss how the ARPES spectra evolve with increasing t .

LEED lattice constant refinement

We acquired many LEED images at normal incidence using incident electron energies ranging from 100 - 300 eV in 2 eV steps for two RuO₂(110) films of different thicknesses, $t = 7 \text{ nm}$ and $t = 48 \text{ nm}$. Representative examples of the raw data (images taken at 200 eV) are contained in the insets to Figure 6.9. For each image, we located the positions of all visible spots and indexed the spots according to their in-plane momentum transfer values $\mathbf{q}_{||} = 2\pi(H/c, K/2d_{1\bar{1}0})$, where H and K are integers and, by our convention, H de-

⁴Throughout the text, we are intentionally equivocating about quoting an exact value for $t_{crit.}$ because it is known to be an inherently non-universal number that depends on kinetic factors, which are strongly influenced by the exact film growth conditions—see, *e.g.*, chapter 2.

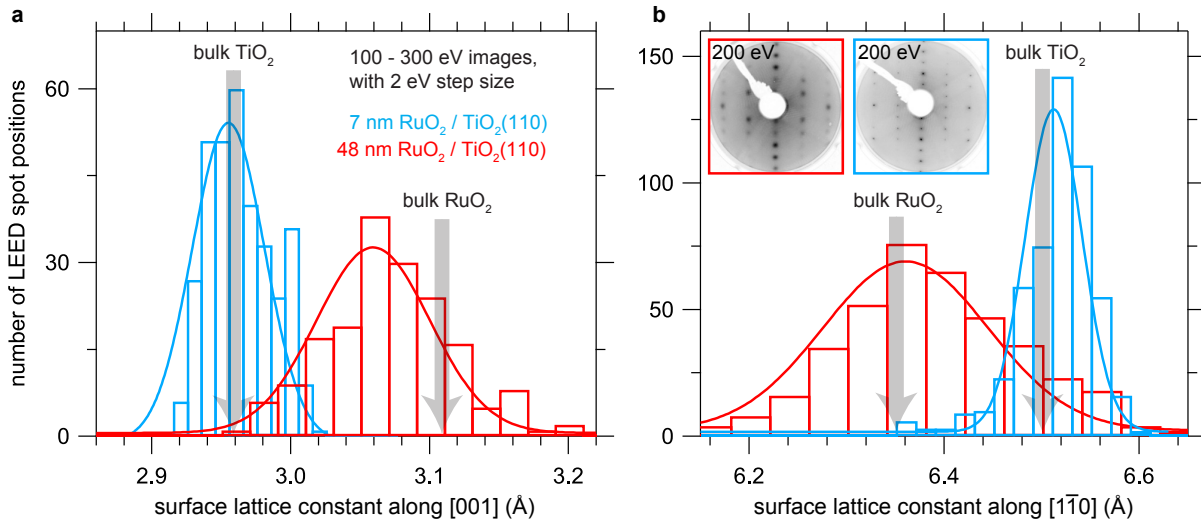


Figure 6.9: Surface lattice constant refinement by LEED spot position analysis for two RuO₂(110) films of different thicknesses, 7 nm (blue) and 48 nm (red). The histograms in panels (a) and (b) summarize the measured values for c and $2d_{1\bar{1}0}$, respectively. For reference, the gray arrows indicate the values expected for a commensurately strained film (bulk TiO₂) and a fully strain-relaxed film (bulk RuO₂).

defines the magnitude of q_{\parallel} along [001] (nearly horizontal in the images in Figure 6.9), and K defines the magnitude of q_{\parallel} along [1 $\bar{1}$ 0] (nearly vertical). We then calculated the distance of all spots from the specular $q_{\parallel} = (0, 0)$ reflection and converted these image distances D (in pixel space) to scattering angles $\sin(\theta)$ (where θ is the angle of each diffracted electron beam relative to the surface normal) based on $D \rightarrow \sin(\theta)$ calibrations that were independently determined from reference measurements on SrTiO₃(001) surfaces having a known lattice constant. Note that these calibrations absorb the overall scaling factors of the spot patterns that depend on the working distances between the LEED screen and the samples (and the camera image magnification factors), as well as some higher-order distortions of the spot patterns that result from the samples not being positioned precisely at the center of curvature of the LEED screen (and the screen itself being slightly aspherical).

From these values of $\sin(\theta)$, the electron energies E at which each LEED pattern was recorded, and the (H, K) indices, we compiled lists of lattice constants corresponding to

each fitted spot position. For simplicity in analysis, we restricted our attention to spots having q_{\parallel} purely aligned with $[001]$ or $[1\bar{1}0]$. Elastic scattering and conservation of momentum modulo translations of the surface reciprocal lattice (see, *e.g.*, section 3.4) require that

$$|\mathbf{q}_{\parallel}| = k \sin(\theta) = \sqrt{2m_e E} \sin(\theta) / \hbar , \quad (6.6)$$

which for spots of the type $\mathbf{q}_{\parallel} = 2\pi(H/c, 0)$ and $2\pi(0, K/2d_{1\bar{1}0})$, reduces to:

$$c = \frac{2\pi\hbar H}{\sqrt{2m_e E} \sin(\theta)} \quad \text{and} \quad 2d_{1\bar{1}0} = \frac{2\pi\hbar K}{\sqrt{2m_e E} \sin(\theta)} . \quad (6.7)$$

Here c and $2d_{1\bar{1}0}$ are the surface lattice constants along $[001]$ and $[1\bar{1}0]$ that are expected for an unreconstructed (110)-oriented rutile surface. Histograms of the values obtained in this way for c are displayed in Figure 6.9(a), and the results for $2d_{1\bar{1}0}$ are displayed in Figure 6.9(b). For reference we also indicate by gray arrows the surface lattice constants expected for bulk-terminated TiO_2 ($c = 2.96 \text{ \AA}$, $2d_{1\bar{1}0} = 6.50 \text{ \AA}$) and bulk-terminated RuO_2 ($c = 3.11 \text{ \AA}$, $2d_{1\bar{1}0} = 6.35 \text{ \AA}$). The measured surface lattice constants for the 7 nm thick $\text{RuO}_2(110)$ sample in blue, ($c = 2.96 \pm 0.03 \text{ \AA}$, $2d_{1\bar{1}0} = 6.51 \pm 0.05 \text{ \AA}$), match those of TiO_2 within the $\approx 1.0\%$ resolution of the measurements (the quoted error bars are the standard deviations of the histograms), indicating that this film is (nearly) commensurately strained to the substrate along both $[001]$ and $[1\bar{1}0]$. By contrast, the 48 nm thick $\text{RuO}_2(110)$ sample in red shows broader LEED spots, indicating lower surface crystallinity than the 7 nm thick sample, which results in wider distributions of the extracted lattice constants. Furthermore, the centers of mass of the red distributions, ($c = 3.07 \pm 0.06 \text{ \AA}$, $2d_{1\bar{1}0} = 6.39 \pm 0.11 \text{ \AA}$), are displaced away from the blue distributions towards the values expected for bulk RuO_2 .

Thickness-dependent ARPES data

Based on the results described in Figure 6.9, we expect that most of the epitaxial strains are relaxed at the surface of the 48 nm thick $\text{RuO}_2(110)$ sample, such that its surface electronic structure probed by ARPES is more representative of bulk RuO_2 . At the other extreme, the surface crystal structure of the 7 nm thick $\text{RuO}_2(110)$ sample remains highly strained, and thus is more representative of the idealized case of commensurately strained $\text{RuO}_2(110)$ considered in the constrained DFT structural relaxations in subsection 6.1.2. In order to determine whether the strong strain dependence of $N(E_F)$ anticipated in subsection 6.1.4 is realized in experiment, we compared ARPES data collected for the 7 nm thick and 48 nm thick $\text{RuO}_2(110)$ samples, as shown in Figure 6.10. Figure 6.10 displays $E(\mathbf{k})$ spectra side-by-side for these samples along the same $k_x = \pi/c$ contour from Figure 6.6(c) where the photoemission intensity is dominated by $d_{||}$ states. The higher levels of strain present at the film surface for the 7 nm thick sample cause a substantial shift of the flat bands towards E_F by 120 ± 20 meV relative to the partially strain-relaxed 48 nm thick sample. Integrating the ARPES data over the full measured region of k -space for both samples gives the average energy distribution curves plotted in the middle of Figure 6.10, which show that spectral weight near E_F is enhanced as the $d_{||}$ states move towards E_F , in qualitative agreement with the strain-dependent trend predicted by DFT.

Extracting the DOS near E_F from ARPES data

The main advantage of utilizing film-thickness-dependent strain relaxation to assess strain-dependent changes to the electronic structure is that the comparison of photoemission data collected on different samples is experimentally straightforward. To expound upon this point in more detail: suppose that the primary quantity of interest vis-à-vis strain-induced enhancements of the instability towards superconductivity is the quasi-

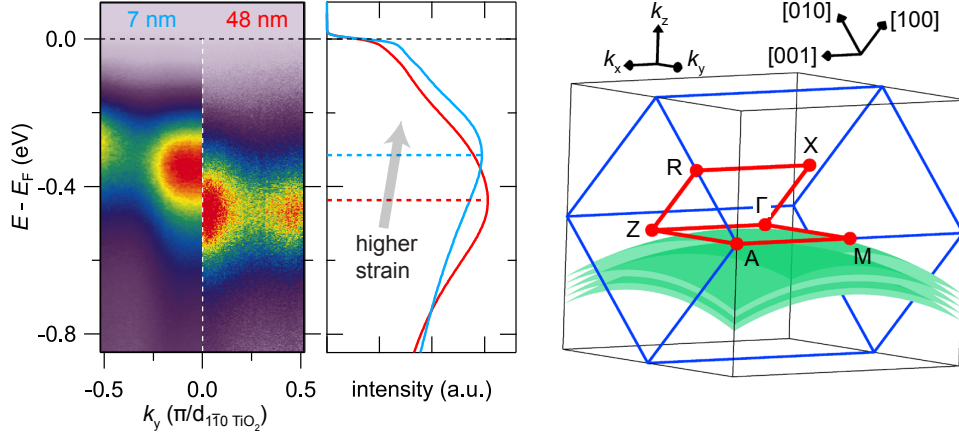


Figure 6.10: Comparison of $E(\mathbf{k})$ spectra along cut (c) from Figure 6.6 for two different $\text{RuO}_2(110)$ samples: a highly strained 7 nm thick film (left), and a partially strain-relaxed 48 nm thick film (right). As a proxy of the full DOS, for these samples we show the energy distribution curves of photoemission intensity averaged over the entire region of \mathbf{k} -space probed experimentally at $h\nu = 21.2$ eV (green regions in the Brillouin zone schematic). These results demonstrate that the epitaxial strains imposed by $\text{TiO}_2(110)$ shift $d_{||}$ states towards E_F and thereby increase $N(E_F)$.

particle density of states near the Fermi level,

$$N(E_F) = \int_{E_F - \delta}^{E_F + \delta} \int_{\text{BZ}} A(\mathbf{k}, \omega) d\mathbf{k} d\omega, \quad (6.8)$$

where $A(\mathbf{k}, \omega)$ is the single-particle spectral function, integrated over all momenta \mathbf{k} in the Brillouin zone (BZ) and over some limited range of energies ω near E_F (δ is some small parameter).

Two separate factors make it impossible to quantitatively extract the total $N(E_F)$ directly from data taken with our lab-based ARPES equipment. First, our inability to continuously vary the photon energy—or equivalently, the kinetic energy of the photoelectrons at E_F —implies that only regions of the Brillouin zone with specific k_z can be probed, *cf.* Equation 6.5. Therefore the full integration over \mathbf{k} in Equation 6.8 cannot be performed in a lab-based ARPES setup, which is especially problematic in a material

such as RuO_2 that has a highly three-dimensional electronic structure depending strongly on k_z —*cf.* Figure 6.7. Second, even if the entire Brillouin zone could be mapped exhaustively, the intensity measured in ARPES is not the initial-state spectral function $A(\mathbf{k}, \omega)$, but rather this quantity multiplied by probabilities (matrix elements) for photoemission (see *e.g.*, section 3.3), which are difficult to calculate theoretically.

While these qualifications in mind, it is also true that interpreting *relative* changes in the photoemission intensity near E_F as a proxy for how $N(E_F)$ varies between different thickness $\text{RuO}_2(110)$ samples will be quite robust, since most of these uncertainties essentially cancel out in such comparisons. The inner potentials will be similar, so our comparison of data integrated over the same range of angles probes the same region of \mathbf{k} -space in both cases—even if it is only some limited fraction of the full Brillouin zone. Likewise, by performing the measurements on different thickness $\text{RuO}_2(110)$ samples with the same photon energy, light polarization, and scattering geometries, the matrix elements for photoemission are guaranteed to be similar.

The main drawback of this approach is that the crystal structures of partially strain-relaxed oxide thin films are typically spatially heterogeneous on sub- μm length scales, containing regions that are nearly coherently strained and regions that show more pronounced effects of strain relaxation—see, *e.g.*, subsection 5.2.3. For a probe such as ARPES that averages over 10–1000 μm length scales, the measured signal is thus some ill-defined average of contributions from these regions with microscopically different crystal and electronic structures, which muddles any simple comparison of the experimental data with the predictions of a theory such as DFT that requires periodic crystal structures as input.

6.3.2 Results on RuO₂(110) and RuO₂(101) films

The second approach discussed above to assess strain-dependent changes to the electronic structure—namely, performing ARPES measurements on commensurately strained RuO₂ thin films synthesized on TiO₂(110) and TiO₂(101) substrates—avoids the complications of spatial heterogeneity in the crystal/electronic structures; however, this comes at the cost of making the comparison between different experimental data sets much less straightforward. To see how this plays out in practice, in Figure 6.11 we present LEED and ARPES data taken on three different RuO₂ thin-film samples: the 7 nm thick and 48 nm thick RuO₂(110) samples from the previous section, as well as a coherently strained 19.3 nm thick RuO₂(101) sample⁵. Figure 6.11(a) shows that all of the samples have LEED spot patterns with the periodicities expected for unreconstructed (110)- and (101)-oriented rutile surfaces. Note that off-specular reciprocal space maps for the RuO₂(101) film measured here are essentially identical to the data presented in Figure 5.8 for a different RuO₂(101) sample of almost the same thickness, and in particular, do not show any signatures of strain relaxation⁶. Therefore, we did not attempt to refine the surface lattice constants of this (101)-oriented sample, as in Figure 6.9; instead we analyzed a few LEED images to confirm that the measured spot positions are roughly consistent with the values of $d_{\bar{1}01} = 5.464 \text{ \AA}$ and $d_{010} = 4.594 \text{ \AA}$ appropriate for a bulk-truncated (1×1) TiO₂(101) surface, and we appeal to the x-ray diffraction results (which offer at least an order of magnitude better \mathbf{q} resolution than LEED data) to argue that the surface of this RuO₂(101) film is indeed commensurately strained to the template set by the underlying TiO₂ substrate.

⁵Recall that the smaller in-plane lattice mismatches present for RuO₂ film growth on TiO₂(101) substrates (+0.04% along $[\bar{1}01]_{\text{rutile}}$ and +2.3% along $[010]_{\text{rutile}}$ at 295 K) imply larger critical thicknesses t_{crit} for epitaxial strain relaxation than for (110)-oriented samples.

⁶Without any hints of epitaxial strain relaxation, there is also no reason to expect layer-dependent in-plane lattice constants that may be different at the surface of the film (*i.e.*, the region probed by ARPES and LEED) than throughout the bulk of the film (the region probed by transport and XRD).

Given that strained $\text{RuO}_2(110)$ samples superconduct at measurable T_c s, while $\text{RuO}_2(101)$ samples and bulk RuO_2 do not, the main question we wanted to address using ARPES was: how does the DOS near the Fermi level $N(E_F)$ evolve between these samples? Recall that from chapter 5, the superconducting transition temperature for weak-coupling electron-phonon mediated superconductors can be expressed as [35, 36, 243]:

$$T_c \sim \omega_{\text{ln}} \exp\left(-\frac{1}{\lambda}\right) = \omega_{\text{ln}} \exp\left(-\frac{M\langle\omega^2\rangle}{N(E_F)\langle I^2\rangle}\right) \quad (6.9)$$

For the reasons discussed above, the relative values of $N(E_F)$ for $\text{RuO}_2(110)$ and $\text{RuO}_2(101)$ cannot be reliably extracted from ARPES data by directly comparing the measured photoemission intensities at E_F . Nonetheless, there is a route to answering whether $N(E_F)$ *increases* in strained $\text{RuO}_2(110)$ compared with strained $\text{RuO}_2(101)$ or bulk RuO_2 : we simply must determine where the flat bands with d_{\parallel} orbital character are located in energy relative to E_F . DFT calculations suggest that if these bands move closer to (further away from) E_F , the total $N(E_F)$ will increase (decrease), respectively. To approximately determine the positions of these bands experimentally, we integrated the photoemission intensity over the color-coded slabs in the Brillouin zone schematic in Figure 6.11(a), plotted the resulting energy distribution curves (EDCs) in Figure 6.11(b), and found the maxima in the EDCs as indicated by the dashed lines. The regions shaded yellow in the Brillouin zone denote where the near- E_F wavefunctions have greater than 90% d_{\parallel} orbital character, according to our DFT + Wannier90 calculations; since all slabs lie in this region, we expect that the dominant contributions to the measured EDCs are from d_{\parallel} initial states. Note that the region of $k_z = k_{110}$ probed by ARPES with He-I α photons on the (110)-oriented samples is well-constrained by analysis of the $E(\mathbf{k})$ dispersions as outlined in Figure 6.7; however, for the (101)-oriented sample the region of $k_z = k_{101}$ probed by ARPES with He-II α photons is merely calculated from the free-electron final state model in Equation 6.5, using

the same inner potential as for $\text{RuO}_2(110)$ ⁷, and thus is subject to greater experimental uncertainties. Nonetheless, the results of this analysis are in qualitative agreement with the strain-dependent trends anticipated by DFT displayed in Figure 6.11(c): in highly strained $\text{RuO}_2(110)$ films, the flat bands move closer to E_F compared with either more strain-relaxed $\text{RuO}_2(110)$ films or commensurately strained $\text{RuO}_2(101)$ films. This modification of the effective d orbital degeneracies boosts the total DOS near E_F , which likely contributes to the enhanced superconducting T_c s observed in highly strained $\text{RuO}_2(110)$, according to increases in the Hopfield parameter $N(E_F) \langle I^2 \rangle$ in Equation 6.9.

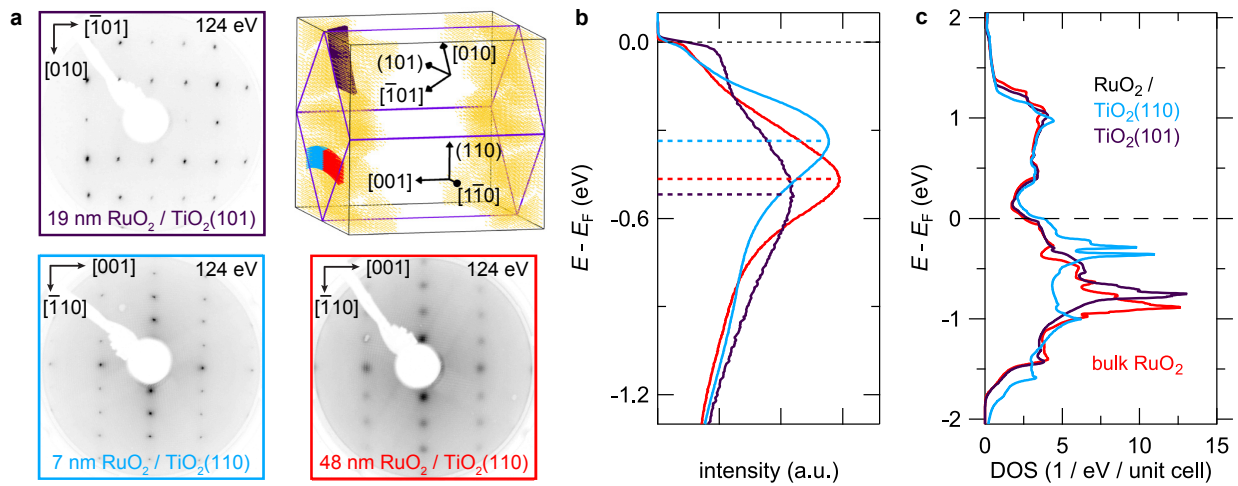


Figure 6.11: (a) LEED patterns recorded at 124 eV for 19 nm thick $\text{RuO}_2(101)$, 7 nm thick $\text{RuO}_2(110)$, and 48 nm thick $\text{RuO}_2(110)$ samples, along with a schematic of the Brillouin zone showing the regions of k -space over which we integrated the ARPES data for these samples to obtain the average energy distribution curves in (b). Yellow regions of the Brillouin zone indicate where the near- E_F Kohn-Sham wavefunctions have > 90% $d_{||}$ orbital character. (b) The colored dashed lines represent the peak positions of the energy distribution curves. By locating the $d_{||}$ -derived flat bands in this way, trends in how $N(E_F)$ evolves with strain can be more reliably extracted from ARPES data than by directly reading off the measured photoemission intensity at E_F , as explained in the text. (c) Expected strain-dependent changes in the total DOS according to DFT + U simulations, reproduced from Figure 6.2.

For completeness, we also performed more extensive ARPES measurements of the electronic structure for the non-superconducting 19.3 nm thick $\text{RuO}_2(101)$ sample from

⁷To generalize Equation 6.5 to a (101)-oriented surface, we must of course also replace quantities such as $2d_{110}$ with d_{101} , etc.

Figure 6.11 with He-I α (21.2 eV) photons, as illustrated in Figure 6.12. Energy distribution curves extracted at certain wavevectors—*e.g.*, as shown in the inset to Figure 6.12(a)—exhibit hints of well-defined quasiparticle peaks near E_F ; however, at most locations in the Fermi surface map, the distribution of intensity is rather broad versus energy and momentum. Naively this is unexpected: all ARPES measurements were conducted at $T \approx 20$ K, where the bulk resistivity of the film is $\rho(20 \text{ K}) \approx 2 \mu\Omega\text{-cm}$, and the surface of this RuO₂(101) film shows excellent crystallinity and is nearly atomically flat, as measured by LEED and x-ray reflectivity. One explanation possibly capable of reconciling the highly metallic and crystalline nature of the sample with the broad spectral features is indicated by panels (b) and (c) in Figure 6.12. In the top row, we show the experimentally measured $E(\mathbf{k})$ spectra along two cuts through \mathbf{k} -space indicated in Figure 6.12(a) by white dashed lines. In the bottom row, we plot the same data (now using a black-white false-color scale), and overlay the DFT-computed bandstructure (as differently colored solid lines) for ranges of $k_z = k_{101}$ spanning a range of $\delta k_z = \pm 0.08 \pi/d_{101} \approx \pm 0.1 \text{ \AA}^{-1}$ about the nominal central value of k_z probed along each cut. To approximately determine the central values of k_z being measured, we allowed the inner potential V_0 to vary in an appropriate generalization of Equation 6.5, similar to the procedure described in Figure 6.7. $V_0 = 10.7$ eV was found to give the best visual agreement with the experimental data; however, the inherently broad spectral features measured experimentally make this procedure somewhat ill-defined and ambiguous, so this number should be treated with some skepticism. More germane for the present discussion than the exact value of V_0 is the observation that the bandstructure depends strongly on k_z in the region of \mathbf{k} -space probed at $h\nu = 21.2$ eV, which can naturally produce measured spectra that are artificially broadened in E and \mathbf{k} relative to the intrinsic lifetimes and decay lengths of quasiparticle excitations inside the solid, according to well-documented final-state “ k_z smearing” effects involved in the photoemission process. To test this hypothesis, we propose that future ARPES measurements of RuO₂(101) should use synchrotron light, to check if other photon energies (*i.e.*,

probing at different locations in \mathbf{k} -space) yield more easily interpretable results. Although $\text{RuO}_2(101)$ films are non-superconducting, they do show intriguing magnetotransport behavior at low temperatures, such as large magnetoresistance that scales linearly with the applied field⁸. Presumably these properties should have some explanation in terms of the underlying bandstructure, but the present work indicates that lab-based ARPES with a helium lamp may not be ideally suited for revealing the electronic structure of these films.

6.4 Discussion and Conclusions

Through a combination of bottom-up materials synthesis by MBE, epitaxial strain engineering, and structural and electrical characterization by multiple techniques, we have demonstrated the first example of a strain-stabilized superconductor in $\text{RuO}_2(110)$ thin films with T_c s up to ≈ 2 K. In this chapter we employed DFT calculations and ARPES experiments to investigate the normal-state electronic structure from which superconductivity emerges in $\text{RuO}_2(110)$, paying special attention to strain-induced changes that may account for the enhanced T_c . Our results show that the primary electronic effect of epitaxial strains in $\text{RuO}_2(110)$ is to alter the relative occupancies of the $d_{||}$ and (d_{xz}, d_{yz}) orbitals as compared with bulk RuO_2 and more lightly strained $\text{RuO}_2(101)$ thin films—and most importantly, to push a large number of states with $d_{||}$ character closer to E_F , which increases $N(E_F)$.

Table 6.2 summarizes the RuO_2 thin-film samples that we measured by ARPES and LEED as part of this dissertation. Although some technical issues at different points in time with both the apparatus used to conduct MBE + ARPES + LEED experiments and with the system used to conduct low-temperature electrical transport experiments have

⁸Unpublished work by Ludi Miao, Yonghun Lee, and the present author.

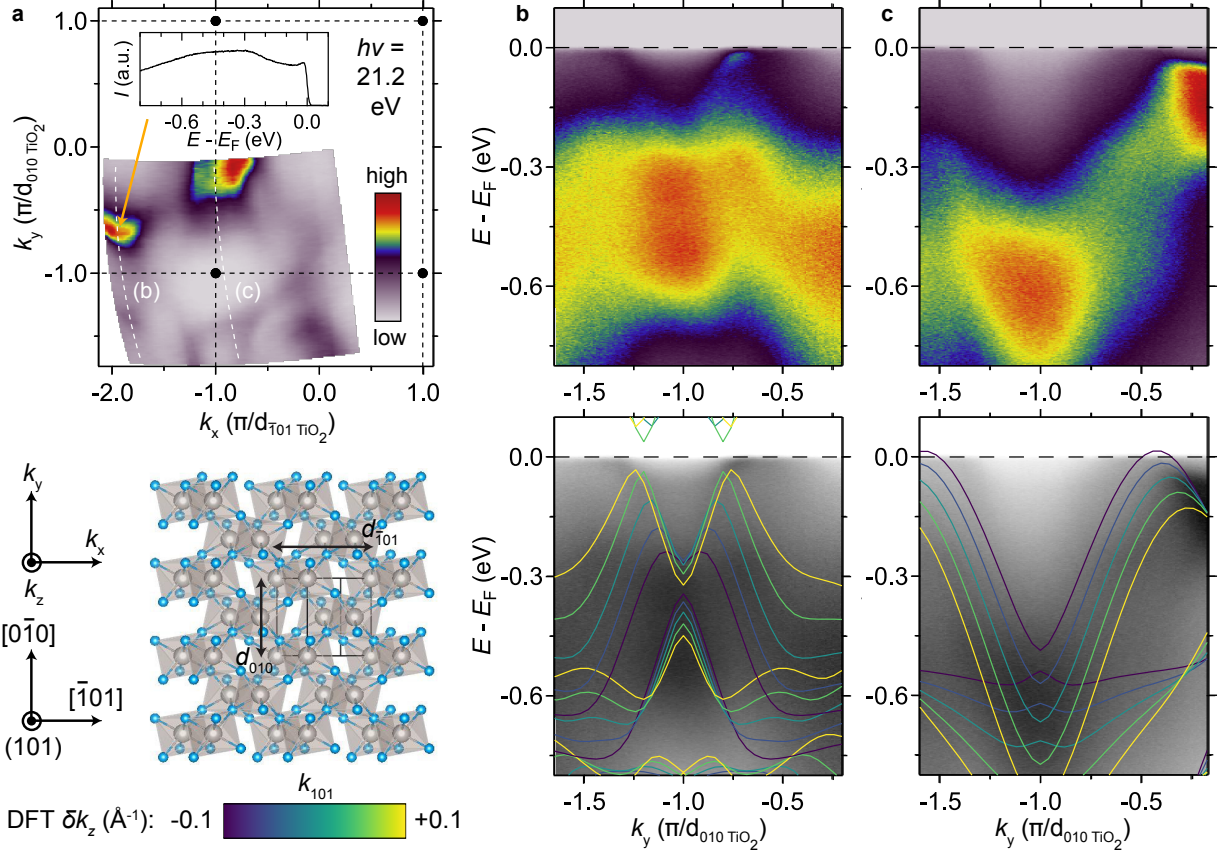


Figure 6.12: (a) 2D slice through the Fermi surface measured for a 19.3 nm thick $\text{RuO}_2(101)$ film with 21.2 eV photons. The surface Brillouin zones are indicated by black dashed lines, corresponding to the size and orientation of the surface unit cell in real space drawn on the crystal structure of RuO_2 viewed in (101) projection. Inset shows an energy distribution curve at the indicated location in \mathbf{k} space. (b - c) $E(\mathbf{k})$ spectra along the cuts indicated by white dashed lines in (a). The bottom row of panels overlays DFT results on the experimental data as color-coded solid lines; each color represents a different value of $k_z = k_{101}$ that span a total range of $\pm 0.1 \text{ \AA}^{-1}$ about the central values.

mostly precluded a direct comparison of photoemission and transport data acquired for exactly the same samples (*cf.* Table 6.2 and Table 5.1), we believe that the trends illustrated in the last two chapters of how the superconductivity and normal-state electronic structure respond to epitaxial strain are robust to inevitable sample-to-sample scatter in the properties measured by different probes. In the future, a more detailed analysis of how aspects of the electronic structure revealed by ARPES—such as $N(E_F)$, the occupancies

of different bands, and the electron-phonon coupling strength—evolve versus film thickness in RuO₂(110) may be a fruitful approach to more definitively establish how these quantities ultimately determine the instability of strained RuO₂ towards superconductivity.

Sample ID	TiO ₂ substrate orientation	T_s (°C)	film thickness (nm)	ARPES measurements	LEED images	Low-temp. $R(T, H)$?
HP1309	(110)	300	7	He-I α Fermi surface map He-I α cuts: $k_{001} = 0, \pi/(2c), \pi/c$ He-II α Fermi surface map He-II α cuts: $k_{001} = 0, \pi/c$ He-I α cut: $k_{001} = 0$ at diff. T	20 - 300 eV, 1 eV steps	no (sample lost)
190209A	(110)	320	48	He-I α Fermi surface map He-I α cuts: $k_{001} = 0, \pi/(2c), \pi/c$ He-II α cuts: $k_{001} = 0, \pi/c$	20 - 400 eV, 2 eV steps	$T_c < 0.4$ K (hints of SC)
190426A	(101)	320	19.3	He-I α Fermi surface map He-I α cuts: $k_{\bar{1}01} = 0, -\pi/d_{\bar{1}01}, -2\pi/d_{\bar{1}01}$ He-II α Fermi surface map	20 - 400 eV, 2 eV steps	$T_c < 0.4$ K (non-SC)
HP-ARPES-1	(110)	300	30.2	sample charged	sample charged	$T_c = 2.49$ K $H_{c\perp}$ TBD
HP-ARPES-2	(110)	300	14.6	sample charged	sample charged	$T_c = 1.66$ K $H_{c\perp}$ TBD
HP-ARPES-3	(110)	300	8.3	He-I α Fermi surface map He-I α cuts: $k_{001} = 0, \pi/(2c), \pi/c$ He-II α cuts: $k_{001} = 0, \pi/c$	20 - 360 eV, 2 eV steps	$T_c = 0.45$ K $H_{c\perp}$ TBD
HP-ARPES-4	(110)	300	19.6	He-I α Fermi surface map He-I α cuts: $k_{001} = 0, \pi/(2c), \pi/c$	20 - 360 eV, 2 eV steps	T_c and $H_{c\perp}$ TBD
HP-ARPES-5	(110)	300	13.3	He-I α Fermi surface map He-I α cuts: $k_{001} = 0, \pi/(2c), \pi/c$ He-II α cut: $k_{001} = \pi/c$	20 - 360 eV, 2 eV steps	T_c and $H_{c\perp}$ TBD

Table 6.2: Summary of different RuO₂ thin-film samples synthesized on TiO₂ substrates that were measured by ARPES and LEED as part of this dissertation. As explained in the text and indicated in the rightmost column, magnetoresistance measurements extending down to ³He temperatures remain to be done for certain samples, whenever the PPMS becomes functional again. For samples where the zero-field superconducting T_c is listed, here we quote the temperature at which the resistance drops to 90% of its residual normal-state value.

More broadly, we believe that our results indicate that a promising strategy to create new transition-metal superconductors is to apply judiciously chosen *anisotropic strains*

that modulate degeneracies among the d orbitals near E_F . Many classic studies of elemental superconductors that have nearly free-electron states spanning E_F derived from (s, p) orbitals exhibit decreases in T_c under hydrostatic pressure, due to lattice stiffening (*i.e.*, increases in the numerator of the exponential in Equation 6.9) overwhelming other effects as the unit cell volume is uniformly reduced [257]. In a limited number of elements where T_c actually *increases* under pressure, pressure-induced electron transfer between $s \rightarrow d$ orbitals has often been suggested as causing the enhanced T_c s; however, pressure changes of > 10 GPa are typically required to, *e.g.*, double T_c [258]. More recently, measurements on single crystals of the unconventional superconductor Sr_2RuO_4 have shown that *uniaxial* pressures of only ≈ 1 GPa can boost T_c by more than a factor of two [68], suggesting that the approach outlined here of redistributing carriers within the d shell may prove to be much more efficacious than hydrostatic pressure for tuning superconductivity in numerous multi-orbital systems of current interest.

In the quest to rationally engineer enhanced superconductivity, theoretical guidance is also essential to interpret these empirical trends in terms of changes to the normal-state electronic structure, and for a given class of materials, to determine the modes of lattice distortions to which superconductivity is expected to respond most sensitively. Owing to its simple crystal structure and modest interactions that are well captured by DFT-based approaches, we propose RuO_2 as a useful benchmark for refining Migdal-Eliashberg-type calculations that aim to compute superconducting properties from *ab initio* electronic and phononic spectral functions [259], and to investigate further possibilities such as phonon softening near a structural instability. Indeed, strong coupling between the lattice and electronic degrees of freedom in rutile-like crystal structures has been well established both theoretically [201] and experimentally in VO_2 , where strain-induced variations in the orbital occupancies can modify the metal-insulator transition by $\delta T_{\text{MIT}} \approx 60$ K [260]. Therefore, it may be promising to explore other rutile compounds for strain-stabilized superconductivity, as opposed to conventional chemical doping [261, 262, 263]. Finally,

since RuO₂/TiO₂(110) is the first known stoichiometric superconductor within the rutile family, further optimization of the superconductivity may enable the creation of structures that integrate superconductivity with other functional properties that have been extensively studied in other rutile compounds, such as high catalytic efficiency [264], half-metallic ferromagnetism [265], and large spin Hall conductivities [266].

CHAPTER 7
CONCLUSIONS AND FUTURE WORK

7.1 Conclusions

In this dissertation, we explored how superconductivity in thin films of two ruthenium oxide compounds, Sr_2RuO_4 and RuO_2 , responds to epitaxial strain. In both cases, we demonstrated that enhanced superconducting transition temperatures (T_c) can be realized by synthesizing films on appropriately lattice-mismatched substrates. Moreover, by employing numerous complementary structural and electrical characterization techniques in concert with first principles calculations, we revealed some of the relevant structure-property relationships for these materials that link the atomic positions to features of the normal-state electronic structure that ultimately determine the condensation energy scale of superconductivity. It is hoped that the work described here spurs further investigations into strain engineering exploiting epitaxy as a method for manipulating superconductivity in ruthenates and, more generically, in any materials where there are multiple transition metal d orbitals spanning E_F . At a theoretical and practical level, it seems manifest by now that *redistributing carriers* among the effective low-energy orbital degrees of freedom can have similarly profound effects on superconductivity as *changing the total carrier density*; we just need to know how to arrange the atoms during materials synthesis to get the near- E_F electrons in regions of \mathbf{k} -space favorable for boosting the instability towards Cooper pairing.

In Sr_2RuO_4 , we showed that films grown on perovskite substrates that apply anisotropic in-plane strains (*e.g.*, $\text{NdGaO}_3(110)$) have significantly enhanced T_c s relative to bulk Sr_2RuO_4 and relative to films grown on substrates that preserve the tetragonal symmetry of the bulk crystal structure (*e.g.*, $\text{LSAT}(001)$). Films such as

$\text{Sr}_2\text{RuO}_4/\text{SrTiO}_3(001)$ that are subject to larger amounts of A_{1g} in-plane tensile strains—which tunes the system towards a Lifshitz transition while preserving the C_4 rotational symmetry of bulk Sr_2RuO_4 —were shown to have more modestly enhanced T_c s. Much attention was paid to how minute concentrations of defects suppress the unconventional superconductivity in Sr_2RuO_4 and thus complicate a straightforward evaluation of strain-induced variations in T_c across different thin-film samples grown on different substrates. If future synthesis and characterization efforts indicate that the presently observed trends in how T_c responds to different modes and magnitudes of biaxial strain have appropriately controlled for these disorder effects, these results call for further computational studies of the underlying mechanism(s) that determine T_c in Sr_2RuO_4 [43, 44], and perhaps call for a more nuanced interpretation of results for bulk Sr_2RuO_4 single crystals under uniaxial pressure [67, 68, 170], which had previously suggested that T_c merely tracks the density of states near E_F as a Van Hove singularity in the normal-state electronic structure approaches E_F .

In RuO_2 , we showed how substrate-imposed strains can be utilized to transmute a normal metal into a superconductor. In particular, we demonstrated that synthesizing RuO_2 thin films on isostructural $\text{TiO}_2(110)$ substrates stabilizes superconductivity under strain, having T_c s up to 2 K; by contrast, more lightly strained RuO_2 thin films grown on $\text{TiO}_2(101)$ substrates are non-superconducting down to the lowest measured temperatures ($T_c < 0.4$ K), consistent with the behavior of bulk RuO_2 . To the best of our knowledge, this work represents the first example of *strain-stabilized superconductivity*, and so a considerable amount of effort was spent on the structural and electrical characterization of $\text{RuO}_2(110)$ thin films to gain insight into the origins of this phenomenon. Utilizing angle-resolved photoemission spectroscopy (ARPES) measurements together with density functional theory (DFT) calculations, we showed that the low-energy electronic structure of rutile systems depends sensitively on anisotropic strains that modulate the effective crystal-field splittings between states with $d_{||}$ and (d_{xz}, d_{yz}) orbital character: com-

pressing the crystal structure along the c axis by several percent depopulates flat bands with $d_{||}$ character away from being nearly fully filled, and thereby substantially increases the density of states near E_F , which likely contributes to the enhanced superconducting T_c s observed in $\text{RuO}_2/\text{TiO}_2(110)$.

The approach employed in this thesis for the creation and study of new superconductors has certain advantages and drawbacks compared to the two alternative strategies that historically have been more commonly utilized (and fantastically successful) in this regard—namely, chemical doping [21] and hydrostatic pressure [267]. Chemical doping has the drawback of explicitly introducing substitutional disorder. In conventional superconductors, this is only a minor theoretical complication that slightly renormalizes T_c and other quantities [149]; however, it can render disorder-sensitive unconventional superconductors such as Sr_2RuO_4 and certain heavy-fermion materials completely non-superconducting [64, 268]. On the positive side, chemical doping can be varied continuously (at least until solubility limits of the dopant are reached), and the dopants can usually be incorporated throughout the crystal in a spatially uniform fashion over length scales much exceeding the natural length scale of superconductivity, the coherence length ξ . Hydrostatic pressure studies avoid the complications of quenched disorder, and moreover, pressure can be varied continuously—this is crucial if, for example, quantum criticality plays any role in enhancing the superconductivity [269]. The main drawback is that sizable pressures are usually required to boost T_c by appreciable amounts [258]; therefore, pressure-enhanced superconductivity exists only transiently inside the confines of specialized pressure cells that are incompatible with most experimental probes of the electronic structure, and certainly inaccessible to any practical applications.

The bottom-up nature of epitaxial strain engineering overcomes many of these challenges: it is static, disorder-free¹, compatible with sophisticated spectroscopic probes of

¹Or perhaps more conservatively, but also more correctly: strain engineering exploiting epitaxy does not *explicitly* introduce additional disorder.

the electronic structure [176], and enables the integration of materials showing enhanced superconductivity with other materials in novel artificial interfaces and device structures [270]. That being said, strain engineering exploiting epitaxy also comes with a few essential drawbacks. First, the levels of strain achievable by this technique are, by definition, discrete; additionally, depending on the thin-film material, there may not be many structurally and chemically compatible substrates available that also happen to span the “interesting” range of lattice constants for tuning the film properties. Second, to change the strain state of the film, a new sample must be grown; this adds to the uncertainty in whether changes to the superconductivity should be ascribed to strain effects, or whether they just reflect unavoidable sample-to-sample scatter. Lastly, the spatial range of the strain fields imposed by the substrate are naturally limited in spatial extent by the critical thickness for strain relaxation $t_{crit.}$. If $t_{crit.}$ is much larger than the spatial extent over which the superconducting wavefunction varies ($t_{crit.} \gg \xi$), this is not a concern, but in thin-film systems where $t_{crit.}$ and ξ are the same order of magnitude ($\approx 1 - 100$ nm)—such as heavily strained RuO_2 and, to a lesser extent, the more lightly strained Sr_2RuO_4 thin films studied in this work—it is oftentimes difficult to disentangle strain-induced variations in the superconducting behavior from effects caused by reduced dimensionality.

7.2 Future Work - Sr_2RuO_4

In the synthesis and characterization of superconducting Sr_2RuO_4 epitaxial thin films, it is clear that the most important item moving forward is to gain a *quantitative* handle on how the defects natively present in these samples degrade T_c . Our work has identified the different types of disorder that are present, how to detect such defects with x-ray diffraction, scanning transmission electron microscopy, and electrical transport measurements, and has *qualitatively* illustrated how these defects couple to the superconductivity. Once a

more quantitative understanding along these lines is reached, it will be possible to more reliably isolate changes in T_c induced by strain (and possibly other effects) from disorder-induced suppressions of T_c . It seems unlikely that Sr_2RuO_4 thin films in the clean limit will ever be synthesized by molecular-beam epitaxy (or other thin-film deposition techniques), based on a rather fundamental (*i.e.*, unavoidable) length scale for structural defects present in the heteroepitaxial growth of $N = 1$ Ruddlesden-Popper films on $N = \infty$ Ruddlesden-Popper substrates—namely, the anti-phase boundaries between film crystallites that nucleate on different terraces of the substrate, which are separated by *perovskite* unit cell step heights. Therefore, solving this issue of defects diminishing the superconductivity will likely not be accomplished by simply making this effect go to zero. Since we laid out and discussed several approaches for tackling this problem in chapter 4, we will not rehash the details here.

Once a more careful experimental and computational accounting of the effects of strain on superconductivity is achieved for Sr_2RuO_4 , it may be fruitful to grow strained thin films of metallic Ca_2RuO_4 and/or Ba_2RuO_4 (which are both metastable phases in bulk) as a means of further tuning the superconductivity in these quasi-two-dimensional ruthenates. Because Ca, Sr, and Ba occupy the same column of the periodic table, they are isovalent; however, their differing ionic sizes sterically produce “chemical strains” on the ruthenium-oxygen bonds, which can induce changes in the Ru-O bond lengths and/or coordinated rotations of the RuO_6 octahedral network. Random alloys containing more than one type of cation on the A-site—as was employed to tune the ferromagnetic tendencies of perovskite ruthenates [118, 119, 120]—will likely contain too much quenched disorder to exhibit superconductivity, but perhaps some combination of chemical- and substrate-imposed strains can be employed to realize enhanced superconducting properties.

7.3 Future Work - RuO₂

The unconventional superconductivity in Sr₂RuO₄ has been intensely studied for nearly 25 years. Accordingly, the existing body of work of what is known about this phase of matter is enormous, even if a comprehensive description of the superconductivity capable of accounting for all of these observations has remained elusive. By contrast, since the superconductivity in strained RuO₂ was not discovered until the work presented in this dissertation, there are very basic questions about this system that remain to be answered conclusively, including:

- Is the superconductivity conventional or unconventional? What is the connection, if any, of spin-density wave order and superconductivity? Do these phases coexist, or compete?
- What is the actual crystal structure of superconducting RuO₂/TiO₂(110) thin films? What role, if any, does the partial strain relaxation observed experimentally play in determining the superconducting properties?—*i.e.*, should we interpret the superconductivity as arising from coherently strained regions in such films, or from the more strain-relaxed regions? More generally, what symmetry modes and magnitudes of externally applied distortions of the crystal structure optimize T_c ?

Numerous future experiments and calculations that may help shed light on these questions have been proposed in chapter 5 and chapter 6, which we will not repeat here for brevity. Once these items have been addressed, it will be possible to provide a more sensible “roadmap” regarding what measurements should be performed to gain a more complete understanding of the electronic structure and strain-stabilized superconductivity in RuO₂, and whether similarly non-trivial modifications of the low-energy physics can be induced by straining other rutile structures, such as WO₂ or

MoO₂ [201, 261, 262, 263, 271]. On the materials side of the equation, perhaps the most important outstanding goal is to devise methods capable of applying large (likely several percent) compressive strains along the rutile c axis² that remain coherent over thicknesses of material that exceed the superconducting coherence length ξ by an order of magnitude (or greater). Until this is accomplished, the observed superconducting properties will likely reflect a muddled mixture of two competing effects: in thicker RuO₂/TiO₂(110) films, spatially heterogeneous c axis strains will result in spatially heterogeneous superconductivity, whereas in thinner RuO₂/TiO₂(110) films having thicknesses approaching (or less than) ξ , simple-minded evaluations of T_c will be complicated by disorder and superconducting fluctuation effects that become more pronounced in reduced dimensions—even though the strain status of such samples is more well-defined.

Unlike in the growth of perovskite oxide thin films, where a multitude of compatible substrates have been developed that span a wide range of in-plane lattice constants, TiO₂ is the only commercially available substrate for the growth of rutile oxide thin films. As illustrated in this dissertation, different orientations of TiO₂ can be employed to impart different amounts of strain on RuO₂, but none of these orientations are particularly well lattice-matched to RuO₂ except TiO₂(101); therefore, we either obtain lightly strained films with essentially bulk-like properties (RuO₂/TiO₂(101)), or heavily strained films having much more interesting properties, but also low critical thicknesses for strain relaxation (RuO₂/TiO₂(110), and also RuO₂/TiO₂(100)). In short, it does not seem that the usual substrate-imposed “strain game” can be played for more fine tuning of superconductivity in RuO₂ thin films. At present, we can envisage three ways of possibly circumventing this issue:

- Grow buffer layers of some other rutile material—*e.g.*, IrO₂ or Ru-doped Ti_{1-x}Ru_xO₂—on top of TiO₂(110) substrates before growing pure RuO₂ films on top

²As explained in previous chapters, we believe that the superconductivity in RuO₂ responds most sensitively to this type of distortion.

of the buffer layers. The buffer-layer thickness and material should be chosen to reduce the amount of substrate-imposed strain (via formation of misfit dislocations), but not totally eliminate the strain. If the buffer layer is metallic, some thought should also be given to how this might affect superconductivity in RuO_2 according to proximity effects. This approach has been previously employed in strain-tuning studies of the metal-insulator transition in VO_2 thin films synthesized on $\text{TiO}_2(001)$ substrates [260]; in this case, RuO_2 was actually used as the buffer layer.

- Grow superlattices on $\text{TiO}_2(110)$ consisting of interleaved thick RuO_2 and thin TiO_2 layers. This is highly non-trivial from the growth perspective, but has been previously demonstrated for IrO_2 [272] and RuO_2 ³. The insertion of periodically spaced TiO_2 layers should help to preserve some of the substrate-imposed strain; it is much less obvious, though, how the inevitable interdiffusion between Ti and Ru might affect the superconductivity, and also what the effective dimensionality of superconductivity would be in such an artificially designed material. Measurements of the in-plane upper critical fields would help to address the latter question.
- Perform uniaxial pressure experiments on RuO_2 , squeezing along the c axis. It is unclear at present whether enough compression could be applied to bulk single crystals of RuO_2 to induce superconductivity in this approach; recent state-of-the-art experiments on ruthenate and cuprate single crystals have demonstrated elastic strains to date of up to $\approx -1\%$ [171]. If this level of strain is not sufficient, a “hybrid” approach of externally applying uniaxial pressure to partially strain relaxed $\text{RuO}_2/\text{TiO}_2(110)$ thin film + substrate samples may prove to be fruitful.

³Unpublished work by Hanjong Paik.

BIBLIOGRAPHY

- [1] Anderson, P. W. More Is Different. *Science* **177**, 393–396 (1972). URL <http://www.sciencemag.org/content/177/4047/393>. [Page 1]
- [2] Bloch, F. Über die Quantenmechanik der Elektronen in Kristallgittern. *Zeitschrift für Physik* **52**, 555–600 (1929). URL <http://link.springer.com/article/10.1007/BF01339455>. [Page 3]
- [3] Boer, J. H. d. & Verwey, E. J. W. Semi-conductors with partially and with completely filled 3d-lattice bands. *Proc. Phys. Soc.* **49**, 59 (1937). URL <http://stacks.iop.org/0959-5309/49/i=4S/a=307>. [Page 4]
- [4] Mott, N. F. & Peierls, R. Discussion of the paper by de Boer and Verwey. *Proc. Phys. Soc.* **49**, 72 (1937). URL <http://stacks.iop.org/0959-5309/49/i=4S/a=308>. [Page 4]
- [5] Slater, J. C. Magnetic Effects and the Hartree-Fock Equation. *Physical Review* **82**, 538–541 (1951). URL <http://link.aps.org/doi/10.1103/PhysRev.82.538>. [Page 4]
- [6] Giannozzi, P. *et al.* QUANTUM ESPRESSO: a modular and open-source software project for quantum simulations of materials. *Journal of Physics: Condensed Matter* **21**, 395502 (19pp) (2009). URL <http://www.quantum-espresso.org>. [Pages 4, 106, and 170]
- [7] Giannozzi, P. *et al.* Advanced capabilities for materials modelling with QUANTUM ESPRESSO. *Journal of Physics: Condensed Matter* **29**, 465901 (2017). URL <http://stacks.iop.org/0953-8984/29/i=46/a=465901>. [Page 4]
- [8] Blaha, P. *et al.* WIEN2k, An Augmented Plane Wave + Local Orbitals Program for Calculating Crystal Properties (Karlheinz Schwarz, Vienna University of Technology, Austria, 2018). [Page 4]
- [9] Kresse, G. & Furthmüller, J. Efficient iterative schemes for ab initio total-energy calculations using a plane-wave basis set. *Physical Review B* **54**, 11169–11186 (1996). URL <https://link.aps.org/doi/10.1103/PhysRevB.54.11169>. [Pages 4, 105, and 171]
- [10] Kresse, G. & Joubert, D. From ultrasoft pseudopotentials to the projector augmented-wave method. *Physical Review B* **59**, 1758–1775 (1999). URL <https://link.aps.org/doi/10.1103/PhysRevB.59.1758>. [Pages 4, 105, and 171]

- [11] Hohenberg, P. & Kohn, W. Inhomogeneous Electron Gas. *Physical Review* **136**, B864–B871 (1964). URL <http://link.aps.org/doi/10.1103/PhysRev.136.B864>. [Page 4]
- [12] Kohn, W. & Sham, L. J. Self-Consistent Equations Including Exchange and Correlation Effects. *Physical Review* **140**, A1133–A1138 (1965). URL <http://link.aps.org/doi/10.1103/PhysRev.140.A1133>. [Page 4]
- [13] Landau, L. D. *Sov. Phys. JETP* **3**, 920 (1957). [Page 5]
- [14] Landau, L. D. *Sov. Phys. JETP* **5**, 101 (1957). [Page 5]
- [15] Landau, L. D. *Sov. Phys. JETP* **8**, 70 (1959). [Page 5]
- [16] Coleman, P. *Introduction to Many-Body Physics* (Cambridge University Press, 2015). [Page 6]
- [17] Georges, A. & Kotliar, G. Hubbard model in infinite dimensions. *Physical Review B* **45**, 6479–6483 (1992). URL <http://link.aps.org/doi/10.1103/PhysRevB.45.6479>. [Page 6]
- [18] Georges, A., Kotliar, G., Krauth, W. & Rozenberg, M. J. Dynamical mean-field theory of strongly correlated fermion systems and the limit of infinite dimensions. *Reviews of Modern Physics* **68**, 13–125 (1996). URL <http://link.aps.org/doi/10.1103/RevModPhys.68.13>. [Page 6]
- [19] Onnes, H. K. *Leiden Comm.* 120b, 122c, 124c (1911). [Page 7]
- [20] Meissner, W. & Ochsenfeld, R. Ein neuer effekt bei eintritt der supraleitfähigkeit. *Die Naturwissenschaften* **21**, 787–788 (1933). URL <http://link.springer.com/10.1007/BF01504252>. [Page 7]
- [21] Bednorz, J. G. & Müller, K. A. Possible high T_c superconductivity in the Ba-La-Cu-O system. *Zeitschrift für Physik B Condensed Matter* **64**, 189–193 (1986). URL <https://doi.org/10.1007/BF01303701>. [Pages 7, 14, 19, and 206]
- [22] Steglich, F. *et al.* Superconductivity in the Presence of Strong Pauli Paramagnetism: CeCu_2Si_2 . *Physical Review Letters* **43**, 1892–1896 (1979). URL <http://link.aps.org/doi/10.1103/PhysRevLett.43.1892>. [Pages 7 and 14]
- [23] London, F. & London, H. The electromagnetic equations of the superconductor. *Proc. R. Soc. Lond. A* **149**, 71–88 (1935-03). URL <http://rspa.royalsocietypublishing.org/content/149/866/71>. [Page 8]

- [24] Ginzburg, V. L. & Landau, L. D. On the theory of superconductivity. *Zh. Eksp. Teor. Fiz.* **20**, 1064–1082 (1950). [Page 8]
- [25] Cooper, L. N. Bound electron pairs in a degenerate Fermi gas. *Phys. Rev.* **104**, 1189–1190 (1956-11-15). URL <https://link.aps.org/doi/10.1103/PhysRev.104.1189>. [Page 8]
- [26] Bardeen, J., Cooper, L. N. & Schrieffer, J. R. Microscopic theory of superconductivity. *Phys. Rev.* **106**, 162–164 (1957-04-01). URL <https://link.aps.org/doi/10.1103/PhysRev.106.162>. [Page 8]
- [27] Bardeen, J., Cooper, L. N. & Schrieffer, J. R. Theory of superconductivity. *Phys. Rev.* **108**, 1175–1204 (1957-12-01). URL <https://link.aps.org/doi/10.1103/PhysRev.108.1175>. [Page 8]
- [28] Balian, R. & Werthamer, N. R. Superconductivity with Pairs in a Relative p Wave. *Physical Review* **131**, 1553–1564 (1963). URL <https://link.aps.org/doi/10.1103/PhysRev.131.1553>. [Page 12]
- [29] Fröhlich, H. Theory of the Superconducting State. I. The Ground State at the Absolute Zero of Temperature. *Physical Review* **79**, 845–856 (1950). URL <https://link.aps.org/doi/10.1103/PhysRev.79.845>. [Page 13]
- [30] Maxwell, E. Isotope effect in the superconductivity of mercury. *Phys. Rev.* **78**, 477–477 (1950-05-15). URL <https://link.aps.org/doi/10.1103/PhysRev.78.477>. [Page 13]
- [31] Maxwell, E. Superconductivity of Sn¹²⁴. *Phys. Rev.* **79**, 173–173 (1950-07-01). URL <https://link.aps.org/doi/10.1103/PhysRev.79.173>. [Page 13]
- [32] Reynolds, C. A., Serin, B. & Nesbitt, L. B. The isotope effect in superconductivity. I. Mercury. *Phys. Rev.* **84**, 691–694 (1951-11-15). URL <https://link.aps.org/doi/10.1103/PhysRev.84.691>. [Page 13]
- [33] Migdal, A. B. *Sov. Phys. JETP* **34**, 996 (1958). [Page 13]
- [34] Eliashberg, G. M. *Sov. Phys. JETP* **11**, 696 (1960). [Page 13]
- [35] McMillan, W. L. Transition Temperature of Strong-Coupled Superconductors. *Physical Review* **167**, 331–344 (1968). URL <https://link.aps.org/doi/10.1103/PhysRev.167.331>. [Pages 14, 162, and 196]

- [36] Allen, P. B. & Dynes, R. C. Transition temperature of strong-coupled superconductors reanalyzed. *Physical Review B* **12**, 905–922 (1975). URL <https://link.aps.org/doi/10.1103/PhysRevB.12.905>. [Pages 14, 162, and 196]
- [37] Maeno, Y. *et al.* Superconductivity in a layered perovskite without copper. *Nature* **372**, 532–534 (1994). URL <http://www.nature.com/nature/journal/v372/n6506/abs/372532a0>. [Pages 14, 30, 84, and 89]
- [38] Kamihara, Y., Watanabe, T., Hirano, M. & Hosono, H. Iron-Based Layered Superconductor La[O_{1-x}F_x]FeAs (x = 0.05-0.12) with T_c = 26 K. *Journal of the American Chemical Society* **130**, 3296–3297 (2008). URL <https://doi.org/10.1021/ja800073m>. [Page 14]
- [39] Kohn, W. & Luttinger, J. M. New Mechanism for Superconductivity. *Physical Review Letters* **15**, 524–526 (1965). URL <https://link.aps.org/doi/10.1103/PhysRevLett.15.524>. [Page 15]
- [40] Luttinger, J. M. New Mechanism for Superconductivity. *Physical Review* **150**, 202–214 (1966). URL <https://link.aps.org/doi/10.1103/PhysRev.150.202>. [Page 15]
- [41] Maiti, S. & Chubukov, A. V. Superconductivity from repulsive interaction. *AIP Conference Proceedings* **1550**, 3–73 (2013). URL <http://aip.scitation.org/doi/abs/10.1063/1.4818400>. [Page 15]
- [42] Chubukov, A. V., Khodas, M. & Fernandes, R. M. Magnetism, Superconductivity, and Spontaneous Orbital Order in Iron-Based Superconductors: Which Comes First and Why? *Physical Review X* **6**, 041045 (2016). URL <https://link.aps.org/doi/10.1103/PhysRevX.6.041045>. [Page 15]
- [43] Hsu, Y.-T. *et al.* Manipulating superconductivity in ruthenates through Fermi surface engineering. *Physical Review B* **94**, 045118 (2016). URL <http://link.aps.org/doi/10.1103/PhysRevB.94.045118>. [Pages 15 and 205]
- [44] Hsu, Y.-T., Rebola, A. F., Fennie, C. J. & Kim, E.-A. Band-structure-dependence of renormalization-group prediction on pairing channels (2017). URL <https://arxiv.org/abs/1701.07884>. [Pages 15 and 205]
- [45] Nair, H. P. *et al.* Synthesis science of SrRuO₃ and CaRuO₃ epitaxial films with high residual resistivity ratios. *APL Materials* **6**, 046101 (2018). URL <https://aip.scitation.org/doi/full/10.1063/1.5023477>. [Pages 18 and 32]
- [46] Nair, H. P. *et al.* Demystifying the growth of superconducting Sr₂RuO₄ thin films.

- APL Materials* **6**, 101108 (2018). URL <http://aip.scitation.org/doi/10.1063/1.5053084>. [Pages 18, 32, 103, and 104]
- [47] Cho, A. Y. & Arthur, J. R. Molecular beam epitaxy. *Progress in Solid State Chemistry* **10**, 157–191 (1975-01-01). URL <http://www.sciencedirect.com/science/journal/pii/0079678675900059>. [Page 18]
- [48] Henini, M. Molecular beam epitaxy: from research to manufacturing. *Thin Solid Films* **306**, 331–337 (1997-09-11). URL <http://www.sciencedirect.com/science/journal/pii/S0040609097002423>. [Page 19]
- [49] Tsui, D. C., Stormer, H. L. & Gossard, A. C. Two-dimensional magnetotransport in the extreme quantum limit. *Phys. Rev. Lett.* **48**, 1559–1562 (1982-05-31). URL <https://link.aps.org/doi/10.1103/PhysRevLett.48.1559>. [Page 19]
- [50] Pfeiffer, L. & West, K. W. The role of MBE in recent quantum hall effect physics discoveries. *Physica E* **20**, 57–64 (2003-12-01). URL <http://www.sciencedirect.com/science/journal/pii/S1386947703005174>. [Page 19]
- [51] Schlom, D. G. & Harris, J. S. MBE Growth of High T_c Superconductors. In *Molecular Beam Epitaxy*, 505–622 (Elsevier, 1995). URL <https://www.sciencedirect.com/science/article/pii/B9780815513711500081>. DOI: 10.1016/B978-081551371-1.50008-1. [Page 19]
- [52] King, P. D. C. *et al.* Atomic-scale control of competing electronic phases in ultrathin LaNiO_3 . *Nature Nanotechnology* **9**, 443–447 (2014). URL <https://www.nature.com/articles/nnano.2014.59>. [Pages 20, 23, and 79]
- [53] Monkman, E. J. *et al.* Quantum many-body interactions in digital oxide superlattices. *Nature Materials* **11**, 855–859 (2012). URL <http://www.nature.com/nmat/journal/v11/n10/full/nmat3405.html>. [Page 20]
- [54] Schlom, D. G., Chen, L.-Q., Pan, X., Schmehl, A. & Zurbuchen, M. A. A thin film approach to engineering functionality into oxides. *J. Am. Ceram. Soc.* **91**, 2429–2454 (2008). URL <http://onlinelibrary.wiley.com/doi/10.1111/j.1551-2916.2008.02556.x/abstract>. [Page 22]
- [55] Knudsen, M. Die Molekularströmung der Gase durch Öffnungen und die Effusion. *Ann. Phys.* **333**, 999–1016 (1909). URL <http://onlinelibrary.wiley.com/doi/10.1002/andp.19093330505/abstract>. [Page 21]
- [56] Nowadnick, E. A. *et al.* Quantifying electronic correlation strength in a complex oxide: A combined DMFT and ARPES study of LaNiO_3 . *Physical Review B* **92**, 245109

- (2015). URL <http://link.aps.org/doi/10.1103/PhysRevB.92.245109>. [Page 23]
- [57] Ruf, J. P., King, P. D. C., Nascimento, V. B., Schlom, D. G. & Shen, K. M. Surface atomic structure of epitaxial LaNiO_3 thin films studied by in situ LEED- $I(V)$. *Physical Review B* **95**, 115418 (2017). URL <http://link.aps.org/doi/10.1103/PhysRevB.95.115418>. [Pages 23, 79, and 80]
- [58] Coleman, E., Siegrist, T., Mixon, D. A., Trevor, P. L. & Trevor, D. J. A versatile low-pressure ozone source. *J. Vac. Sci. Technol.* **9**, 2408–2409 (1991). URL <http://avs.scitation.org/doi/abs/10.1116/1.577288>. [Page 24]
- [59] Zhukov, V., Popova, I. & Yates, J. T. Delivery of pure ozone in ultrahigh vacuum. *J. Vac. Sci. Technol.* **18**, 992–994 (2000). URL <http://avs.scitation.org/doi/10.1116/1.582288>. [Page 24]
- [60] Nie, Y. F. *et al.* Atomically precise interfaces from non-stoichiometric deposition. *Nature Communications* **5** (2014). URL <http://www.nature.com/ncomms/2014/140804/ncomms5530/abs/ncomms5530.html>. [Page 28]
- [61] Sullivan, M. C. *et al.* Complex oxide growth using simultaneous in situ reflection high-energy electron diffraction and x-ray reflectivity: When is one layer complete? *Applied Physics Letters* **106**, 031604 (2015). URL <http://scitation.aip.org/content/aip/journal/apl/106/3/10.1063/1.4906419>. [Page 29]
- [62] Perry, R. S. *et al.* Metamagnetism and Critical Fluctuations in High Quality Single Crystals of the Bilayer Ruthenate $\text{Sr}_3\text{Ru}_2\text{O}_7$. *Physical Review Letters* **86**, 2661–2664 (2001). URL <http://link.aps.org/doi/10.1103/PhysRevLett.86.2661>. [Pages 30, 84, and 125]
- [63] Capogna, L. *et al.* Sensitivity to Disorder of the Metallic State in the Ruthenates. *Physical Review Letters* **88**, 076602 (2002). URL <http://link.aps.org/doi/10.1103/PhysRevLett.88.076602>. [Pages 30, 124, and 125]
- [64] Mackenzie, A. P. Extremely Strong Dependence of Superconductivity on Disorder in Sr_2RuO_4 . *Physical Review Letters* **80**, 161–164 (1998). [Pages 30, 34, 84, 91, 92, 111, 112, 113, and 206]
- [65] Schneider, M. *et al.* Low-Energy Electronic Properties of Clean CaRuO_3 : Elusive Landau Quasiparticles. *Physical Review Letters* **112**, 206403 (2014). URL <http://link.aps.org/doi/10.1103/PhysRevLett.112.206403>. [Pages 30 and 125]

- [66] Liu, Y., Nair, H. P., Ruf, J. P., Schlom, D. G. & Shen, K. M. Revealing the hidden heavy Fermi liquid in CaRuO_3 . *Physical Review B* **98**, 041110 (2018). URL <https://link.aps.org/doi/10.1103/PhysRevB.98.041110>. [Page 30]
- [67] Hicks, C. W. *et al.* Strong Increase of T_c of Sr_2RuO_4 Under Both Tensile and Compressive Strain. *Science* **344**, 283–285 (2014). URL <http://science.sciencemag.org/content/344/6181/283>. [Pages 30, 96, 98, and 205]
- [68] Steppke, A. *et al.* Strong peak in T_c of Sr_2RuO_4 under uniaxial pressure. *Science* **355**, eaaf9398 (2017). URL <http://science.sciencemag.org/content/355/6321/eaaf9398>. [Pages 30, 96, 97, 202, and 205]
- [69] Brodsky, D. O. *et al.* Strain and vector magnetic field tuning of the anomalous phase in $\text{Sr}_3\text{Ru}_2\text{O}_7$. *Science Advances* **3**, e1501804 (2017). URL <http://advances.sciencemag.org/content/3/2/e1501804>. [Page 30]
- [70] Arthur, J. R. Interaction of Ga and As_2 Molecular Beams with GaAs Surfaces. *Journal of Applied Physics* **39**, 4032–4034 (1968). URL <http://aip.scitation.org/doi/10.1063/1.1656901>. [Page 31]
- [71] Brahlek, M., Zhang, L., Eaton, C., Zhang, H.-T. & Engel-Herbert, R. Accessing a growth window for SrVO_3 thin films. *Applied Physics Letters* **107**, 143108 (2015). URL <http://aip.scitation.org/doi/10.1063/1.4932198>. [Page 34]
- [72] Schlom, D. G. *et al.* Elastic strain engineering of ferroic oxides. *MRS Bulletin* **39**, 118–130 (2014). URL <https://doi.org/10.1557/mrs.2014.1>. [Page 35]
- [73] Matthews, J. W. & Blakeslee, A. E. Defects in epitaxial multilayers: I. Misfit dislocations. *Journal of Crystal Growth* **27**, 118–125 (1974). URL <http://www.sciencedirect.com/science/article/pii/S0022024874800552>. [Page 36]
- [74] Wang, T., Ganguly, K., Marshall, P., Xu, P. & Jalan, B. Critical thickness and strain relaxation in molecular beam epitaxy-grown SrTiO_3 films. *Applied Physics Letters* **103**, 212904 (2013). URL <http://aip.scitation.org/doi/full/10.1063/1.4833248>. [Pages 36 and 155]
- [75] Waasmaier, D. & Kirfel, A. New analytical scattering-factor functions for free atoms and ions. *Acta Crystallographica Section A Foundations of Crystallography* **51**, 416–431 (1995). URL <http://scripts.iucr.org/cgi-bin/paper?S0108767394013292>. [Page 39]
- [76] Smith, E. H., King, P. D. C., Soukiassian, A., Ast, D. G. & Schlom, D. G. Hybrid

- reflections from multiple x-ray scattering in epitaxial oxide films. *Applied Physics Letters* **111**, 131903 (2017). URL <http://aip.scitation.org/doi/abs/10.1063/1.4993477>. [Page 39]
- [77] Björck, M. & Andersson, G. *GenX* : an extensible X-ray reflectivity refinement program utilizing differential evolution. *Journal of Applied Crystallography* **40**, 1174–1178 (2007). URL <http://scripts.iucr.org/cgi-bin/paper?S0021889807045086>. [Page 43]
- [78] Parratt, L. G. Surface Studies of Solids by Total Reflection of X-Rays. *Physical Review* **95**, 359–369 (1954). URL <https://link.aps.org/doi/10.1103/PhysRev.95.359>. [Page 43]
- [79] Csiszar, S. I. & Tjeng, L. H. *X-ray diffraction and X-ray absorption of strained CoO and MnO thin films*. Ph.D. thesis, University of Groningen (2005). [Pages 48 and 155]
- [80] Einstein, A. Über einen die Erzeugung und Verwandlung des Lichtes betreffenden heuristischen Gesichtspunkt. *Ann. Phys.* **322**, 132–148 (1905). URL <http://onlinelibrary.wiley.com/doi/10.1002/andp.19053220607/abstract>. [Page 55]
- [81] Millikan, R. A. A Direct Photoelectric Determination of Planck's "h". *Phys. Rev.* **7**, 355–388 (1916). URL <https://link.aps.org/doi/10.1103/PhysRev.7.355>. [Page 56]
- [82] Berglund, C. N. & Spicer, W. E. Photoemission Studies of Copper and Silver: Theory. *Phys. Rev.* **136**, A1030–A1044 (1964). URL <https://link.aps.org/doi/10.1103/PhysRev.136.A1030>. [Page 57]
- [83] Berglund, C. N. & Spicer, W. E. Photoemission Studies of Copper and Silver: Experiment. *Phys. Rev.* **136**, A1044–A1064 (1964). URL <https://link.aps.org/doi/10.1103/PhysRev.136.A1044>. [Page 57]
- [84] Spicer, W. E. & Berglund, C. N. *d* Band of Copper. *Phys. Rev. Lett.* **12**, 9–11 (1964). URL <https://link.aps.org/doi/10.1103/PhysRevLett.12.9>. [Page 57]
- [85] Kane, E. O. Implications of Crystal Momentum Conservation in Photoelectric Emission for Band-Structure Measurements. *Phys. Rev. Lett.* **12**, 97–98 (1964). URL <https://link.aps.org/doi/10.1103/PhysRevLett.12.97>. [Page 57]
- [86] Gobeli, G. W., Allen, F. G. & Kane, E. O. Polarization Evidence for Momentum Conservation in Photoelectric Emission from Germanium and Silicon. *Phys. Rev. Lett.* **12**,

- 94–97 (1964). URL <https://link.aps.org/doi/10.1103/PhysRevLett.12.94>. [Page 57]
- [87] Harter, J. W. *Angle-resolved photoemission of $Sr_{1-x}La_2CuO_2$ thin films grown by molecular-beam epitaxy*. Doctoral dissertation, Cornell University, Ithaca, NY (2013). [Pages 57 and 67]
- [88] Traum, M. M., Smith, N. V. & Di Salvo, F. J. Angular Dependence of Photoemission and Atomic Orbitals in the Layer Compound $1T-TaSe_2$. *Phys. Rev. Lett.* **32**, 1241–1244 (1974). URL <https://link.aps.org/doi/10.1103/PhysRevLett.32.1241>. [Page 58]
- [89] Smith, N. V., Traum, M. M. & Di Salvo, F. J. Mapping energy bands in layer compounds from the angular dependence of ultraviolet photoemission. *Solid State Communications* **15**, 211–214 (1974). URL <http://www.sciencedirect.com/science/article/pii/0038109874907431>. [Page 58]
- [90] Damascelli, A., Hussain, Z. & Shen, Z.-X. Angle-resolved photoemission studies of the cuprate superconductors. *Reviews of Modern Physics* **75**, 473–541 (2003). URL <http://link.aps.org/doi/10.1103/RevModPhys.75.473>. [Pages 59, 61, and 64]
- [91] Glassford, K. M. & Chelikowsky, J. R. Electron transport properties in RuO_2 rutile. *Physical Review B* **49**, 7107–7114 (1994). URL <https://link.aps.org/doi/10.1103/PhysRevB.49.7107>. [Pages 64, 139, 140, 141, 142, 147, and 182]
- [92] Valla, T., Fedorov, A. V., Johnson, P. D. & Hulbert, S. L. Many-Body Effects in Angle-Resolved Photoemission: Quasiparticle Energy and Lifetime of a $Mo(110)$ Surface State. *Physical Review Letters* **83**, 2085–2088 (1999). URL <http://link.aps.org/doi/10.1103/PhysRevLett.83.2085>. [Pages 64 and 186]
- [93] Ingle, N. J. C. *et al.* Quantitative analysis of Sr_2RuO_4 angle-resolved photoemission spectra: Many-body interactions in a model Fermi liquid. *Physical Review B* **72**, 205114 (2005). URL <http://link.aps.org/doi/10.1103/PhysRevB.72.205114>. [Page 64]
- [94] Shirley, D. A. High-Resolution X-Ray Photoemission Spectrum of the Valence Bands of Gold. *Physical Review B* **5**, 4709–4714 (1972). URL <http://link.aps.org/doi/10.1103/PhysRevB.5.4709>. [Page 65]
- [95] Végh, J. The Shirley background revised. *Journal of Electron Spectroscopy and Related Phenomena* **151**, 159–164 (2006). URL <http://www.sciencedirect.com/science/article/pii/S0368204805005220>. [Page 65]

- [96] Seah, M. P. & Dench, W. A. Quantitative electron spectroscopy of surfaces: A standard data base for electron inelastic mean free paths in solids. *Surface and Interface Analysis* **1**, 2–11 (1979). URL <http://onlinelibrary.wiley.com/doi/10.1002/sia.740010103/abstract>. [Pages 65 and 76]
- [97] Chiang, T. C., Knapp, J. A., Aono, M. & Eastman, D. E. Angle-resolved photoemission, valence-band dispersions $E(k)$, and electron and hole lifetimes for GaAs. *Physical Review B* **21**, 3513–3522 (1980). URL <http://link.aps.org/doi/10.1103/PhysRevB.21.3513>. [Page 67]
- [98] Monkman, E. J. *Revealing electronic structure in atomically-engineered manganite thin films*. Doctoral dissertation, Cornell University, Ithaca, NY (2014). [Page 67]
- [99] Shai, D. E. *Angle-resolved photoemission spectroscopy of ferromagnetic EuO and SrRuO₃ thin films*. Doctoral dissertation, Cornell University, Ithaca, NY (2014). [Page 67]
- [100] Wei, H. I. *Electronic structure and ordered phases in epitaxially-stabilized n-type cuprates*. Doctoral dissertation, Cornell University, Ithaca, NY (2018). [Pages 68 and 69]
- [101] LEED Lecture Notes. URL http://w0.rz-berlin.mpg.de/th/www/site/uploads/Events/lecture_summer_term_2006_3.pdf. [Page 76]
- [102] Davisson, C. J. & Germer, L. H. Reflection of Electrons by a Crystal of Nickel. *Proceedings of the National Academy of Sciences of the United States of America* **14**, 317–322 (1928). URL <https://www.ncbi.nlm.nih.gov/pmc/articles/PMC1085484/>. [Page 76]
- [103] Pendry, J. B. *Low energy electron diffraction: the theory and its application to determination of surface structure* (Academic Press, London; New York, 1974). OCLC: 1093141. [Page 77]
- [104] Van Hove, M. A., Weinberg, W. H. & Chan, C.-M. *Low-Energy Electron Diffraction*, vol. 6 of *Springer Series in Surface Sciences* (Springer, Berlin, Heidelberg, 1986). URL <http://link.springer.com/10.1007/978-3-642-82721-1>. [Page 77]
- [105] Heinz, K. LEED and DLEED as modern tools for quantitative surface structure determination. *Reports on Progress in Physics* **58**, 637 (1995). URL <http://iopscience.iop.org/0034-4885/58/6/003>. [Page 77]
- [106] Rous, P. J. *et al.* Tensor LEED: A Technique for High-Speed Surface-Structure Determination. *Physical Review Letters* **57**, 2951–2954 (1986). URL <http://link.aps.org/doi/10.1103/PhysRevLett.57.2951>. [Page 77]

- [107] Kottcke, M. & Heinz, K. A new approach to automated structure optimization in LEED intensity analysis. *Surface Science* **376**, 352–366 (1997). URL <http://www.sciencedirect.com/science/article/pii/S0039602896013076>. [Page 77]
- [108] Blum, V. & Heinz, K. Fast LEED intensity calculations for surface crystallography using Tensor LEED. *Computer Physics Communications* **134**, 392–425 (2001). URL <http://www.sciencedirect.com/science/article/pii/S0010465500002095>. [Page 77]
- [109] Pendry, J. B. Reliability factors for LEED calculations. *Journal of Physics C: Solid State Physics* **13**, 937 (1980). URL <http://iopscience.iop.org/0022-3719/13/5/024>. [Page 78]
- [110] Nascimento, V. B. *et al.* Procedure for LEED $I(V)$ structural analysis of metal oxide surfaces: $\text{Ca}_{1.5}\text{Sr}_{0.5}\text{RuO}_4(001)$. *Physical Review B* **75**, 035408 (2007). URL <http://link.aps.org/doi/10.1103/PhysRevB.75.035408>. [Page 79]
- [111] Moore, R. G. *et al.* A Surface-Tailored, Purely Electronic, Mott Metal-to-Insulator Transition. *Science* **318**, 615–619 (2007). URL <http://www.sciencemag.org/content/318/5850/615>. [Page 79]
- [112] Moore, R. G. *et al.* Manifestations of Broken Symmetry: The Surface Phases of $\text{Ca}_{2-x}\text{Sr}_x\text{RuO}_4$. *Physical Review Letters* **100**, 066102 (2008). URL <http://link.aps.org/doi/10.1103/PhysRevLett.100.066102>. [Page 79]
- [113] Nascimento, V. B. *et al.* Surface-Stabilized Nonferromagnetic Ordering of a Layered Ferromagnetic Manganite. *Physical Review Letters* **103**, 227201 (2009). URL <http://link.aps.org/doi/10.1103/PhysRevLett.103.227201>. [Page 79]
- [114] Kumah, D. P. *et al.* Effect of Surface Termination on the Electronic Properties of LaNiO_3 Films. *Physical Review Applied* **2**, 054004 (2014). URL <http://link.aps.org/doi/10.1103/PhysRevApplied.2.054004>. [Page 79]
- [115] Kumah, D. P. *et al.* Tuning the Structure of Nickelates to Achieve Two-Dimensional Electron Conduction. *Advanced Materials* **26**, 1935–1940 (2014). URL <http://onlinelibrary.wiley.com/doi/10.1002/adma.201304256/abstract>. [Page 79]
- [116] Ruddlesden, S. N. & Popper, P. The compound $\text{Sr}_3\text{Ti}_2\text{O}_7$ and its structure. *Acta Crystallographica* **11**, 54–55 (1958). URL [//scripts.iucr.org/cgi-bin/paper?a02171](http://scripts.iucr.org/cgi-bin/paper?a02171). [Page 83]

- [117] Callaghan, A., Moeller, C. W. & Ward, R. Magnetic Interactions in Ternary Ruthenium Oxides. *Inorganic Chemistry* **5**, 1572–1576 (1966). URL <https://doi.org/10.1021/ic50043a023>. [Page 84]
- [118] Jin, C.-Q. *et al.* High-pressure synthesis of the cubic perovskite BaRuO₃ and evolution of ferromagnetism in ARuO₃ (A = Ca, Sr, Ba) ruthenates. *Proceedings of the National Academy of Sciences* **105**, 7115–7119 (2008). URL <http://www.pnas.org/content/105/20/7115>. [Pages 84 and 208]
- [119] Zhou, J.-S. *et al.* Critical Behavior of the Ferromagnetic Perovskite BaRuO₃. *Physical Review Letters* **101**, 077206 (2008). URL <http://link.aps.org/doi/10.1103/PhysRevLett.101.077206>. [Pages 84 and 208]
- [120] Cheng, J.-G., Zhou, J.-S. & Goodenough, J. B. Lattice effects on ferromagnetism in perovskite ruthenates. *Proceedings of the National Academy of Sciences* **110**, 13312–13315 (2013). URL <http://www.pnas.org/content/110/33/13312>. [Pages 84 and 208]
- [121] Lester, C. *et al.* Field-tunable spin-density-wave phases in Sr₃Ru₂O₇. *Nature Materials* **14**, 373–378 (2015). URL <http://www.nature.com/articles/nmat4181>. [Page 84]
- [122] Walz, L. & Lichtenberg, F. Refinement of the structure of Sr₂RuO₄ with 100 and 295 K X-ray data. *Acta Crystallographica Section C: Crystal Structure Communications* **49**, 1268–1270 (1993). URL <http://scripts.iucr.org/cgi-bin/paper?sh1024>. [Pages 84 and 104]
- [123] Vogt, T. & Buttrey, D. J. Low-temperature structural behavior of Sr₂RuO₄. *Physical Review B* **52**, R9843–R9846 (1995). URL <http://link.aps.org/doi/10.1103/PhysRevB.52.R9843>. [Pages 84 and 104]
- [124] Braden, M., Moudden, A. H., Nishizaki, S., Maeno, Y. & Fujita, T. Structural analysis of Sr₂RuO₄. *Physica C: Superconductivity* **273**, 248–254 (1997). URL <http://www.sciencedirect.com/science/article/pii/S0921453496006375>. [Pages 84 and 85]
- [125] Chmaissem, O. Thermal expansion and compressibility of Sr₂RuO₄. *Physical Review B* **57**, 5067–5070 (1998). [Page 84]
- [126] Braden, M., Reichardt, W., Sidis, Y., Mao, Z. & Maeno, Y. Lattice dynamics and electron-phonon coupling in Sr₂RuO₄: Inelastic neutron scattering and shell-model calculations. *Physical Review B* **76**, 014505 (2007). URL <https://link.aps.org/doi/10.1103/PhysRevB.76.014505>. [Pages 84 and 85]

- [127] Braden, M., André, G., Nakatsuji, S. & Maeno, Y. Crystal and magnetic structure of Ca_2RuO_4 : Magnetoelastic coupling and the metal-insulator transition. *Physical Review B* **58**, 847–861 (1998). URL <http://link.aps.org/doi/10.1103/PhysRevB.58.847>. [Page 84]
- [128] Friedt, O. *et al.* Structural and magnetic aspects of the metal-insulator transition in $\text{Ca}_{2-x}\text{Sr}_x\text{RuO}_4$. *Physical Review B* **63**, 174432 (2001). URL <http://link.aps.org/doi/10.1103/PhysRevB.63.174432>. [Page 84]
- [129] Yin, Z. P., Haule, K. & Kotliar, G. Kinetic frustration and the nature of the magnetic and paramagnetic states in iron pnictides and iron chalcogenides. *Nature Materials* **10**, 932–935 (2011). URL <http://www.nature.com/nmat/journal/v10/n12/full/nmat3120.html>. [Page 86]
- [130] Mravlje, J. *et al.* Coherence-Incoherence Crossover and the Mass-Renormalization Puzzles in Sr_2RuO_4 . *Physical Review Letters* **106**, 096401 (2011). URL <http://link.aps.org/doi/10.1103/PhysRevLett.106.096401>. [Pages 86, 89, 178, and 182]
- [131] de' Medici, L., Mravlje, J. & Georges, A. Janus-Faced Influence of Hund's Rule Coupling in Strongly Correlated Materials. *Physical Review Letters* **107**, 256401 (2011). URL <http://link.aps.org/doi/10.1103/PhysRevLett.107.256401>. [Page 86]
- [132] Georges, A., Medici, L. d. & Mravlje, J. Strong Correlations from Hund's Coupling. *Annual Review of Condensed Matter Physics* **4**, 137–178 (2013). URL <http://dx.doi.org/10.1146/annurev-conmatphys-020911-125045>. [Page 86]
- [133] Mravlje, J. Thermopower and Entropy: Lessons from Sr_2RuO_4 . *Physical Review Letters* **117** (2016). [Page 86]
- [134] Maeno, Y. *et al.* Two-Dimensional Fermi Liquid Behavior of the Superconductor Sr_2RuO_4 . *Journal of the Physical Society of Japan* **66**, 1405–1408 (1997). URL <https://journals-jps-jp/doi/abs/10.1143/JPSJ.66.1405>. [Page 87]
- [135] Ishida, K. *et al.* Anisotropic pairing in superconducting Sr_2RuO_4 : Ru NMR and NQR studies. *Physical Review B* **56**, R505–R508 (1997). URL <https://link.aps.org/doi/10.1103/PhysRevB.56.R505>. [Page 87]
- [136] Bergemann, C., Mackenzie, A. P., Julian, S. R., Forsythe, D. & Ohmichi, E. Quasi-two-dimensional Fermi liquid properties of the unconventional superconductor Sr_2RuO_4 . *Advances in Physics* **52**, 639–725 (2003). URL <http://www.tandfonline.com/doi/abs/10.1080/00018730310001621737>. [Pages 87 and 88]

- [137] Mackenzie, A. P. Quantum Oscillations in the Layered Perovskite Superconductor Sr_2RuO_4 . *Physical Review Letters* **76**, 3786–3789 (1996). [Pages 87, 88, 92, and 182]
- [138] Bergemann, C., Julian, S. R., Mackenzie, A. P., NishiZaki, S. & Maeno, Y. Detailed Topography of the Fermi Surface of Sr_2RuO_4 . *Physical Review Letters* **84**, 2662–2665 (2000). URL <https://link.aps.org/doi/10.1103/PhysRevLett.84.2662>. [Page 87]
- [139] Damascelli, A. *et al.* Fermi Surface, Surface States, and Surface Reconstruction in Sr_2RuO_4 . *Physical Review Letters* **85**, 5194–5197 (2000). URL <http://link.aps.org/doi/10.1103/PhysRevLett.85.5194>. [Page 87]
- [140] Tamai, A. *et al.* High-Resolution Photoemission on Sr_2RuO_4 Reveals Correlation-Enhanced Effective Spin-Orbit Coupling and Dominantly Local Self-Energies. *Physical Review X* **9**, 021048 (2019). URL <https://link.aps.org/doi/10.1103/PhysRevX.9.021048>. [Pages 88, 106, 182, and 186]
- [141] Rice, T. M. & Sigrist, M. Sr_2RuO_4 : an electronic analogue of ^3He ? *Journal of Physics: Condensed Matter* **7**, L643 (1995). URL <http://stacks.iop.org/0953-8984/7/i=47/a=002>. [Page 89]
- [142] Ishida, K. *et al.* Spin-triplet superconductivity in Sr_2RuO_4 identified by ^{17}O Knight shift. *Nature* **396**, 658 (1998). URL <https://www.nature.com/articles/25315>. [Pages 89 and 92]
- [143] Duffy, J. A. *et al.* Polarized-Neutron Scattering Study of the Cooper-Pair Moment in Sr_2RuO_4 . *Physical Review Letters* **85**, 5412–5415 (2000). URL <https://link.aps.org/doi/10.1103/PhysRevLett.85.5412>. [Page 89]
- [144] Nelson, K. D., Mao, Z. Q., Maeno, Y. & Liu, Y. Odd-Parity Superconductivity in Sr_2RuO_4 . *Science* **306**, 1151–1154 (2004). URL <http://science.sciencemag.org/content/306/5699/1151>. [Page 89]
- [145] Pustogow, A. *et al.* Constraints on the superconducting order parameter in Sr_2RuO_4 from oxygen-17 nuclear magnetic resonance. *Nature* **574**, 72–75 (2019). URL <http://www.nature.com/articles/s41586-019-1596-2>. [Pages 89 and 92]
- [146] Mackenzie, A. P. & Maeno, Y. The superconductivity of Sr_2RuO_4 and the physics of spin-triplet pairing. *Reviews of Modern Physics* **75**, 657–712 (2003). URL <http://link.aps.org/doi/10.1103/RevModPhys.75.657>. [Page 90]
- [147] Maeno, Y., Kittaka, S., Nomura, T., Yonezawa, S. & Ishida, K. Evaluation of Spin-Triplet Superconductivity in Sr_2RuO_4 . *Journal of the Physical Society of Japan*

- 81, 011009 (2011). URL <http://journals.jps.jp/doi/abs/10.1143/JPSJ.81.011009>. [Page 90]
- [148] Mackenzie, A. P., Scaffidi, T., Hicks, C. W. & Maeno, Y. Even odder after twenty-three years: the superconducting order parameter puzzle of Sr_2RuO_4 . *npj Quantum Materials* **2**, 1–9 (2017). URL <http://www.nature.com/articles/s41535-017-0045-4>. [Pages 90 and 93]
- [149] Anderson, P. W. Theory of dirty superconductors. *Journal of Physics and Chemistry of Solids* **11**, 26–30 (1959). URL <http://www.sciencedirect.com/science/article/pii/0022369759900368>. [Pages 90 and 206]
- [150] Mao, Z. Q. Suppression of superconductivity in Sr_2RuO_4 . *Physical Review B* **60**, 610–614 (1999). [Page 91]
- [151] Kikugawa, N. & Maeno, Y. Non-Fermi-Liquid Behavior in Sr_2RuO_4 with Nonmagnetic Impurities. *Physical Review Letters* **89**, 117001 (2002). URL <https://link.aps.org/doi/10.1103/PhysRevLett.89.117001>. [Pages 91 and 125]
- [152] Akima, T., NishiZaki, S. & Maeno, Y. Intrinsic Superconducting Parameters of Sr_2RuO_4 . *Journal of the Physical Society of Japan* **68**, 694–695 (1999). URL <https://journals-jps-jp/doi/abs/10.1143/JPSJ.68.694>. [Pages 91 and 116]
- [153] Bobowski, J. S. *et al.* Improved Single-Crystal Growth of Sr_2RuO_4 . *Condensed Matter* **4**, 6 (2019). URL <https://www.mdpi.com/2410-3896/4/1/6>. [Page 91]
- [154] Ishida, K., Manago, M. & Maeno, Y. Reduction of the ^{17}O Knight shift in the Superconducting State and the Heat-up Effect by NMR Pulses on Sr_2RuO_4 (2019). URL <https://arxiv.org/abs/1907.12236v2>. [Page 93]
- [155] Rømer, A. T., Scherer, D. D., Eremin, I. M., Hirschfeld, P. J. & Andersen, B. M. Knight Shift and Leading Superconducting Instability From Spin Fluctuations in Sr_2RuO_4 . *arXiv:1905.04782 [cond-mat]* (2019). URL <http://arxiv.org/abs/1905.04782>. [Page 93]
- [156] Luke, G. M. *et al.* Time-reversal symmetry-breaking superconductivity in Sr_2RuO_4 . *Nature* **394**, 558 (1998). URL <https://www.nature.com/articles/29038>. [Page 93]
- [157] Xia, J., Maeno, Y., Beyersdorf, P. T., Fejer, M. M. & Kapitulnik, A. High Resolution Polar Kerr Effect Measurements of Sr_2RuO_4 : Evidence for Broken Time-Reversal Symmetry in the Superconducting State. *Physical Review Letters* **97**,

- 167002 (2006). URL <https://link.aps.org/doi/10.1103/PhysRevLett.97.167002>. [Page 93]
- [158] Kirtley, J. R. *et al.* Upper limit on spontaneous supercurrents in Sr_2RuO_4 . *Physical Review B* **76**, 014526 (2007). URL <https://link.aps.org/doi/10.1103/PhysRevB.76.014526>. [Page 94]
- [159] Hicks, C. W. *et al.* Limits on superconductivity-related magnetization in Sr_2RuO_4 and $\text{PrOs}_4\text{Sb}_{12}$ from scanning SQUID microscopy. *Physical Review B* **81**, 214501 (2010). URL <https://link.aps.org/doi/10.1103/PhysRevB.81.214501>. [Page 94]
- [160] NishiZaki, S., Maeno, Y. & Mao, Z. Changes in the Superconducting State of Sr_2RuO_4 under Magnetic Fields Probed by Specific Heat. *Journal of the Physical Society of Japan* **69**, 572–578 (2000). URL <http://journals.jps.jp/doi/abs/10.1143/JPSJ.69.572>. [Page 94]
- [161] Izawa, K. *et al.* Superconducting Gap Structure of Spin-Triplet Superconductor Sr_2RuO_4 Studied by Thermal Conductivity. *Physical Review Letters* **86**, 2653–2656 (2001). URL <https://link.aps.org/doi/10.1103/PhysRevLett.86.2653>. [Page 95]
- [162] Tanatar, M. A. *et al.* Anisotropy of Magnetothermal Conductivity in Sr_2RuO_4 . *Physical Review Letters* **86**, 2649–2652 (2001). URL <https://link.aps.org/doi/10.1103/PhysRevLett.86.2649>. [Page 95]
- [163] Hassinger, E. Vertical Line Nodes in the Superconducting Gap Structure of Sr_2RuO_4 . *Physical Review X* **7** (2017). [Page 95]
- [164] Bonalde, I. *et al.* Temperature Dependence of the Penetration Depth in Sr_2RuO_4 : Evidence for Nodes in the Gap Function. *Physical Review Letters* **85**, 4775–4778 (2000). URL <https://link.aps.org/doi/10.1103/PhysRevLett.85.4775>. [Page 95]
- [165] Lupien, C. *et al.* Ultrasound Attenuation in Sr_2RuO_4 : An Angle-Resolved Study of the Superconducting Gap Function. *Physical Review Letters* **86**, 5986–5989 (2001). URL <https://link.aps.org/doi/10.1103/PhysRevLett.86.5986>. [Page 95]
- [166] Firmo, I. A. *et al.* Evidence from tunneling spectroscopy for a quasi-one-dimensional origin of superconductivity in Sr_2RuO_4 . *Physical Review B* **88**, 134521 (2013). URL <http://link.aps.org/doi/10.1103/PhysRevB.88.134521>. [Page 95]

- [167] Forsythe, D. *et al.* Evolution of Fermi-Liquid Interactions in Sr_2RuO_4 under Pressure. *Physical Review Letters* **89**, 166402 (2002). URL <https://link.aps.org/doi/10.1103/PhysRevLett.89.166402>. [Page 95]
- [168] Nakatsuji, S. & Maeno, Y. Quasi-Two-Dimensional Mott Transition System $\text{Ca}_{2-x}\text{Sr}_x\text{RuO}_4$. *Physical Review Letters* **84**, 2666–2669 (2000). URL <http://link.aps.org/doi/10.1103/PhysRevLett.84.2666>. [Page 96]
- [169] Shen, K. M. *et al.* Evolution of the Fermi Surface and Quasiparticle Renormalization through a van Hove Singularity in $\text{Sr}_{2-y}\text{La}_y\text{RuO}_4$. *Physical Review Letters* **99**, 187001 (2007). URL <http://link.aps.org/doi/10.1103/PhysRevLett.99.187001>. [Page 96]
- [170] Barber, M., Gibbs, A., Maeno, Y., Mackenzie, A. & Hicks, C. Resistivity in the Vicinity of a van Hove Singularity: Sr_2RuO_4 under Uniaxial Pressure. *Physical Review Letters* **120**, 076602 (2018). URL <https://link.aps.org/doi/10.1103/PhysRevLett.120.076602>. [Pages 96, 99, 100, 124, and 205]
- [171] Barber, M. E. The Physics of Sr_2RuO_4 Approaching a Van Hove Singularity. In *Uniaxial Stress Technique and Investigations of Correlated Electron Systems*, Springer Theses, 49–109 (Springer, Cham, 2018). URL https://link.springer.com/chapter/10.1007/978-3-319-93973-5_3. [Pages 96, 99, and 211]
- [172] Watson, C. A., Gibbs, A. S., Mackenzie, A. P., Hicks, C. W. & Moler, K. A. Micron-scale measurements of low anisotropic strain response of local T_c in Sr_2RuO_4 . *Physical Review B* **98**, 094521 (2018). URL <https://link.aps.org/doi/10.1103/PhysRevB.98.094521>. [Page 98]
- [173] Li, Y.-S. *et al.* High precision heat capacity measurements on Sr_2RuO_4 under uniaxial pressure. *arXiv:1906.07597 [cond-mat]* (2019). URL <http://arxiv.org/abs/1906.07597>. ArXiv: 1906.07597. [Page 98]
- [174] Sunko, V. *et al.* Direct observation of a uniaxial stress-driven Lifshitz transition in Sr_2RuO_4 . *npj Quantum Materials* **4**, 1–7 (2019). URL <http://www.nature.com/articles/s41535-019-0185-9>. [Page 100]
- [175] Liu, Y.-C., Zhang, F.-C., Rice, T. M. & Wang, Q.-H. Theory of the evolution of superconductivity in Sr_2RuO_4 under anisotropic strain. *npj Quantum Materials* **2**, 12 (2017). URL <https://www.nature.com/articles/s41535-017-0014-y>. [Page 102]
- [176] Burganov, B. *et al.* Strain Control of Fermiology and Many-Body Interactions in Two-Dimensional Ruthenates. *Physical Review Letters* **116**, 197003

- (2016). URL <http://link.aps.org/doi/10.1103/PhysRevLett.116.197003>. [Pages 102, 109, 110, 163, and 207]
- [177] Zurbuchen, M. A. *et al.* Suppression of superconductivity by crystallographic defects in epitaxial Sr₂RuO₄ films. *Applied Physics Letters* **78**, 2351–2353 (2001). URL <http://scitation.aip.org/content/aip/journal/apl/78/16/10.1063/1.1364659>. [Page 104]
- [178] Zurbuchen, M. A. *et al.* Defect generation by preferred nucleation in epitaxial Sr₂RuO₄/LaAlO₃. *Applied Physics Letters* **83**, 3891–3893 (2003). URL <http://aip.scitation.org/doi/10.1063/1.1624631>. [Page 104]
- [179] Krockenberger, Y. *et al.* Growth of superconducting Sr₂RuO₄ thin films. *Applied Physics Letters* **97**, 082502 (2010). URL <http://scitation.aip.org/content/aip/journal/apl/97/8/10.1063/1.3481363>. [Page 104]
- [180] Cao, J. *et al.* Enhanced localized superconductivity in Sr₂RuO₄ thin film by pulsed laser deposition. *Superconductor Science and Technology* **29**, 095005 (2016). URL <http://stacks.iop.org/0953-2048/29/i=9/a=095005>. [Pages 104 and 123]
- [181] Uchida, M. *et al.* Molecular beam epitaxy growth of superconducting Sr₂RuO₄ films. *APL Materials* **5**, 106108 (2017). URL <http://aip.scitation.org/doi/10.1063/1.5007342>. [Page 104]
- [182] Dal Corso, A. Pseudopotentials periodic table: From H to Pu. *Computational Materials Science* **95**, 337–350 (2014). URL <http://www.sciencedirect.com/science/article/pii/S0927025614005187>. [Pages 106 and 170]
- [183] Haverkort, M. W. Strong Spin-Orbit Coupling Effects on the Fermi Surface of Sr₂RuO₄. *Physical Review Letters* **101** (2008). [Page 106]
- [184] Zhang, G., Gorelov, E., Sarvestani, E. & Pavarini, E. Fermi Surface of Sr₂RuO₄: Spin-Orbit and Anisotropic Coulomb Interaction Effects. *Physical Review Letters* **116**, 106402 (2016). URL <http://link.aps.org/doi/10.1103/PhysRevLett.116.106402>. [Page 106]
- [185] Kim, M., Mravlje, J., Ferrero, M., Parcollet, O. & Georges, A. Spin-Orbit Coupling and Electronic Correlations in Sr₂RuO₄. *Physical Review Letters* **120**, 126401 (2018). URL <https://link.aps.org/doi/10.1103/PhysRevLett.120.126401>. [Page 106]
- [186] Mostofi, A. A. *et al.* An updated version of wannier90: A tool for obtain-

- ing maximally-localised Wannier functions. *Computer Physics Communications* **185**, 2309–2310 (2014). URL <http://www.sciencedirect.com/science/article/pii/S001046551400157X>. [Pages 107 and 170]
- [187] Perdew, J. P., Burke, K. & Ernzerhof, M. Generalized Gradient Approximation Made Simple. *Physical Review Letters* **77**, 3865–3868 (1996). URL <https://link.aps.org/doi/10.1103/PhysRevLett.77.3865>. [Pages 107 and 170]
- [188] Facio, J. I., Mravlje, J., Pourovskii, L., Cornaglia, P. S. & Vildosola, V. Spin-orbit and anisotropic strain effects on the electronic correlations in Sr₂RuO₄. *Physical Review B* **98**, 085121 (2018). URL <https://link.aps.org/doi/10.1103/PhysRevB.98.085121>. [Page 110]
- [189] Scheurer, M. S., Agterberg, D. F. & Schmalian, J. Selection rules for Cooper pairing in two-dimensional interfaces and sheets. *npj Quantum Materials* **2**, 1–8 (2017). URL <http://www.nature.com/articles/s41535-016-0008-1>. [Page 116]
- [190] Uchida, M. *et al.* Anomalous enhancement of upper critical field in Sr₂RuO₄ thin films. *Physical Review B* **99**, 161111 (2019). URL <https://link.aps.org/doi/10.1103/PhysRevB.99.161111>. [Page 116]
- [191] Kim, G. *et al.* Electronic and vibrational signatures of ruthenium vacancies in Sr₂RuO₄ thin films. *Physical Review Materials* **3**, 094802 (2019). URL <https://link.aps.org/doi/10.1103/PhysRevMaterials.3.094802>. [Page 118]
- [192] Siemons, W. *et al.* Dependence of the electronic structure of SrRuO₃ and its degree of correlation on cation off-stoichiometry. *Physical Review B* **76**, 075126 (2007). URL <http://link.aps.org/doi/10.1103/PhysRevB.76.075126>. [Page 118]
- [193] Nelson, J. B. & Riley, D. P. An experimental investigation of extrapolation methods in the derivation of accurate unit-cell dimensions of crystals. *Proceedings of the Physical Society* **57**, 160–177 (1945). [Page 122]
- [194] Ariosa, D., Cancellieri, C., Lin, P. H. & Pavuna, D. Self-ordering of random intercalates in thin films of cuprate superconductors: Growth model and x-ray diffraction diagnosis. *Physical Review B* **75**, 184505 (2007). URL <https://link.aps.org/doi/10.1103/PhysRevB.75.184505>. [Page 123]
- [195] Cancellieri, C., Lin, P. H., Ariosa, D. & Pavuna, D. Embedded polytypes in Bi₂Sr_{2-x}La_xCuO₆ thin films grown by laser ablation. *Physical Review B* **76**, 174520 (2007). URL <https://link.aps.org/doi/10.1103/PhysRevB.76.174520>. [Page 123]

- [196] Tamai, A. *et al.* Fermi Surface and van Hove Singularities in the Itinerant Metamagnet $\text{Sr}_3\text{Ru}_2\text{O}_7$. *Physical Review Letters* **101**, 026407 (2008). URL <http://link.aps.org/doi/10.1103/PhysRevLett.101.026407>. [Page 125]
- [197] Wu, J., Bollinger, A. T., He, X. & Božović, I. Spontaneous breaking of rotational symmetry in copper oxide superconductors. *Nature* **547**, 432–435 (2017). URL <http://www.nature.com/nature/journal/v547/n7664/full/nature23290.html?foxtrotcallback=true>. [Page 126]
- [198] van der Pauw, L. J. A method of measuring the resistivity and Hall coefficient on lamellae of arbitrary shape. *Philips Technical Review* **20**, 220–224 (1958). [Page 126]
- [199] Goodenough, J. B. *Magnetism and the Chemical Bond*, vol. 1 of *Interscience Monographs on Chemistry* (John Wiley, New York, 1963). [Page 134]
- [200] Goodenough, J. B. Transition-Metal Oxides With Metallic Conductivity. *Bull. Soc. Chim. France* **Vol: No. 4** (1965). URL <https://www.osti.gov/biblio/4616194>. [Page 134]
- [201] Eyert, V., Horny, R., Höck, K.-H. & Horn, S. Embedded Peierls instability and the electronic structure of MoO_2 . *Journal of Physics: Condensed Matter* **12**, 4923 (2000). URL <http://stacks.iop.org/0953-8984/12/i=23/a=303>. [Pages 136, 202, and 210]
- [202] Eyert, V. The metal-insulator transitions of VO_2 : A band theoretical approach. *Annalen der Physik* **11**, 650–704 (2002). URL [http://onlinelibrary.wiley.com/doi/10.1002/1521-3889\(200210\)11:9<650::AID-ANDP650>3.0.CO;2-K/abstract](http://onlinelibrary.wiley.com/doi/10.1002/1521-3889(200210)11:9<650::AID-ANDP650>3.0.CO;2-K/abstract). [Pages 136 and 170]
- [203] Eyert, V. VO_2 : A Novel View from Band Theory. *Physical Review Letters* **107**, 016401 (2011). URL <https://link.aps.org/doi/10.1103/PhysRevLett.107.016401>. [Page 136]
- [204] Berlijn, T. *et al.* Itinerant Antiferromagnetism in RuO_2 . *Physical Review Letters* **118**, 077201 (2017). URL <https://link.aps.org/doi/10.1103/PhysRevLett.118.077201>. [Pages 138, 139, 142, 144, 151, 153, 170, 172, 174, 177, and 178]
- [205] Rogers, D. B., Shannon, R. D., Sleight, A. W. & Gillson, J. L. Crystal chemistry of metal dioxides with rutile-related structures. *Inorganic Chemistry* **8**, 841–849 (1969). URL <https://doi.org/10.1021/ic50074a029>. [Page 138]
- [206] Butler, S. R. & Gillson, J. L. Crystal growth, electrical resistivity and lattice parameters of RuO_2 and IrO_2 . *Materials Research Bulletin* **6**, 81–89

- (1971). URL <http://www.sciencedirect.com/science/article/pii/0025540871900924>. [Page 138]
- [207] Rao, K. V. K. & Iyengar, L. X-ray studies on the thermal expansion of ruthenium dioxide. *Acta Crystallographica Section A: Crystal Physics, Diffraction, Theoretical and General Crystallography* **25**, 302–303 (1969). URL [//scripts.iucr.org/cgi-bin/paper?a06458](http://scripts.iucr.org/cgi-bin/paper?a06458). [Page 138]
- [208] Ryden, W. D., Lawson, A. W. & Sartain, C. C. Temperature dependence of the resistivity of RuO₂ and IrO₂. *Physics Letters A* **26**, 209–210 (1968). URL <http://www.sciencedirect.com/science/article/pii/0375960168901266>. [Pages 138, 140, 141, and 147]
- [209] Ryden, W. D. Electrical Transport Properties of IrO₂ and RuO₂. *Physical Review B* **1**, 1494–1500 (1970). [Page 138]
- [210] Passenheim, B. C. & McCollum, D. C. Heat Capacity of RuO₂ and IrO₂ between 0.54° and 10°K. *The Journal of Chemical Physics* **51**, 320–321 (1969). URL <https://aip.scitation.org/doi/abs/10.1063/1.1671725>. [Pages 140, 141, and 182]
- [211] Marcus, S. M. Measurement of the magnetoresistance in the transition metal oxide RuO₂. *Physics Letters A* **28**, 191–192 (1968). URL <http://www.sciencedirect.com/science/article/pii/0375960168901941>. [Page 140]
- [212] Slivka, R. T. & Langenberg, D. N. Azbel'-Kaner cyclotron resonance in ruthenium dioxide. *Physics Letters A* **28**, 169–170 (1968). URL <http://www.sciencedirect.com/science/article/pii/0375960168901801>. [Pages 140 and 141]
- [213] Graebner, J. E., Greiner, E. S. & Ryden, W. D. Magnetothermal oscillations in RuO₂, OsO₂, and IrO₂. *Physical Review B* **13**, 2426–2432 (1976). URL <https://link.aps.org/doi/10.1103/PhysRevB.13.2426>. [Page 140]
- [214] Lin, J. J. *et al.* Low temperature electrical transport properties of RuO₂ and IrO₂ single crystals. *Journal of Physics: Condensed Matter* **16**, 8035 (2004). URL <http://stacks.iop.org/0953-8984/16/i=45/a=025>. [Pages 142, 145, and 146]
- [215] Zhu, Z. *et al.* Anomalous Antiferromagnetism in Metallic RuO₂ Determined by Resonant X-ray Scattering. *Physical Review Letters* **122**, 017202 (2019). URL <https://link.aps.org/doi/10.1103/PhysRevLett.122.017202>. [Pages 142 and 178]

- [216] Nair, S. *et al.* Magnetism and superconductivity driven by identical 4f states in a heavy-fermion metal. *Proceedings of the National Academy of Sciences* **107**, 9537–9540 (2010). URL <https://www.pnas.org/content/107/21/9537>. [Page 143]
- [217] Harter, J. W. *et al.* Nodeless Superconducting Phase Arising from a Strong (π, π) Antiferromagnetic Phase in the Infinite-Layer Electron-Doped $\text{Sr}_{1-x}\text{La}_x\text{CuO}_2$ Compound. *Physical Review Letters* **109**, 267001 (2012). URL <http://link.aps.org/doi/10.1103/PhysRevLett.109.267001>. [Page 143]
- [218] Hamidian, M. H. *et al.* Detection of a Cooper-pair density wave in $\text{Bi}_2\text{Sr}_2\text{CaCu}_2\text{O}_{8+x}$. *Nature* **532**, 343–347 (2016). URL <http://www.nature.com/articles/nature17411>. [Page 143]
- [219] Edkins, S. D. *et al.* Magnetic field-induced pair density wave state in the cuprate vortex halo. *Science* **364**, 976–980 (2019). URL <http://science.sciencemag.org/content/364/6444/976>. [Page 143]
- [220] Yamamoto, Y., Nakajima, K., Ohsawa, T., Matsumoto, Y. & Koinuma, H. Preparation of Atomically Smooth TiO_2 Single Crystal Surfaces and Their Photochemical Property. *Japanese Journal of Applied Physics* **44**, L511 (2005). URL <https://iopscience.iop.org/article/10.1143/JJAP.44.L511/meta>. [Page 144]
- [221] Burdett, J. K., Hughbanks, T., Miller, G. J., Richardson, J. W. & Smith, J. V. Structural-electronic relationships in inorganic solids: powder neutron diffraction studies of the rutile and anatase polymorphs of titanium dioxide at 15 and 295 K. *Journal of the American Chemical Society* **109**, 3639–3646 (1987). URL <http://pubs.acs.org/doi/abs/10.1021/ja00246a021>. [Pages 144, 153, and 172]
- [222] Miccoli, I., Edler, F., Pfnür, H. & Tegenkamp, C. The 100th anniversary of the four-point probe technique: the role of probe geometries in isotropic and anisotropic systems. *Journal of Physics: Condensed Matter* **27**, 223201 (2015). URL <http://stacks.iop.org/0953-8984/27/i=22/a=223201>. [Page 147]
- [223] Schneider, C. W., Thiel, S., Hammerl, G., Richter, C. & Mannhart, J. Microlithography of electron gases formed at interfaces in oxide heterostructures. *Applied Physics Letters* **89**, 122101 (2006). URL <http://aip.scitation.org/doi/10.1063/1.2354422>. [Page 147]
- [224] Hsu, J. W. P. & Kapitulnik, A. Superconducting transition, fluctuation, and vortex motion in a two-dimensional single-crystal Nb film. *Physical Review B* **45**, 4819–4835 (1992). URL <https://link.aps.org/doi/10.1103/PhysRevB.45.4819>. [Page 149]

- [225] Kim, M., Kozuka, Y., Bell, C., Hikita, Y. & Hwang, H. Y. Intrinsic spin-orbit coupling in superconducting δ -doped SrTiO₃ heterostructures. *Physical Review B* **86**, 085121 (2012). URL <https://link.aps.org/doi/10.1103/PhysRevB.86.085121>. [Page 149]
- [226] Werthamer, N. R., Helfand, E. & Hohenberg, P. C. Temperature and Purity Dependence of the Superconducting Critical Field, h_{c2} . III. Electron Spin and Spin-Orbit Effects. *Physical Review* **147**, 295–302 (1966). URL <https://link.aps.org/doi/10.1103/PhysRev.147.295>. [Page 150]
- [227] Wissberg, S. & Kalisky, B. Large-scale modulation in the superconducting properties of thin films due to domains in the SrTiO₃ substrate. *Physical Review B* **95**, 144510 (2017). URL <https://link.aps.org/doi/10.1103/PhysRevB.95.144510>. [Page 151]
- [228] Kalisky, B. *et al.* Stripes of increased diamagnetic susceptibility in underdoped superconducting BaFe_{1-x}Co_xAs₂ single crystals: Evidence for an enhanced superfluid density at twin boundaries. *Physical Review B* **81**, 184513 (2010). URL <https://link.aps.org/doi/10.1103/PhysRevB.81.184513>. [Page 151]
- [229] Kalisky, B. *et al.* Behavior of vortices near twin boundaries in underdoped BaFe_{1-x}Co_xAs₂. *Physical Review B* **83**, 064511 (2011). URL <https://link.aps.org/doi/10.1103/PhysRevB.83.064511>. [Page 151]
- [230] Paik, H. *et al.* Transport properties of ultra-thin VO₂ films on (001) TiO₂ grown by reactive molecular-beam epitaxy. *Applied Physics Letters* **107**, 163101 (2015). URL <https://aip.scitation.org/doi/10.1063/1.4932123>. [Page 151]
- [231] He, S. *et al.* Phase diagram and electronic indication of high-temperature superconductivity at 65 K in single-layer FeSe films. *Nature Materials* **12**, 605–610 (2013). URL <http://www.nature.com/nmat/journal/v12/n7/full/nmat3648.html>. [Page 151]
- [232] Yoshimatsu, K., Sakata, O. & Ohtomo, A. Superconductivity in Ti₄O₇ and γ -Ti₃O₅ films. *Scientific Reports* **7**, 12544 (2017). URL <https://www.nature.com/articles/s41598-017-12815-4>. [Page 151]
- [233] Gozar, A. *et al.* High-temperature interface superconductivity between metallic and insulating copper oxides. *Nature* **455**, 782–785 (2008). URL <http://www.nature.com/nature/journal/v455/n7214/full/nature07293.html>. [Page 151]
- [234] Miceli, P. F. & Palmstrøm, C. J. X-ray scattering from rotational disorder in epitaxial films: An unconventional mosaic crystal. *Physical Review B* **51**, 5506–5509

- (1995). URL <https://link.aps.org/doi/10.1103/PhysRevB.51.5506>. [Page 155]
- [235] Miceli, P. F., Weatherwax, J., Krentsel, T. & Palmstrøm, C. J. Specular and diffuse reflectivity from thin films containing misfit dislocations. *Physica B: Condensed Matter* **221**, 230–234 (1996). URL <http://www.sciencedirect.com/science/article/pii/0921452695009302>. [Page 155]
- [236] Kortan, A. R., Hong, M., Kwo, J., Mannaerts, J. P. & Kopylov, N. Structure of epitaxial Gd_2O_3 films grown on GaAs(100). *Physical Review B* **60**, 10913–10918 (1999). URL <https://link.aps.org/doi/10.1103/PhysRevB.60.10913>. [Pages 155 and 158]
- [237] Barabash, R. I., Donner, W. & Dosch, H. X-ray scattering from misfit dislocations in heteroepitaxial films: The case of Nb(110) on Al_2O_3 . *Applied Physics Letters* **78**, 443–445 (2001). URL <http://aip.scitation.org/doi/10.1063/1.1342215>. [Page 155]
- [238] Biegalski, M. D. *et al.* Critical thickness of high structural quality SrTiO_3 films grown on orthorhombic (101) DyScO_3 . *Journal of Applied Physics* **104**, 114109 (2008). URL <http://aip.scitation.org/doi/10.1063/1.3037216>. [Pages 155 and 158]
- [239] Kaganer, V. M., Köhler, R., Schmidbauer, M., Opitz, R. & Jenichen, B. X-ray diffraction peaks due to misfit dislocations in heteroepitaxial structures. *Physical Review B* **55**, 1793–1810 (1997). URL <https://link.aps.org/doi/10.1103/PhysRevB.55.1793>. [Page 155]
- [240] Warusawithana, M. P. *et al.* A Ferroelectric Oxide Made Directly on Silicon. *Science* **324**, 367–370 (2009). URL <http://science.sciencemag.org/content/324/5925/367>. [Page 159]
- [241] Glatz, A., Aranson, I. S., Baturina, T. I., Chtchelkatchev, N. M. & Vinokur, V. M. Self-organized superconducting textures in thin films. *Physical Review B* **84**, 024508 (2011). URL <https://link.aps.org/doi/10.1103/PhysRevB.84.024508>. [Page 159]
- [242] Eley, S., Gopalakrishnan, S., Goldbart, P. M. & Mason, N. Approaching zero-temperature metallic states in mesoscopic superconductor–normal–superconductor arrays. *Nature Physics* **8**, nphys2154 (2011). URL <https://www.nature.com/articles/nphys2154>. [Page 159]
- [243] Hopfield, J. J. Angular Momentum and Transition-Metal Superconductivity. *Phys-*

- ical Review* **186**, 443–451 (1969). URL <https://link.aps.org/doi/10.1103/PhysRev.186.443>. [Pages 163 and 196]
- [244] Hopfield, J. J. On the systematics of high T_c in transition metal materials. *Physica* **55**, 41–49 (1971). URL <http://www.sciencedirect.com/science/article/pii/0031891471902394>. [Page 163]
- [245] Stokes, H. T., Hatch, D. M. & Campbell, B. J. ISOTROPY Software Suite. URL <http://iso.byu.edu>. [Page 171]
- [246] Momma, K. & Izumi, F. VESTA 3 for three-dimensional visualization of crystal, volumetric and morphology data. *Journal of Applied Crystallography* **44**, 1272–1276 (2011). URL <http://scripts.iucr.org/cgi-bin/paper?db5098>. [Page 171]
- [247] Ahn, K.-H., Hariki, A., Lee, K.-W. & Kuneš, J. Antiferromagnetism in RuO_2 as d -wave Pomeranchuk instability. *Physical Review B* **99**, 184432 (2019). URL <https://link.aps.org/doi/10.1103/PhysRevB.99.184432>. [Pages 178 and 187]
- [248] Sutter, D. *et al.* Hallmarks of Hund’s coupling in the Mott insulator Ca_2RuO_4 . *Nature Communications* **8**, 15176 (2017). URL <http://www.nature.com/ncomms/2017/170505/ncomms15176/full/ncomms15176.html>. [Page 178]
- [249] Riccò, S. *et al.* In situ strain tuning of the metal-insulator-transition of Ca_2RuO_4 in angle-resolved photoemission experiments. *Nature Communications* **9**, 4535 (2018). URL <https://www.nature.com/articles/s41467-018-06945-0>. [Page 182]
- [250] Sutter, D. *et al.* Orbitally selective breakdown of Fermi liquid quasiparticles in $\text{Ca}_{1.8}\text{Sr}_{0.2}\text{RuO}_4$. *Physical Review B* **99**, 121115 (2019). URL <https://link.aps.org/doi/10.1103/PhysRevB.99.121115>. [Page 182]
- [251] Lanzara, A. *et al.* Evidence for ubiquitous strong electron–phonon coupling in high-temperature superconductors. *Nature* **412**, 510–514 (2001). URL <http://www.nature.com/articles/35087518>. [Page 186]
- [252] Iwasawa, H. *et al.* High-Energy Anomaly in the Band Dispersion of the Ruthenate Superconductor. *Physical Review Letters* **109**, 066404 (2012). URL <https://link.aps.org/doi/10.1103/PhysRevLett.109.066404>. [Page 186]
- [253] Iwasawa, H. *et al.* ‘True’ bosonic coupling strength in strongly correlated superconductors. *Scientific Reports* **3**, 1–4 (2013). URL <http://www.nature.com/articles/srep01930>. [Page 186]

- [254] Tamai, A. *et al.* Spin-orbit splitting of the Shockley surface state on Cu(111). *Physical Review B* **87**, 075113 (2013). URL <https://link.aps.org/doi/10.1103/PhysRevB.87.075113>. [Page 186]
- [255] Kim, Y. D. *et al.* Characterization of Various Oxygen Species on an Oxide Surface: RuO₂(110). *The Journal of Physical Chemistry B* **105**, 3752–3758 (2001). URL <https://doi.org/10.1021/jp003213j>. [Page 186]
- [256] Jovic, V. *et al.* Dirac nodal lines and flat-band surface state in the functional oxide RuO₂. *Physical Review B* **98**, 241101 (2018). URL <https://link.aps.org/doi/10.1103/PhysRevB.98.241101>. [Page 187]
- [257] Smith, T. F. & Chu, C. W. Will Pressure Destroy Superconductivity? *Physical Review* **159**, 353–358 (1967). URL <https://link.aps.org/doi/10.1103/PhysRev.159.353>. [Page 202]
- [258] Hamlin, J. J. Superconductivity in the metallic elements at high pressures. *Physica C: Superconductivity and its Applications* **514**, 59–76 (2015). URL <http://www.sciencedirect.com/science/article/pii/S0921453415000593>. [Pages 202 and 206]
- [259] Margine, E. R. & Giustino, F. Anisotropic Migdal-Eliashberg theory using Wannier functions. *Physical Review B* **87**, 024505 (2013). URL <https://link.aps.org/doi/10.1103/PhysRevB.87.024505>. [Page 202]
- [260] Aetukuri, N. B. *et al.* Control of the metal-insulator transition in vanadium dioxide by modifying orbital occupancy. *Nature Physics* **9**, 661–666 (2013). URL <http://www.nature.com/nphys/journal/v9/n10/full/nphys2733.html>. [Pages 202 and 211]
- [261] Alves, L. M. S. *et al.* Unconventional metallic behavior and superconductivity in the K-Mo-O system. *Physical Review B* **81**, 174532 (2010). URL <https://link.aps.org/doi/10.1103/PhysRevB.81.174532>. [Pages 202 and 210]
- [262] Alves, L. M. S. *et al.* Superconductivity and magnetism in the K_xMoO_{2-δ}. *Journal of Applied Physics* **112**, 073923 (2012). URL <http://aip.scitation.org/doi/10.1063/1.4757003>. [Pages 202 and 210]
- [263] Parker, D., Idrobo, J. C., Cantoni, C. & Sefat, A. S. Evidence for superconductivity at T_c = 12 K in oxygen-deficient MoO_{2-δ} and properties of molybdenum arsenide and oxide binaries. *Physical Review B* **90**, 054505 (2014). URL <https://link.aps.org/doi/10.1103/PhysRevB.90.054505>. [Pages 202 and 210]

- [264] Diebold, U. The surface science of titanium dioxide. *Surface Science Reports* **48**, 53–229 (2003). URL <http://www.sciencedirect.com/science/article/pii/S0167572902001000>. [Page 203]
- [265] Bisti, F. *et al.* Weakly-Correlated Nature of Ferromagnetism in Nonsymmorphic CrO₂ Revealed by Bulk-Sensitive Soft-X-Ray ARPES. *Physical Review X* **7**, 041067 (2017). URL <https://link.aps.org/doi/10.1103/PhysRevX.7.041067>. [Page 203]
- [266] Sun, Y., Zhang, Y., Liu, C.-X., Felser, C. & Yan, B. Dirac nodal lines and induced spin Hall effect in metallic rutile oxides. *Physical Review B* **95**, 235104 (2017). URL <https://link.aps.org/doi/10.1103/PhysRevB.95.235104>. [Page 203]
- [267] Sizoo, G. J. & Onnes, H. K. Further experiments with liquid helium. cb. influence of elastic deformation on the supraconductivity of tin and indium. *Commun. Phys. Lab. Univ. Leiden* **180b** (1925). [Page 206]
- [268] Dalichaouch, Y. *et al.* Impurity Scattering and Triplet Superconductivity in UPt₃. *Physical Review Letters* **75**, 3938–3941 (1995). URL <https://link.aps.org/doi/10.1103/PhysRevLett.75.3938>. [Page 206]
- [269] Mathur, N. D. *et al.* Magnetically mediated superconductivity in heavy fermion compounds. *Nature* **394**, 39–43 (1998). URL <http://www.nature.com/nature/journal/v394/n6688/full/394039a0.html>. [Page 206]
- [270] Ohtomo, A. & Hwang, H. Y. A high-mobility electron gas at the LaAlO₃/SrTiO₃ heterointerface. *Nature* **427**, 423 (2004). URL <https://www.nature.com/articles/nature02308>. [Page 207]
- [271] Moosburger-Will, J. *et al.* Fermi surface of MoO₂ studied by angle-resolved photoemission spectroscopy, de Haas–van Alphen measurements, and electronic structure calculations. *Physical Review B* **79**, 115113 (2009). URL <https://link.aps.org/doi/10.1103/PhysRevB.79.115113>. [Page 210]
- [272] Kawasaki, J. K. *et al.* Rutile IrO₂/TiO₂ superlattices: A hyperconnected analog to the Ruddelsden-Popper structure. *Physical Review Materials* **2**, 054206 (2018). URL <https://link.aps.org/doi/10.1103/PhysRevMaterials.2.054206>. [Page 211]